Nanoarchitectonics of Ultraporous Nanoparticle Networks for High Performance UV Photodetectors

Noushin Nasiri-Varg

March 2017

A thesis submitted for the degree of Doctor of Philosophy of
The Australian National University

The research described in this thesis is my own original work, except where otherwise acknowledged.

Noushin Nasiri
March 2017

This thesis is dedicated to my parents, Ebrahim and Behjat, who have always loved me unconditionally and whose good examples have taught me to work hard for the things that I aspire to achieve.

And also to my best and lovely friend, Leila, who has been a constant source of support and encouragement during the challenges of my PhD life.

Acknowledgements

I would like to express my sincere gratitude to my primary supervisor A/Prof. Antonio Tricoli, for his constant support and guidance over the last four years. I have grown a lot during this PhD and have always been able to count on Antonio throughout the many lab moves, failed and successful experiments, paper submissions and even my science communication journey. I would like to thank you for encouraging my research and for allowing me to grow as a research scientist. Your advice on both research as well as on my career have been priceless. I would also like to thank my committee members, Prof. Qinghua Qin and Dr. Matt Doolan for serving as my committee members even at hardship.

A special thank you to A/Prof. Lan Fu, who was not a member of my supervisory panel but treated me as one of her students in terms of offering her time and valuable knowledge during my PhD program. How lucky I was to have your support in these tough years of my life!

Through this PhD program, I have been lucky enough to work with several excellent research groups. I would like to acknowledge the assistance of many people who contributed to this research including Dr. Tobias Elmoe, A/Prof. Dave Nisbet, Dr. Thomas White, Dr. Fiona Black, Prof. Zbigniew Stachurski, Dr. Frank Brink and Dr. Kaushal Vora.

I would like to thank all my colleagues at the Nanotechnology Research Laboratory (NRL) for their friendship and support, and for creating an energetic working environment. A special thanks to Mr. Renheng Bo, who has been with me since the very beginning of this project and has patiently worked with me through the many trials and difficulties of my PhD program. Thank you!

I cannot forget friends who went through hard times together, cheered me on, and celebrated each accomplishment. And finally, my deep and sincere gratitude to my family for their continuous and unparalleled love, help and support. Words cannot express how grateful I am to my parents for all of the sacrifices that they have made on my behalf.

List of Publications

Published Articles

1- Antonio Tricoli, Noushin Nasiri, Sayan De, "*Wearable and Miniaturized Sensor Technologies for Personalized and Preventive Medicine*", **Advanced Functional Materials,** DOI: 10.1002/adfm.201605271, **2017**.

2- Noushin Nasiri, Renheng Bo, Lan Fu, Antonio Tricoli, "*Three-dimensional nano-heterojunction networks: a highly performing structure for fast visible-blind UV photodetectors*", **Nanoscale**, 9, 2059-2067, **2017**.

3- William SY Wong, Guanyu Liu, Noushin Nasiri, Chonglei Hao, Zuankai Wang, Antonio Tricoli, *"Omnidirectional Self-Assembly of Transparent Superoleophobic Nanotextures"*, **ACS Nano**, 11, 587–596, **2017**.

4- Renheng Bo, Noushin Nasiri, Hongjun Chen, Domenico Caputo, Lan Fu, Antonio Tricoli, *"Low-Voltage High-Performance UV Photodetectors: an Interplay between Grain Boundaries and Debye Length"*, **ACS Applied Material and Interfaces**, 9, 2606–2615, **2017**.

5- Yahuitl Osorio Mayon, Noushin Nasiri, Thomas P White, Antonio Tricoli, Kylie R Catchpole, *"Flame-made ultra-porous* TiO_2 *layers for perovskite solar cells"*, **Nanotechnology**, 27, 505403, **2016**.

6- Noushin Nasiri, Renheng Bo, Tak Fu Hung, Vellaisamy A.L. Roy, Lan Fu, Antonio Tricoli, "*Tunable Band-Selective UV-Photodetectors by 3D Self-Assembly of Heterogeneous Nanoparticle Networks*", **Advanced Functional Materials**, 26, 7359-7366, **2016**.

7- Noushin Nasiri, Renheng Bo, Hongjun Chen, Thomas P White, Lan Fu, Antonio Tricoli, "*Structural Engineering of Nano-Grain Boundaries for Low-Voltage UV-Photodetectors with Gigantic Photo-o Dark-Current Ratios*", **Advanced Optical Materials**, 4, 1787-1795, **2016**.

8- Antonio Tricoli, Noushin Nasiri, Hongjun Chen, Anna S Wallerand, Marco Righettoni, "*Ultra-Rapid Synthesis of Highly Porous and Robust Hierarchical ZnO Films for Dye Sensitized Solar Cells*", **Solar Energy**, 136, 553-559, **2016**.

9- Guanyu Liu, Siva Krishna Karuturi, Alexandr N Simonov, Monika Fekete, Hongjun Chen, Noushin Nasiri, Nhien H Le, Parvathala Reddy Narangari, Mykhaylo Lysevych, Thomas R Gengenbach, Adrian Lowe, Hark Hoe Tan, Chennupati Jagadish, Leone Spiccia, Antonio Tricoli, "*Robust Sub-Monolayers of* Co_3O_4 *Nano-Islands: A Highly Transparent Morphology for Efficient Water Oxidation Catalysis*", **Advanced Energy Materials**, 6, 1600697, **2016**.

10- Noushin Nasiri, Anthony Ceramidas, Shayanti Mukherjee, Anitha Panneerselvan, David R Nisbet, Antonio Tricoli, "*Ultra-Porous Nanoparticle Networks: A Biomimetic Coating Morphology for Enhanced Cellular Response and Infiltration*", **Scientific Reports**, 6, 24305, **2016**.

11- Guanyu Liu, William SY Wong, Noushin Nasiri, Antonio Tricoli, "*Ultraporous Superhydrophobic Gas-Permeable Nano-Layers by Scalable Solvent-Free One-Step* Self-Assembly", **Nanoscale**, 8, 6085-6093, **2016**.

12- Guanyu Liu, Jeremy Hall, Noushin Nasiri, Thomas Gengenbach, Leone Spiccia, Mun Hon Cheah, Antonio Tricoli, "*Scalable Synthesis of Efficient Water Oxidation Catalysts: Insights into the Activity of Flame-Made Manganese Oxide Nanocrystals*", **ChemSusChem**, 8, 4162, **2015**.

13- Noushin Nasiri, Renheng Bo, Fan Wang, Lan Fu, Antonio Tricoli, "*Ultraporous Electron-Depleted ZnO Nanoparticle Networks for Highly Sensitive Portable Visible-Blind UV Photodetectors*", **Advanced Materials**, 27, 4336-4343, **2015**.

14- William SY Wong, Noushin Nasiri, Guanyu Liu, Nicholas Rumsey-Hill, Vincent SJ Craig, David R Nisbet, Antonio Tricoli, "*Flexible Transparent Hierarchical Nanomesh for Rose Petal-Like Droplet Manipulation and Lossless Transfer*", **Advanced Materials Interfaces**, 2, 1500071, **2015**.

15- Noushin Nasiri, Tobias D Elmøe, Yun Liu, Qing H. Qin, Antonio Tricoli, “*Self-Assembly Dynamics and Accumulation Mechanisms of Ultra-Fine Nanoparticles”*, **Nanoscale**, 7, 9859-9867, **2015**.

16- William SY Wong, N Nasiri, AL Rodriguez, DR Nisbet, A Tricoli, “*Hierarchical Amorphous Nanofibers for Transparent Inherently Super-Hydrophilic Coatings*”, **Journal of Materials Chemistry A**, 2 , 15575-15581, **2014**.

Commonly Used Acronyms

UV	Ultraviolet
UNN	Ultraporous nanoparticle network
CMOS	Complementary metal–oxide–semiconductor
0D	Zero dimensional
1D	One dimensional
2D	Two dimensional
3D	Three dimensional
LEDs	Light-emitting diodes
CB	Conduction band
VB	Valence band
EQE	External Quantum Efficiency
LDR	Linear Dynamic Range
QDs	Quantum dots
VLS	Vapour-liquid-solid
CVD	Chemical vapour deposition
PLD	Pulsed laser deposition
ALD	Atomic laser deposition
MBE	Molecular beam epitaxy
MOCVD	Metal-organic chemical vapour deposition
SEM	Scanning Electron Microscopy
TCO	Transparent conductive oxide
TNRCs	Transferable TiO_2 nanorod cloths
FTO	Fluorine-doped tin oxide
PTE	Polyethylene terephthalate
UFP	Ultra-fine particles
TEM	Transmission electron microscopy
SD	Surface density
PET	Poly-ethylene-terephthalate
FSP	Flame spray pyrolysis
HAB	Height above the burner
RTD	Resistance temperature detector
XRD	X-Ray diffraction

BET	Brunauer-Emmett-Teller
SSA	Specific surface area
Vis	Visible
NIR	Near infrared
DC	Direct current
FTIR	Fourier Transfer Infrared Spectroscopy
IMONNs	Integrated metal-oxide nanoparticle networks
HMDSO	Hexamethyldisiloxane
TTIP	Titanium isopropoxide
EDX	Energy-dispersive X-ray
3DNH	Three-dimensional network of nanoscale heterojunctions
LD	Light density
SSB	Surface band bending
HAp	Hydroxyapatite
BCP	Biphasic calcium phosphate
WLI	White light interferometer
PBS	Phosphate buffered saline
TCP	Tissue culture plates
HMDS	Hexamethyldisilazane
BSA	Bovine serum albumin
DSC	Differential scanning calorimetry

Nomenclature

R	Responsivity
I_{ph}	Output current per unit area
P_{opt}	Illumination power per unit area
D	Detectivity
A	Effective area
B	Bandwidth
NEP	Noise-equivalent power
e	Electron charge
I_{dark}	Dark current
G	Photoconductive gain
N_{el} ($N_{electron}$)	Number of electrons collected per unit time
N_{ph} (N_{photon})	Number of absorbed photons per unit time
I_{photo}	Photo current
hv	Photon energy of incident light
P	Power of incident light
η	Quantum efficiency.
Φ	Photon flux
d_p	Particle diameter
F_d	Film thickness
L_d	Domain length
ε_{film}	Average film porosity
ε_{min}	Minimal film porosity
ε_{q-a}	Quasi-asymptotic film porosity
Pe	Péclet-number
D_p	Diffusion coefficient
v	Particle translational velocity
K_b	Boltzmann constant
T	Temperature
f	Friction coefficient
K_n	Knudsen number
μ	Viscosity

λ	Wavelength
C_c	Cunningham correction factor
T_F	Aerosol temperature
T_S	Surface temperature
T_p	Particle temperature
μ_F	Fluid dynamic viscosity
v_T	Thermophoretic velocity
ρ_F	Fluid density
δ_T	Boundary layer thickness
K_T	Thermophoretic coefficient
A_{dp}	Horizontal shadowed area
π	Pi number
A_{stat}	Collision area
A_{dyn}	Horizontal swept area
X	Brownian displacement
A_{over}	Overlapped area
K_{RPF}	Randomly Path Factor
λ_{dp}	Particle mean free path
t	Travelled time
α_{max}	Maximal incident angle
δ	Debye length
T_{Film}	Film average transmittance
$I_{Film-Out}$	Transmittance through the glass
T_{Glass}	Glass transmittance
d_{BET}	Particle sauter diameter
d_{TEM}	Average particle diamter
d_{XRD}	Average crystal size
nc	Carrier concentration
T_d	Deposition time
R_a	Root mean square (rms) surface roughness

Abstract

Accurate detection of ultraviolet radiation is critical to many technologies including wearable devices for skin cancer prevention, optical communication systems and missile launch detection. Si-based photodetectors, relying on n-p type semiconductor homojunction technology, are the most established commercial solution for measurement of ultraviolet light. These devices have some significant shortcomings including high operation voltage, the requirement of longpass filters to block low energy photons and cooling systems to reduce noise and leakage current. This significantly hinders their integration in wearable technologies and alternative solutions are intensively sought. Here, we report a hierarchical design and a rapid synthesis approach for the fabrication of highly performing visible-blind photodetectors based on wide bandgap semiconductors. Combined nano- and micro-scale fine-tuning of the film optical and electrical properties results in record-high photo-currents (milliampere) while preserving pico-ampere dark-currents and excellent selectivity to ultra-low ultraviolet (UV) light densities. In addition, we show that structural engineering of the nanoparticle grain boundaries can drastically enhance the performance of ultraporous nanoparticle network (UNN) photodetectors leading to gigantic photo to dark current ratios with low operation voltages (< 1 V). This is attributed to the optimal interplay of surface depletion and carrier conduction resulting in the formation of an open-neck grain boundary morphology. This is a significant improvement over state-of-the-art devices where a compromise is necessary between high photo-current and low dark-currents. As a result, these photodetectors do not require bulky and costly read-out circuitry and can be directly integrated in portable Complementary metal–oxide–semiconductor (CMOS) based electronics that is currently utilized in many wearable devices.

Furthermore, we present a highly performing nanoscale architecture for band-selective UV-photodetectors that features unique tunability and miniaturization potential. The device layout relies on the three dimensional (3D) integration of ultraporous layers of tailored nanoparticles. By tailoring the transmittance window between the indirect band gap of titanium dioxide (TiO_2) nanoparticles and the sharp edge of the direct band gap of zinc oxide (ZnO), we achieve a band-selective photoresponse with tunable bandwidth to less than 30 nm. However, a standing challenge with wide bandgap photodetectors is to drastically improve the sluggish response time of these nanostructured devices. In this research, we also present a three-dimensional nanoscale heterojunction architecture for fast-responsive visible-blind UV photodetectors. The device layout consists of p-type nickel oxide (NiO) clusters densely packed on the surface of an ultraporous network of electron-depleted n-type ZnO nanoparticles featuring a significant decrease in the rise and decay times compared to the pure ZnO device. These drastic enhancements in photoresponse dynamics are attributed to the stronger surface band bending and improved electron-hole separation of the nanoscale NiO/ZnO interface. These findings demonstrate a superior architecture for the engineering of miniaturized wearable UV-photodetectors with largely suppressed dark-currents, fast photo-current dynamics and ultra-low power consumption.

Table of Content

Chapter One

Wide bandgap Semiconductors for Visible-Blind Ultraviolet Photodetectors

1.1 Introduction

Wide bandgap semiconductors are an important class of materials for electronic and optoelectronic applications. Concerning the former, wide bandgap semiconductors are used in high power and high temperature electronic applications. These materials are also ideal for electronic applications where radiation hardness is required. With regards to the latter, ultraviolet, blue and green emitting semiconductor photodetectors, lasers and Light-emitting diodes (LEDs), and solid-state electroluminescent flat panel displays are examples of optoelectronic applications of wide bandgap semiconductors.

Wide bandgap ultraviolet photodetectors have gained particular momentum for their application in the area of ultraviolet optoelectronics, such as space communications, flame and missile launch detectors, and chemical sensors.[1-4] As the most common devices for UV photodetection, silicon photodetectors exhibit some intrinsic limitations, such as difficulty of blocking out visible and infrared photons and degradation of devices under UV irradiation. By contrast, for wide bandgap semiconductor-based UV photodetectors, these types of limitations are easily ruled out because of their wide and direct bandgaps and ability to operate in harsh environmental conditions. The ideal photodetector is generally designed to display a high responsivity, a good linearity of the photocurrent as a function of the incident optical power, a low noise level, and good visible rejection (i.e., high spectral selectivity). A short response time can also be of great importance in applications where a real-time fast signal treatment is necessary.

Recently, the use of low-dimensional wide-bandgap semiconductor nanostructures materials with tailored geometry as building blocks for visible-blind UV photodetectors has attracted intense attention. The electrical integration of synthesized low-dimensional nanostructures has been achieved with lithography and optical integration, which promises high speeds and greater device versatility. Low-dimensional nanostructures can be divided into zero-dimensional, one-dimensional (1D) and two-dimensional (2D) nanostructures, based on their shapes and morphologies. These wide bandgap semiconductor nanostructures, such as quantum dots (QDs), nanotubes, nanowires, nanorods, nanobelts, nanocables, core/shell structures, nanostructure arrays, epitaxial film and heterostructures are expected to play key roles in visible-blind UV photodetectors. Compared with UV photodetectors based on traditional thin-film and bulk materials, low-dimensional UV nanostructured photodetectors usually have the advantage of higher responsivity and photoconductivity gain because of their high surface-area-to-volume ratios and the reduced dimension of the effective conductive channel.

Generally, the large surface-to-volume ratio significantly increases the number of surface trap states and prolongs the photocarrier lifetime. In addition, the reduced dimensionality can confine the active area of the charge carrier and shorten the transit time. For fabrication of visible-blind UV photodetectors, many wide-bandgap materials with bandgap larger than 3.3eV have been investigated as building blocks of visible-blind UV photodetectors, including gallium nitride (GaN), tin oxide (SnO_2), TiO_2, silicon carbide (SiC) and ZnO. Furthermore, nano- and microstructured wide bandgap UV photodetectors have been produced by several methods, such as physical vapour deposition including magnetron sputtering[5-7] and pulsed laser deposition,[8-11] chemical vapour deposition,[12-13] flame spray pyrolysis[14] and sol-gel.[15-16]

In this chapter, we provide a comprehensive review of the state-of-the-art research activities on wide bandgap semiconductor UV photodetectors. We concentrate on a number of different semiconductors reported as potential wide bandgap materials for various photodetecting applications and on a variety of nanostructured morphologies fabricated in the area of high-performance UV photodetectors.

1.2 Photodetection Mechanism

Wide bandgap semiconductors have been investigated under different conditions to understand the fundamental process and enhancing the response to the UV light. The key principle on which photodetection relies is the conversion of absorbed photons into an electrical signal. The photoresponse characteristics of nanostructured devices are significantly influenced by a number of factors, such as the presence of different amounts of defect concentration in the material, crystallographic orientation, grain size, and processing condition. These factors could influence the photoresponse characteristics and explain the large variation in photoresponse results previously reported by various groups for the same material. Several different mechanisms by which this can be accomplished in ultraviolet photodetectors have been reported. Herein, we mainly focus on three different type of device structure, which can serve as a guideline for understanding the structural-functional relations of nanostructured photodetector devices fabricated by several synthesis methods.

1.2.1 Photoresistors

A photoconductor, consisting of a semiconductor with two ohmic contacts, is essentially a radiation-sensitive resistor. The schematic structure and operation of the photoconductor are shown in Figure 1.1a,b. ZnO is the most common UV photoresistor investigated in detail by a number of groups resulting in significantly high photodetection performance. The high photodetection properties of ZnO are the results of oxygen-related hole-trap states at the photodetector surface.[2,17] In fact, the surface traps tend to adsorb oxygen molecules from the air causing capture of free electrons from the n-type semiconductor (Figure 1.2).[14] This leads to the formation of an electron depletion region near the surface which induces surface band bending and significantly decreases the device's conductance (Figure 1.2c). Such a surface band bending establishes an internal electric filed, which can spatially separate photo-generated electron-holes leading to suppressed photo-carrier recombination and dramatically prolonging carrier life-times. These effects are particularly prominent in nanocrystalline films, where the surface area is large and the depletion regions may extend throughout the entire bulk of the film.

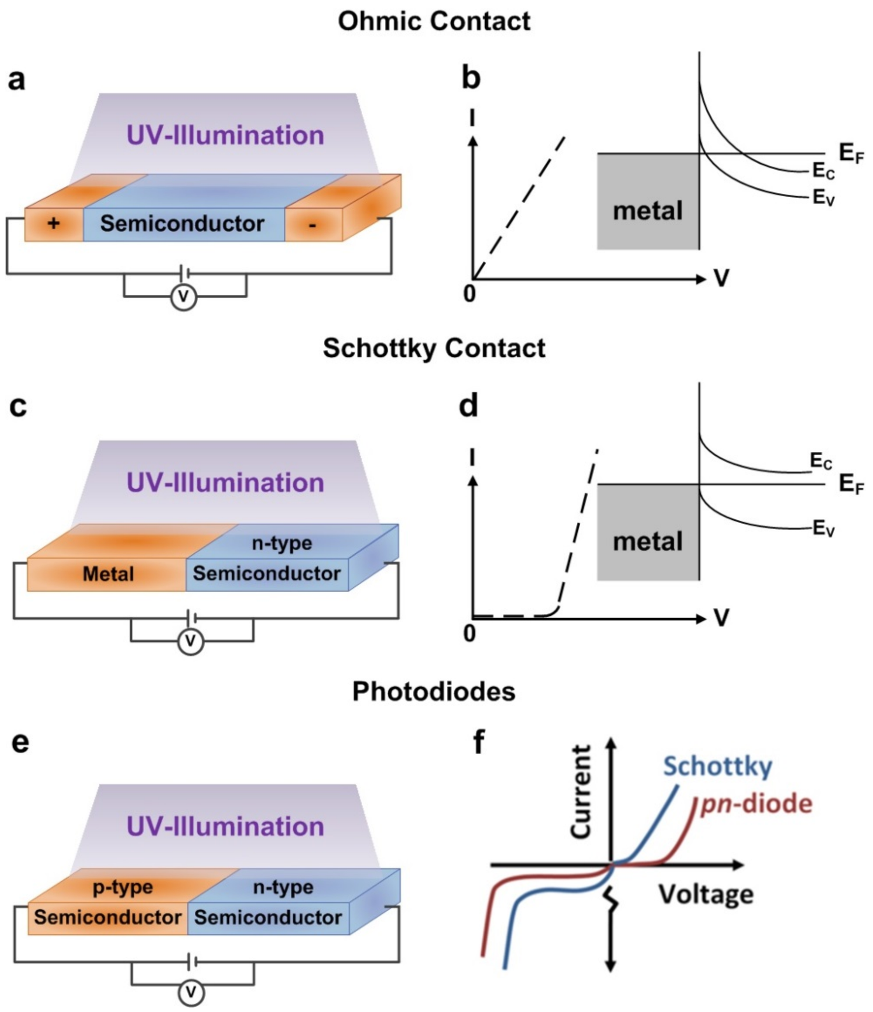

Figure 1.1 *Schematic and current-voltage characteristic of (a,b) Ohmic contact photoresistor, (c,d) Schottky contact and (e,f) photodiodes.*

Upon illumination with photon energy higher or equal to the semiconductor band gap, electron-hole pairs are generated. In fact, the electrons in the valence band (VB) could be excited to the connection band (CB) with simultaneous generation of the same number of holes in the VB (Figure 1.2b). The holes that migrate to the surface along the potential gradient produced by band-bending either discharge the negatively charged adsorbed oxygen ions to photodesorb oxygen from the surfaces or effectively get trapped at the ZnO surfaces

(Figure 1.2b,d). This results in an increase in the free carrier concentration and a decrease in the width of the depletion layer (Figure 1.2b,d). When the UV illumination is turned off, the residual accumulated holes recombine with the unpaired electrons, while oxygen is gradually reabsorbed into the surface resulting in a slow current decay.

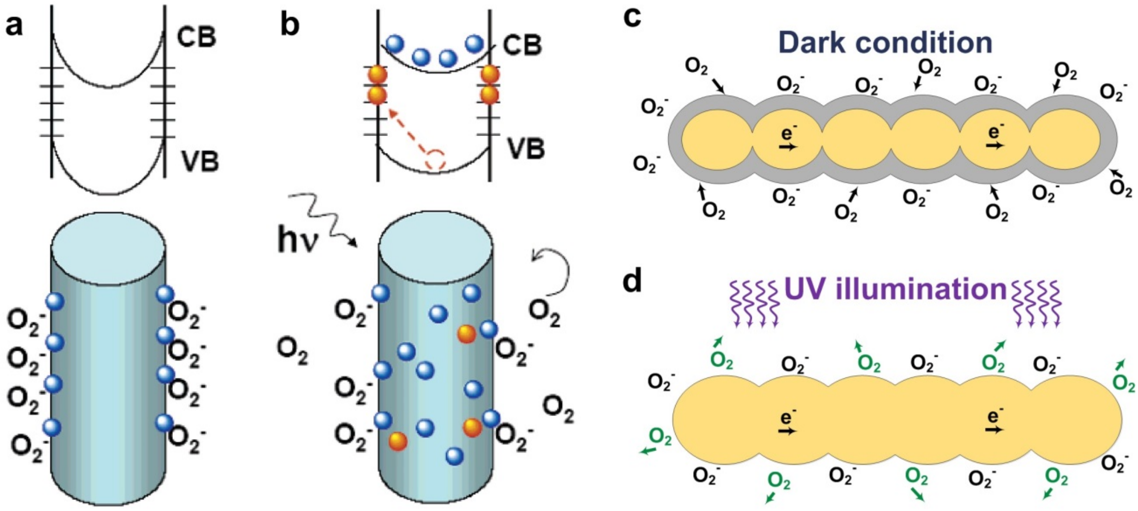

Figure 1.2. *Schematic of a (a,b) nanowire and a (c,d) nanoparticles network photoconductor under (a,c) dark condition and (b,d) UV illumination. In the dark condition (a,c), oxygen molecules adsorbed at the surface that capture the free electron present in the n-type semiconductor forming low-conductivity depletion layer near the surface. Under UV illumination (b,d), photogenerated holes migrate to the surface and are trapped, leaving behind unpaired electrons in the naowire that contribute to the photocurrent. The lifetime of the unpaired electrons is further increased by oxygen molecules desorption from the surface when holes neutralize the oxygen ions.*

1.2.2 Schottky Contacts

Schottky diodes in their simplest form consist of a metal layer, such as gold, silver and aluminum, in contact with a moderately doped n-type semiconductor. Figure 1.1c,d present the schematic structure of the Schottky contact photodetector. It is a unipolar device because it has electrons as majority carriers on both sides of the junction. Hence, there is no depletion layer formed near the junction and no significant current from the metal to the semiconductor with reverse bias. Thus, the delay present in the junction diodes due to hole-electron recombination time is absent here.

Due to the electrostatic barrier between the metal and the semiconductor caused by the difference in their work functions, the Schottky contact devices exhibit a rectifying behaviour. Here, two mechanisms contribute to the photoresponse. The first is the ‘‘primary current’’ maintained by carriers optically generated in the depletion region. The ‘‘secondary current’’ is due to the lowering of the Schottky barrier caused by illumination and trapping at interface states. In fact, in the Schottky contact devices, the photogenerated electron-hole pairs can be separated quickly by the local electric field at the Schottky barrier region, which would reduce the electron-hole recombination rates and increase the carrier lifetime, resulting in an increase in the free carrier density. The increased carrier density in the semiconductor photodetector changes the Fermi energy and the work function of semiconductor, resulting in the reduction of the Schottky barrier height and width between the semiconductor layer and electrodes. Both of these account for the high photocurrent on-off ratio and rapid rising speed of the UV detectors based on Schottky. Once the UV illumination is turned off, electron-hole pairs will quickly recombine in the photodetector device and the Schottky barrier is recovered, which may explain the fast recovery speed in these types of UV photodetectors.

1.2.3 Photodiodes

A photodiode is a p-n junction or p-i-n structure which is commonly used in a variety of applications, including UV photodetection. The device consists of a highly-doped transparent p-type layer and an n-type highly doped layer (Figure 1.1e) with an undoped absorbing layer in the middle in the case of p-i-n structure. When p-type and n-type materials are placed in contact with each other, the junction behaves very differently than either type of material alone (Figure 1.1f). Specifically, current will flow readily in one direction (forward biased) but not in the other (reverse biased), creating the basic diode (Figure 1.1f). This non-reversing behavior arises from the nature of the charge transport process in the two types of materials. In the p-type region, there are holes from the acceptor impurities and in the n-type region there are extra electrons. When a p-n junction is formed, some of the electrons from the n-region which have reached the conduction band are free to diffuse across the junction and combine with holes. Filling a hole makes a negative ion and leaves behind a positive ion on the n-side. A space charge builds up, creating a depletion region which inhibits any further electron transfer unless it is helped by putting a forward bias on the junction. Under UV illumination, the photogenerated electron-hole pairs contribute to an induced photocurrent with a large transport under reverse bias.

1.3 Key Figures of Merit

Photodetection is a process of converting light signals to electric signals including three physical mechanisms of light harvesting, exciton separation, and charge carrier transport to corresponding electrodes. In order to quantify and compare the performance of different types of photodetectors, it is essential to have an in-depth understanding of their figures of merit. In the past several decades, a number of different figures of merit have been introduced in order to characterize UV photodetectors. Here we only discuss the figures of merit that are currently accepted and used by several groups in the UV photodetecting field.

1.3.1 Responsivity

By definition, responsivity is the ratio of photo-current obtained by a device per unit area to the incident light power at a given wavelength and can be calculated as follows:

$$R = \frac{I_{ph}}{P_{opt}} \tag{1-1}$$

where I_{ph} is the output current obtained by the device per unit area and P_{opt} is the illumination power on the detection area of the device. The spectral response of the photodetector is obtained by plotting the responsivity against the wavelength, and usually follows the absorption spectrum of the photosensitive semiconductor material used for the fabrication of the detector.

1.3.2 Specific Detectivity

Another important figure of merit is the detectivity, which represents the ability to detect signal from noise and is defined as:

$$D = \frac{\sqrt{AB}}{NEP} \tag{1-2}$$

where A is the effective area of the detector, B is bandwidth and NEP is the noise-equivalent power. If the dark-current is the major contribution to the noise limiting the detectivity, this equation can be simplified as follows[18]:

$$D = \frac{R}{\left(2e\,.\frac{I_{dark}}{A}\right)^{1/2}} \tag{1-3}$$

where R is the responsivity, e is the electron charge (1.6 × 10^{-19} coulombs) and I_{Dark} is the dark current of the device.

1.3.3 Photoconductive Gain

By definition, photoconductive gain (G) is defined as the ratio of the number of electrons collected per unit time (N_{el}) to the number of absorbed photons per unit time (N_{ph}) which can be derived by:

$$G = \frac{N_{electron}}{N_{photon}} = \left(\frac{I_{photo} - I_{dark}}{e}\right)\left(\frac{hv}{P}\right)\frac{1}{\eta} \tag{1-4}$$

Where I_{photo}, is the photo current, I_{dark}, is the dark current, e is the electron charge (1.6 × 10^{-19} coulombs), hv is the photon energy of incident light (5.37 × 10^{-19} J for 370 nm), P is the power of incident light and η is the quantum efficiency.

1.3.4 External Quantum Efficiency (EQE)

The efficiency of light energy utilization can be described by EQE:

$$EQE = \frac{I_{photo}}{e\Phi} = \frac{hv}{e}\frac{I_{photo}}{P} \tag{1-5}$$

where I_{photo} is the photo current, e is the electron charge (1.6×10^{-19} coulombs), Φ is the photon flux, defined as the number of incident photons, hv is the energy of one single photon and P is the power of incident light.

1.3.5 Linear Dynamic Range (LDR)

The LDR of a detector is a measurement of the minimum detectable signal, to the maximum signal that will start to compress the detector. LDR is one of the important figures of merit for a photodetector which is defined as the maximum linear response of the device divided by the detector noise. Most detectors eventually become non-linear as sample size is increased and this upper point is usually well defined. The LDR can be calculated as:

$$LDR = 20\log(\frac{I_{photo}}{I_{dark}}) \qquad (1\text{-}5)$$

where I_{photo} is the photocurrent and I_{dark} is the dark current.

1.4 Photodetector's Nanostructure

1.4.1 Zero Dimensional (0D) Nanostructures

Quantum dots (QDs) are small semiconducting nanocrystals (2-10 nm)[19] that can be made of a variety of different elements, such as silicon (Si),[20-21] cadmium selenide (CdSe)[22-23] or cadmium sulphide (CdS).[24-25] The size, energy levels and emission colour of QDs can be precisely controlled, which makes them extremely useful in a variety of applications. Because of their reduced size, QDs behave differently from bulk solids due to the quantum-confinement effects that are responsible for their remarkably attractive properties.[19] These semiconducting materials are able to absorb light and transform it into different colours when they release the absorbed energy.[26] The specific colour that QD produced depends on their size (Figure 1.3a) and not the material.[26] In fact, their bandgap changes in accordance with their size due to quantum confinement. When light excites the QD, the larger the size of the dot, the lower the energy waves would be, resulting in a redder light.[27] In contrast, reducing the side of QDs leads to exciting a bluer light (Figure 1.3a).[27]

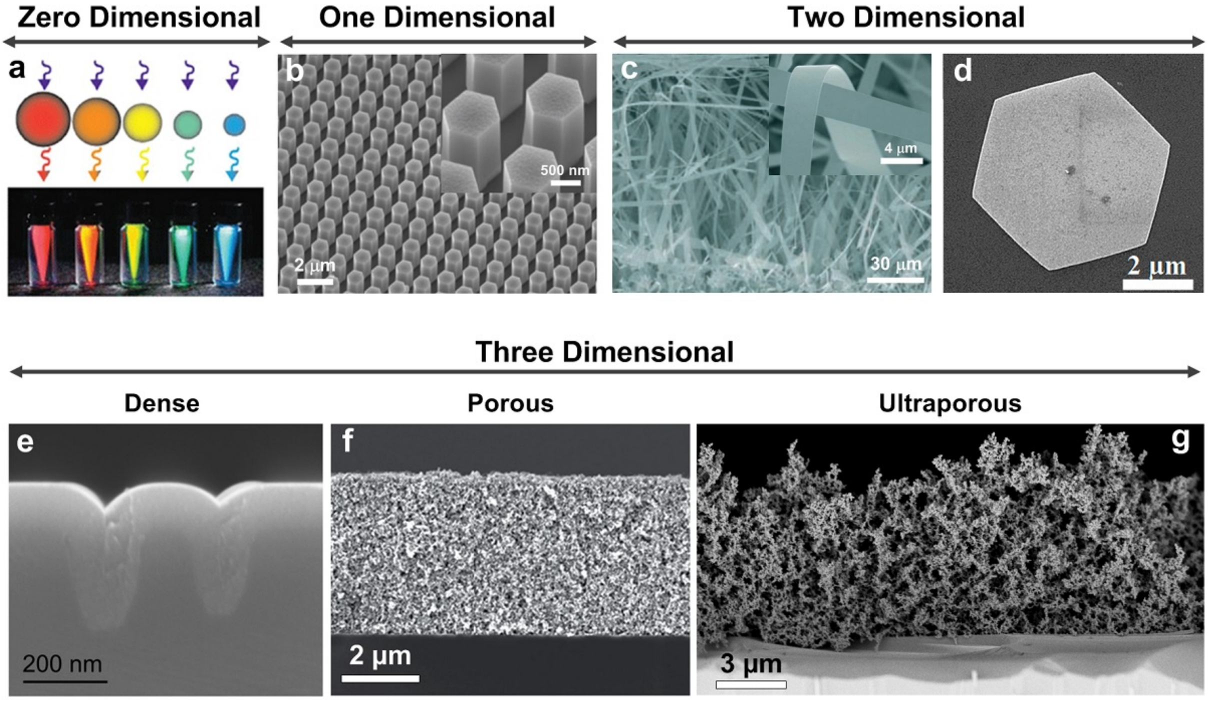

Figure 1.3. *(a) Colloidal quantum dots irradiated with a UV light. Different sized quantum dots emit different colour light due to quantum confinement. SEM image of (b) regularly patterned ZnO nanorods grown with the hydrothermal method,*[28] *(c) belt-like structure fabricated by an improved vapour-liquid-solid (VLS) process with a uniform belt thickness of ~200 nm*[29] *and (d) ZnO nanodisk with a diameter of 5 µm fabricated by drop-casting process.*[30] *Cross-sectional SEM image of (e) dense* TiO_2 *structure grown on silicon slot structures using atomic layer deposition technique,*[31] *(f) porous* TiO_2 *film on the silicon substrate fabricated by spin-coating technique*[32] *and (g) ultraporous nanoparticles network made by flame spray pyrolysis system.*[14]

History of QDs begins with their first discovery in glass crystals in the 1980s by A. I. Ekimov and his colleagues at the loffe Physical-Technical Institute in St. Petersburg.[33] They noticed unusual optical spectra from samples of glass containing the semiconductors cadmium sulphide or cadmium selenide.[33] Systematic advancement in the science and technology of QDs came after 1984, when Luis Brus discovered the relation between size and bandgap for semiconductor nanoparticles.[34] However, it took nearly a decade for a new level in QD research to reach with the successful synthesis of colloidal Cd_X (X = S, Se, Te) QDs with size-tunable band-edge absorption and emissions.[35] To date, various methods have been developed to synthesize monodisperse and solution-stable QDs of less than 10 nm, including hydrothermal method,[36] electrochemical strategies,[37] the solution chemistry method,[38] and the ultrasonic and microwave method.[39]

1.4.2 One Dimensional (1D) Nanostructures

1.4.2.1 Nanowires

Nanowires are 1D nanomaterials with diameters in the order of a few hundred nanometres or less, and lengths ranging from several hundreds of nanometre to as long as a few centimetres.[40-41] Because of their nanoscale dimensions in the radial direction, they have size confinement effects that give them novel physical properties compared to bulk materials. Benefitting from a large surface-to-volume ratio and a Debye length comparable to their small size, 1D semiconductor nanostructures are considered the most promising building blocks for photodetectors with superior sensitivity, high quantum efficiency, and fast response speed.[42-45] The length and diameter of nanowires as well as their alignment affect the emission and absorption properties and need to be controlled since they dominate the physical, chemical and optical states of nanowires.[40,42,46] In fact, the critical device size is defined during the growth process and can be controlled with atomic scale resolution. The key issue related to the growth of nanowires is how to induce 1D crystal growth in a controlled manner. Regarding this, many approaches have been studied, including vapour-liquid-solid (VLS),[47] chemical vapour deposition (CVD),[13,48-49] wet synthesis[50] and pulsed laser deposition (PLD).[51]

1.4.2.2 Nanorods

Similar to the nanowires, nanorods with a dimension range from 1 to 500 nm (Figure 1.3b), have been the focus of considerable attention because of their potential to answer fundamental questions about one-dimensional systems and their critical role in different applications ranging from molecular electronics to novel scanning microscopy probes.[52-54] In the device applications of nanorods, it is important not only to grow nanorods with a high degree of regularity and uniformity in terms of their height and cross-sectional size, but also to accurately control their positions (Figure 1.3b).[55-57] Good control of nanorods position and shape can improve the performance of fabricated electronic and optoelectronic devices.[11,56,58]

1.4.3 Two Dimensional (2D) Nanostructures

Nanobelts, with intermediate morphology between one and two dimensional (Figure 1.3c), have been intensively studied in the last few years, because they may be the ideal system to fully understand dimensionally confined transport phenomena and building functional devices along individual nanobelts.[1,29,59-60] They were reported by Wang and co-workers for the first time in 2001[61] as a structurally controlled nanomaterial with well-defined facets, unique growth directions, and a typical rectangular cross section. With large surface areas exposed to the light, various kinds of nanobelts have been assembled into nanoscale optical devices.

As mentioned previously, nanostructured materials with lower dimensionality can lead to higher optical responses as compared to their bulk counterparts. In fact, the electron and hole energy states become discrete due to the spatial confinement, which will considerably prolong the photocarrier lifetime.[62-63] However, the electrical performance of QD devices is limited due to the severe scattering from a very large number of grain boundaries within the QD device with the nanoscale grain size.[64] For the 1D materials, the incomplete surface coverage is considered as a drawback for their photodetection performance.[62] Therefore, ultrathin 2D nanostructures are more able to satisfy the requirements of ultrathin structures, low-cost, portability, and mechanical stability in high performance flexile optoelectronic devices.[65] In addition, it has been reported that polar facets of some nanostructures, such as ZnO, contain more oxygen vacancies than the other facets, which have a significant impact on the electronic properties and enhance the efficiency of the electron-hole separation.[30,66] Hence, the efficient separation of charges and the low dimensionality of the conductive volume should be particularly significant for the presented thin nanodisks (Figure 1.3d) combining large surface-to-volume ratio and polar exposed facets.[30] In fact, the high quality of single crystal ZnO nanodisks and nanosheets results in a reduction of the disadvantageous effects of grain boundary recombination, as well as enhancing carrier transport, providing a high active area of the charge carriers. Compared to the QDs zero dimensional structure and the nanowires, nanorods and nanoribbons one dimensional structure, the 2D structures can be more compatible with available micro-fabrication techniques, and can be more easily transformed into more complex structures.[67]

1.4.4 Nanostructured Films

1.4.4.1 Dense Structures

Nanostructured dense films (Figure 1.3e) fabricated by different methods such as atomic laser deposition (ALD) and molecular beam epitaxy (MBE) have been investigated in the past decades as UV photodetectors resulting in high photodetection properties and fast photoresponse to UV illumination. Ultrathin nanostructured films are of particular interest, due to the device potential involving the quantum confinement effects. The optoelectronic properties of nanometer-thickness films, however, are often controlled by the surface-dominated phenomena due to the large surface-to-volume ratio. In fact, extremely thin films with thickness smaller than twice Debye length are required to ensure the participation of the whole structure in the photodetection mechanism avoiding the formation of non-electron-depleted domain that could act as bottlenecks. However, this ultralow thickness might results in low conductivity and poor mechanical stability of the device.

1.4.4.2 Porous Structures

The porous nanostructured films (Figure 1.3f) are the most common structures used in UV photodetection field due to their higher active area resulting in more adsorptive capacity enhancing the photodetection performance of the fabricated device. Several methods, such as hydrothermal, sol-gel and other wet synthesis methods are utilized previously to fabricate porous nanostructure films as UV photodetectors. The surface area of the nonporous films made by wet synthesis methods is also found to be highly dependent on the number of coatings on the substrate. In fact, a single layer film is a porous structure regardless of the film thickness. While, if the film is prepared with multi-layers, the pores in the first layer will be filled by the following layer. Compared to the dense films, porous structures enhance light harvesting by reducing the reflection and the transmission. Two reasons are responsible for higher light absorption of the porous sample. One is the film thickness and the other is the stronger light scattering in a porous sample. The porous film is recognized to enhance the light harvesting due to light scattering within the pores by increasing the optical path length of light, especially in the wavelength range corresponding to the band edge. The results suggest that the porous structure can enhance light absorption more effectively near band edge region.

1.4.4.3 Ultraporous Structures

Very recently, ultraporous nanoparticle networks (98% porosity) have been reported[14,68-70] as a highly performing super-structural design (Figure 1.3g) for visible-blind UV-photodetectors. The authors claimed that in addition to the particle morphology,[10] film thickness,[71] and grain necking,[66] a key structural property impacting the performance of wide bandgap photodetectors is the film porosity.[14,68-70]

Figure 1.4 present the *I-V* characteristic of spin-coated porous nanostructure[72] and flame-made ultraporous ZnO-based photodetectors[14] at the applied bias of 5 V but different density of UV light. This comparison revealed a 10^3 order of magnitude lower photo-current of ca. 2 mA for spin-coated porous structure even under 8 time higher light density (830 μW.cm^{-2}).[72] While the ultraporous structure resulted in higher photo-current of 1.2 mA at very low light density of 100 μW.cm^{-2}.[14] As a result, it is found that the ultraporous structures have a superior performance as photodetectors offering several advantages such as high photocurrents (miliampere), low dark currents (nanoampere) and detection limit of low light densities at low operation voltages. In fact, the strong penetration of light in these ultraporous nanostructures allow photo-excitation of the bottom layers of the device resulting in significantly higher light absorption and electrical conductivity compared to the other nanostructured films.[14,72] In contrast, for the porous structures with the film porosity between 40% and 60%, the higher proportion of UV light might be absorbed by the top layers of the device which are not connected to the electrodes,[72] resulting in absorption of significantly smaller fraction of incoming UV light in bottom layers of the film, and thus lower optical density.

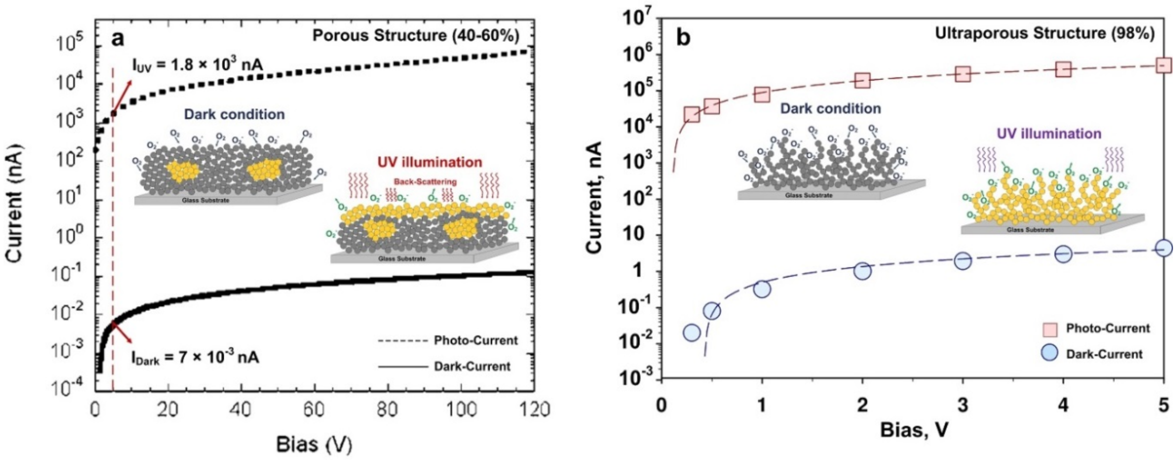

Figure 1.4. *I-V characteristics of ZnO-based photodetectors with porous structure fabricated by spin-coating method*[72] *in comparison with ultraporous structure made by flame spray pyrolysis synthesis.*[14] *The photodetection properties of the fabricated devices were investigated under UV illumination with the light density of 830 and 100 μW.cm*$^{-2}$*, for porous and ultraporous structures, respectively.*

1.5 Materials

There are a number of semiconductors reported as potential wide bandgap materials for various photodetection applications, such as chemical, environmental, and biological analysis, monitoring flame and radiation detection, astronomical studies, and optical communications. In this section, recent progresses in UV photodetection properties are highlighted with respect to several kinds of wide bandgap semiconductors, including TiO_2,[73-76] SiC,[77-78] ZnO,[14,44,72,79] GaN[80-82] and SnO_2.[42,83]

1.5.1 SiC-based photodetectors

SiC is considered as one of the most important wide band gap materials (~2.2-3.0 eV)[84-85] in the development of UV photodetectors because of their large gains, high signal-to-noise ratios and solar-blind operation.[77,86-87] These properties make SiC a promising material in certain applications for monitoring the UV spectrum without the need for solar rejection filters.[88-89] Furthermore, semiconductor SiC offers a high thermal conductivity (~120 $W.m^{-1}K^{-1}$),[90-91] high hardness and Young's modulus (typically ~450 GPa compared with ~130 GPa for Si),[92-93] and an outstanding long term stability even under high-intensity UV radiation and high operating temperature.[77,89] This combination of excellent electronic and mechanical properties offers many possibilities for using SiC as a material for a wide range of sensors, particularly in applications featuring high temperatures or hostile environments.[78,94-96]

The SiC exists in a large number of polytypes which are different crystal structures built from the same Si-C sub-unit organized into a variety of stacking sequences.[97-98] There are over 100 of these polytypes known,[99] but the majority of research and development has focused on 3C, 6H and 4H.[84,86-87,100] Among them, the 4H-SiC (3.2 eV)[101] is the most common polytype for electronic devices, due to its overall superior material properties.[102-104]

Typically, 4H-SiC based UV photodetectors achieve photosensitivity spectrum of 200-380 nm and peak responsivity at around 290 nm.[102-104]

Nanostructured SiC has superior properties compared to bulk SiC for applications in light-emitting diodes and UV photodetectors due to the higher light-emission efficiency. The first commercial nanostructured photodetector device based on SiC was fabricated on p-type 6H-SiC in 1993[105] and presented a very low dark current of about 100 nA.cm^{-2} at 1.0 V reverse bias even at a temperature of 200°C.[105] Recently more and more research groups have paid attention to the development of high-performance UV photodetectors using 4H-SiC material systems.[77,103-104,106-107] For example, by using laser plasma deposition system, Aldalbahi et al.[77] developed a 2 μm thick SiC film on Si-wafer with a responsivity of up to 0.18 A.W^{-1} at illumination density of 2 mW.cm^{-2}, which is significantly higher compared to the SiC UV detectors previously reported (0.03-0.08 A.W$^{-1)}$.[106,108-109] In addition, a response time of 18 s under 350 nm wavelength of incident radiation was observed.[77]

1.5.2 GaN-based photodetectors

GaN with a room-temperature bandgap of 3.39 eV (366 nm) is among the most promising material for semiconductor photonic devices operating in the UV regions of the spectrum.[40,44,82,110] The transparency of high quality GaN at wavelengths longer than the band gap[111-112] make it an ideal material for photodetectors capable of rejecting near infrared and visible regions of the solar spectrum while retaining near unity quantum efficiency in the UV.[113] The superior radiation hardness and high temperature resistance of GaN make the fabricated devices suitable for working in extreme conditions.[114] Moreover, by using its alloys with aluminium and indium, the cut-off wavelength will be tunable in the range from 366 nm to 200 nm.[115]

Various types of GaN-based photodetectors have been reported, including p-n junctions,[116-118] Schottky barrier photodetectors,[119-121] solar-blind ultraviolet photodetectors,[122-124] and UV avalanche photodiodes.[125-127] The motivation to investigation *p-n* photodetectors is to take advantage of its structure for better sensitivity and faster response.[116-118] Chen *et al.*[80] were the first to report a self-powered GaN p-n junction photodetectors with an abrupt wavelength cut-off at 370 nm, a responsivity of 90 mA.W^{-1} at 370 and a response time of ∼0.4 ms at 325 nm at zero bias.

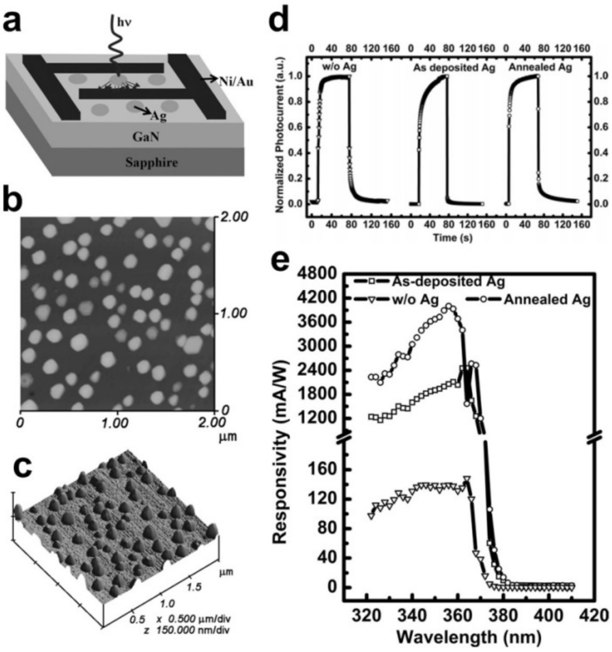

Figure 1.5. *(a) Schematic and (b,c) AFM analysis of the GaN-based photodetector fabricated using MOCVD after Ag nanoparticles deposition.[113] The (d) photoresponse and (e) responsivity of the GaN-based photodetectors with and without Ag under an applied bias of 5 V.[113]*

Recently[113] nanoplasmonic enhancement using Ag nanoparticles was proposed as a great method for improving the performance of GaN-based devices. Li et al.[113] have reported that through the excitation of the surface plasmon, the incident light interacts with Ag nanoparticle and significantly enhances the scattering cross-section (Figure 1.5a-c). They have grown a ∼3 μm thick GaN epilayer on a sapphire substrate using metal-organic chemical vapour deposition (MOCVD) and Ag metal nanoparticles were deposited on the surface of GaN by electron beam evaporation (Figure 1.5a). The responsivity of the fabricated device increased by a factor of 30 with annealed Ag nanoparticles on the GaN surface from 0.148 $A.W^{-1}$ to 4.0 $A.W^{-1}$ (Figure 1.5d,e).[113]

Schottky structure is also a good choice of producing GaN-based ultraviolet photodetectors since it does not need the realization of p-type GaN material. However, fabricating high performance GaN Schottky barrier ultraviolet photodetector is still challenging due to the problem of surface states, which increase the recombination of photo-generated electron-hole pairs.[128-129] To accelerate the development of GaN Schottky barrier photodetectors, it is necessary to reduce the negative influence of surface states on their performance.

1.5.3 SnO_2-based photodetectors

Among a variety of semiconductor compounds available for UV detecting application, SnO_2 is a very interesting n-type semiconductor with a wide direct bandgap of ≈3.6 eV (≈340 nm)[8,130] and transparency in the visible-light region of the spectrum,[41,131] and thus has been proposed to be applied as a potential material for visible-blind photodetectors.[74,132] In addition, SnO_2 found its application in field emission since it has a relatively low work function (4.7 eV)[133-134] in contrast to carbon nanotube (5 eV)[135-136] and ZnO (5.3 eV).[137-138] The electrical conductivity of intrinsic SnO_2 depends strongly on the surface properties of this material. In fact, surface molecular adsorption/desorption affects the band modulation and space-charge layer which make SnO_2 an important conductance-type gas-sensing material.[139-142] Due to the complicated spatial arrangement, the hierarchical architectures can provide extraordinarily high activated surface area[141-142] and also robustness.[143] Thus far, the reported SnO_2 nanostructures are mostly one dimensional structures, such as nanowires,[144-147] nanorods,[58,148-149] nanobelts,[59,150-151] and nanotubes.[152-154]

Recently, thin SnO_2 nanowires with uniform diameter of 26 nm (Figure 1.6a) were synthesized by a facile VLS process with Au-layer as catalyst (Figure 1.6b).[42] The fabricated photodetector exhibited a photo-current and dark-current of 2.1 μA and 19.4 nA with I_{UV}/I_{dark} ratio of 10^2 (Figure 1.6e) under 320 nm light illumination with the density of 0.91 mW.cm^{-2}.[42] In another approach,[130] a 2D SnO_2 monolayer nanofilm (Figure 1.6c,d) was fabricated using an oil-water interfacial self-assembly method resulting in a significantly higher photocurrent of 375 μA (Figure 1.6f) at the same light illumination and applied bias. However, the device exhibited low photo- to dark-current ratio of only 4[130] due to a significantly higher dark-current of 90 μA (Figure 1.6f).[130]

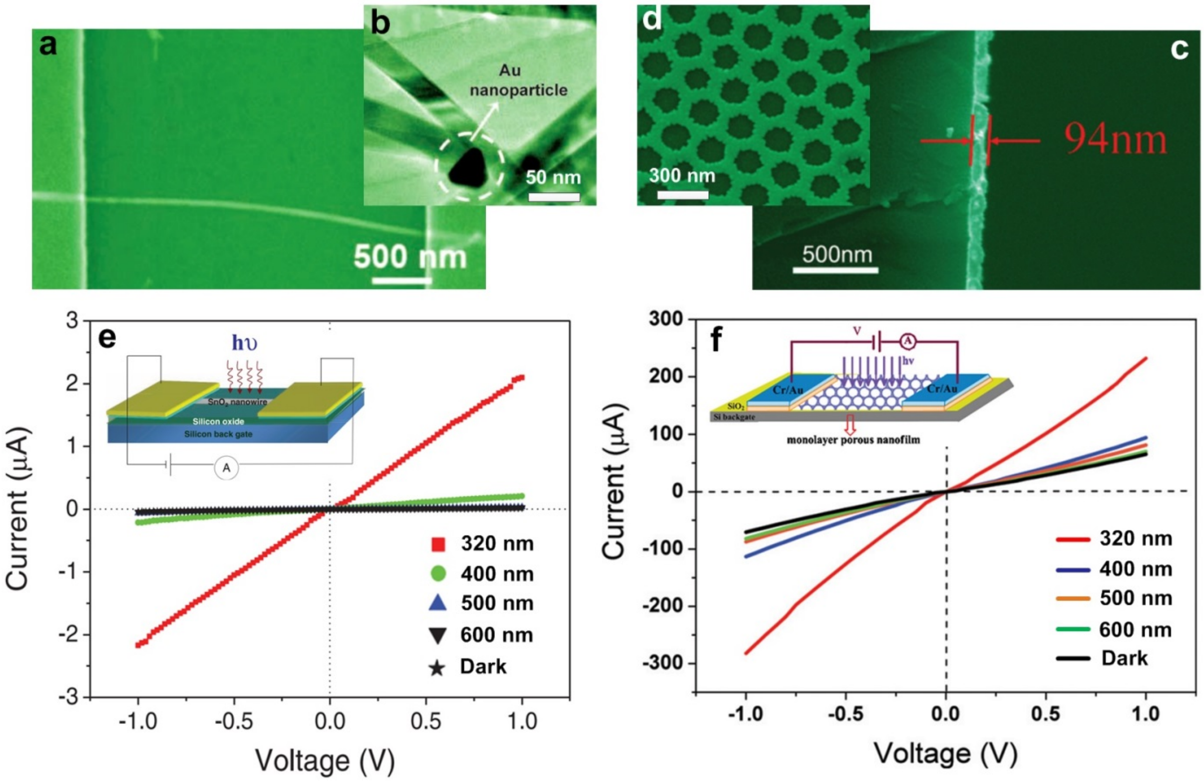

Figure 1.6. *(a) SEM image of a SnO_2-nanowire photodetector and (b) and the observed gold (Au) nanoparticle is indicated by a circle.[42] (c) The cross-sectional and (d) surface SEM images of 2D ordered SnO_2 nanofilms.[130] The I–V characteristics of the (e) SnO_2-nanowire photodetector[42] and (f) 2D ordered SnO_2 nanofilm[130] illuminated with light of four different wavelengths and under dark conditions. The schematic illustration of the fabricated nanowire and 2D ordered photodetectors are presented in inset (e) and (f), respectively.*

This higher dark-current is attributed to the significantly larger number of nanoparticle neighbours in the 2D SnO_2 monolayer film that results in higher electrical conductivity.[14] In fact, this low photo- to dark-current ratio is attributed to poor penetration of light into the film limiting the photo-excitation to the top film layers.[14] Higher thickness of the 2D SnO_2 monolayer (94 nm)[130] compared to a thinner diameter of the SnO_2 nanowire (less than 26 nm) fabricated by Hu et al.[42] might lead to formation of gas-tight SnO_2 domains, which are not electron depleted and thus less sensitive to light (Figure 1.6e).[14] While in the case of nanowire device, a higher volume fraction of the nanowire is electron-depleted in the dark condition resulting in considerably lower dark-current of only 19.4 nA (Figure 1.6f)[42] at the applied bias of 1V.

1.5.4 TiO_2-based photodetectors

TiO_2 is a well-known transparent conductive oxide (TCO) which is particularly suitable for UV detection against a background with infrared and visible light.[76,155] Due to the appropriate bandgap (3.2 eV for anatase[75,156] and 3.0 eV for rutile[157-158]), distinctive absorption characteristics,[159] high refractive index,[73,160] and low fabrication cost, TiO_2 is emerging as a promising material for photodetectors. With large specific surface areas, 1D TiO_2 nanostructures gained special attention in recent years due to their excellent performance in many well-known research areas.[53,76,158]

Recently, 1D nanostructure of assembled free-standing TiO_2 attracted great interest in this field because of its transferable feature for special applications.[155,159] Using carbon cloth as an efficiently sacrificial template (Figure 1.7b,c), Wang et al.[155] reported the first synthesis of flexible and transferable TiO_2 nanorod cloths (TNRCs) from a fast and catalyst-free microwave heating route with post heating treatment at 800°C (Figure 1.7a-c). This novel hierarchical structure of interlaced hollow fibres with nanorods on the surface (Figure 1.7c) can be readily transferred onto a fluorine-doped tin oxide (FTO), Ti foil and polyethylene terephthalate (PTE) providing a promising way to develop devices for applications in many emerging research fields, such as flexible solar cells[161] and flexible electronic devices.[46]

Their fabricated TNRC-based photodetectors illustrated a good sensitivity of ca. 7 at different illumination wavelengths of 365 and 254 nm.[155] However, the device exhibited a low responsivity (0.015 A.W^{-1}) under light illumination of 1.25 mW.cm^{-2} and the applied bias of -1 V. In another approach, Zou et al.[76] reported a very high UV-sensitive photoconductance of a pure TiO_2 nanotube arrays (Figure 1.7d) made by electrochemical anodization which resulted in a great photosensitivity (>10^4) and also a fast response with rise time and decay time of only 0.5 and 0.7 s, respectively.[76] The high responsivity of 13 A.W^{-1} was also found under 1.06 mW.cm^{-2} UV (312 nm) illumination at 2.5 V bias (Figure 1.7d).[76] This high responsivity mainly comes from the internal gain induced by desorption of oxygen from the nanotube large surfaces (Figure 1.7e,f) and the reduction of the Schottky barrier at TiO_2/Ag contact under UV illumination.[76,162]

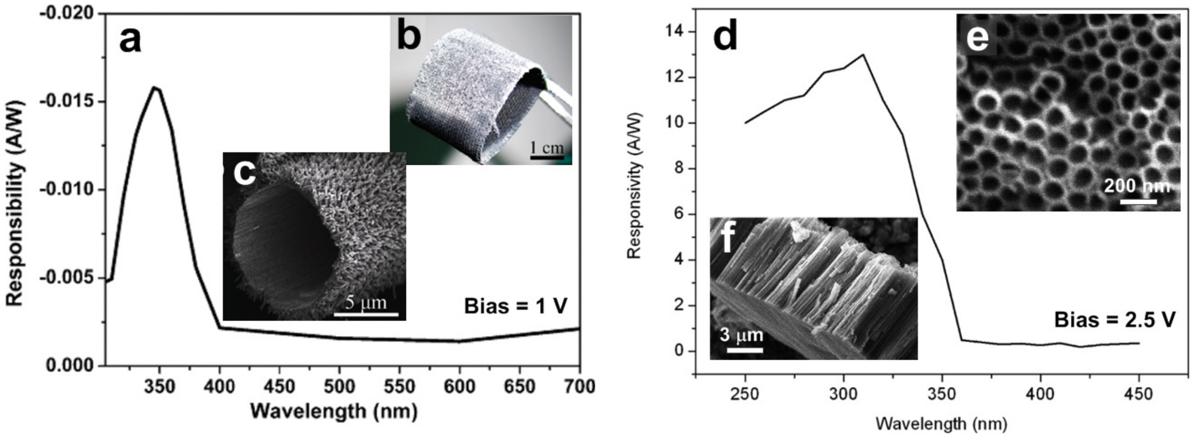

Figure 1.7. *Spectral response of (a) the TNRC-based device*[155] *and (d) TiO_2 nanotube array device*[76] *at a bias of 1 and 2.5 V, respectively. (b,c) Optical image of the flexible carbon cloths partly grown with TiO_2 nanorods. (e) Top and (f) cross-sectional view SEM images of the as-anodized TiO_2 nanotube arrays made by electrochemical anodization.*

1.5.5 ZnO-based photodetectors

With wide direct bandgap (3.37 eV) and large exciton binding energy (≈60 meV) at room temperature,[14,72,163] ZnO nanostructures are amongst the most investigated materials for different nanotechnological applications, such as field effect transistors, diodes, surface acoustic wave devices, electromechanical devices, and gas sensors.[2,14,50,54,164-165] Among various applications for ZnO semiconductors, the UV photodetector is an excellent device that has a wide range of chemical and environmental detecting applications.[3,49,72,132,166-168]

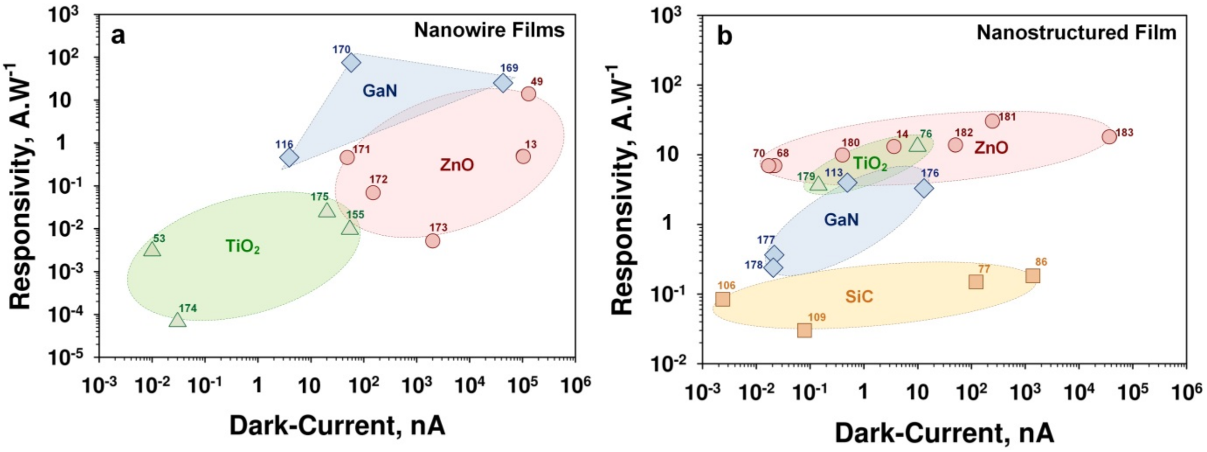

Figure 1.8. *Responsivity and dark current of (a) nanowires and (b) nanostructured UV photodetectors made by different wide bandgap semiconductors.*[13-14,49,53,68,70,76-77,86,106,109,113,116,155,169-183]

Figure 1.8a,b present the responsivity and dark-current of nanowires and nanostructured devices made by different materials, such as GaN, TiO_2, SiC and ZnO. For all different materials, higher responsivity results from a higher dark-current (Figure 1.8a,b). According to the literature, a higher device responsivity is usually obtained by increasing the applied voltage,[49,72] device aspect ratio,[72] and/or structural density.[184] Liu et al.[49] fabricated a ZnO micro/nanowire arrays device on single-layer graphene sheets using CVD method featuring a high responsivity of ca. 14 A.W^{-1}, which is significantly high compared to ZnO-based UV photodetectors. However, considering an applied bias of 8.5 V used in their research, the device responsivity can be calculated as 1.62 A.W^{-1} per volt, which is not high compared to the literature. In another approach, a highly performing dense films of electron-depleted ZnO nanoparticles was fabricated using spin-coating method resulting in a high responsivity of 26 A.W^{-1}. However, due to a very low device aspect ratio of ca. 0.75, a giant applied voltage of 120 V was used to achieve this high UV responsivity. In fact, simply increasing the voltage or changing the device aspect ratio/structure density is not an optimal way to increase the device performance.

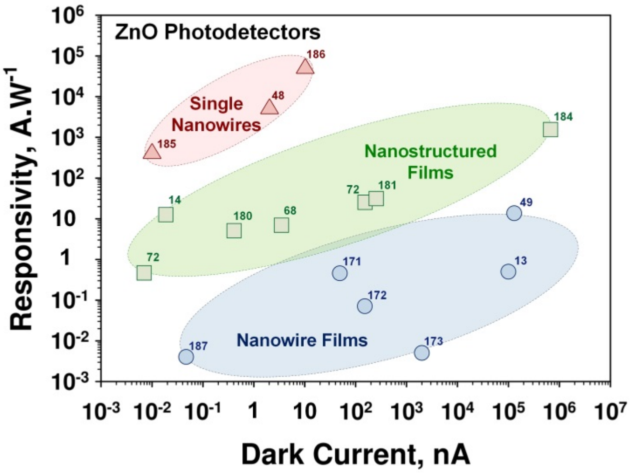

Figure 1.9. *The responsivity and dark-current of ZnO-based photodetectors with different nanostructured morphology.*[13-14,48-49,68,72,171-173,180-181,184-187]

Figure 1.9 illustrates the device responsivity and dark-current for ZnO-based photodetectors with different structural morphology, such as single nanowires, nanostructured and nanowire films. As mentioned above, for all different nanostructured morphologies, the higher responsivity results from a higher dark-current. Surprisingly, single nanowire devices obtained the highest UV photoresponsivity with considerably low dark-current. This high responsivity might be attributed to the effective surface area considered in device responsivity. In fact, for single nanowire device, the cross-sectional area is usually considered as effective surface area in responsivity measurement while the entire outer area of the nanowire is exposing to UV light and contributing to the light absorption.

Recently, Liu et al.[43] have fabricated ZnO nanowires with the diameter of 150 nm (Figure 1.10a) and a length of about 10 μm using CVD method featured a low dark current of 9.7 pA and a photo- to dark- current ratio of about 10^3 at the applied bias of 5V (Figure 1.10c) and under the light density of 1.3 mW.cm^{-2}.[43] In addition, they have reported that the photodetection properties of their device have been improved significantly by decorating the ZnO nanowires using Au nanoparticles (Figure 1.10a) resulting in an ultralow dark current of

0.13 pA and I_{photo}/I_{dark} ratio of 5×10^6 (Figure 1.10c). Nevertheless, similar to the other ZnO-based UV photodetectors,[14,188] their device exhibited a slow response speed (25 s and 40 s rise time and 10 s and 300s decay time with and without Au decoration) due to the inherent defects, such as oxygen vacancies and zinc interstitials.[43]

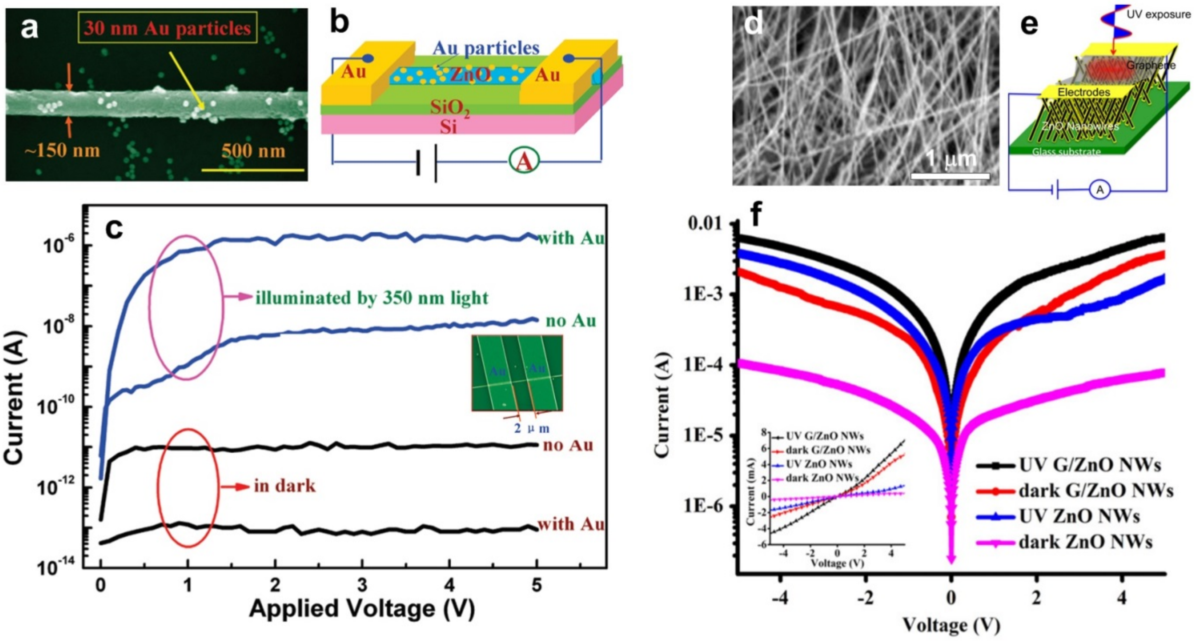

Figure 1.10. *SEM image and schematic of (a,b) ZnO nanowire with Au nanoparticles[43] and (d,e) ZnO nanowires[189] fabricated by CVD and thermal oxidation, respectively. I-V characteristics of (c) single nanowire[43] and (f) multi nanowires[189] devices both in dark and under 350 nm UV light illumination with the light density of 1.3 mW.cm^{-2}.*

In another approach, Boruah et al.[189] fabricated highly dense ZnO nanowires grown on a glass substrate by thermal oxidation of metallic Zn thin film in air. Later, they used the reactive thermal evaporation (RTE) process to deposit the Aluminum electrodes of 300 nm thickness on top of the graphene with a gap of 90 μm between the electrodes. Their fabricated device featured a significantly higher photo-current of 1.65 mA (5 orders of magnitude) compared to Liu et al.[43], at the same applied bias and light density. This higher photo-current might be attributed to the higher solid mass of ZnO nanowires compared to a single nanowire resulting in a greater number of photogenerated electron-hole pairs. However, increasing the number of nanowires resulted in a considerably higher dark-current of 80 mA compared to the very low dark-current of only 9.7 pA for single ZnO nanowire device. As a result, the photo- to dark-current ratio decreased from 10^3 of the single nanowire to only 20 of multi nanowires device. In fact, the device conductivity increases significantly by increasing the number of nanowires (higher mass) used in the photodetector.

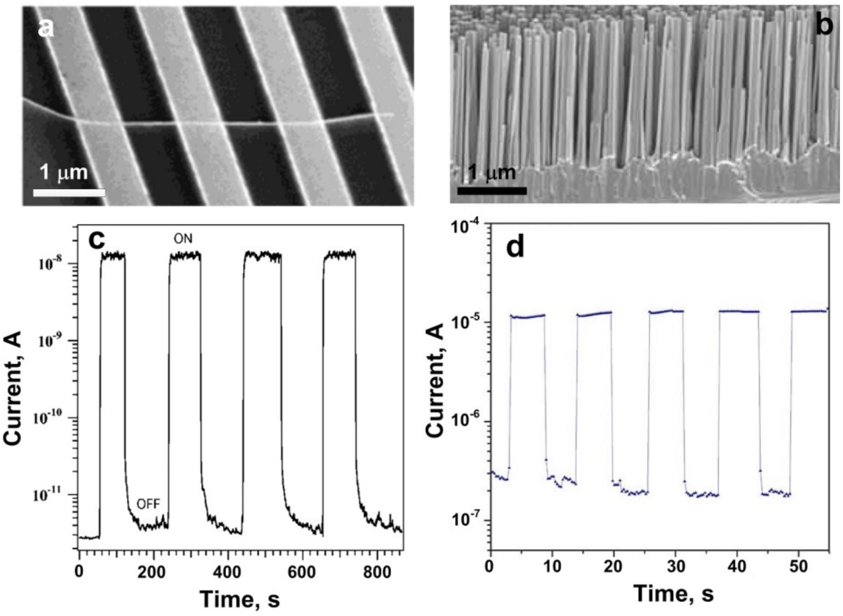

Figure 1.11. *SEM image and measured photo response as a function of time as the UV lamp switched on and off for (a) an individual ZnO nanowire*[190] *and (b) a multi ZnO nanowires device*[191] *fabricated by vapour phase transport process and self-catalysed VLS process, respectively.*

Similar results were obtained by kind et al.[190] using an individual ZnO nanowire device in comparison with the results reported for low temperature synthesized vertical ZnO nanowires.[191] In fact, under the same applied bias of 5 V and light density of 0.3 mW.cm^{-2}, the photo-current increased significantly from 0.25 μA of the single nanowire[190] to 13.5 μA of the vertical ZnO nanowires device,[191] while the photo- to dark-current ratio decreased with more than 3 orders of magnitude due to a higher dark current of 0.2 μA of multi nanowires device[191] compared to only 1 pA of the single nanowire.[190]

1.6 Summary and outlook

Advanced in wide bandgap semiconductors have opened the possibility of developing low-cost selective UV photodetectors, capable of operating in harsh atmospheres and featuring significantly high photodetection performances compared with their Si-based counterparts. Several research have been done to fabricate wide bandgap UV photodetectors featuring high photodetection performances, such as high responsivity, detectivity, photoconductive gain, EQE%, and LDR. Different nanostructured morphology, such as 0D, 1D, 2D and 3D nanostructured devices (nanostructured films) were investigated previously in order to achieve the highest photodetection performance. Among the variety of nanostructured devices, 1D nanomaterials with diameters of a few nanometers or less exhibited significantly higher photodetection performances due to their high surface-to-the-volume ratio compared to the other nanostructured devices. In addition, a variety of wide bandgap semiconductors including TiO_2, SiC, ZnO, GaN and SnO_2 were investigated in the last decades as potential materials for UV photodetection applications. Among all wide band gap semiconductors, ZnO is the most investigated material for UV photodetectors applications due to its wide direct bandgap of 3.37 eV at room temperature, ease of fabrication and high transmittance for visible light. However, increasing the performance of ZnO-based photodetectors, particularly their response speed, is still one of the major issues of these types of UV photodetectors, and continuing efforts have been devoted to this issue.

In this thesis, I will investigate the fabrication, photodetection performance and also the detection mechanism of ultraporous nanostructured networks made by self-assembly deposition of hot ZnO nanoparticle aerosols on a glass substrate with interdigitated electrodes. The fabricated nanostructured device will be presented as a highly performing super-structural design due to their extremely high porosity (98%) featuring very high surface-to-the-volume ratio compared to the previously reported nanostructured films (porosity of up to 60%). The findings achieved by this research demonstrated a highly performing structure and a flexible and scalable platform technology for the rapid low-cost fabrication and integration of ultraviolet photodetectors in CMOS-compatible portable devices.

1.7 References

1. Hu, L.; Yan, J.; Liao, M.; Xiang, H.; Gong, X.; Zhang, L.; Fang, X., An Optimized Ultraviolet-A Light Photodetector with Wide-Range Photoresponse Based on ZnS/ZnO Biaxial Nanobelt. *Adv. Mater.* **2012,** *24*, 2305-2309.

2. Liu, X.; Gu, L.; Zhang, Q.; Wu, J.; Long, Y.; Fan, Z., All-printable band-edge modulated ZnO nanowire photodetectors with ultra-high detectivity. *Nature Commun.* **2014,** *5*, 4007.

3. Sun, F.; Shan, C.-X.; Wang, S.-P.; Li, B.-H.; Zhang, Z.-Z.; Yang, C.-L.; Shen, D.-Z., Ultraviolet photodetectors fabricated from ZnO p–i–n homojunction structures. *Mater. Chem. Phys.* **2011,** *129*, 27-29.

4. Yang, Q.; Guo, X.; Wang, W.; Zhang, Y.; Xu, S.; Lien, D. H.; Wang, Z. L., Enhancing Sensitivity of a Single ZnO Micro-/Nanowire Photodetector by Piezo-phototronic Effect. *ACS Nano* **2010,** *4*, 6285-6291.

5. Chen, C.; Cheng, Y.; Dai, Q.; Song, H., Radio Frequency Magnetron Sputtering Deposition of TiO_2 Thin Films and Their Perovskite Solar Cell Applications. *Sci. Rep.* **2015,** *5*, 17684.

6. Jiang, D.; Tian, C.; Yang, G.; Qin, J.; Liang, Q.; Zhao, J.; Hou, J.; Gao, S., $MgxZn_{1-x}O$ solar-blind photodetectors fabricated by RF magnetron sputtering with combinatorial targets. *Mater. Res. Bull.* **2015,** *67*, 158-161.

7. Sharma, P.; Sreenivas, K.; Rao, K., Analysis of ultraviolet photoconductivity in ZnO films prepared by unbalanced magnetron sputtering. *J. Appl. Phys.* **2003,** *93*, 3963-3970.

8. Gaidi, M.; Hajjaji, A.; Smirani, R.; Bessais, B.; El Khakani, M., Structure and photoluminescence of ultrathin films of SnO_2 nanoparticles synthesized by means of pulsed laser deposition. *J. Appl. Phys.* **2010,** *108*, 063537.

9. Hernandez-Como, N.; Moreno, S.; Mejia, I.; Quevedo-Lopez, M. A., Low-temperature processed ZnO and CdS photodetectors deposited by pulsed laser deposition. *Semicond. Sci. Technol.* **2014,** *29*, 085008.

10. Shewale, P. S.; Yu, Y. S., Structural, surface morphological and UV photodetection properties of pulsed laser deposited Mg-doped ZnO nanorods: Effect of growth time. *J. Alloys Compd.* **2016,** *654*, 79-86.

11. Shewale, P. S.; Yu, Y. S., The effects of pulse repetition rate on the structural, surface morphological and UV photodetection properties of pulsed laser deposited Mg-doped ZnO nanorods. *Ceram. Int.* **2016,** *42*, 7125-7134.

12. Tsao, J. Y.; Ehrlich, D. J., Patterned photonucleation of chemical vapor deposition of Al by UV-laser photodeposition. *Appl. Phys. Lett.* **1984,** *45*, 617-619.

13. Xu, L.; Li, X.; Zhan, Z.; Wang, L.; Feng, S.; Chai, X.; Lu, W.; Shen, J.; Weng, Z.; Sun, J., Catalyst-Free, Selective Growth of ZnO Nanowires on SiO_2 by Chemical Vapor Deposition for Transfer-Free Fabrication of UV Photodetectors. *ACS Appl. Mater. Interfaces* **2015,** *7*, 20264-20271.

14. Nasiri, N.; Bo, R.; Wang, F.; Fu, L.; Tricoli, A., Ultraporous Electron-Depleted ZnO Nanoparticle Networks for Highly Sensitive Portable Visible-Blind UV Photodetectors. *Adv. Mater.* **2015,** *27*, 4336-4343.

15. Rajan, A.; Yadav, H. K.; Gupta, V.; Tomar, M., Sol–gel derived Ag-doped ZnO thin film for UV photodetector with enhanced response. *J. Mater. Sci.* **2013,** *48*, 7994-8002.

16. Xie, Y.; Huang, H.; Yang, W.; Wu, Z., Low dark current metal-semiconductor-metal ultraviolet photodetectors based on sol-gel-derived TiO_2 films. *J. Appl. Phys.* **2011,** *109*, 023114.

17. Ali, G. M.; Singh, S.; Chakrabarti, P., Fabrication and Characterization of ZnO Photodetectors with High Gain. *J. Nanoelectron. Optoe.* **2009,** *4*, 316-320.

18. Gong, X.; Tong, M.; Xia, Y.; Cai, W.; Moon, J. S.; Cao, Y.; Yu, G.; Shieh, C.-L.; Nilsson, B.; Heeger, A. J., High-Detectivity Polymer Photodetectors with Spectral Response from 300 nm to 1450 nm. *Science* **2009,** *325*, 1665-1667.

19. Drbohlavova, J.; Adam, V.; Kizek, R.; Hubalek, J., Quantum Dots - Characterization, Preparation and Usage in Biological Systems. *Int. J. Mol. Sci.* **2009,** *10*, 656-673.

20. Rossi, A.; Tanttu, T.; Tan, K. Y.; Iisakka, I.; Zhao, R.; Chan, K. W.; Tettamanzi, G. C.; Rogge, S.; Dzurak, A. S.; Möttönen, M., An Accurate Single-Electron Pump Based on a Highly Tunable Silicon Quantum Dot. *Nano Lett.* **2014,** *14*, 3405-3411.

21. Yang, C. H.; Rossi, A.; Ruskov, R.; Lai, N. S.; Mohiyaddin, F. A.; Lee, S.; Tahan, C.; Klimeck, G.; Morello, A.; Dzurak, A. S., Spin-valley lifetimes in a silicon quantum dot with tunable valley splitting. *Nature Commun.* **2013,** *4*, 2069.

22. Guo, S.; Bao, D.; Upadhyayula, S.; Wang, W.; Guvenc, A. B.; Kyle, J. R.; Hosseinibay, H.; Bozhilov, K. N.; Vullev, V. I.; Ozkan, C. S.; Ozkan, M., Photoinduced Electron Transfer Between Pyridine Coated Cadmium Selenide Quantum Dots and Single Sheet Graphene. *Adv. Funct. Mater.* **2013,** *23*, 5199-5211.

23. Pan, Z.; Zhao, K.; Wang, J.; Zhang, H.; Feng, Y.; Zhong, X., Near Infrared Absorption of $CdSe_xTe_{1-x}$ Alloyed Quantum Dot Sensitized Solar Cells with More than 6% Efficiency and High Stability. *ACS Nano* **2013,** *7*, 5215-5222.

24. Luo, J.; Wei, H.; Huang, Q.; Hu, X.; Zhao, H.; Yu, R.; Li, D.; Luo, Y.; Meng, Q., Highly efficient core-shell $CuInS_2$-Mn doped CdS quantum dot sensitized solar cells. *Chem. Commun.* **2013,** *49*, 3881-3883.

25. Roelofs, K. E.; Brennan, T. P.; Dominguez, J. C.; Bailie, C. D.; Margulis, G. Y.; Hoke, E. T.; McGehee, M. D.; Bent, S. F., Effect of Al_2O_3 Recombination Barrier Layers Deposited by Atomic Layer Deposition in Solid-State CdS Quantum Dot-Sensitized Solar Cells. *J. Phys. Chem. C* **2013,** *117*, 5584-5592.

26. Kairdolf, B. A.; Smith, A. M.; Stokes, T. H.; Wang, M. D.; Young, A. N.; Nie, S., Semiconductor quantum dots for bioimaging and biodiagnostic applications. *Annu. Rev. Anal. Chem.* **2013,** *6*, 143.

27. Luo, P. G.; Sahu, S.; Yang, S.-T.; Sonkar, S. K.; Wang, J.; Wang, H.; LeCroy, G. E.; Cao, L.; Sun, Y.-P., Carbon "quantum" dots for optical bioimaging. *J. Mater. Chem. B* **2013,** *1*, 2116-2127.

28. Yao, Y.-F.; Shen, C.-H.; Chen, W.-F.; Shih, P.-Y.; Chou, W.-H.; Su, C.-Y.; Chen, H.-S.; Liao, C.-H.; Chang, W.-M.; Kiang, Y.-W.; Yang, C. C., Void Structures in Regularly Patterned ZnO Nanorods Grown with the Hydrothermal Method. *J. Nanomater.* **2014,** *2014*, 11.

29. Li, L.; Wu, P.; Fang, X.; Zhai, T.; Dai, L.; Liao, M.; Koide, Y.; Wang, H.; Bando, Y.; Golberg, D., Single-Crystalline CdS Nanobelts for Excellent Field-Emitters and Ultrahigh Quantum-Efficiency Photodetectors. *Adv. Mater.* **2010,** *22*, 3161-3165.

30. Alenezi, M. R.; Alshammari, A. S.; Alzanki, T. H.; Jarowski, P.; Henley, S. J.; Silva, S. R. P., ZnO Nanodisk Based UV Detectors with Printed Electrodes. *Langmuir* **2014,** *30*, 3913-3921.

31. Alasaarela, T.; Saastamoinen, T.; Hiltunen, J.; Säynätjoki, A.; Tervonen, A.; Stenberg, P.; Kuittinen, M.; Honkanen, S., Atomic layer deposited titanium dioxide and its application in resonant waveguide grating. *Appl. Opt.* **2010,** *49*, 4321-4325.

32. Mani, J.; Sakeek, H.; Habouti, S.; Dietze, M.; Es-Souni, M., Macro-meso-porous TiO_2, ZnO and ZnO-TiO_2-composite thick films. Properties and application to photocatalysis. *Catal. Sci. Tech* **2012,** *2*, 379-385.

33. Ekimov, A. I.; Onushchenko, A. A., Quantum size effect in three-dimensional microscopic semiconductor crystals. *ZhETF Pisma Redaktsiiu* **1981,** *34*, 363.

34. Brus, L. E., Electron–electron and electron-hole interactions in small semiconductor crystallites: The size dependence of the lowest excited electronic state. *J. Chem. Phys* **1984,** *80*, 4403-4409.

35. Murray, C.; Norris, D. J.; Bawendi, M. G., Synthesis and characterization of nearly monodisperse CdE (E= sulfur, selenium, tellurium) semiconductor nanocrystallites. *J. Am. Chem. Soc.* **1993,** *115*, 8706-8715.

36. Pan, D.; Zhang, J.; Li, Z.; Wu, M., Hydrothermal Route for Cutting Graphene Sheets into Blue-Luminescent Graphene Quantum Dots. *Adv. Mater.* **2010,** *22*, 734-738.

37. Lu, J.; Yang, J.-x.; Wang, J.; Lim, A.; Wang, S.; Loh, K. P., One-Pot Synthesis of Fluorescent Carbon Nanoribbons, Nanoparticles, and Graphene by the Exfoliation of Graphite in Ionic Liquids. *ACS Nano* **2009,** *3*, 2367-2375.

38. Pan, D.; Xi, C.; Li, Z.; Wang, L.; Chen, Z.; Lu, B.; Wu, M., Electrophoretic fabrication of highly robust, efficient, and benign heterojunction photoelectrocatalysts based on graphene-quantum-dot sensitized TiO_2 nanotube arrays. *J. Mater. Chem. A* **2013,** *1*, 3551-3555.

39. Zhuo, S.; Shao, M.; Lee, S.-T., Upconversion and Downconversion Fluorescent Graphene Quantum Dots: Ultrasonic Preparation and Photocatalysis. *ACS Nano* **2012,** *6*, 1059-1064.

40. Calarco, R.; Marso, M.; Richter, T.; Aykanat, A. I.; Meijers, R.; Hart, A. V.; Stoica, T.; Luth, H., Size-dependent photoconductivity in MBE-grown GaN-nanowires. *Nano Lett.* **2005,** *5*, 981–984.

41. Dattoli, E. N.; Wan, Q.; Guo, W.; Chen, Y.; Pan, X.; Lu, W., Fully Transparent Thin-Film Transistor Devices Based on SnO_2 Nanowires. *Nano Lett.* **2007,** *7*, 2463-2469.

42. Hu, L.; Yan, J.; Liao, M.; Wu, L.; Fang, X., Ultrahigh external quantum efficiency from thin SnO_2 nanowire ultraviolet photodetectors. *small* **2011,** *7*, 1012-1017.

43. Liu, K.; Sakurai, M.; Liao, M.; Aono, M., Giant Improvement of the Performance of ZnO Nanowire Photodetectors by Au Nanoparticles. *J. Phys. Chem. C* **2010,** *114*, 19835-19839.

44. Lupan, O.; Pauporté, T.; Viana, B., Low-Voltage UV-Electroluminescence from ZnO-Nanowire Array/p-GaN Light-Emitting Diodes. *Adv. Mater.* **2010,** *22*, 3298-3302.

45. Zhang, H.; Babichev, A.; Jacopin, G.; Lavenus, P.; Julien, F.; Egorov, A. Y.; Zhang, J.; Pauporté, T.; Tchernycheva, M., Characterization and modeling of a ZnO nanowire ultraviolet photodetector with graphene transparent contact. *J. Appl. Phys.* **2013,** *114*, 234505.

46. Shen, G.; Xu, J.; Wang, X.; Huang, H.; Chen, D., Growth of Directly Transferable In_2O_3 Nanowire Mats for Transparent Thin-film Transistor Applications. *Adv. Mater.* **2011,** *23*, 771-775.

47. Wei, L.; Charles, M. L., Semiconductor nanowires. *J. Phys. D: Appl. Phys.* **2006,** *39*, R387.

48. Zhou, X.; Zhang, Q.; Gan, L.; Li, X.; Li, H.; Zhang, Y.; Golberg, D.; Zhai, T., High-Performance Solar-Blind Deep Ultraviolet Photodetector Based on Individual Single-Crystalline Zn_2GeO_4 Nanowire. *Adv. Funct. Mater.* **2016,** *26*, 704-712.

49. Liu, J.; Lu, R.; Xu, G.; Wu, J.; Thapa, P.; Moore, D., Development of a Seedless Floating Growth Process in Solution for Synthesis of Crystalline ZnO Micro/Nanowire Arrays on Graphene: Towards High-Performance Nanohybrid Ultraviolet Photodetectors. *Adv. Funct. Mater.* **2013,** *23*, 4941-4948.

50. Ahn, S.-E.; Ji, H. J.; Kim, K.; Kim, G. T.; Bae, C. H.; Park, S. M.; Kim, Y.-K.; Ha, J. S., Origin of the slow photoresponse in an individual sol-gel synthesized ZnO nanowire. *Appl. Phys. Lett.* **2007,** *90*, 153106.

51. Rai, S. C.; Wang, K.; Ding, Y.; Marmon, J. K.; Bhatt, M.; Zhang, Y.; Zhou, W.; Wang, Z. L., Piezo-phototronic effect enhanced UV/visible photodetector based on fully wide band gap type-II ZnO/ZnS core/shell nanowire array. *ACS nano* **2015,** *9*, 6419-6427.

52. Ahsanulhaq, Q.; Umar, A.; Hahn, Y. B., Growth of aligned ZnO nanorods and nanopencils on ZnO/Si in aqueous solution: growth mechanism and structural and optical properties. *Nanotechnology* **2007,** *18*, 115603.

53. Han, Y.; Fan, C.; Wu, G.; Chen, H.-Z.; Wang, M., Low-Temperature Solution Processed Utraviolet Photodetector Based on an Ordered TiO_2 Nanorod Array–Polymer Hybrid. *J. Phys. Chem. C* **2011,** *115*, 13438-13445.

54. Hatch, S. M.; Briscoe, J.; Dunn, S., A Self-Powered ZnO-Nanorod/CuSCN UV Photodetector Exhibiting Rapid Response. *Adv. Mater.* **2013,** *25*, 867-871.

55. Su, Y. K.; Peng, S. M.; Ji, L. W.; Wu, C. Z.; Cheng, W. B.; Liu, C. H., Ultraviolet ZnO Nanorod Photosensors. *Langmuir* **2010,** *26*, 603-606.

56. Zhang, X. Y.; Qin, J. Q.; Xue, Y. N.; Yu, P. F.; Zhang, B.; Wang, L. M., Effect of aspect ratio and surface defects on the photocatalytic activity of ZnO nanorods. *Sci Rep.* **2014,** *4*, 4596.

57. Zhou, H.; Gui, P.; Yu, Q.; Mei, J.; Wang, H.; Fang, G., Self-powered, visible-blind ultraviolet photodetector based on n-ZnO nanorods/i-MgO/p-GaN structure light-emitting diodes. *J. Mater. Chem. C* **2015,** *3*, 990-994.

58. Kar, A.; Kundu, S.; Patra, A., Surface Defect-Related Luminescence Properties of SnO_2 Nanorods and Nanoparticles. *J. Phys. Chem. C* **2011,** *115*, 118-124.

59. Butt, F. K.; Cao, C.; Khan, W. S.; Safdar, M.; Fu, X.; Tahir, M.; Idrees, F.; Ali, Z.; Nabi, G.; Yu, D., Electrical and optical properties of single zigzag SnO_2 nanobelts. *CrystEngComm* **2013,** *15*, 2106-2112.

60. Jin, W.; Ke, Y.; Lijun, L.; Jianwen, X.; Dejian, S.; Yu'e, X.; Ziqiang, Z., Controllable synthesis and field emission properties of SnO_2 zigzag nanobelts. *J. Phys. D: Appl. Phys.* **2008,** *41*, 185302.

61. Pan, Z. W.; Dai, Z. R.; Wang, Z. L., Nanobelts of Semiconducting Oxides. *Science* **2001,** *291*, 1947-1949.

62. Akhavan, S.; Guzelturk, B.; Sharma, V. K.; Demir, H. V., Large-area semi-transparent light-sensitive nanocrystal skins. *Opt. Express* **2012,** *20*, 25255-25266.

63. Heo, K.; Lee, H.; Park, Y.; Park, J.; Lim, H.-J.; Yoon, D.; Lee, C.; Kim, M.; Cheong, H.; Park, J.; Jian, J.; Hong, S., Aligned networks of cadmium sulfide nanowires for highly flexible photodetectors with improved photoconductive responses. *J. Mater. Chem.* **2012,** *22*, 2173-2179.

64. Chen, G.; Yu, Y.; Zheng, K.; Ding, T.; Wang, W.; Jiang, Y.; Yang, Q., Fabrication of Ultrathin Bi_2S_3 Nanosheets for High-Performance, Flexible, Visible-NIR Photodetectors. *Small* **2015,** *11*, 2848-2855.

65. Hu, P.; Wang, L.; Yoon, M.; Zhang, J.; Feng, W.; Wang, X.; Wen, Z.; Idrobo, J. C.; Miyamoto, Y.; Geohegan, D. B.; Xiao, K., Highly Responsive Ultrathin GaS Nanosheet Photodetectors on Rigid and Flexible Substrates. *Nano Lett.* **2013,** *13*, 1649-1654.

66. McLaren, A.; Valdes-Solis, T.; Li, G.; Tsang, S. C., Shape and Size Effects of ZnO Nanocrystals on Photocatalytic Activity. *J. Am. Chem. Soc.* **2009,** *131*, 12540-12541.

67. Feng, W.; Wang, X.; Zhang, J.; Wang, L.; Zheng, W.; Hu, P.; Cao, W.; Yang, B., Synthesis of two-dimensional β-Ga_2O_3 nanosheets for high-performance solar blind photodetectors. *J. Mater. Chem. C* **2014,** *2*, 3254-3259.

68. Nasiri, N.; Bo, R.; Chen, H.; White, T. P.; Fu, L.; Tricoli, A., Structural Engineering of Nano-Grain Boundaries for Low-Voltage UV-Photodetectors with Gigantic Photo- to Dark-Current Ratios. *Adv. Opt. Mater.* **2016,** *4*, 1787-1795.

69. Nasiri, N.; Bo, R.; Fu, L.; Tricoli, A., Three-dimensional nano-heterojunction networks: a highly performing structure for fast visible-blind UV photodetectors. *Nanoscale* **2017,** *9*, 2059-2067.

70. Nasiri, N.; Bo, R.; Hung, T. F.; Roy, V. A. L.; Fu, L.; Tricoli, A., Tunable Band-Selective UV-Photodetectors by 3D Self-Assembly of Heterogeneous Nanoparticle Networks. *Adv. Funct. Mater.* **2016,** *26*, 7359-7366.

71. Tüzemen, E. Ş.; Eker, S.; Kavak, H.; Esen, R., Dependence of film thickness on the structural and optical properties of ZnO thin films. *Appl. Surf. Sci.* **2009,** *255*, 6195-6200.

72. Jin, Y.; Wang, J.; Sun, B.; Blakesley, J. C.; Greenham, N. C., Solution-Processed Ultraviolet Photodetectors Based on Colloidal ZnO Nanoparticles. *Nano Lett.* **2008,** *8*, 1649-1653.

73. Chang, C.-C.; Cheng, L.-P.; Huang, F.-H.; Lin, C.-Y.; Hsieh, C.-F.; Wang, W.-H., Preparation and characterization of TiO_2 hybrid sol for UV-curable high-refractive-index organic–inorganic hybrid thin films. *J. Sol-Gel Sci. Technol.* **2010,** *55*, 199-206.

74. Li, X.; Gao, C.; Duan, H.; Lu, B.; Wang, Y.; Chen, L.; Zhang, Z.; Pan, X.; Xie, E., High-Performance Photoelectrochemical-Type Self-Powered UV Photodetector Using Epitaxial TiO_2/SnO_2 Branched Heterojunction Nanostructure. *Small* **2013,** *9*, 2005-2011.

75. Yin, W.-J.; Chen, S.; Yang, J.-H.; Gong, X.-G.; Yan, Y.; Wei, S.-H., Effective band gap narrowing of anatase TiO_2 by strain along a soft crystal direction. *Appl. Phys. Lett.* **2010,** *96*, 221901.

76. Zou, J.; Zhang, Q.; Huang, K.; Marzari, N., Ultraviolet Photodetectors Based on Anodic TiO_2 Nanotube Arrays. *J. Phys. Chem. C* **2010,** *114*, 10725-10729.

77. Aldalbahi, A.; Li, E.; Rivera, M.; Velazquez, R.; Altalhi, T.; Peng, X.; Feng, P. X., A new approach for fabrications of SiC based photodetectors. *Sci. Rep.* **2016,** *6*.

78. Casady, J. B.; Johnson, R. W., Status of silicon carbide (SiC) as a wide-bandgap semiconductor for high-temperature applications: A review. *Solid State Electron.* **1996,** *39*, 1409-1422.

79. Tian, C.; Jiang, D.; Li, B.; Lin, J.; Zhao, Y.; Yuan, W.; Zhao, J.; Liang, Q.; Gao, S.; Hou, J., Performance enhancement of ZnO UV photodetectors by surface plasmons. *ACS Appl. Mater. Interfaces* **2014,** *6*, 2162-2166.

80. Chen, Q.; Khan, M. A.; Sun, C.; Yang, J., Visible-blind ultraviolet photodetectors based on GaN pn junctions. *Electron. Lett.* **1995,** *31*, 1781-1782.

81. Li, J.; Zhao, M.; Wang, X., High performance Schottky UV photodetectors based on epitaxial AlGaN thin film. *Physica B: Condens. Matter* **2010,** *405*, 996-998.

82. Rigutti, L.; Tchernycheva, M.; De Luna Bugallo, A.; Jacopin, G.; Julien, F. H.; Zagonel, L. F.; March, K.; Stephan, O.; Kociak, M.; Songmuang, R., Ultraviolet Photodetector Based on GaN/AlN Quantum Disks in a Single Nanowire. *Nano Lett.* **2010,** *10*, 2939-2943.

83. Deng, K.; Lu, H.; Shi, Z.; Liu, Q.; Li, L., Flexible Three-Dimensional SnO_2 Nanowire Arrays: Atomic Layer Deposition-Assisted Synthesis, Excellent Photodetectors, and Field Emitters. *ACS Appl. Mater. Interfaces* **2013,** *5*, 7845-7851.

84. Chen, J.; Tang, W.; Xin, L.; Shi, Q., Band gap characterization and photoluminescence properties of SiC nanowires. *Appl. Phys. A* **2011,** *102*, 213-217.

85. Lin, S.; Chen, Z.; Liang, P.; Jiang, D.; Xie, H., Room-temperature ferromagnetism of vanadium-doped 6H–SiC. *Chem. Phys. Lett.* **2010,** *496*, 56-58.

86. Qu, Y.; Wu, Z.; Ai, M.; Guo, D.; An, Y.; Yang, H.; Li, L.; Tang, W., Enhanced Ga_2O_3/SiC ultraviolet photodetector with graphene top electrodes. *J. Alloys Compd.* **2016,** *680*, 247-251.

87. Zhang, H. X.; Feng, P. X.; Makarov, V.; Weiner, B. R.; Morell, G., Synthesis of nanostructured SiC using the pulsed laser deposition technique. *Mater. Res. Bull.* **2009,** *44*, 184-188.

88. Sang, L.; Liao, M.; Sumiya, M., A Comprehensive Review of Semiconductor Ultraviolet Photodetectors: From Thin Film to One-Dimensional Nanostructures. *Sensors* **2013,** *13*, 10482.

89. Wright, N. G.; Horsfall, A. B., SiC sensors: a review. *J. Phys. D: Appl. Phys.* **2007,** *40*, 6345.

90. Sigl, L. S., Thermal conductivity of liquid phase sintered silicon carbide. *J. Eur. Ceram. Soc.* **2003,** *23*, 1115-1122.

91. Kinoshita, T.; Munekawa, S., Effect of grain boundary segregation on thermal conductivity of hot-pressed silicon carbide. *Acta Mater.* **1997,** *45*, 2001-2012.

92. Shu, K.-M.; Tu, G. C., The microstructure and the thermal expansion characteristics of Cu/SiC_p composites. *Mater. Sci. Eng., A* **2003,** *349*, 236-247.

93. Chou, Y.-S.; Green, D. J., Silicon Carbide Platelet/Alumina Composites: II, Mechanical Properties. *J. Am. Ceram. Soc.* **1993,** *76*, 1452-1458.

94. Palmour, J. W.; Edmond, J. A.; Kong, H. S.; Carter, C. H., 6H-silicon carbide devices and applications. *Physica B: Condens. Matter* **1993,** *185*, 461-465.

95. Heuer, A. H.; Lou, V. L. K., Volatility Diagrams for Silica, Silicon Nitride, and Silicon Carbide and Their Application to High-Temperature Decomposition and Oxidation. *J. Am. Ceram. Soc.* **1990,** *73*, 2789-2803.

96. Willander, M.; Friesel, M.; Wahab, Q.-u.; Straumal, B., Silicon carbide and diamond for high temperature device applications. *J. Mater. Sci.* **2006,** *17*, 1-25.

97. Wenzien, B.; Käckell, P.; Bechstedt, F.; Cappellini, G., Quasiparticle band structure of silicon carbide polytypes. *Phys. Rev. B* **1995,** *52*, 10897-10905.

98. Devaty, R. P.; Choyke, W. J., Optical Characterization of Silicon Carbide Polytypes. *Phys. Status Solidi A* **1997,** *162*, 5-38.

99. Daulton, T. L.; Bernatowicz, T. J.; Lewis, R. S.; Messenger, S.; Stadermann, F. J.; Amari, S., Polytype Distribution in Circumstellar Silicon Carbide. *Science* **2002,** *296*, 1852-1855.

100. Rafique, S.; Han, L.; Zorman, C. A.; Zhao, H., Synthesis of wide bandgap β-Ga_2O_3 rods on 3C-SiC-on-Si. *Cryst. Growth Des.* **2015**, *16*, 511–517.

101. Li, Y.; Chen, C.; Li, J.-T.; Yang, Y.; Lin, Z.-M., Surface charges and optical characteristic of colloidal cubic SiC nanocrystals. *Nanoscale Res. Lett.* **2011,** *6*, 1-7.

102. Chen, B.; Matsuhata, H.; Sekiguchi, T.; Ichinoseki, K.; Okumura, H., Surface defects and accompanying imperfections in 4H–SiC: Optical, structural and electrical characterization. *Acta Mater.* **2012,** *60*, 51-58.

103. Iwamoto, N.; Johnson, B. C.; Hoshino, N.; Ito, M.; Tsuchida, H.; Kojima, K.; Ohshima, T., Defect-induced performance degradation of 4H-SiC Schottky barrier diode particle detectors. *J. Appl. Phys.* **2013,** *113*, 143714.

104. Tsunenobu, K.; Yuichiro, N.; Toshihiko, H.; Jun, S., Enhancement of Carrier Lifetimes in n-Type 4H-SiC Epitaxial Layers by Improved Surface Passivation. *Appl. Phys. Express* **2010,** *3*, 121201.

105. Brown, D. M.; Downey, E. T.; Ghezzo, M.; Kretchmer, J. W.; Saia, R. J.; Liu, Y. S.; Edmond, J. A.; Gati, G.; Pimbley, J. M.; Schneider, W. E., Silicon carbide UV photodiodes. *IEEE Trans. Electron Dev.* **1993,** *40*, 325-333.

106. Chen, B.; Yang, Y.; Xie, X.; Wang, N.; Ma, Z.; Song, K.; Zhang, X., Analysis of temperature-dependent characteristics of a 4H-SiC metal-semiconductor-metal ultraviolet photodetector. *Chin. Sci. Bull.* **2012,** *57*, 4427-4433.

107. Prasai, D.; John, W.; Weixelbaum, L.; Krüger, O.; Wagner, G.; Sperfeld, P.; Nowy, S.; Friedrich, D.; Winter, S.; Weiss, T., Highly reliable silicon carbide photodiodes for visible-blind ultraviolet detector applications. *J. Mater. Res.* **2013,** *28*, 33-37.

108. Biondo, S.; Lazar, M.; Ottaviani, L.; Vervisch, W.; Le Borgne, V.; El Khakani, M. A.; Duchaine, J.; Milesi, F.; Palais, O.; Planson, D., 4H-silicon carbide thin junction based ultraviolet photodetectors. *Thin Solid Films* **2012,** *522*, 17-19.

109. Lien, W.-C.; Tsai, D.-S.; Lien, D.-H.; Senesky, D. G.; He, J.-H.; Pisano, A. P., 4H–SiC Metal–Semiconductor–Metal Ultraviolet Photodetectors in Operation of 450. *IEEE Electr. Device L.* **2012,** *33*, 1586-1588.

110. Wang, R. X.; Yang, L. C.; Zhang, Y. M.; Xu, S. J.; Fu, K.; Zhang, B. S.; Wang, J. F.; Xu, K.; Yang, H., The effect of Ga-doped nanocrystalline ZnO electrode on deep-ultraviolet enhanced GaN photodetector. *Appl. Phys. Lett.* **2013,** *102*, 212104.

111. Akyol, F.; Krishnamoorthy, S.; Rajan, S., Tunneling-based carrier regeneration in cascaded GaN light emitting diodes to overcome efficiency droop. *Appl. Phys. Lett.* **2013,** *103*, 081107.

112. Tomotaka, N.; Akio, W.; Takashi, E., Ultraviolet Photodetectors Using Transparent Gate AlGaN/GaN High Electron Mobility Transistor on Silicon Substrate. *Jpn. J. Appl. Phys.* **2013,** *52*, 01AG06.

113. Li, D.; Sun, X.; Song, H.; Li, Z.; Chen, Y.; Jiang, H.; Miao, G., Realization of a High-Performance GaN UV Detector by Nanoplasmonic Enhancement. *Adv. Mater.* **2012,** *24*, 845-849.

114. Monroy, E.; Munoz, E.; Sánchez, F.; Calle, F.; Calleja, E.; Beaumont, B.; Gibart, P.; Munoz, J.; Cussó, F., High-performance GaN pn junction photodetectors for solar ultraviolet applications. *Semicond. Sci. Technol.* **1998,** *13*, 1042.

115. Razeghi, M.; Rogalski, A., Semiconductor ultraviolet detectors. *J. Appl. Phys.* **1996,** *79*, 7433-7473.

116. Andres de Luna, B.; Maria, T.; Gwenole, J.; Lorenzo, R.; François Henri, J.; Shu-Ting, C.; Yuan-Ting, L.; Po-Han, T.; Li-Wei, T., Visible-blind photodetector based on p–i–n junction GaN nanowire ensembles. *Nanotechnology* **2010,** *21*, 315201.

117. Mohd Yusoff, M. Z.; Baharin, A.; Hassan, Z.; Abu Hassan, H.; Abdullah, M. J., MBE growth of GaN pn-junction photodetector on AlN/Si(1 1 1) substrate with Ni/Ag as ohmic contact. *Superlattices Microstruct.* **2013,** *56*, 35-44.

118. Bie, Y.-Q.; Liao, Z.-M.; Zhang, H.-Z.; Li, G.-R.; Ye, Y.; Zhou, Y.-B.; Xu, J.; Qin, Z.-X.; Dai, L.; Yu, D.-P., Self-Powered, Ultrafast, Visible-Blind UV Detection and Optical Logical Operation based on ZnO/GaN Nanoscale p-n Junctions. *Adv. Mater.* **2011,** *23*, 649-653.

119. Chang, P. C.; Su, Y. K.; Lee, K. J.; Yu, C. L.; Chang, S. J.; Liu, C. H., Improved performance of GaN-based Schottky barrier photodetectors by annealing Ir/Pt Schottky contact in O_2. *J. Alloys Compd.* **2010,** *504*,, S429-S431.

120. Lee, K. H.; Chang, P. C.; Chang, S. J.; Wu, S. L., GaN-based Schottky barrier ultraviolet photodetector with a 5-pair AlGaN–GaN intermediate layer. *Phys. Status Solidi A* **2012,** *209*, 579-584.

121. Li, D.; Sun, X.; Song, H.; Li, Z.; Jiang, H.; Chen, Y.; Miao, G.; Shen, B., Effect of asymmetric Schottky barrier on GaN-based metal-semiconductor-metal ultraviolet detector. *Appl. Phys. Lett.* **2011,** *99*, 261102.

122. Cicek, E.; McClintock, R.; Cho, C. Y.; Rahnema, B.; Razeghi, M., $Al_xGa_{1-x}N$-based back-illuminated solar-blind photodetectors with external quantum efficiency of 89%. *Appl. Phys. Lett.* **2013,** *103*, 191108.

123. Srour, H.; Salvestrini, J. P.; Ahaitouf, A.; Gautier, S.; Moudakir, T.; Assouar, B.; Abarkan, M.; Hamady, S.; Ougazzaden, A., Solar blind metal-semiconductor-metal ultraviolet photodetectors using quasi-alloy of BGaN/GaN superlattices. *Appl. Phys. Lett.* **2011,** *99*, 221101.

124. Weng, W. Y.; Hsueh, T. J.; Chang, S. J.; Huang, G. J.; Hsueh, H. T., A Solar-Blind Photodetector Prepared by Furnace Oxidization of GaN Thin Film. *IEEE Sens. J.* **2011,** *11*, 999-1003.

125. Huang, Y.; Chen, D. J.; Lu, H.; Dong, K. X.; Zhang, R.; Zheng, Y. D.; Li, L.; Li, Z. H., Back-illuminated separate absorption and multiplication AlGaN solar-blind avalanche photodiodes. *Appl. Phys. Lett.* **2012,** *101*, 253516.

126. Wang, X.; Hu, W.; Pan, M.; Hou, L.; Xie, W.; Xu, J.; Li, X.; Chen, X.; Lu, W., Study of gain and photoresponse characteristics for back-illuminated separate absorption and multiplication GaN avalanche photodiodes. *J. Appl. Phys.* **2014,** *115*, 013103.

127. Zhou, Q.; McIntosh, D. C.; Lu, Z.; Campbell, J. C.; Sampath, A. V.; Shen, H.; Wraback, M., GaN/SiC avalanche photodiodes. *Appl. Phys. Lett.* **2011,** *99*, 131110.

128. Higashiwaki, M.; Chowdhury, S.; Swenson, B. L.; Mishra, U. K., Effects of oxidation on surface chemical states and barrier height of AlGaN/GaN heterostructures. *Appl. Phys. Lett.* **2010,** *97*, 222104.

129. Huang, S.; Chen, H.; Chen, K. J., Effects of the fluorine plasma treatment on the surface potential and Schottky barrier height of $Al_xGa_{1-x}N$/GaN heterostructures. *Appl. Phys. Lett.* **2010,** *96*, 233510.

130. Chen, H.; Hu, L.; Fang, X.; Wu, L., General Fabrication of Monolayer SnO_2 Nanonets for High-Performance Ultraviolet Photodetectors. *Adv. Funct. Mater.* **2012,** *22*, 1229-1235.

131. Nadarajah, A.; Carnes, M. E.; Kast, M. G.; Johnson, D. W.; Boettcher, S. W., Aqueous Solution Processing of F-Doped SnO_2 Transparent Conducting Oxide Films Using a Reactive Tin(II) Hydroxide Nitrate Nanoscale Cluster. *Chemistry of Materials* **2013,** *25*, 4080-4087.

132. Tian, W.; Zhai, T.; Zhang, C.; Li, S.-L.; Wang, X.; Liu, F.; Liu, D.; Cai, X.; Tsukagoshi, K.; Golberg, D.; Bando, Y., Low-Cost Fully Transparent Ultraviolet Photodetectors Based on Electrospun ZnO-SnO_2 Heterojunction Nanofibers. *Adv. Mater.* **2013,** *25*, 4625-4630.

133. Li-Li, X.; Shuang, Y.; Zhao-Hui, C.; Yu-Jin, C.; Xin-Yu, X., Enhanced gas sensing performance of $SnO_2/\alpha\text{-}MoO_3$ heterostructure nanobelts. *Nanotechnology* **2011,** *22*, 225502.

134. Yu, S.; Zhang, W.; Li, L.; Xu, D.; Dong, H.; Jin, Y., Optimization of SnO_2/Ag/SnO_2 tri-layer films as transparent composite electrode with high figure of merit. *Thin Solid Films* **2014,** *552*, 150-154.

135. Collins, P. G.; Zettl, A., A simple and robust electron beam source from carbon nanotubes. *Appl. Phys. Lett.* **1996,** *69*, 1969-1971.

136. Martel, R.; Derycke, V.; Lavoie, C.; Appenzeller, J.; Chan, K. K.; Tersoff, J.; Avouris, P., Ambipolar Electrical Transport in Semiconducting Single-Wall Carbon Nanotubes. *Physical Review Letters* **2001,** *87*, 256805.

137. Xu, C. X.; Sun, X. W.; Chen, B. J., Field emission from gallium-doped zinc oxide nanofiber array. *Appl. Phys. Lett.* **2004,** *84*, 1540-1542.

138. You, J. B.; Zhang, X. W.; Cai, P. F.; Dong, J. J.; Gao, Y.; Yin, Z. G.; Chen, N. F.; Wang, R. Z.; Yan, H., Enhancement of field emission of the ZnO film by the reduced work function and the increased conductivity via hydrogen plasma treatment. *Appl. Phys. Lett.* **2009,** *94*, 262105.

139. Chakraborty, S.; Sen, A.; Maiti, H. S., Selective detection of methane and butane by temperature modulation in iron doped tin oxide sensors. *Sens. Actuators B Chem.* **2006,** *115*, 610-613.

140. Wurzinger, O.; Reinhardt, G., CO-sensing properties of doped SnO_2 sensors in H_2-rich gases. *Sens. Actuators B Chem.* **2004,** *103*, 104-110.

141. Tricoli, A.; Graf, M.; Pratsinis, S. E., Optimal Doping for Enhanced SnO_2 Sensitivity and Thermal Stability. *Adv. Funct. Mater.* **2008,** *18*, 1969-1976.

142. Tricoli, A.; Pratsinis, S. E., Dispersed Nanoelectrode Devices. *Nature Nanotechnol.* **2010,** *5*, 54-60.

143. Liu, Y.; Jiao, Y.; Yin, B.; Zhang, S.; Qu, F.; Wu, X., Hierarchical semiconductor oxide photocatalyst: a case of the SnO2 microflower. *Nano-Micro Letters* **2013,** *5*, 234-241.

144. Fang, X.; Yan, J.; Hu, L.; Liu, H.; Lee, P. S., Thin SnO_2 Nanowires with Uniform Diameter as Excellent Field Emitters: A Stability of More Than 2400 Minutes. *Adv. Funct. Mater.* **2012,** *22*, 1613-1622.

145. Gu, M.; Kushima, A.; Shao, Y.; Zhang, J.-G.; Liu, J.; Browning, N. D.; Li, J.; Wang, C., Probing the Failure Mechanism of SnO_2 Nanowires for Sodium-Ion Batteries. *Nano Lett.* **2013,** *13*, 5203-5211.

146. Guan, C.; Wang, X.; Zhang, Q.; Fan, Z.; Zhang, H.; Fan, H. J., Highly Stable and Reversible Lithium Storage in SnO_2 Nanowires Surface Coated with a Uniform Hollow Shell by Atomic Layer Deposition. *Nano Lett.* **2014,** *14*, 4852-4858.

147. Yan, J.; Sumboja, A.; Khoo, E.; Lee, P. S., V_2O_5 Loaded on SnO_2 Nanowires for High-Rate Li Ion Batteries. *Adv. Mater.* **2011,** *23*, 746-750.

148. Huang, H.; Ong, C. Y.; Guo, J.; White, T.; Tse, M. S.; Tan, O. K., Pt surface modification of SnO_2 nanorod arrays for CO and H_2 sensors. *Nanoscale* **2010,** *2*, 1203-1207.

149. Xi, G.; Ye, J., Ultrathin SnO_2 Nanorods: Template- and Surfactant-Free Solution Phase Synthesis, Growth Mechanism, Optical, Gas-Sensing, and Surface Adsorption Properties. *Inorg. Chem.* **2010,** *49*, 2302-2309.

150. Kim, I.-D.; Jeon, E.-K.; Choi, S.-H.; Choi, D.-K.; Tuller, H. L., Electrospun SnO_2 nanofiber mats with thermo-compression step for gas sensing applications. *J. Electroceram.* **2010,** *25*, 159-167.

151. Wang, S.; Cheng, G.; Cheng, K.; Jiang, X.; Du, Z., The current image of single SnO_2 nanobelt nanodevice studied by conductive atomic force microscopy. *Nanoscale Res. Lett.* **2011,** *6*, 1-6.

152. Chen, X.; Guo, Z.; Xu, W.-H.; Yao, H.-B.; Li, M.-Q.; Liu, J.-H.; Huang, X.-J.; Yu, S.-H., Templating Synthesis of SnO_2 Nanotubes Loaded with Ag_2O Nanoparticles and Their Enhanced Gas Sensing Properties. *Adv. Funct. Mater.* **2011,** *21*, 2049-2056.

153. Shi, L.; Lin, H., Preparation of Band Gap Tunable SnO_2 Nanotubes and Their Ethanol Sensing Properties. *Langmuir* **2011,** *27*, 3977-3981.

154. Ye, J.; Zhang, H.; Yang, R.; Li, X.; Qi, L., Morphology-Controlled Synthesis of SnO_2 Nanotubes by Using 1D Silica Mesostructures as Sacrificial Templates and Their Applications in Lithium-Ion Batteries. *Small* **2010,** *6*, 296-306.

155. Wang, Z.; Wang, H.; Liu, B.; Qiu, W.; Zhang, J.; Ran, S.; Huang, H.; Xu, J.; Han, H.; Chen, D., Transferable and flexible nanorod-assembled TiO_2 cloths for dye-sensitized solar cells, photodetectors, and photocatalysts. *ACS nano* **2011,** *5*, 8412-8419.

156. Xiang, Q.; Yu, J.; Wang, W.; Jaroniec, M., Nitrogen self-doped nanosized TiO_2 sheets with exposed {001} facets for enhanced visible-light photocatalytic activity. *Chem. Commun.* **2011,** *47*, 6906-6908.

157. Hoang, S.; Guo, S.; Hahn, N. T.; Bard, A. J.; Mullins, C. B., Visible Light Driven Photoelectrochemical Water Oxidation on Nitrogen-Modified TiO_2 Nanowires. *Nano Lett.* **2012,** *12*, 26-32.

158. Wang, G.; Wang, H.; Ling, Y.; Tang, Y.; Yang, X.; Fitzmorris, R. C.; Wang, C.; Zhang, J. Z.; Li, Y., Hydrogen-Treated TiO_2 Nanowire Arrays for Photoelectrochemical Water Splitting. *Nano Lett.* **2011,** *11*, 3026-3033.

159. Wang, M. Z.; Liang, F. X.; Nie, B.; Zeng, L. H.; Zheng, L. X.; Lv, P.; Yu, Y. Q.; Xie, C.; Li, Y. Y.; Luo, L. B., TiO_2 nanotube array/monolayer graphene film Schottky junction ultraviolet light photodetectors. *Part. Part. Syst. Charact.* **2013,** *30*, 630-636.

160. Liu, B.-T.; Tang, S.-J.; Yu, Y.-Y.; Lin, S.-H., High-refractive-index polymer/inorganic hybrid films containing high TiO_2 contents. *Colloids Surf., A* **2011,** *377*, 138-143.

161. Yamaguchi, T.; Tobe, N.; Matsumoto, D.; Arakawa, H., Highly efficient plastic substrate dye-sensitized solar cells using a compression method for preparation of TiO_2 photoelectrodes. *Chem. Commun.* **2007**, 4767-4769.

162. Xue, H.; Kong, X.; Liu, Z.; Liu, C.; Zhou, J.; Chen, W.; Ruan, S.; Xu, Q., TiO_2 based metal-semiconductor-metal ultraviolet photodetectors. *Appl. Phys. Lett.* **2007,** *90*, 1118.

163. Gedamu, D.; Paulowicz, I.; Kaps, S.; Lupan, O.; Wille, S.; Haidarschin, G.; Mishra, Y. K.; Adelung, R., Rapid Fabrication Technique for Interpenetrated ZnO Nanotetrapod Networks for Fast UV Sensors. *Adv. Mater.* **2014,** *26*, 1541-1550.

164. Bera, A.; Basak, D., Photoluminescence and photoconductivity of ZnS-coated ZnO nanowires. *ACS Appl. Mater. Interfaces* **2010,** *2*, 408-12.

165. Ko, S. H.; Lee, D.; Kang, H. W.; Nam, K. H.; Yeo, J. Y.; Hong, S. J.; Grigoropoulos, C. P.; Sung, H. J., Nanoforest of Hydrothermally Grown Hierarchical ZnO Nanowires for a High Efficiency Dye-Sensitized Solar Cell. *Nano Lett.* **2011,** *11*, 666-671.

166. Shao, D.; Yu, M.; Sun, H.; Hu, T.; lian, J.; Sawyer, S., High responsivity, fast ultraviolet photodetector fabricated from ZnO nanoparticle-graphene core-shell structures. *Nanoscale* **2013,** *5*, 3664-3667.

167. Tian, W.; Zhang, C.; Zhai, T.; Li, S.-L.; Wang, X.; Liu, J.; Jie, X.; Liu, D.; Liao, M.; Koide, Y.; Golberg, D.; Bando, Y., Flexible Ultraviolet Photodetectors with Broad Photoresponse Based on Branched ZnS-ZnO Heterostructure Nanofilms. *Adv. Mater.* **2014,** *26*, 3088-3093.

168. Tsai, S.-Y.; Hon, M.-H.; Lu, Y.-M., Fabrication of transparent p-NiO/n-ZnO heterojunction devices for ultraviolet photodetectors. *Solid State Electron.* **2011,** *63*, 37-41.

169. Babichev, A.; Zhang, H.; Lavenus, P.; Julien, F.; Egorov, A. Y.; Lin, Y.; Tu, L.; Tchernycheva, M., GaN nanowire ultraviolet photodetector with a graphene transparent contact. *Appl. Phys. Lett.* **2013,** *103*, 201103.

170. Weng, W. Y.; Hsueh, T. J.; Chang, S. J.; Wang, S. B.; Hsueh, H. T.; Huang, G. J., A High-Responsivity GaN Nanowire UV Photodetector. *IEEE Journal of Selected Topics in Quantum Electronics* **2011,** *17*, 996-1001.

171. Afal, A.; Coskun, S.; Emrah Unalan, H., All solution processed, nanowire enhanced ultraviolet photodetectors. *Appl. Phys. Lett.* **2013,** *102*, 043503.

172. Luo, L.; Zhang, Y.; Mao, S. S.; Lin, L., Fabrication and characterization of ZnO nanowires based UV photodiodes. *Sens Actuators A Phys.* **2006,** *127*, 201-206.

173. Lin, C.-C.; Lin, W.-H.; Li, Y.-Y., Synthesis of ZnO Nanowires and Their Applications as an Ultraviolet Photodetector. *J. Nanosci. Nanotechnol.* **2009,** *9*, 2813-2819.

174. Tsai, T.-Y.; Chang, S.-J.; Weng, W.-Y.; Hsu, C.-L.; Wang, S.-H.; Chiu, C.-J.; Hsueh, T.-J.; Chang, S.-P., A visible-blind TiO_2 nanowire photodetector. *J. Electrochem. Soc* **2012,** *159*, J132-J135.

175. Xie, Y.; Wei, L.; Wei, G.; Li, Q.; Wang, D.; Chen, Y.; Yan, S.; Liu, G.; Mei, L.; Jiao, J., A self-powered UV photodetector based on TiO_2 nanorod arrays. *Nanoscale Res. Lett.* **2013,** *8*, 1-6.

176. Sang, L.; Liao, M.; Koide, Y.; Sumiya, M., High-temperature ultraviolet detection based on InGaN Schottky photodiodes. *Appl. Phys. Lett.* **2011,** *99*, 031115.

177. Chang, P.-C.; Yu, C.-L., InGaN⁄GaN multi-quantum-well ultraviolet photosensors by capping an unactivated Mg-doped GaN layer. *Appl. Phys. Lett.* **2007,** *91*, 141113.

178. Butun, B.; Tut, T.; Ulker, E.; Yelboga, T.; Ozbay, E., High-performance visible-blind GaN-based pin photodetectors. *Appl. Phys. Lett.* **2008,** *92*, 33507-33507.

179. Xing, J.; Wei, H.; Guo, E.-J.; Yang, F., Highly sensitive fast-response UV photodetectors based on epitaxial TiO_2 films. *J. Phys. D: Appl. Phys.* **2011,** *44*, 375104.

180. Liu, M.; Kim, H. K., Ultraviolet detection with ultrathin ZnO epitaxial films treated with oxygen plasma. *Appl. Phys. Lett.* **2004,** *84*, 173-175.

181. Liu, K. W.; Ma, J. G.; Zhang, J. Y.; Lu, Y. M.; Jiang, D. Y.; Li, B. H.; Zhao, D. X.; Zhang, Z. Z.; Yao, B.; Shen, D. Z., Ultraviolet photoconductive detector with high visible rejection and fast photoresponse based on ZnO thin film. *Solid State Electron.* **2007,** *51*, 757-761.

182. Chen, M.; Hu, L.; Xu, J.; Liao, M.; Wu, L.; Fang, X., ZnO Hollow-Sphere Nanofilm-Based High-Performance and Low-Cost Photodetector. *Small* **2011,** *7*, 2449-2453.

183. Xu, Q. A.; Zhang, J. W.; Ju, K. R.; Yang, X. D.; Hou, X., ZnO thin film photoconductive ultraviolet detector with fast photoresponse. *J. Cryst. Growth* **2006,** *289*, 44-47.

184. Bi, Z.; Yang, X.; Zhang, J.; Bian, X.; Wang, D.; Zhang, X.; Hou, X., A Back-Illuminated Vertical-Structure Ultraviolet Photodetector Based on an RF-Sputtered ZnO Film. *J. Electron. Mater.* **2009,** *38*, 609-612.

185. Kouklin, N., Cu-Doped ZnO Nanowires for Efficient and Multispectral Photodetection Applications. *Adv. Mater.* **2008,** *20*, 2190-2194.

186. Soci, C.; Zhang, A.; Xiang, B.; Dayeh, S. A.; Aplin, D. P. R.; Park, J.; Bao, X. Y.; Lo, Y. H.; Wang, D., ZnO Nanowire UV Photodetectors with High Internal Gain. *Nano Lett.* **2007,** *7*, 1003-1009.

187. Yanbo, L.; Florent Della, V.; Mathieu, S.; Ichiro, Y.; Jean-Jacques, D., High-performance UV detector made of ultra-long ZnO bridging nanowires. *Nanotechnology* **2009,** *20*, 045501.

188. Retamal, J. R. D.; Chen, C.-Y.; Lien, D.-H.; Huang, M. R. S.; Lin, C.-A.; Liu, C.-P.; He, J.-H., Concurrent Improvement in Photogain and Speed of a Metal Oxide Nanowire Photodetector through Enhancing Surface Band Bending via Incorporating a Nanoscale Heterojunction. *ACS Photonics* **2014,** *1*, 354-359.

189. Boruah, B. D.; Ferry, D. B.; Mukherjee, A.; Misra, A., Few-layer graphene/ZnO nanowires based high performance UV photodetector. *Nanotechnology* **2015,** *26*, 235703.

190. Kind, H.; Yan, H. Q.; Messer, B.; Law, M.; Yang, P. D., Nanowire ultraviolet photodetectors and optical switches. *Adv. Mater.* **2002,** *14,* 158–160.

191. Hsu, C.-L.; Chang, S.-J.; Lin, Y.-R.; Li, P.-C.; Lin, T.-S.; Tsai, S.-Y.; Lu, T.-H.; Chen, I. C., Ultraviolet photodetectors with low temperature synthesized vertical ZnO nanowires. *Chem. Phys. Lett.* **2005,** *416*, 75-78.

Chapter Two

Self-Assembly Dynamics and Accumulation Mechanisms of Ultra-Fine Nanoparticles

Publication relevant to this chapter:

Noushin Nasiri, Tobias D Elmøe, Yun Liu, Qing H. Qin, Antonio Tricoli, "*Self-Assembly Dynamics and Accumulation Mechanisms of Ultra-Fine Nanoparticles*", **Nanoscale**, 7, 9859-9867, **2015**.

Abstract

The self-assembly of nanomaterials into three-dimensional hierarchical structures is a fundamental step impacting a large number of synthetic and natural processes. These range from the scalable fabrication of nano-devices such as batteries, sensors and third generation solar cells to the uptake and accumulation of particulate pollution in the lung alveoli. Here, we show that the dynamic behaviours of ultra-fine particles (UFP < 100 nm) diverge significantly from that of sub- and micro equivalents. For freely diffusing bodies, this leads to the formation of stochastically reproducible films that mimic the morphology and density of ballistically deposited ones. A novel deposition mechanism and regime are proposed that successfully capture the full spectrum of size-dependent self-assembly dynamics. These findings are a significant step toward the engineering of scalable parallel nano-fabrication approaches, and the understanding of the interaction of unbound nanostructures with their surroundings**.**

2.1 Introduction

Understanding the interaction of nanomaterials with their surrounding is focus of a rising multi-disciplinary research effort. This has become a main priority as both energy generation by hydrocarbon combustion and the development of scalable nano-fabrication processes are rapidly increasing the anthropogenic production and emission of nanostructures. The ultra-fine component of these emissions (< 100 nm) is sufficiently small to penetrate the cardiovascular system upon uptake in the lungs and induce oxidative stress with a resultant dysfunction of lung endothelial cells[1]. This underlies the development of various diseases[2] with epidemiological studies showing a correlation between environmental particulate air pollution and a range of endpoints of lung morbidity and mortality[3-4]. In addition, the commercial production of highly performing nanomaterial-based devices such as high-storage capacity batteries, sensors and solar cells requires scalable fabrication processes. A major challenge is to develop methods that enable robust integration of zero-, one- and three-dimensional nanomaterial with sub-micrometre accuracy and control.

Amongst scalable self-assembly routes, gas-phase nucleation/clustering and aerosol deposition are at the core of industrial nanomaterial production with several nanostructured commodities such as carbon black, Titania pigments and fumed silica produced in megatons per year by flame synthesis[5]. Collision and coalescence of bodies in the gas-phase is a widespread process[6-7] that controls the self-assembly of matter from initial atoms[8] to molecular clusters[9] and their rapid growth into nano- and micro-scale particles[10-11]. Collision and dwell conditions govern the resulting body density and morphology. Non- and poorly-coalescing bodies undergoing Brownian collision, for example, can rapidly form fractal-like structures such as soot[12-13], deemed a main agent in environmentally induced lung cancer[14-16] and carbon-black, a key material in tire and ink production. Synthesis of three-dimensional nanostructures has been demonstrated by deposition of diffusing nanoparticles. This is a scalable low-cost route for the wafer-level parallel fabrication of highly performing nano-devices[17-18] with potential for emerging technologies such as third-harmonic-upconversion antennas.[19] However, the limitations and commercial potential of aerosol-based approaches is ultimately determined by the ability of controlling the accumulation and self-assembly dynamics of nanomaterials on a surface.[20]

The dynamics of nanomaterials in the gas phase is usually described in terms of the ratio between the constant displacement induced by an advective velocity and the stochastically-distributed one induced by Brownian motion, namely the Péclet number (Pe). Several studies[21-23] have proposed that the resulting key structural properties and morphologies are determined by this ratio alone and are independent of the depositing body size. For example, spherical particles of 5 and 500 nm colliding with a solid surface at a constant Péclet number are expected to lead to the self-assembly of films with the same morphology. However, recent findings[24-25] have questioned the validity of these models and underlying assumptions. Numerical solutions to the Langevin's equation of motion have shown an up to 500% increase in film density for deposition of 5 nm spherical particles in the diffusion regime. Similar discrepancies from the Péclet-scaling law were observed by direct Monte Carlo simulations for deposition of 10 nm spheres. As interfacial phenomena are a determinant factor in the interaction of nanomaterial with their surroundings[26] an improved understanding of nanostructure deposition and accumulation is of significant potential impact to our health and nano-fabrication capabilities.

Here, the dynamics of unbound nanoparticles is investigated over three orders of magnitude in scale aiming to determine a comprehensive mechanistic description of their accumulation and self-assembly behaviours. Particle displacement is computed by large-scale, grid-free numerical solutions of the Langevin's equation of motion from the ballistic to the diffusion regime. Validation of the resulting morphologies is pursued by aerosol deposition of freely diffusing nanoparticles and topographical mapping by atomic force and scanning electron microscopes. A novel deposition regime that combines features of ballistic- and diffusion-driven dynamics is proposed. This enables quantitative predictions of micro- to nano-particle interaction with their surroundings providing a unified model of their diverging self-assembly mechanisms.

2.2 Results and Discussion

Initially, conditions were determined to capture the multi-scale porosities and hierarchical film structures resulting from the directed (ballistic regime) and undirected (diffusion regime) self-assembly of nanoparticles[20]. To this aim, the dynamics of monodisperse spheres with a diameter (d_p) of 50 nm was simulated by grid-free solution of the Langevin equation of motion as it is discussed further.

2.2.1 Computational Model Outline

Figure 2.1 shows a schematic of a simulation domain consisting of drop and deposition cell. The particles are monodisperse with a constant diameter (5, 10, 30 and 50 nm) and a solid density of 1000 kg.m^{-3}. Particle dynamics is modelled for isothermal condition at 298 K and considering deposition of one particle at a time. In order to obtain true random motion before deposition, a particle is initially released in a cell where particle deposition and film growth are not allowed (Figure 2.1, drop domain). The drop domain height for particle release was equal to $20d_p$ for all simulations. The next particle is released after deposition of the previous one. Deposition occurs when a particle touches another particle or the horizontal surface at the end of the deposition domain using a sticking coefficient of 100%. Electrical charge, Van der Walls force and extra inter-molecular forces are neglected. The impact of temperature and air environment is already accounted in diffusion coefficient and advective velocity. Surface-bond agglomerates were identified by a subroutine determining the neighbor particles in physical connections. More details about the model outline are reported elsewhere[27].

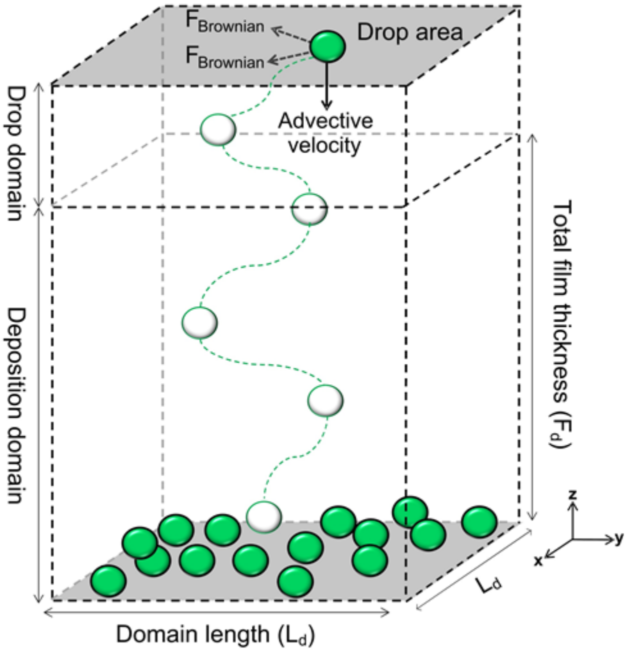

Figure 2.1. *Schematic of the simulated domain and deposition conditions for nanoparticles on a flat substrate reaching a constant film thickness. Particles are inserted at the drop point and flow downstream.*

2.2.2 Simulation Domain Optimization

Domain independent properties were obtained by asymptotic convergence of the film morphologies with increasing deposition surface/domain size (Figure 2.2 and Figure 2.3). For small Péclet-numbers, the advective velocity is nearby zero resulting in a diffusion driven deposition (diffusive regime/limit). For large Péclet-numbers, the advective velocity is dominant resulting in a ballistic limited deposition (ballistic regime). The simulations were repeated five times to obtain statistically relevant morphologies. The resulting particle distributions were investigated as a function of the total film thickness (F_d) and deposition surface size (Figure 2.2a, b). The side (L_d) of the square deposition surface was increased from $20d_p$ to $140d_p$ (Figure 2.2a, b) to assess the impact of geometrical simulation constrains on the resulting film morphology (Figure 2.2a, b, insets). In the diffusion regime, the average film porosity (ε_{film}), calculated from 5 independent simulations, decreased rapidly with increasing total film thickness (Figure 2.2a) reaching a minimum between 0.5 and 1 µm. Further increasing the film thickness resulted in a slow quasi-asymptotic porosity increase. This porosity profile was consistent for all deposition surface size (Figure 2.2a, empty and full circles). However, its magnitude varied substantially with the deposition surface dimension. Increasing the surface side from $20d_p$ (Figure 2.2a, empty circles) to $140d_p$ (full circles) increased the minimal ($\varepsilon_{\mathrm{min}}$) and quasi-asymptotic ($\varepsilon_{\mathrm{q\text{-}a}}$) porosities from 0.966 to 0.983 and 0.973 to 0.987, respectively. This represents an up to 59% variation in film density and indicates that the deposition surface size has a considerable impact on the resulting film properties. This is in line with previous particle dynamics simulations (Table 2.1) and partially explains the considerable higher film densities reported in the diffusion regime for small deposition surface ($L_d = 30d_p$)[21, 24, 25]. It is worth to mention that the simulation properties are independent of the volume. In fact, the self-assembly of the nanoparticles depends on the Péclet number, particle’s size and its advective velocity.

A different dependency from the simulation constrains was observed in the ballistic regime. There, the average porosity profiles (Figure 2.2b) did not feature a minimum but decreased monotonously with increasing total film thickness converging to a quasi-asymptotic value of 0.865 and 0.857 for a deposition surface side of $20d_p$ and $140d_p$, respectively. This corresponded to a maximal film density variation of 5.9% and thus 10 times smaller than that in the diffusion regime. Detailed analysis of the film morphologies (Figure 2.2a, b, insets) revealed that, upon deposition of the first particle layer, main agglomerates forms orthogonally from the deposition surface. These growths by collecting most of the incoming particle flux; effectively shadowing the deeper film layers. The differences observed in the diffusion and ballistic regimes are attributed to the different horizontal spread (surface density) of these surface-bonded agglomerates.

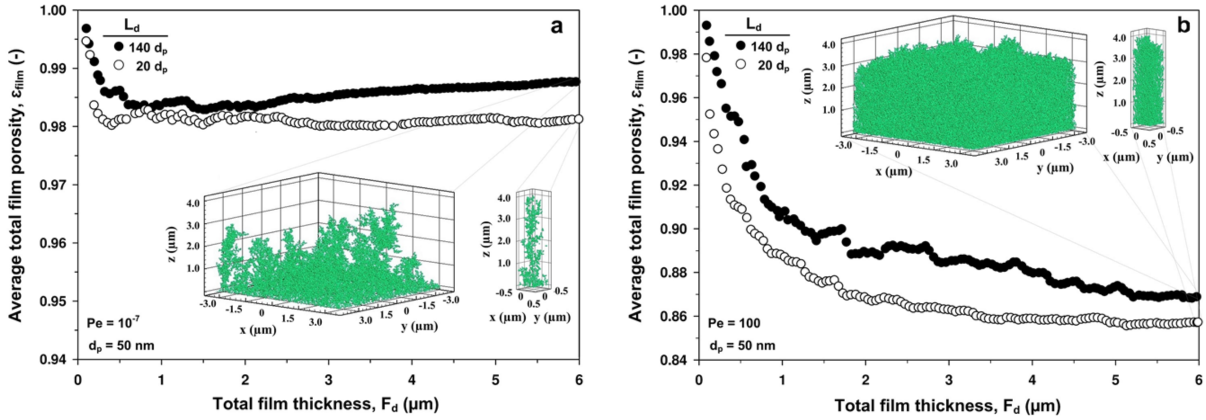

Figure 2.2. *Average film porosity (ε_{film}) as a function of total film thickness (F_d) with particle diameter of 50 nm and two domain lengths ($30d_p$ and $140d_p$) in the (a) diffusion and (b) ballistic regime.*

In the diffusion regime, sufficiently large deposition surfaces enabled to simulate both inter- and intra-agglomerate film porosities (Figure 2.2a, inset ii). In contrast, a small deposition surface restricted the film morphology to that of single agglomerate (Figure 2.2a, inset i) forcefully increasing the resulting film density. This was not the case for the ballistic regime (Figure 2.2b) as the resulting agglomerate horizontal spread was considerably smaller. As a result in the ballistic limit, both small (inset i) and large (inset ii) deposition surfaces were able to capture the inter- and intra-agglomerate film porosities. This was further supported by visual rendering of the deposited particle three-dimensional distributions (Figure 2.2b, insets). These showed nearly indistinguishable film morphologies for large and small deposition surfaces. For all deposition conditions ($10^{-7} \leq \mathrm{Pe} \leq 100$), it was found that the average film porosity (Figure 2.3a, b) increased with increasing deposition surface dimension and converged for $L_d \geq 100d_p$. This is in line with previous particle dynamics results[23,27] showing consistent film densities for a simulation surface side larger than $100d_p$

(Table 1). As a result, here, further investigation of the deposition dynamics was conducted with a large simulation surface size of $140d_p$ that enabled the self-assembly of more realistic film structures.

Table 2.1. Comparison of film key structural parameters obtained by particle deposition dynamics.

Particle Diameter	**Peclet-Number**	**Domain Length**	**Film Thickness**	**Deposition Surface**	**Average Film Porosity (ε_{film})**	**Ref.**
50 nm	10^{-7}-100	$140d_p$	$120d_p$	Flat Square	0.990 - 0.867	This Work
30 nm					0.988 - 0.867	
10 nm					0.973 - 0.861	
5 nm					0.957 - 0.859	
50 nm	10^{-2}-10	$200d_p$	$180d_p$	Cylindrical Capillary Walls	0.98 - 0.86[b]	27
a[a]	10^{-1}-100	$512d_p$	$400d_p$	Flat Square	0.98 - 0.86[b]	23
30 nm	10^{-7}-100	$30d_p$	$160d_p$	Flat Square	0.965 - 0.84	25
10 nm					0.925 - 0.84	
5 nm					0.90 - 0.84	
30 nm	Diffusion & Ballistic Regime	$30d_p$	$50d_p$	Flat Square	0.969 - 0.848 [b]	21
10 nm	Diffusion Regime	$30d_p$	$100d_p$	Flat Square	0.93	24
a[a]	10^{-1}-100	$512d_p$	--	Flat Square	0.98 - 0.86[b]	28

[a] The domain was structured in a cubic subdomain lattice with a side length of a.

[b] The average porosity was estimated from the plateau packing density (Φ_{sl}).

Increasing the Pe number from 10^{-7} (Figure 2.3a, pure diffusion regime) to 100 (Figure 2.3b, pure ballistic regime) leads to decreasing the porosity of composed film at all surface sizes. This significant change is attributed to the deposition style of the particles during transition from diffusion to the ballistic regime. In fact, at a small Pe number the particle transport is dominated by diffusion and its movement is scattered towards the deposition surface. In that case, the deposited film grows with a fractal-like structure.

In addition, it was found that small deposition surfaces having a square side (L_d) smaller than 120 times the particle diameter leads to up 59% artificially higher film densities. This is attributed to the physical constrains that are not sufficient to achieve periodic symmetry conditions and thus do not enable establishment of the multi-scale nano- and micro-porosity observed by aerosol deposition of nanoparticles and agglomerates[29]. This explains the drastic increase in film densities (ca. 500%) predicted in the diffusion regime for deposition of ultra-fine nanoparticles (d_p < 30 nm) by recent small-domain-constrained studies[21,25]. As a result, all further simulations were conducted with a large domain size of $140d_p$ that enables the self-assembly of more realistic, hierarchical film morphologies.

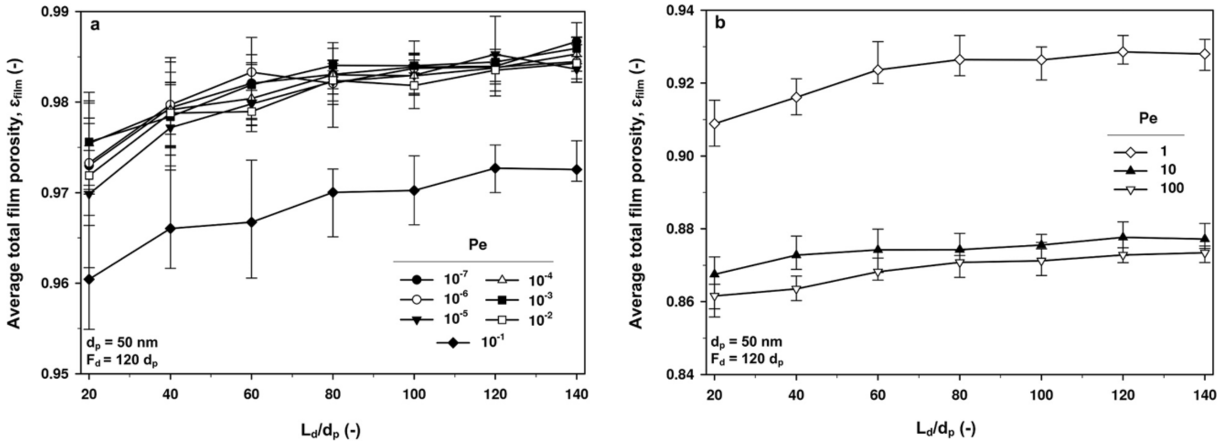

Figure 2.3. *Average film porosity (ε_{film}) for spherical nanoparticles with a diameter of 50 nm as a function of domain length ($20d_p$ to $140d_p$) from (a) diffusion to the (b) ballistic regime.*

2.2.3 Model Validation

Validation of these numerical results was obtained by comparison of the converged nanoparticle solid fraction with previous large-scale Monte Carlo simulations (Table 2.1) showing good agreement and a characteristic S-shaped dependency from the Péclet number in line with very recent results[28] (Figure 2.4). Figure 2.4 shows the values for plateau packing density as a function of the Pe number for particle diameter of 50 nm in comparison to Rodriguez-Perez et al.[23] and Castillo et al.[28] on flat surface deposition and Elmøe et al.[27] on a porous substrate. The resulted packing density is in agreement with these results. Rodriguez-

Perez et al.[23] and Castillo et al.[28] studied the particle deposition on a flat surface with structured grid domain resulting in an increase of order and density. Elmøe et al.[27] simulated the particle deposition on a porous capillary substrate. The domain length used by both researches was sufficiently large ($512d_p$ and $80d_p$)[23,27,28] leading to a good agreement with the results presented here. While, for Dreyer et al.[24] and Ogunsola et al.[22], the domain length was not sufficiently resulting lower final porosities ($30d_p$ and $40d_p$ respectively) (Table 2.1).

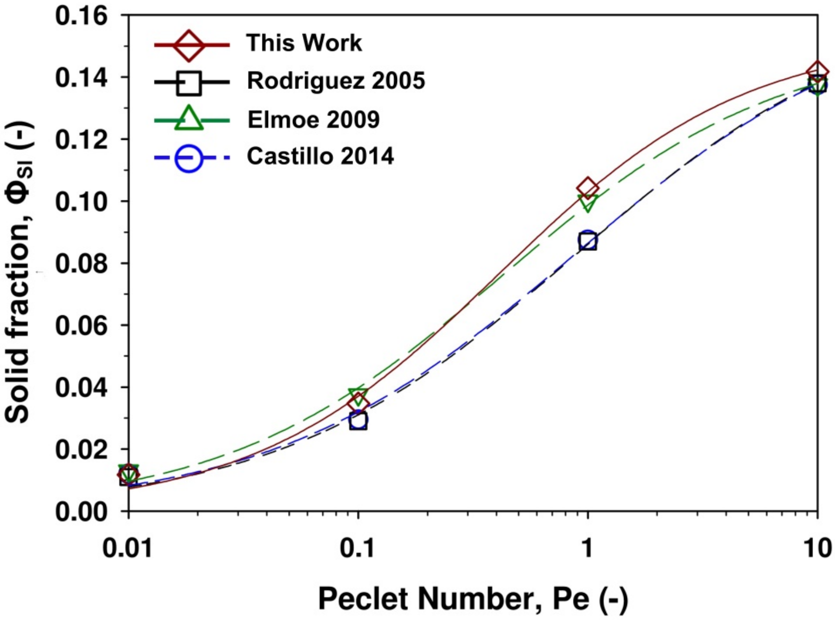

Figure 2.4. *Plateau solid fraction as a function of the Pe number for deposition of single spherical particles of 50 nm in diameter by this work (diamond) and comparison with previous researches obtained for flat deposition surfaces*[23,28] *(rectangles and circle) and capillary*[27] *(triangles).*

2.2.4 Self-Assembly Dynamics of Nanoparticle Films

To determine the impact of the nanoparticle size on the film self-assembly dynamics, the structural properties obtained by deposition of 50 and 5 nm particles were further investigated. Figure 2.5 shows sections of the hierarchical morphologies formed by their self-assembly in the diffusion and ballistic regimes. Each contiguous set of touching particles, a surface-formed and bond agglomerate was labelled with a colour. It was found that independently of the deposition regime and particle size, nanoparticle film self-assembly is driven by the formation of parallel agglomerates growing in the vertical direction (Figure 2.5). However, the density and horizontal spreading of these agglomerates was strongly dependent from the particle size and deposition conditions leading to significantly different morphologies and structural properties.

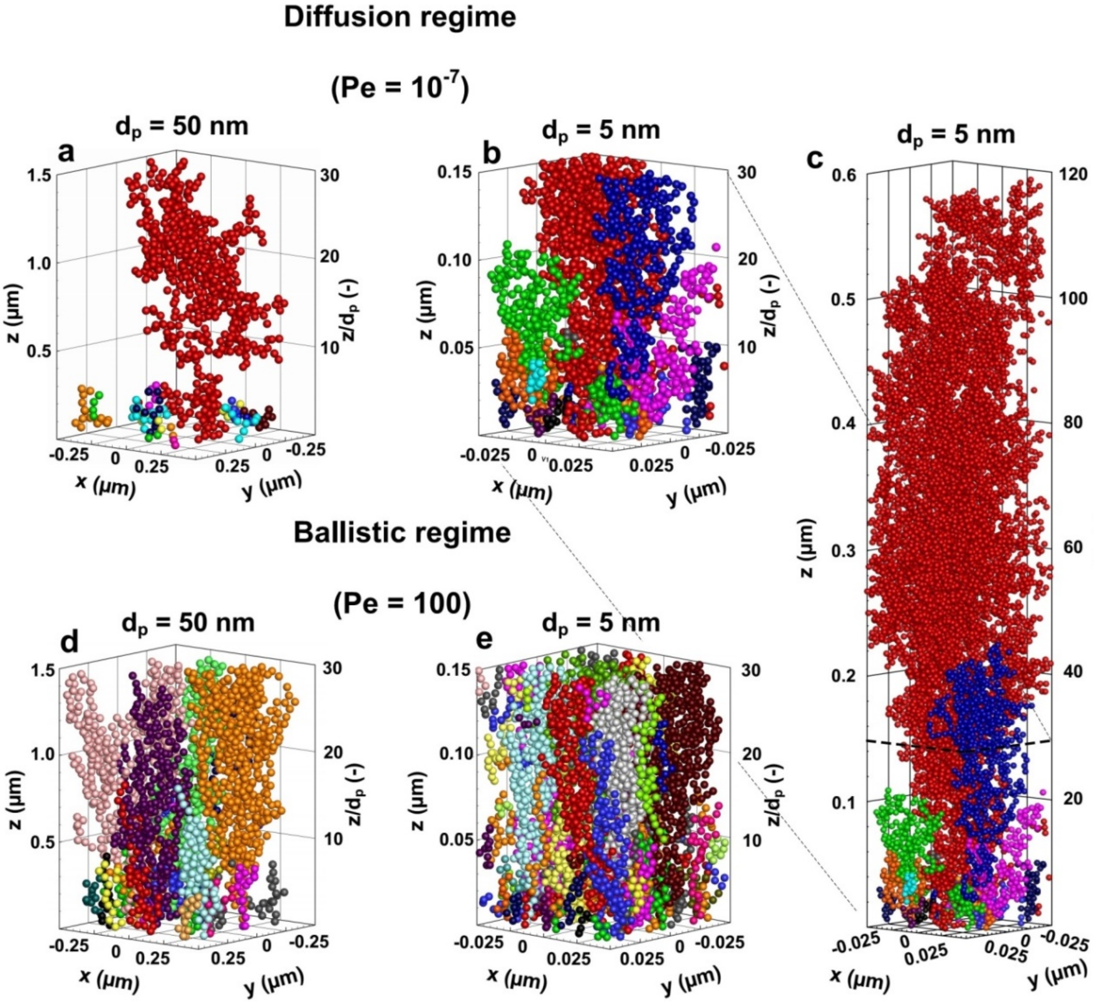

__Figure. 2.5.__ Three dimensional plots of film sections self-assembled in the diffusion (a,b,c) and ballistic (d,e) regimes for particle 50 nm (a,d) and 5 nm (b,c,e) in diameter. Each contiguous set of particles (surface-bond agglomerate) was labelled with a colour.

For the 50 nm particles, two distinct characteristic accumulation behaviours were determined. In the diffusion regime, the film morphology was characterized (Figure 2.5a) by the rapid establishment of a prevailing agglomerate in the first $10d_p$ of thickness. These large structures shadowed the deposition surface collecting the incoming nanoparticle flux. At $20d_p$ thickness, a single agglomerate became prevalent spreading over a horizontal surface of $10d_p$×$10d_p$ Further increasing the film thickness did not result in additional horizontal growth but in a series of laterally-confined agglomerates growing in parallel. This branch-like vertical growth is in line with the morphology observed for aerosol-deposited TiO_2[30] and SnO_2[31] nanoparticle films utilized as porous dye sensitized solar cells electrodes and chemical sensors, respectively. In contrast, ballistically-driven deposition led to a different films structure (Figure 2.5d). There it was not possible to identify prevailing agglomerate. Instead, several parallel agglomerates grew from the deposition surface. This is attributed to the relatively small path swept by each depositing particle at high Péclet numbers and in line with the high film density observed by deposition of nanoparticle aerosols in burner low-pressure impactors[32].

In contrast, the 5 nm particles did not feature these two opposite structural regimes. Instead, in the first $10d_p$ film thickness, both diffusion- (Figure 2.5b) and ballistic-driven (Figure 2.5e) growth revealed the same structural densities and morphologies as those observed for the 50 nm particles in the ballistic regime (Figure 2.5d). After $40d_p$ thickness (Figure 2.5c), diffusion-driven deposition of 5 nm particles led to the establishment of a single surface-bond agglomerate morphology. This is in line with the initial densification computed with decreasing particle size at low Péclet numbers. Furthermore, it shows that the self-assembly dynamics of ultra-fine spheres having a diameter below 50 nm differ from that expected for purely diffusive bodies and, close to the substrate interface, approaches ballistic-induced self-assembly. This is attributed to a self-induced variation of the collision mechanism with decreasing particle size leading to similar partially vertically-directed straight collision trajectories as for ballistic bodies. These findings explain the high density observed for thin nanoparticle patterns obtained by parallel electrodynamics focusing of charged particle-laden aerosols[17].

2.2.5 Particle Size-Dependent Structural Properties

The correlations between key film structural properties and particle size were further investigated by computation of the film density profiles (Figure 2.6) as a function of the particle diameters in the ballistic (Pe = 100) and diffusion regimes (Pe = 10^{-7}). It was found that in the former all particle sizes lead to identical packing density profiles (Figure 2.6a). In contrast, in the diffusion regime the surface density of the first particle layer increases by more than 200% with decreasing particle diameter from 50 to 5 nm. Furthermore, film growth (Figure 2.6b) did not lead to the establishment of a constant/plateau-density as for ballistically-driven self-assembly (Figure 2.6a). Instead, for diffusion-driven deposition, the density decreased continuously from an initial maximum near the substrate interface to a minimum on the top film surface. This is particularly relevant with respect to the accumulation of ambient UFP in the lung alveoli and the nano-fabrication of three-dimensional nanostructured layers as in both systems particle deposition is, usually, diffusion-driven. The high and variable densities of the nanoparticle-substrate interfaces, reported here, indicate that the established Péclet-scaling laws cannot be applied to model the interaction and accumulation of diffusive nanoparticles with their surroundings.

Further investigation of the nanoparticle film morphologies revealed a unique structure. Both for the ballistic and diffusion regimes, a ripple-like density profile (Figure 2.6a,b insets) was observed in the first $10d_p$ film thickness. This was characterized by three main peaks representing the maxima and minima of the local slice densities. The first density peak was located at $0.8d_p$ height from the deposition surface and, for ballistic deposition (Figure 2.6a, inset), reached the highest slice packing density of 0.3 and thus nearly half of the random close packing density (0.64) for monodisperse spheres. This is attributed to the discrete dimension of the depositing nanoparticles. In fact, for deposition of a single layer of spheres on a flat surface, the maximal density will always be found at a film height of $0.5d_p$. Here, the shift from $0.5d_p$ to $0.8d_p$ height is attributed to the intercalation of the layer during three-dimensional growth.

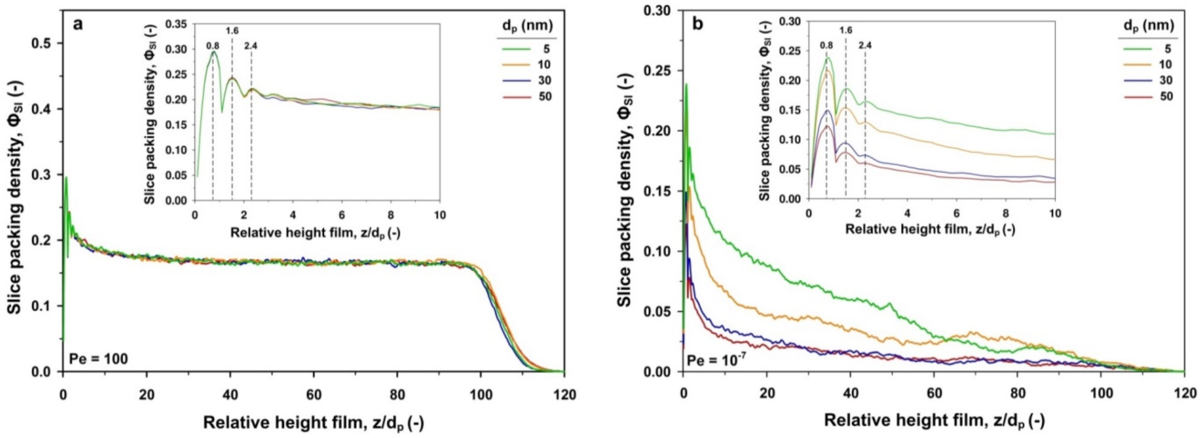

Figure. 2.6. *Representative slice packing density profiles (a) in the ballistic and (b) diffusion regimes as a function of the particle diameter from 50 to 5 nm. Three main density maxima (a, b, insets) are determined at 0.8, 1.6, and 2.4 relative film thicknesses (z/d_p). The magnitude of these maxima is (a) independent from the particle diameter in the ballistic regime while (b) increases by more than 100% with decreasing particle size in the diffusion regime.*

The second and third density peaks (Figure 2.6a,b inset) were found consistently at $1.6d_p$ and $2.4d_p$ thickness and attributed to the second and third particle layer maxima. Further smaller peaks were found at alternating film heights above $2.4d_p$ but their position and intensity did not converge among different simulations resulting in a destructive interference. This suggests that upon a thickness of $2.4d_p$, the film morphology evolves from a two- to a three-dimensional disordered state. However, while for ballistically driven deposition the peaks' magnitude was independent from the particle size (Figure 2.6a, inset), in the diffusion regime (Figure 2.6b, inset) it increases with decreasing particle diameter. The first peak ($0.8d_p$) slice packing density increased from 0.122 to 0.239 with decreasing particle size from 50 to 5 nm. As a result, a 5 nm nanoparticle film had an initially 100% higher density than that made of 50 nm particles. This significant densification of the substrate-nanoparticle interface explains the rapid shunting of nanoparticle-based ultra-sensitive sensors made by aerosol deposition of ca. 5 nm particle layers.[18] Furthermore, it indicates that the mechanisms governing the accumulation of particles on an interface change with decreasing size. This leads to a significantly stronger substrate-nanoparticle interaction than previously modelled with sub-micro and micro-scale particles in the diffusion regime[23].

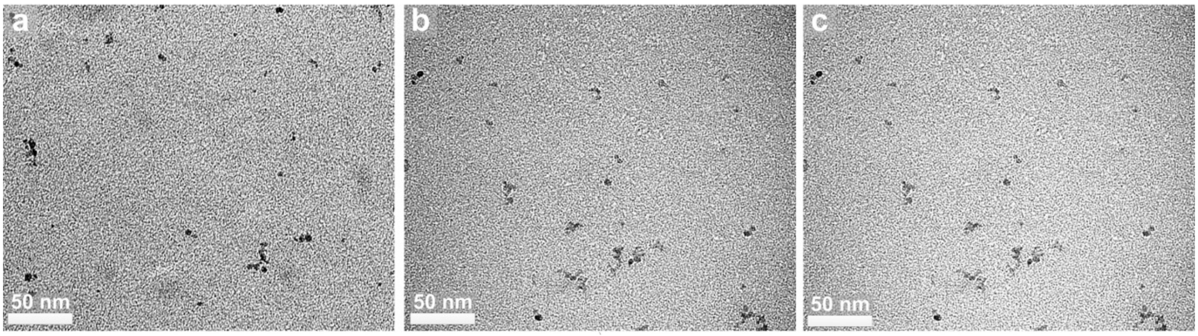

Figure 2.7. *TEM image of deposited non-agglomerated TiO_2 particles on TEM grid by flame spray pyrolysis.*

The validity of these predictions was assessed by characterization of the interface morphology obtained by deposition of particle-laden aerosols on polished Si-wafers. A hot TiO_2 aerosol with an average particle diameter of 5 nm and a narrow size distribution was produced by flame synthesis of organometallic precursor as previously reported in details[33]. This aerosol was orthogonally impinged on a polished Si-wafer resulting in a thermophoretically-driven[34] particle flux directed toward the wafer surface. The aerosol concentration and deposition conditions were controlled by the precursor concentration, dilution and temperature gradient[20] resulting in nearly non-agglomerated nanoparticles as determined by thermophoretic sampling on transmission electron microscopy (TEM) grids (Figure 2.7) and deposition Péclet numbers of 10^{-1}-10^{-2} (as computed in section 4.4.1). It was found that by sufficiently decreasing the deposition time a quasi-monolayer of particles in contact with the substrate surface could be self-assembled.

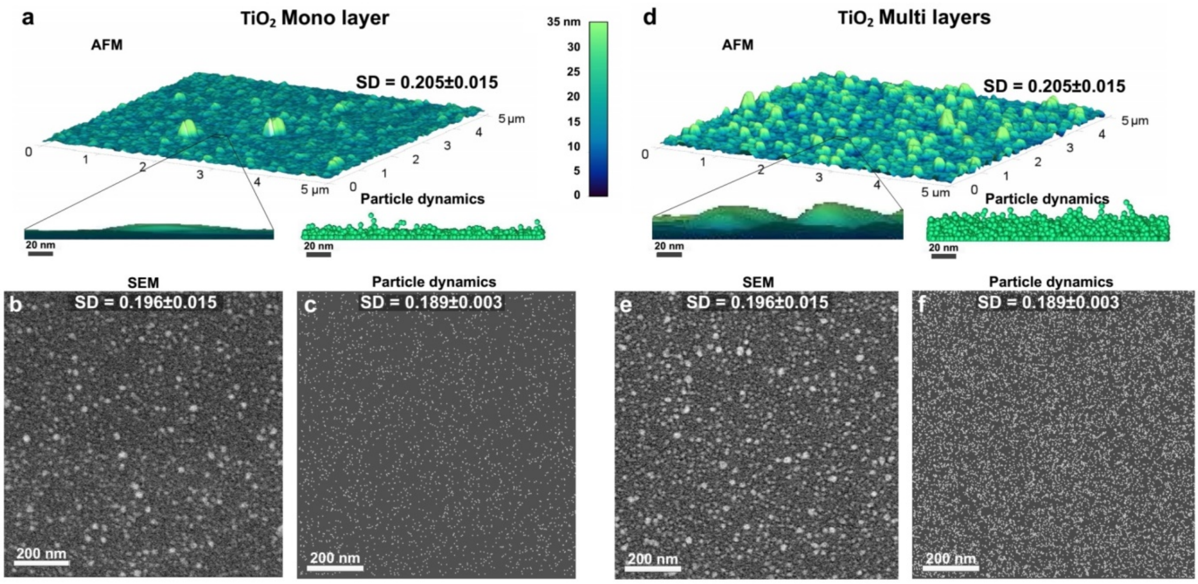

Figure 2.8. *AFM topography and SEM images of (a, b) a quasi-monolayer and (d, e) a multi-layer of* TiO_2 *nanoparticles (5 nm in diameter) aerosol-deposited on polished Si-wafers. The AFM and SEM analysis revealed a consistent surface density (SD) of 0.2±0.015. Comparison of 5 nm particle size distributions computed by Langevin dynamics show comparable cross-sectional (a,b, insets) and (c, f) horizontal morphological features.*

Figure 2.8a shows an atomic force microscopy (AFM) topographical scan of the Si-wafer surface upon deposition of a complete first layer of nanoparticles. The surface was characterized by nano-scale roughness with most peaks having an average height of ca. 5 nm in good agreement with the TiO_2 particle size. Some few peaks with a maximal height of ca. 17 nm were randomly distributed on the surface and are attributed to the initial formation of surface-bond agglomerates. Particle deposition and initial film self-assembly was confirmed by scanning electron microscopy (SEM) analysis (Figure 2.8b). Simulation of 5 nm particle deposition at comparable conditions (Pe = 10^{-2}) and with a maximal film thickness corresponding to that measured by AFM (17 nm) led to structural similar morphologies (Figure 2.8c). These were also characterized by a rough matt of 5 nm asperities with some few higher peaks randomly spread on the surface. The impact of the temperature difference between the simulations and the flame-made aerosol deposition experiments was accounted by the computation of the Péclet number that results in the same diffusion coefficient to advection velocity ratio. The larger mean free path of the experimental particles is expected to lead to only slightly higher interface densities as the ratio between mean free path and particle size is close to one for both experimental and simulated particles.

Comparison of the film side view obtained by AFM and particle dynamics (Figure 2.8a, insets) showed consistent cross-sections with, however, smoother film height variations observed by AFM. This was attributed to the limited AFM inter-particle resolution not enabling to resolve small gaps between the deposited particles. Doubling the aerosol exposure time nearly doubled the film thickness (Figure 2.8d) leading to a maximal film height of nearly 35 nm. This is in line with the constant film growth rates reported for thermophoretic deposition of flame-made nanoparticle aerosols[20]. This confirms further that upon deposition of the first nanoparticle monolayer (Figure 2.8a,b) the film growth proceed mainly by self-assembly of parallel agglomerates vertically-aligned to the deposition surface (Figure 2.8b,c).

This morphology was equivalent to that obtained by simulation of 5 nm nanoparticle deposition and a maximal film thickness of 35 nm (Figure 2.8d inset). A main difference between the simulated (Figure 2.8c,f) and aerosol-deposited films was the larger variation in size observed by SEM (Figure 2.8b,e). This is attributed to both the polydisperse nature of the flame-made nanoparticles, and the limited resolution of the SEM not being able to discern primary particles of 5 nm within single agglomerates. Analysis of the nanoparticle surface by AFM and SEM revealed a surface density (SD) of 0.20±0.015 and thus very close to that (0.19±0.003) predicted by particle dynamics.

2.3 Experimental Validation

2.3.1 Péclet-Number Computation

Péclet-number is a non-dimensional number defined as:

$$Pe = \frac{\left({}^{d_p}/_{2}\right)v}{D_p} \tag{2.1}$$

where d_p is the particle diameter, v is the particle translational velocity and D_p is the diffusion coefficient. The diffusion coefficient, D_p, of a particle in a fluid is calculated by the Stokes-Einstein equation:

$$D = \frac{K_b T}{f} \tag{2.2}$$

where K_b is the Boltzmann constant ($1.3806488 \times 10^{-23}$ $m^2 kg.s^{-2} K^{-1}$), T is the temperature and f is the friction coefficient of the particle in the fluid. In continuum ($k_n << 1$), transition ($K_n \approx 1$), and free molecular regime ($k_n >> 1$), where the friction coefficient, f, is calculated by:

$$f = 3\pi\mu d_p \qquad \text{for } k_n<<1 \tag{2.3}$$

$$f = \frac{3\pi\mu d_p}{C_c} \qquad \text{for } k_n\approx 1 \text{ and } k_n>>1 \tag{2.4}$$

where μ is the viscosity of the medium, d_p is the particle diameter, K_n is the Knudsen number ($K_n=2\lambda_{gas}/d_p$, λ_{gas} is the gas molecule mean free path), and C_c is the Cunningham correction factor which is equal to:

$$C_c = 1 + K_n(A_1 + A_2 e^{-\frac{2A_3}{K_n}}) \tag{2.5}$$

where the values for A_1, A_2 and A_3 in the air are equal to 1.21, 0.40 and 0.78, respectively. The aerosol temperature (T_F) near the substrate is 773 K as experimentally presented. The fluid dynamic viscosity (μ_F) at 773 K and C_c for K_n of 10-100 are 3.481×10^{-5} kg.m^{-1}.s^{-1} and 100 respectively. This calculation leads to a friction and diffusion coefficient of 1.64×10^{-14} kg.s^{-1} and 6.5×10^{-7} m^2.s^{-1} which is in agreement with D reported by other researchers[20,29]. In the absence of electrical forces, the main nanoparticle deposition mechanisms are Brownian diffusion, thermophoresis and impaction. The thermophoretic velocity, v_T, is usually described as[20]:

$$v_T = -K_T \frac{\mu_F(T_F - T_S)}{\rho_F \delta_T T_P} \tag{2.6}$$

where T_P is the particle temperature (approximated by the average of the aerosol (T_F) and surface (T_S) temperatures), ρ_F is the fluid density, δ_T is the boundary layer thickness and K_T is the thermophoretic coefficient which is usually assumed independent of the particle size equal to 0.55. A surface temperature (T_S) of 410 K, a small boundary layer thickness between 0.01-1 mm and the air density of 0.4565 kg.m^{-3} at 773 K. This leads to an advective velocity of 2.57 m.s^{-1}.Using diffusion coefficient of 6.5×10^{-7} m^2.s^{-1} results in a Péclet-number between 10^{-3}-10^{-1}.

2.3.2 Analytical Model

The different mechanisms for particle deposition at ballistic, randomly oriented ballistic and diffusion regimes is shown in Figure 2.9. The scaled particle SD is computed as a ratio of horizontal area shadowed by a deposited particle to that required for a particle to deposit. The horizontal area shadowed by a particle (A_{dp}) with the diameter of d_p is calculated from the following equation (Figure 2.9a, insets):

$$A_{dp} = \frac{\pi d_p^2}{4} \tag{2.7}$$

This value is constant for all different regimes as the particle size is constant. However, the required area for a particle to deposit is different for different regimes. In the ballistic regime, the advective velocity is dominant and particle deposits on a straight orthogonal trajectory to the surface due to the high advective velocity. In this case, the collision area for a particle to deposition on the surface before colliding with any other particle can be calculated as follows:

$$A_{stat} = \pi d_p^2 \tag{2.8}$$

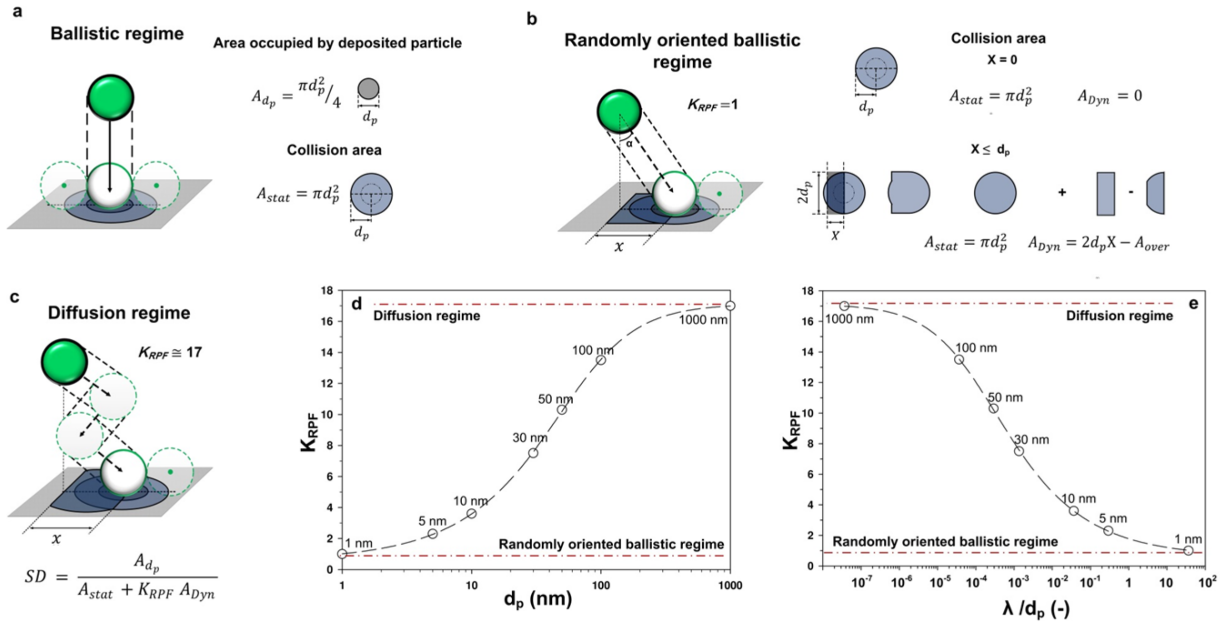

Figure 2.9. *Different deposition mechanism and scaled particle surface density in (a) ballistic, (b) randomly oriented ballistic and c, diffusion regime as a function of the (d) particle diameter and (e) mean free path. The increase in travelled path for diffusive particle ($\lambda_p/\boldsymbol{d_p}$<1) is accounted through the K_{RPF} factor as discussed in details in the analytical model section.*

Despite different mechanism for particle deposition, this is the minimum area a particle requires to deposit on the surface without touching any other ones. The lowest porosity of the ballistic films and the highest SD are attributed to this minimum collision area required for particle (Figure 2.9a) when the particle dynamic is dominated by high advective velocity. In the randomly oriented ballistic regime, the particle is sufficiently small (d_p < 10 nm) and touches the surface on a single Brownian displacement (Figure 2.9b). The collision area calculated for these particles is the sum of the minimal area required for particle deposition (A_{stat}) and the additional horizontal area swept by a particle due to the Brownian displacement, X, within the potential collision length, d_p, (A_{dyn}). Thus, the collision area is calculated from the following equation:

$$A_{stat} + A_{dyn} = \pi d_p^2 + (2d_pX - A_{over}) \tag{2.9}$$

where A_{over} is the area overlapped between the minimal area required for deposition and that due to single-step Brownian displacement which can be calculated as below:

$$A_{over} = 2\int_0^X d_P^2 - y^2)d_y = X\sqrt{d_P^2 - X^2)} + d_P^2 sin^{-1}(\frac{X}{d_P}) \tag{2.10}$$

$$A_{over} = d_P^2 \left[\bar{X}\sqrt{1 - \bar{X}^2)} + sin^{-1}(\bar{X})\right] \tag{2.11}$$

The collision area of a particle in randomly oriented ballistic regime is calculated using equations (4.9) and (4.11):

$$A_{stat} + A_{dyn} = d_p^2\left[\pi + 2\bar{X} - \bar{X}\sqrt{1 - \bar{X}^2} + sin^{-1}(\bar{X})\right] \tag{2.12}$$

This results in a scaled particle SD equal to:

$$SD = \frac{A_{dp}}{A_{stat} + K_{RPF}A_{dyn}} \tag{4.13}$$

where the K_{RPF} is the Randomly Path Factor and for a single-step Brownian displacement is equal to 1.

$$SD = \frac{\pi}{4\left[\pi + 2\bar{X} - \left[\bar{X}\sqrt{1 - \bar{X}^2} + sin^{-1}(\bar{X})\right]\right]} \tag{2.8}$$

For the diffusion regime, the amount of Brownian steps increases due to the particle mean free path (λ_{dp}) becoming smaller in the collision length (Figure 2.9d). The obtained K_{RPF}

factors resulting in an s-shaped profile between particle size and particle mean free path as a function of K_{RPF} factor.

2.3.3 Computation of the Brownian Displacement through the Collision Length

The Brownian's motion induced horizontal displacement within the vertical collision length (d_p) was computed from the average transition time as a function of particle size and Péclet-number:

$$v.t + X = d_P \tag{2.14}$$

where v is the particle velocity, t is the time, X is the Brownian displacement and d_p is the particle diameter. Following the Stokes-Einstein equation, the distance travelled by a particle suspended in a fluid is related to the diffusion coefficient of the particle in that fluid, D_p, and the travelled time, t:

$$X = \sqrt{(2D_p.t)} \tag{2.15}$$

This leads to:

$$d_P^2 - \left(2d_p.v + 2D_p\right)t + v^2t^2 = 0 \tag{2.16}$$

Solution of quadratic equation results in a transition time, (t):

$$t = \frac{d_P}{v} + \frac{D}{v} - \frac{\sqrt{D^2 + 2d_p.v.D}}{v^2} \tag{2.17}$$

By replacing this time in equation (2.16), we obtained an average Brownian displacement, (X):

$$X^2 = \frac{2d_PD}{v} + \frac{D^2}{v^2} - \frac{2D\sqrt{D^2 + 2d_PvD}}{v^2} \tag{2.18}$$

Considering the Péclet-number definition:

$$Pe = \frac{\left({}^{d_P}/_2\right)v}{D} \tag{2.19}$$

This leads to a Brownian displacement, X, equal to (Figure 2.10):

$$X = d_P \sqrt{\frac{1}{Pe} + \frac{1}{2Pe^2} - \frac{1}{2Pe^2}\sqrt{1 + 4Pe}} \tag{2.20}$$

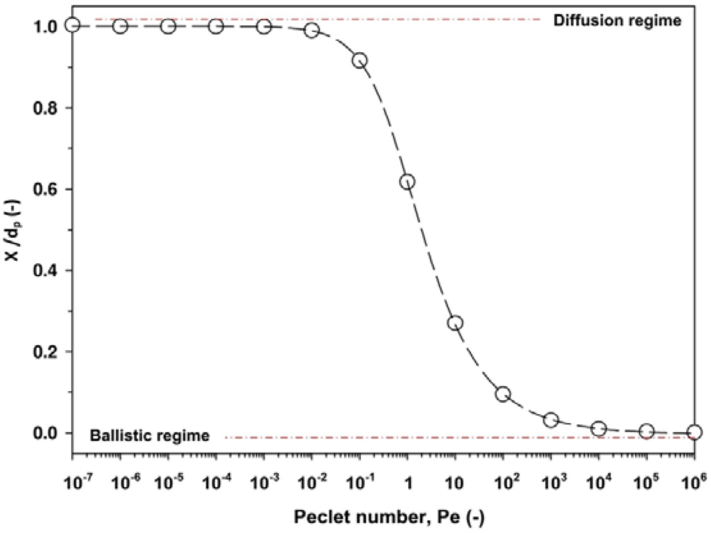

Figure 2.10. *Brownian displacement to the collision length (d_P) ratio as a function of Péclet-number.*

2.4 Self-Assembly Mechanisms and Regimes

The mechanisms underlying this interface densification and diverging self-assembly dynamics were assessed by analysis of the first particle layer/surface density (Figure 2.11) over a comprehensive range of deposition conditions. Independently of the particle size, all density profiles had an S-shaped dependence from the Péclet number (Figure 2.11a) and converged toward a density of 0.25 in the ballistic regime. However, at low Péclet numbers, the surface density was a function of the particle size. There, decreasing the particle size from 50 to 5 nm increased the surface density from 0.11 to 0.19. This is in very good agreement with the AFM- and SEM- surface densities (0.20±0.015) obtained by aerosol deposition of 5 nm particles at a Péclet number of 10^{-2} - 10^{-1} (Figure 2.8a).

Here, it is proposed that the increase in interface density with decreasing particle size is due to a decrease in the horizontal area swept by the particle during its transition through the collision length. The latter can be computed by the minimal vertical collision distance from a particle deposited in the first layer and for monodisperse particles is equal to d_p.

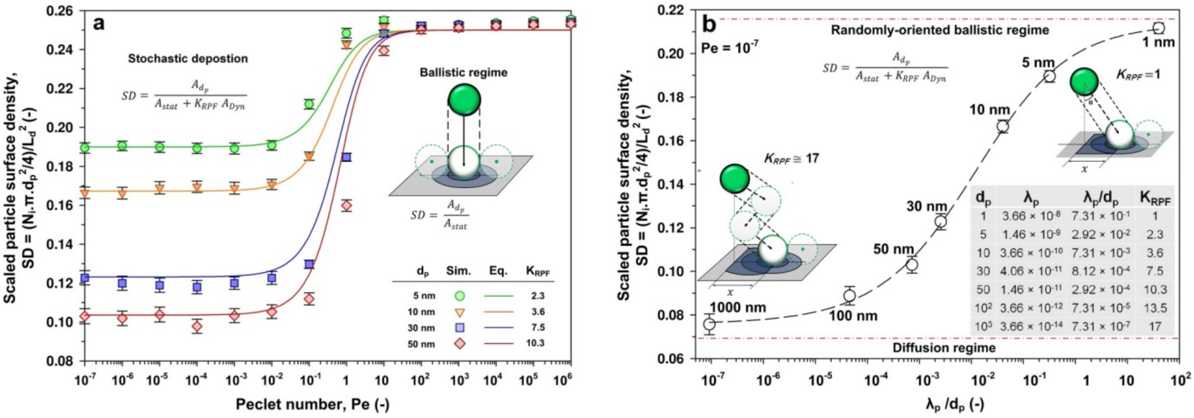

d_p	λ_p	λ_p/d_p	K_{RPF}
1	3.66×10^{-8}	7.31×10^{-1}	1
5	1.46×10^{-9}	2.92×10^{-2}	2.3
10	3.66×10^{-10}	7.31×10^{-3}	3.6
30	4.06×10^{-11}	8.12×10^{-4}	7.5
50	1.46×10^{-11}	2.92×10^{-4}	10.3
10^2	3.66×10^{-12}	7.31×10^{-5}	13.5
10^3	3.66×10^{-14}	7.31×10^{-7}	17

Figure 2.11. *Scaled particle surface density as a function (a) of the Péclet number and (b) particle mean free to diameter ratio at Pe =* 10^{-7} *for different particle sizes. Comparison of the SD computed by (a, symbols) Langevin dynamics and (a, lines) modelled by equation (4.23) with corresponding* K_{RPF} *show excellent agreement. Departure from the diffusion regime is observed (b) already for particles smaller than 100 nm.*

Although in the diffusion regime both small (e.g. 5 nm) and large (≥ 50 nm) particles are expected to deposit by a random path, this is not always true within a small collision distance (Figure 2.11b, insets). In particular, if the collision length (d_P) is smaller than the particle mean free path (λ_p) than the particle can move on a straight trajectory before collision with the surface. This results in a decrease of the horizontal area swept by the particle and therefore of its collision likelihood. As a result, more ultra-fine particles can reach the deposition surface resulting in the higher interface density computed with decreasing particle size (Figure 2.11a).

This accumulation mechanism was validated by development of a comprehensive analytical model for the first layer density (Figure 2.9a, lines). As it is discussed in details in section 4.4.2, the average surface density was estimated by the ratio between the horizontal projections of the area occupied by a sphere (A_{dp}) and that required ($A_{stat} + K_{RPF}.A_{dyn}$) to travel through the collision length (d_p):

$$SD = \frac{A_{dp}}{A_{stat} + K_{RPF}.A_{dyn}} \tag{2.21}$$

with A_{dp} being the horizontal area ($\pi d_p^2/4$) occupied by a deposited spherical particle, A_{stat} being the horizontal collision area (πd_p^2) of a depositing particle, A_{dyn} being the horizontal projection of the area swept by a particle moving at an incident angle α through the collision length, α being the angle between the vertical axis and the trajectory of a particle moving horizontally due to Brownian displacement (X) and vertically due to a advective velocity and Brownian displacement (v.t+X), and K_{RPF} being the additional path the resulting straight diagonal line swept by a particle due to the stochastic nature of diffusion. The horizontal projection of the area swept (A_{dyn}) is only a function of the particle size and Péclet number, and thus of the relative Brownian displacement ($\overline{X} = X/d_p$):

$$A_{dyn} = 2d_p^2\overline{X} - d_p^2\left[\overline{X}\sqrt{1-\overline{X}^2} + Sin^{-1}(\overline{X})\right] \tag{2.22}$$

This leads to a general analytical equation for the first layer density with the only variables being the relative Brownian displacement and swept path (K_{RPF} factor):

$$SD = \frac{\pi}{4\left[\pi + K_{RPF}(2\overline{X} - \left[\overline{X}\sqrt{1-\overline{X}^2} + Sin^{-1}(\overline{X})\right]\right]} \tag{2.23}$$

The validity of this analytical model (Figure 2.11a, lines) was assessed against the surface density computed by particle dynamics simulation (Figure 2.11a, symbols). For all particle size and Péclet number, equation (2.23) shows an excellent agreement with the numerical results with minor deviations observed only in the transition regime (Pe = 10^{-1}-1). In the ballistic regime, the Brownian-induced displacement within the collision length approaches zero resulting in A_{dyn}<<A_{stat}, and thus to a converging surface density ≈ A_{dp}/A_{stat} = 0.25 (Figure 2.9). In contrast, at low Péclet numbers, the area swept by a depositing particle within the potential collision length increases leading to A_{dyn}≈A_{stat}, and thus, for the 50 nm particles, in up to 50% less dense interface than in the ballistic regime (Figure 2.11a).

It was found that the length of the swept path and thus the magnitude of the K_{RPF} factor decreased with decreasing particle size leading to more dense interfaces. This is attributed to the different deposition mechanisms. In fact, while purely diffusive particles (≥ 50 nm) perform a random trajectory within the collision length, sufficiently small particles can cross it on a straight line (Figure 2.9) due to their mean free path being larger than the collision length/particle diameter. However, such (straight) ballistic deposition behaviour differs from that in the ballistic regime, as the depositing particle trajectory is not orthogonal to the substrate but has an incident angle determined from the ratio between vertical and horizontal displacement. The maximal incident angle (α_{max}) was found at Pe << 1 and represents an orthogonal, nearly isosceles, triangle having as hypotenuse the particle trajectory (Figure 2.9). This regime, here after referred as randomly-oriented ballistic regime, requires a larger area for a particle to deposit than in the pure ballistic regime but a considerably smaller than for purely diffusive bodies. This is in good agreement with the observed film (Figure 2.6b) and interface (Figure 2.11a) densification with decreasing particle size.

The conditions for departure from the diffusion to the randomly-oriented ballistic deposition regime and their impact on the K_{RPF} factor were investigated for quasi-purely diffusing bodies (Pe of 10^{-7}). Figure 2.11b shows the resulting interface density at a Péclet number of 10^{-7} as a function of the ratio between particle mean free path (λ_p) and collision length (d_p) and particle size from the micro-scale (1 μm) to the ultra-fine range (1 nm). The resulting monolayer density showed an S-shaped dependency from the λ_{p}/d_p ratio approaching 0.21 and 0.08 for 1 and 1000 nm particles, respectively. Most importantly, in the randomly-oriented ballistic limit the K_{RPF} factor converged toward 1. This is in excellent agreement with the proposed straight single-diagonal step deposition model and explains the different deposition mechanism observed for small (< 100 nm) nanoparticles.

In contrast, for large sub- and micro-scale particles having a mean free path considerably smaller than their diameter a true random walk is achieved throughout the collision length. This results in an increased swept path (K_{RPF}) approaching 17 times that travelled by the smallest particles (Figure 2.11b). These findings show that the dynamics of ultra-fine nanoparticles (< 100 nm) is not accurately captured by the diffusion regime, and their accumulation mechanism relies outside the validity of established Péclet scaling laws. Furthermore, as the swept path do not depend only from the particle size but from its ratio with the particle mean free path, with increasing surrounding temperature large nanoparticles will result in similar interface densifications as smaller ones.

Here, in contrast to previous studies[21,24-25] we have shown that the densification of films synthesized by self-assembly of diffusive ultra-fine particles does not involve the whole film structure but is confined to a certain thickness from the deposition surface. As a result, sufficiently thick films (> $80d_p$) converge toward the same density (Figure 2.6b). This densification is attributed to the straight diagonal trajectory followed by sufficiently small (< 100 nm) ultra-fine particles within the collision length with the deposited particle layer. Also in contrast to previous reports, this densification was observed to become predominant already below 100 nm, and thus for the whole ultra-fine particle range. An S-shaped densification was observed with particle size varying from 1 μm to 1 nm identifying that the strongest morphology variation are expected between a particle size of 5 to 100 nm. Amongst other, this model is a significant step toward the large-scale fabrication of emerging nano-devices such as third-harmonic-upconversion antennas where ultra-fine semiconductor nanoparticles (< 25 nm) need to be precisely collocated in the small gap (e.g. 35 nm) of a plasmonic nanorod dimer[19]. With respect to the self-assembly of polydisperse aerosols, often encountered in realistic conditions, two contrasting mechanisms are expected. Deposition of small particles on the surface of larger ones is known to increase the total film density by partially filling the pores between large particles. On the other side, if small particles would deposit on the deposition surface close to a, previously deposited, larger particles than the relative collision length would be increased resulting in a smaller mean free path to collision ratio. This would in turn decrease the film density close to the interface. As a result, the effect of polydispersity is not trivial and cannot be predicted independently from the specific size distribution, free mean path to average particle size ratio and film thickness.

2.5 Conclusions

A novel mechanistic description of the self-assembly mechanisms of nanoparticles into three-dimensional structures was presented. It was found that the structural properties of hierarchical films made of ultra-fine particles diverge from that expected in diffusion regime for sub-micron and micro equivalents leading to up to 300% denser interface morphologies. A new randomly-oriented ballistic deposition regime was successfully proposed to account for the collision and densification mechanisms of nanostructures. This enabled precise prediction of their accumulation and clustering dynamics by a simple analytical model that accounts for the degree of randomness of the deposition process.

In all regimes, the formation of surface-bond fractal-like agglomerates was determined as a main mechanism for the establishment of hierarchical morphologies. These findings are a significant step toward the understanding of the interaction of suspended nanostructures with their surroundings. This is of immediate impact to the engineering of several synthetic and natural nano-fabrication processes. For example, it elucidates the rapid achievement of electrical percolation in dispersed nanoelectrode devices, a bottleneck in improving the conductivity of nanoparticle films. It enables modeling and engineering of the properties of nano-patterned structures by scalable means such as electrodynamics focusing. Furthermore, this model can be applied to the investigation of the inflammatory effects of ultrafine particles (UFP < 100 nm) in human lungs providing new insights on the interaction of nanomaterials with delicate biological interfaces.

2.6 References

1. Mo., Y.; Wan., R.; Feng., L.; Chien., S.; Tollerud., D. J.; Zhang., Q., Combination effects of cigarette smoke extract and ambient ultrafine particles on endothelial cells. *Toxicol. In Vitro.* **2012,** *26*, 295-303.

2. Donaldson., K.; Li., X. Y.; MacNee., W., Ultrafine (nanometre) particle mediated lung injury. *J. Aerosol Sci.* **1998,** *29*, 553-560.

3. Armstead., A. L.; Arena., C. B.; Li., B., Exploring the potential role of tungsten carbide cobalt (WC-Co) nanoparticle internalization in observed toxicity toward lung epithelial cells in vitro. *Toxicol. Appl. Pharm.* **2014,** *278*, 1-8.

4. Kawanaka., Y.; Matsumoto., E.; Sakamoto., K.; Yun., S.-J., Estimation of the contribution of ultrafine particles to lung deposition of particle-bound mutagens in the atmosphere. *Sci. Total. Environ.* **2011,** *409*, 1033-1038.

5. Pratsinis., S. E., Flame aerosol synthesis of ceramic powders. *Prog. Energy Combust. Sci.* **1998,** *24*, 197-219.

6. Hurley., P.; Manins., P.; Lee., S.; Boyle., R.; Ng., Y. L.; Dewundege., P., Year-long, high-resolution, urban airshed modelling: verification of TAPM predictions of smog and particles in Melbourne, Australia. *Atmos. Environ.* **2003,** *37*, 1899-1910.

7. Stolaki., S.; Haeffelin., M.; Lac., C.; Dupont., J. C.; Elias., T.; Masson., V., Influence of aerosols on the life cycle of a radiation fog event. A numerical and observational study. *Atmos. Res.* **2014,** *151*, 146-161.

8. Zhang., Z.; Lagally., M. G., Atomistic processes in the early stages of thin-film growth. *Science* **1997,** *276*, 377-383.

9. Dent., W. R. F.; Wyatt., M. C.; Roberge., A.; Augereau., J.-C.; Casassus., S.; Corder., S.; Greaves., J. S.; de Gregorio-Monsalvo., I.; Hales., A.; Jackson., A. P.; Hughes., A. M.; Lagrange., A.-M.; Matthews., B.; Wilner., D., Molecular gas clumps from the destruction of icy bodies in the β pictoris debris disk. *Science* **2014,** *343*, 1490-1492.

10. Lee., J.-H.; Lee., E. K.; Joo., W.-J.; Jang., Y.; Kim., B.-S.; Lim., J. Y.; Choi., S.-H.; Ahn., S. J.; Ahn., J. R.; Park., M.-H.; Yang., C.-W.; Choi., B. L.; Hwang., S.-W.; Whang., D., Wafer-scale growth of single-crystal monolayer graphene on reusable hydrogen-terminated germanium. *Science* **2014,** *344*, 286-289.

11. Lupulescu., A. I.; Rimer., J. D., In situ imaging of silicalite-1 surface growth reveals the mechanism of crystallization. *Science* **2014,** *344*, 729-732.

12. Eggersdorfer., M. L.; Kadau., D.; Herrmann., H. J.; Pratsinis., S. E., Multiparticle sintering dynamics: from fractal-like aggregates to compact structures. *Langmuir* **2011,** *27*, 6358-6367.

13. van Herrikhuyzen., J.; Janssen., R. A. J.; Meijer., E. W.; Meskers., S. C. J.; Schenning., A. P. H. J., Fractal-like self-assembly of oligo(p-phenylene vinylene) capped gold nanoparticles. *J. Am. Chem. Soc.* **2005,** *128*, 686-687.

14. Bueno-López., A., Diesel soot combustion ceria catalysts. *Appl. Catal., B.* **2014,** *146*, 1-11.

15. Oravisjärvi., K.; Pietikäinen., M.; Ruuskanen., J.; Niemi., S.; Laurén., M.; Voutilainen., A.; Keiski., R. L.; Rautio., A., Diesel particle composition after exhaust after-treatment of an off-

road diesel engine and modeling of deposition into the human lung. *J. Aerosol Sci.* **2014,** *69*, 32-47.

16. Wierzbicka., A.; Nilsson., P. T.; Rissler., J.; Sallsten., G.; Xu., Y.; Pagels., J. H.; Albin., M.; Österberg., K.; Strandberg., B.; Eriksson., A.; Bohgard., M.; Bergemalm-Rynell., K.; Gudmundsson., A., Detailed diesel exhaust characteristics including particle surface area and lung deposited dose for better understanding of health effects in human chamber exposure studies. *Atmos. Environ.* **2014,** *86*, 212-219.

17. Kim., H.; Kim., J.; Yang., H.; Suh., J.; Kim., T.; Han., B.; Kim., S.; Kim., D. S.; Pikhitsa., P. V.; Choi., M., Parallel patterning of nanoparticles via electrodynamic focusing of charged aerosols. *Nature Nanotechnol.* **2006,** *1*, 117-121.

18. Tricoli., A.; Pratsinis., S. E., Dispersed nanoelectrode devices. *Nature Nanotechnol.* **2010,** *5*, 54-60.

19. Aouani, H.; Rahmani, M.; Navarro-Cia, M.; Maier, S. A., Third-harmonic-upconversion enhancement from a single semiconductor nanoparticle coupled to a plasmonic antenna. *Nature Nanotechnol.* **2014,** *9*, 290-294.

20. Tricoli., A.; Elmøe., T. D., Flame spray pyrolysis synthesis and aerosol deposition of nanoparticle films. *AIChE J.* **2012,** *58*, 3578-3588.

21. Kulkarni., P.; Biswas., P., A Brownian dynamics simulation to predict morphology of nanoparticle deposits in the presence of interparticle interactions. *Aerosol Sci. Technol.* **2004,** *38*, 541-554.

22. Ogunsola., O.; Ehrman., S., A Monte Carlo and continuum study of mechanical properties of nanoparticle based films. *J. Nanopart. Res.* **2008,** *10*, 31-39.

23. Rodríguez-Pérez., D.; Castillo., J. L.; Antoranz., J. C., Relationship between particle deposit characteristics and the mechanism of particle arrival. *Phys. Rev. E* **2005,** *72*, 021403.

24. Dreyer., J. A. H.; Riefler., N.; Pesch., G. R.; Karamehmedović., M.; Fritsching., U.; Teoh., W. Y.; Mädler., L., Simulation of gas diffusion in highly porous nanostructures by direct simulation Monte Carlo. *Chem. Eng. Sci.* **2014,** *105*, 69-76.

25. Mädler., L.; A Lall., A.; K Friedlander., S., One-step aerosol synthesis of nanoparticle agglomerate films: simulation of film porosity and thickness. *Nanotechnology* **2006,** *17*, 4783.

26. Cabral., H.; Matsumoto., Y.; Mizuno., K.; Chen., Q.; Murakami., M.; Kimura., M.; Terada., Y.; Kano., M. R.; Miyazono., K.; Uesaka., M.; Nishiyama., N.; Kataoka., K., Accumulation of sub-100 nm polymeric micelles in poorly permeable tumours depends on size. *Nature Nanotechnol.* **2011,** *6*, 815-823.

27. Elmøe., T. D.; Tricoli., A.; Grunwaldt., J.-D.; Pratsinis., S. E., Filtration of nanoparticles: Evolution of cake structure and pressure-drop. *J. Aerosol Sci.* **2009,** *40*, 965-981.

28. Castillo, J. L.; Martin, S.; Rodriguez-Perez, D.; Perea, A.; Garcia-Ybarra, P. L., Morphology and Nanostructure of Granular Materials Built from Nanoparticles. *KONA Powder Part. J.* **2014,** *31*, 214-233.

29. Tricoli, A.; Graf, M.; Mayer, F.; Kuühne, S.; Hierlemann, A.; Pratsinis, S. E., Micropatterning Layers by Flame Aerosol Deposition-Annealing. *Adv. Mater.* **2008,** *20*, 3005-3010.

30. Tricoli, A.; Wallerand, A. S.; Righettoni, M., Highly Porous TiO_2 Films for Dye Sensitized Solar Cells. *J. Mater. Chem.* **2012,** *22*, 14254.

31. Liu, Y.; Koep, E.; Liu, M., A Highly Sensitive and Fast-Responding SnO_2 Sensor Fabricated by Combustion Chemical Vapor Deposition. *Chem. Mater.* **2005,** *17*, 3997-4000.

32. Keskinen, H.; Tricoli, A.; Marjamäki, M.; Mäkelä, J. M.; Pratsinis, S. E., Size-selected agglomerates of SnO_2 nanoparticles as gas sensors. *J. Appl. Phys.* **2009,** *106*, 084316.

33. Tricoli, A.; Righettoni, M.; Pratsinis, S. E., Anti-Fogging Nanofibrous SiO_2 and Nanostructured SiO_2-TiO_2 Films Made by Rapid Flame Deposition and In Situ Annealing. *Langmuir* **2009,** *25*, 12578-12584.

34. Mädler., L.; Roessler., A.; Pratsinis., S. E.; Sahm., T.; Gurlo., A.; Barsan., N.; Weimar., U., Direct formation of highly porous gas-sensing films by in situ thermophoretic deposition of flame-made Pt/SnO_2 nanoparticles. *Sens. Actuators B Chem.* **2006,** *114*, 283-295.

Chapter Three

Ultra-Porous Electron-Depleted ZnO Nanoparticle Networks for Highly Sensitive Portable Visible-Blind UV-Photodetectors

Publication relevant to this chapter:

Noushin Nasiri, Renheng Bo, Fan Wang, Lan Fu, Antonio Tricoli, "*Ultraporous Electron-Depleted ZnO Nanoparticle Networks for Highly Sensitive Portable Visible-Blind UV Photodetectors*", **Advanced Materials**, 27, 4336–4343, **2015**.

Abstract

The importance of UV detectors is growing because of the demand for wide range of environmental, military, industrial, flame sensing, water sterilization, and early missile plume detection applications. Here, we report a hierarchical design and a rapid synthesis approach for the fabrication of highly performing visible-blind photodetectors. Combined nano- and micro-scale fine-tuning of the film optical and electrical properties results in record-high milliampere photo-currents while preserving nano-ampere dark-currents and excellent selectivity to ultra-low UV light intensity. This is a significant improvement over state-of-the-art devices where a compromise is necessary between high photo-current and low dark-currents. As a result, these photodetectors do not require bulky and costly read-out circuitry and can be directly integrated in portable CMOS-based electronics that is currently utilized in many wearable devices.

3.1 Introduction

Portable visible-blind photodetectors have a wide range of application including UV dosage monitoring for skin cancer prevention, flame and missile launch detection, optical communication and astronomy.[1-3] Si-based photodetectors, relying on n-p type semiconductor homojunction technology, are the most established commercial solution for measurement of ultraviolet light. These devices have some significant shortcomings including high operation voltage, the requirement of longpass filters to block low energy photons and cooling systems to reduce noise and leakage current. This significantly hinders their integration in wearable technologies and alternative solutions are intensively sought.[4-5] Wide bandgap nanostructured semiconductors such as TiO_2 and ZnO are inherently visible-blind and can detect low concentration of ultraviolet light by a different mechanism, namely photo-generated variations in the concentration of surface-states.[2,6]

Amongst highly performing materials, zinc oxide is a promising transparent metal oxide with a room temperature bandgap of 3.37 eV that matches well the lower edge of the visible light spectrum.[3,7] Nano- and micro-structured ZnO photodetectors have been produced by several methods such as RF magnetron sputtering,[8] sol-gel,[9-10] chemical vapor deposition[11] and pulsed laser deposition[12] demonstrating significant improvement over bulk equivalents. Recently, Ji et al.[13] have demonstrated fabrication of flexible devices with up to 1.56×10^3 photo- (I_{photo}) to dark-current (I_{dark}) ratio at a bias of 3 V by epitaxial growth of ZnO films on poly-ethylene-terephthalate (PET). Drop-coating of PET substrates with ZnO quantum dots - graphene solutions resulted in up to nearly 10 times higher I_{photo}/I_{dark} ratio indicating further optimization potential of morphology and composition. However, these results[14] were obtained at very high light intensities of 300[13] and 6 $W.cm^{-2}$,[14] respectively, that are outside the range of many applications. To date, amongst the highest response to moderate UV light intensities has been achieved by electrospun ZnO-SnO_2 nanofibers films featuring a

I_{photo}/I_{dark} of 4.6×10^3 at 10 V under a UV light intensity of 0.45 mW cm^{-2}.[5] Despite these significant improvements in the photo- to dark-current ratio, the magnitude of these devices' photo-current reached a maximum of only 35 nA at a bias of 2.4 V[1]. This is quite low and makes them incompatible with integrated CMOS micro-circuitry utilized in state-of-the-art portable devices such as smartphones, watches and security devices. Up to 900 µA photo-currents (Table 5.1)[15] have recently been achieved by more conductive but less light-sensitive structures. However, this results in high dark-currents of 1.5 µA and reduced signal to noise ratio[15] that undermine many of the high photo-current advantages.

Here, we present a novel hierarchical morphology for UV-blind photodetectors that results in excellent selectivity, record high milliampere photo-currents to very low ultraviolet light intensities and nanoampere dark-currents. We demonstrate the rapid (≤ 100s) one-step synthesis and self-assembly of transparent ultra-porous films composed of electron-depleted crystalline ZnO nanoparticles on low-cost glass substrates. Optimization of the film structure is performed resulting into absorption of more than 80% of the incoming ultraviolet radiation and transmission of nearly 90% of the visible light. Characterization of the photodetector performance is pursued at very low light intensity (0.1 mW.cm^{-2}) resulting in the highest (3.4×10^5) photo- to dark-current ratio so far reported. These findings demonstrate a highly performing structure and a flexible and scalable platform technology for the rapid low-cost fabrication and integration of ultraviolet photodetectors in CMOS-compatible portable devices.

3.2 Experimental

3.2.1 Nanoparticles Deposition

A flame spray pyrolysis (FSP) system was used for the synthesis and direct deposition of ZnO nanoparticles films onto the glass substrates featuring a set of interdigitated electrodes. A solution of Zinc Naphthenate (10% Zn, Sigma Aldrich) and Xylene (Sigma Aldrich) was prepared with a total Zn-metal atom concentration of 0.3 mol.l^{-1}. This solution was supplied at a rate of 5 ml.min^{-1} through a syringe pump, and dispersed into a fine spray with 7 L.min^{-1} oxygen at a constant pressure drop of 2 bars. The spray was ignited by supporting premixed methane/oxygen flames (CH_4 = 1.2 L.min^{-1}, O_2 = 2 L.min^{-1}). A water-cooled substrate holder placed at 20 cm height above the burner (HAB) was utilized to keep the substrate temperature below 150 °C. The photodetector substrates were made of glass with interdigitated gold lines with 5μm width and spacing and a total electrode area of 7×5 mm (G-IDEAU5, DropSens, Oviedo, Spain). All substrates were cleaned with multiple ethanol/drying cycles before nanoparticles deposition. For measurement of the film resistance in pure nitrogen gas and with 1% oxygen, alumina substrate (0.8 mm thick) with interdigitated Pt lines with 200 μm width and 300 μm spacing were used. The substrates had a Pt resistance temperature detector (RTD) on one side and a Pt heater on the other side. The overall dimensions of the alumina substrate were 15 mm × 13 mm (Electronic Design Center, Case Western Reserve University, Cleveland, OH, USA).

3.2.2 Materials Characterization

The morphology and patterning characteristics of the deposited particles and films were investigated by a Hitachi H7100FA transmission electron microscope (TEM) at 100 kV and an analytical scanning electron microscopy (SEM), using Zeiss Ultraplus (FESEM) at 3 kV. The crystal phases, size (d_{XRD}) and surface compositions were characterized by X-Ray diffraction using Bruker system (XRD, D_2 Phaser, U.S.A) equipped with Cu Ka radiation of average wavelength 1.54059 Å. The Brunauer-Emmett-Teller specific surface area (BET, SSA) of the deposited nanoparticles was measured by N_2 adsorption using a porosity analyzer (Micromeritics, TriStar II, U.S.A). The nanoparticles were degassed at 200 °C for 8 hours prior to analysis. The substrates were kept in a furnace (Brother High Temperature Furnace XD-1.2KN) at 300 °C for 12 h, at ambient pressure prior photo-detecting tests, to stabilize the nanoparticle size and avoid resistive-sintering during the photo-detection measurements.

3.2.3 Photodetection Analysis

Absorbance spectra of the ultra-porous and dense ZnO films deposited were measured with a Perkin-Elmer (Lambda 1050 UV/Vis/NIR) Spectrophotometer and a 150 mm integrating sphere. All optical measurements were carried out at room temperature. The For *I-V* measurements, DC currents were measured using a Picoammeter / Voltage source (Model 6487, Keithley). The detection of UV light was performed using a Newport Xenon lamp source 66920 and the UV-vis absorption spectra were recorded in the wavelength range 250–500 nm using Princeton Instrument Acton SP2500 (0.500m Imaging Triple Grating Monochromator/Spectrograph).

3.3 Results and Discussion

3.3.1 Nanostructured Device Characterization

Figure 3.1a-c shows a schematic of the photodetector fabrication by liquid-fed spray flame synthesis and aerosol deposition. A hot ZnO nanoparticle aerosol was generated by atomization and combustion of a zinc naphtenate solution. The particle size was controlled by the Zn-atom precursor solution concentration that was set to 0.3 mol.l^{-1}. Transmission electron microscopy (TEM) analysis revealed (Figure 3.2a) a spherical shape and a visible (d_{TEM}) average particle diameter of ca. 19 nm. Some rod-like structures were also observed (Figure 3.3) which is in line with previous reports on the flame synthesis of larger ZnO nano-powders and it is attributed to preferential growth along the (100) plane.[16] It is worth to mention that the fraction of rod-like particles was computed by analysis and counting 300 ZnO nanoparticles. It was found that the rod-like fraction was less than 12% for the precursor concentration of 0.3 mol.L^{-1}.[17] In addition, as the deposited particles (both spherical and lodlike ones) are smaller than twice the Debye length and thus, fully electron depleted, the nanoparticle's shape might have no significant effect on the device photoconductivity.

This nanoparticle aerosol was orthogonally impinged on the water-cooled glass substrates resulting in the rapid self-assembly of ultra-porous nanoparticle films with a very high film growth rate of 5.5 µm.min^{-1}. The substrate surface temperature (Figure 3.1c) was kept below 150 ºC by a water-cooled substrate holder, and thus the temperature was too low to induce sintering of the ZnO nanoparticles within the maximal deposition time of 100 s utilized here. In fact, the particle diameters determined by nitrogen adsorption (BET) and TEM analysis of the powders collected from the substrate and filter were (d_{BET}) 16 nm and 18 nm and (d_{TEM}) 19 nm and 21 nm, respectively, confirming that no sintering finds place on the substrate during deposition. As a result, the film morphology (Figure 3.2) was mainly determined by the particle deposition dynamics[18] resulting in an 98% porous network of nanoparticles that is hold together by weak van der Waals forces[19].

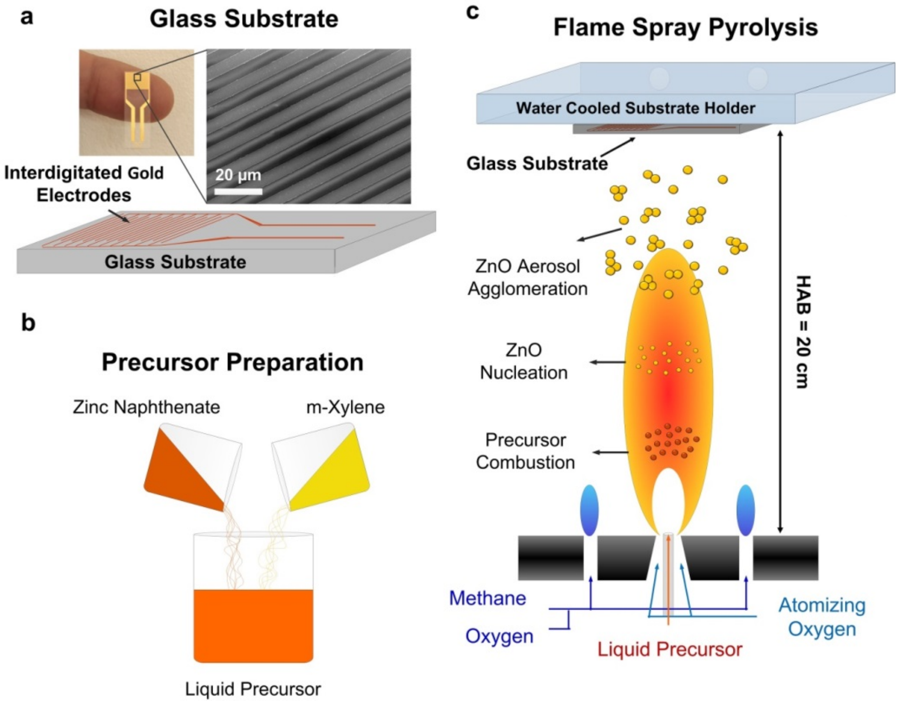

Figure 3.1. *Schematics of a (a) photodetector substrate and (b,c) flame spray pyrolysis synthesis and aerosol self-assembly of ultra-porous films made of electron-depleted ZnO nanoparticles at 20 cm height above the burner (HAB).*

To decrease grain boundary barriers to electron conduction and increase the film mechanical stability, these fragile nanoparticle networks were post-sintered at 300 ºC for 12 h. This step had no measurable effects on the film morphology and crystallinity. It was, however, detectable by a small increase in crystal size (d_{XRD}) from 11.7 to 13.3 nm indicating inter-particle sintering and grain boundary necking. Figure 3.4 shows X-Ray Diffraction (XRD) and Fourier Transfer Infrared Spectroscopy (FTIR) patterns of particles collected from the filter and the photodetector substrates before and after sintering. All the XRD spectra correspond to the hexagonal wurtzite ZnO (JCPDS No. 36-1451) structure.[5,20] Zinc oxide has a hexagonal-close-packed crystal structure composed of alternating planes of Zn and O atoms.[11] Height et al.[16] reported an increased XRD lattice aspect ratio between the (100) and (002) planes by increasing the concentration of dopants during flame-synthesis. This ultimately led to increasingly more accentuated rode-shaped nanostructures.

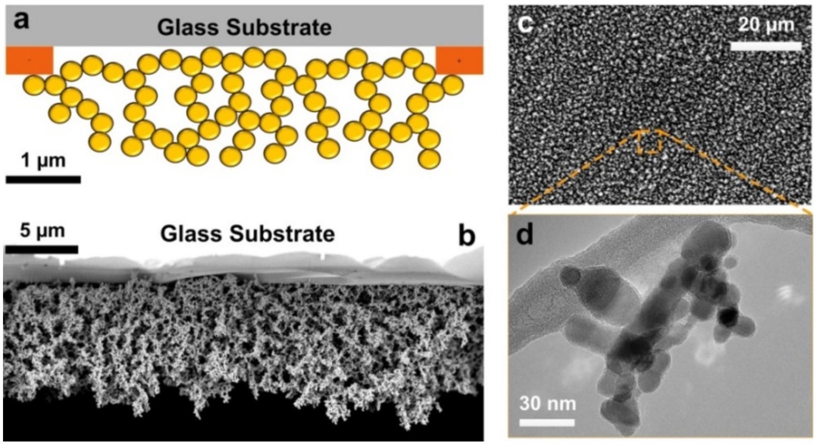

Figure 3.2. *(a) Schematics, (b) cross-section and (c) top view SEM images of a uniform and homogenous flame-made film composed of (d) mostly spherical-particles with an average TEM size of 19 nm.*

Here, the (100)/(002) planes aspect ratio was found to be close to unity (1.05+/-0.05) and consistent for the particles collected from filter and substrate. This is in line with the predominant spherical-shape observed by TEM analysis (Figure 3.3) indicating homogenous particle growth by condensation and Brownian coagulation. During and after fabrication, the photosensitive semiconductor surface can be contaminated by impurities. These usually undermine the device performance. The defect and impurity content in the flame-made ZnO nanoparticles and in the self-assembled ZnO films were characterized by FTIR (Figure 3.4b). The broad peaks at 3455 and 1146 cm^{-1} are assigned to the O-H stretching vibration of hydroxyl groups and attributed to adsorption of atmospheric moisture.[21] The residual hydroxyl peaks may be ascribed to the surface adsorption of ambient water. Two sharp peaks around 1600 and 1400 cm^{-1} are attributed to the asymmetrical and symmetrical stretching of zinc carboxylate, respectively.[22] The spectral signature of these C-H impurities completely disappears upon sintering at 300 °C. As a result, the post-sintered ZnO films had a highly pure surface with no detectable organic or inorganic contaminants.

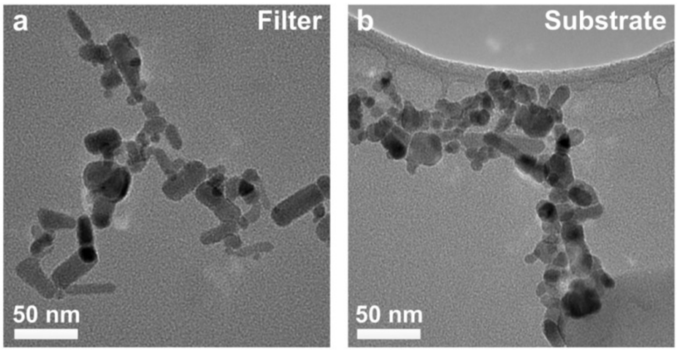

Figure 3.3. *TEM images of flame-made ZnO particles collected from (a) the filter (HAB of 50 cm) and (b) the substrate (HAB of 20 cm).*

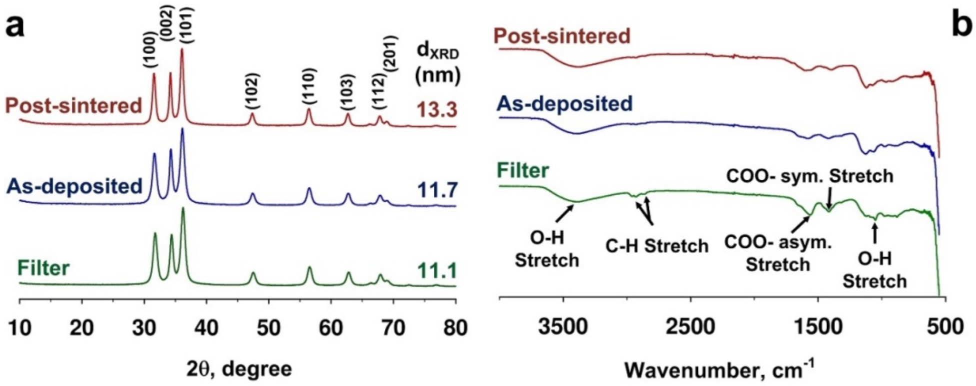

Figure 3.4. *The (a) XRD and (b) FTIR patterns of the ZnO particles collected on the filters and substrate before and after sintering reveal a Wurtzite crystal structure and high purity.*

3.3.2 Optical Properties

Figure 3.5 shows the optical transmittance of the ZnO films deposited on blank glass substrates as a function of the deposition time. All films were highly transparent to visible light with a relatively sharp cut-off below 370 nm. This is quite close to the end of the visible spectrum 400 nm and well within the UV-A range (400 - 320 nm). The film average integral transmittance for visible light, computed by subtraction of the fraction lost through the glass substrates (Figure 3.5, circles), decreased from 99% to 90% with increasing deposition time from 15 to 100 s in line with the increase in film thickness. Optical images of the films placed over a printed paper (Figure 3.5, inset) reveal a highly transparent surface up to a deposition time of 100 s. This is particularly noteworthy as the resulting visible film thickness, measured by SEM, was ca. 10 μm (Figure 3.6c).

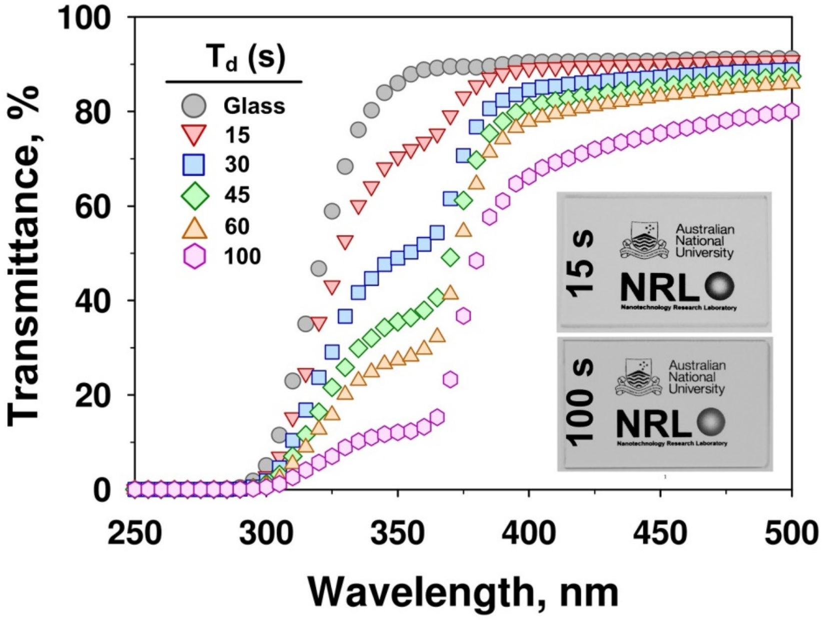

Figure 3.5. *Optical transmittance spectra of ultraporous ZnO films deposited on blank glass substrates as a function of the aerosol deposition time and of a blank glass substrate (circles). Inset: Optical images of ZnO films deposited for 15 and 100 s on glass substrates placed over a printed paper.*

This superior transparency was attributed to the unique film morphology and the non-scattering nature of the small ZnO primary particles. Figure 3.6 show exemplary films obtained by deposition of the hot nanoparticle aerosols on blank glass substrates for 100 s. At high magnification (Figure 3.6b), it is revealed that these aerosol self-assembled films have a very homogenous surface characterized by micro-sized pores between thin bridges of partially sintered ZnO nanoparticles resulting in an ultra-high average film porosity of 98%. This results in a ZnO mass(/bulk) thickness of ca. 200 nm and it is in line with the optical thickness of 152 and 244 nm estimated by the Beer-Lambert law from the transmittance spectra (Figure 3.5) at $\lambda = 375$ nm with an extinction coefficient of 8×10^4 and 5×10^4 cm^{-1}, respectively.[23]

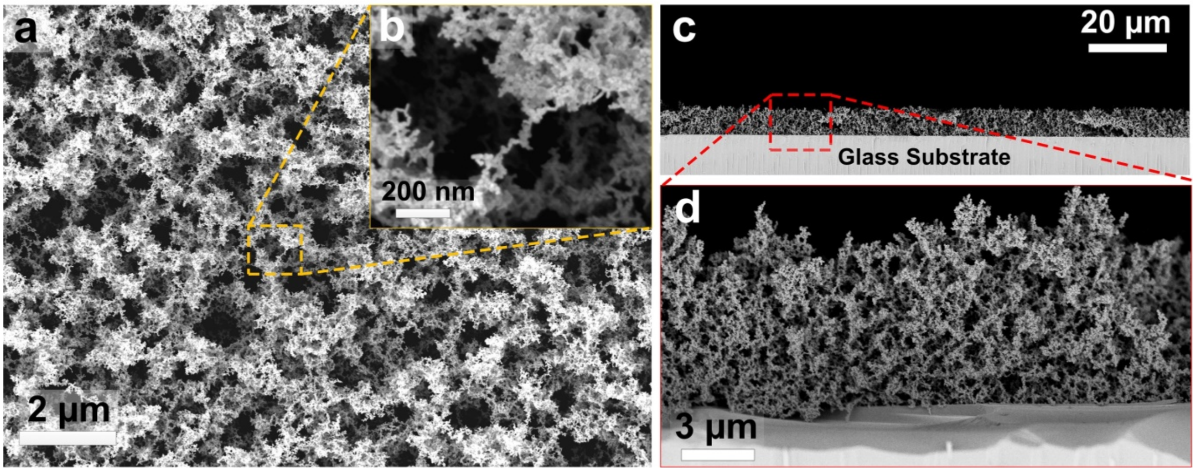

Figure 3.6. *SEM images of an exemplary film deposited for 100 s on a glass substrate reveal a highly porous and uniform (a,b) top surface and (c,d) cross-section.*

Analysis of the film cross-sections (Figure 3.6c-d) revealed a homogeneous thickness over several hundred micrometres (Figure 3.6c) with no visible cracks and other defects.[24] This morphology is similar to that previously reported for as-prepared flame-made SnO_2 chemical sensors[19] further confirming that, independently of the composition, aerosol self-assembly leads to highly reproducible, statically equivalent film morphologies[18,25]. However, in contrast to previous studies on aerosol-deposited SnO_2 and WO_3 films where high-temperature in-situ flame-annealing was utilized as a second step to mechanically stabilize the films and improve the electrical conductivity,[19,26-27] here the lower thermodynamic stability of ZnO enabled low temperature sintering, and thus to preserve the initial film porosity.

3.3.3 Photodetection Properties

The photo- to dark-current (I_{photo}/I_{dark}) and the UV to visible light current (I_{photo}/I_{vis}) ratios are two key figures of merit for visible-blind photodetectors. Figure 3.7 shows the *I-V* response of the thickest films, with a deposition time of 100 s, to the edge of the visible spectrum (390 - 410 nm) and to representative UV-A radiation (350 - 370 nm). All the samples had very low dark-currents (≤ 5 nA) up to a bias of 5 V corresponding to a total film resistance of nearly 1 Gohm at room temperature. This is attributed to both the strong impact of surface states on the ZnO conductivity and to the very high film porosity that results in a small number of neighbouring particles.

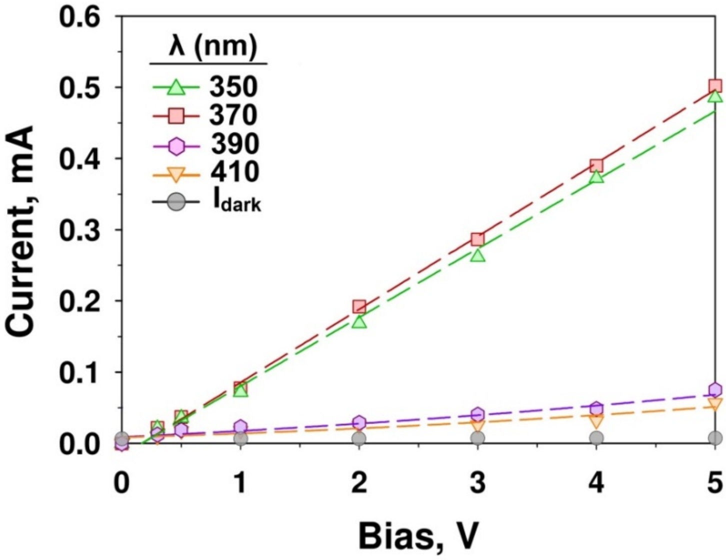

Figure 3.7. *I-V characteristics of the ZnO ultra-porous photodetectors as a function of the applied light and bias.*

For sufficiently small nanoparticles the high density of surface states results in significant electron depletion and thus very low dark current that represent an off-state of the device. In contrast under illumination (on-state), the *I-V* response was linear indicating an ohmic behaviour and sufficient availability of charge carriers to maintain a very high photo-current.

At a wavelength of 370 nm and at a very low illumination intensity of 40 µW/cm^2, the photocurrent reached up to 521 µA. This is more than five order of magnitude higher than the dark-current (3.61 nA) and demonstrate a highly sensitive sensing mechanism. It is important to note that although the light intensity used here (40 µW.cm^{-2}) was ca. 23-times lower than that commonly utilized to probe state-of-the-art metal-oxide photodetectors,[4] it still resulted in the highest I_{photo}/I_{dark} ratios (1.4×10^5) so far reported at low bias for wide bandgap semiconductor devices (Table 3.1).

3.3.4 Photodetection Mechanism

This strong response is attributed to the unique morphology and composition of these films. With respect to the former, the very high porosity of these nanoparticle networks facilitates the penetration of oxygen into the lowest nanoparticle layers (Figure 3.8a,c). This ensures the participation of the whole film in the sensing mechanism avoiding formation of non-electron-depleted and/or light-insensitive domains that could act as bottlenecks reducing the relative increase in the film electrical conductivity and thus tampering the photo- to dark-current ratio. This feature arises mainly from the high film porosity (98%). In stark contrast, deposition of the same nanoparticles by spin-coating led to non-transparent, considerably less porous structures (40 - 60%).

Figure 3.9 shows the transmittance and absorbance spectra of an aerosol-deposited ultra-porous film (95% porosity) and a spin-coated dense one (50% porosity) on glass substrate composed of the same flame-made ZnO nanoparticles and having the same optical density (ca. 0.7) in the near UV. For wavelengths below ZnO bandgap (λ = 360 nm), the ultra-porous film absorbs ca. 84% of the incoming light while the spin-coated film absorbs 74%. Considering that the films have similar UV transmittance, the lower UV absorption of the spin-coated films is likely attributed to higher back-scattering.

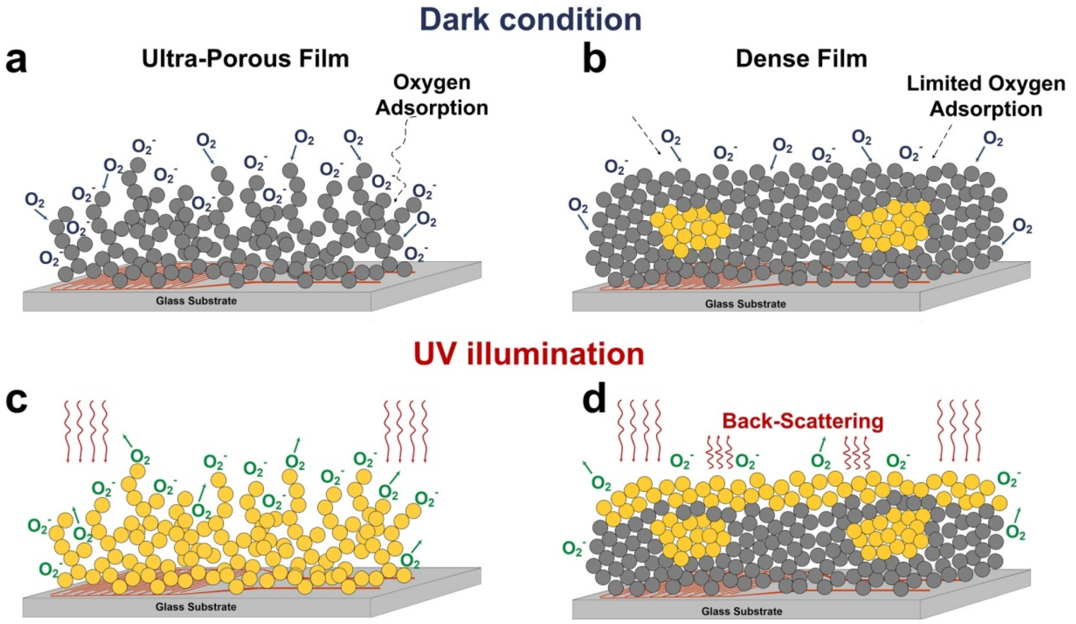

Figure 3.8. *Schematic model of the photo-response mechanisms of ZnO nanoparticle films based on the adsorption and desorption of molecular oxygen[2] in (a,c) ultra-porous and (b,d) dense films. The high porosity (a,c) of these electron-depleted nanoparticle networks facilitates the penetration of oxygen and light into the lowest particle layers close to the electrodes. In contrast, the dense films (b,d) may result in the formation of non-electron-depleted and light insensitive domains.*

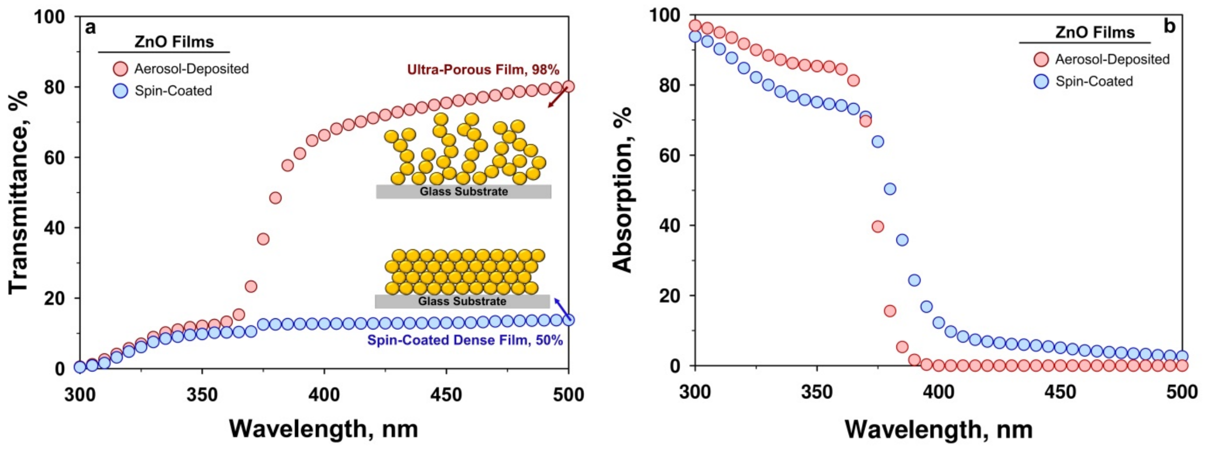

Figure 3.9. *(a) Transmittance and (b) absorption spectra of an aerosol-deposited ultra-porous film (red circles) and a spin-coated one (blue circles) both composed of the same flame-made ZnO nanoparticles and having the same light transmittance at the edge of the ZnO bandgap (ca. 370 nm).*

The other critical feature of these flame-made photodetectors is the ultra-fine ZnO nanoparticle size. Similarly to chemoresistive gas sensors,[24,26] the ultraviolet light sensing mechanism of wide bandgap semiconductor depends from the ratio between their Debye length and the primary particle size[26] (Figure 3.10). Due to the high porosity and hierarchical micro-pore size of these films, oxygen molecules can adsorb down to the deepest film layers (Figure 3.8a). Adsorption of O_2 on the ZnO nanoparticle surface results in the trapping of electron from the semiconductor conduction band.[26] This forms an electron-depleted layer within the semiconductor Debye length from the surface. During illumination, the photo-generated holes can travel to the surface along potential gradient and desorb oxygen molecules from the surface (Figure 3.8c), resulting in an increase in the free carrier concentration within this depletion layer.[20] The transduction of this photo-response on the semiconductor conductivity, and thus photo-current, depends mainly from the ratio between the Debye length (δ) and the primary particle size (d_p). If d_p is larger than twice δ than a light-insensitive conduction channel is formed. This leads to relatively high dark current and exposure to UV light results only in the modulation of the conduction channel width.

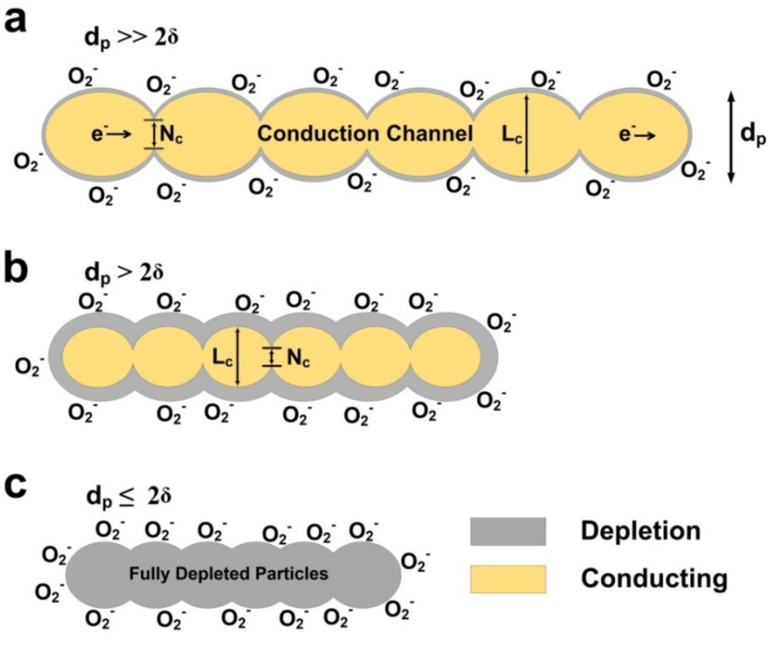

Figure 3.10. *As a function of the ratio between the particle diameter (d_p) and the Debye length (δ), three photo-detection mechanisms (a-c) are expected[6]. Particle size larger than twice the Debye length of ZnO leads to grain boundary or surface controlled responses with limited photo- to dark-current ratios, whereas particle size smaller than twice the Debye length leads to fully depleted nanostructures with an on/off switching behaviour.*

Decreasing this channel and thus the particle size increases the contribution of the light-sensitive domains to the total film conductivity resulting in higher photo-response. Usually, a main distinction is made for d_p >> 2δ where the sensing mechanism is controlled by electron-transport at the grain boundary and d_p > 2δ where a significant portion of the bulk participate to light sensing (Figure 3.10).

In contrast, if d_p ≤ 2δ than the whole particle is electron-depleted. This leads to highly resistive films with very low dark-currents. For this ultra-fine structures, exposure to ultraviolet light create a conduction channel resulting in a drastic increase in electrical conductivity and, potentially, very high photo-currents. For our ZnO films the Debye length[24] can be computed as following[28]:

$$\delta = \sqrt{\frac{\varepsilon_s K_b T}{e^2 nc}} \tag{3.1}$$

where ε_s is the static dielectric constant ($13.5\times8.5\times10^{-12}$ F/m in ZnO), K_b is the Boltzmann's constant (1.38×10^{-23}J/K), T is an absolute temperature (K), e is the electrical charge of the carrier (1.6×10^{-19} C), and nc is the carrier concentration (ca. 5×10^{16} cm^{-3})[29]. At room temperature (T = 298 K) for ZnO, this results in a Debye length of ca. 19 nm. Considering that the primary particle size (d_{BET}) of the flame-made ZnO is 16 nm and the crystal size is 13 nm, here, the low dark-current and the very high photo- to dark-current ratio of these films are partially attributed to the fully electron-depleted state of the nanoparticle network (Figure 4e, d_p ≤ 2δ).

This was confirmed by measurement of the resistance of the thick ZnO films aerosol-deposited for 100 s on gold interdigitated electrodes with back heaters (Figure 3.11). In pure nitrogen gas, the resistance decreased from 0.298 to 0.126 Mohm by increasing the sensor temperature from 150 to 240 ºC. This is line with the behaviour expected by for n-type semiconductors such as ZnO. Increasing the O_2 concentration from zero to 1% increased the film resistance by nearly 300 times (from 0.298 to 87 Mohm at 150 ºC). Similar results were obtained up to a film temperature of 240 ºC. This indicates that the conductivity of these ultra-porous electron-depleted ZnO films is manly controlled by adsorption and desorption O_2 molecules. The high porosity of these films is beneficial to ensure penetration of oxygen and thus formation of electron-depleted ZnO particles in the whole film structure and in particular in the lowest layers adjacent to the electrodes (Figure 3.8a,c).

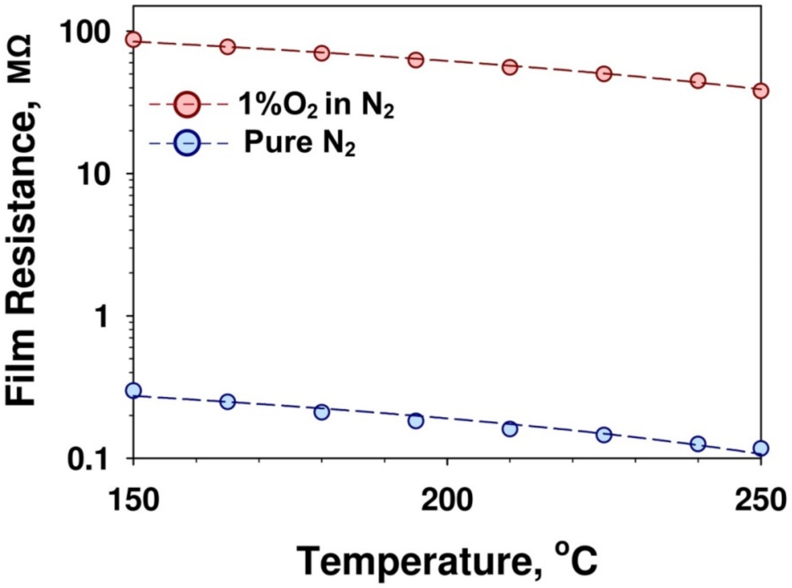

Figure 3.11. *Film resistance in* N_2 *as a function of the temperature* O_2 *content.*

To assess the impact of the film morphology on the resulting photodetector performance, the photo-response of denser (spin-coated) films having an average porosity of ca. 50% and the same UV optical density (0.7) of the ultra-porous films (Figure 3.12) was further investigated. All dense films had a very high dark-current ranging from micro- to milliampere and very low photo- to dark-current ratio (ca. 1). The high dark-current was attributed to the denser morphology (ca. 50% porosity) of the spin-coated films that results in a significantly larger number of neighbouring particles and drastically higher film electrical conductivity than the ultra-porous films. Also, as oxygen penetration may be limited in the dense films, some of the ZnO particles may not be fully electron-depleted leading to higher conductivity.

The low photo-currents indicate that the amount of photo-excited extra carriers in the dense films is significantly less than in the ultra-porous ones.

As schematically described in Figure 3.8, this is likely attributed to two main structural differences. First, the lower porosity decreases the penetration of oxygen and may lead to formation of gas-tight ZnO domains that are not fully electron-depleted and thus less sensitive to light (Figure 3.8b). Second, the higher UV light back-scattering of the dense films (Figure 3.9) suggest that a larger fraction of the incoming light may be trapped and absorbed in the top layers relatively far away from the electrodes (Figure 3.8d). Both these effect may lead to the formation of light-insensitive domains reducing the amounts of photo-excited extra carriers.

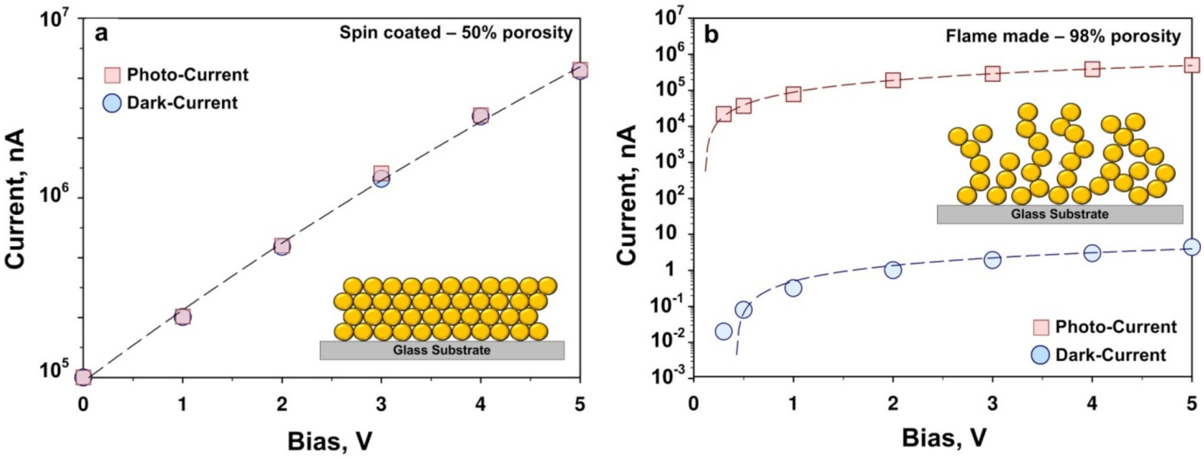

Figure 3.12. *Photo- and dark-currents of (a) a spin-coated and (b) ultra-porous films composed of the same flame-made ZnO nanoparticles and having both an optical density of ca. 0.7 at λ of 370 nm.*

It should be noted that highly performing dense films of electron-depleted ZnO nanoparticles have been previously obtained by spin-coating.[2] However, these thin films had low UV optical density (ca. 0.3) and a very low electrode aspect ratio (ca. 0.75) resulting in lower photo-currents (ca. 1.8 μA at a bias of 5 V and 0.84 mW.cm^{-2} UV light intensity) than the one achieved here by the ultra-porous films (1.2 mA at 5 V and 0.1 mW.cm^{-2}). These results show that electron-depleted particles are critical but not sufficient to obtain milliampere high photo- and nanoampere low dark-currents at low UV light intensities. The ultra-porous film morphology, developed here, is a key structural property required to individually optimize photo-excitation and electrical conductivity.

Figure 3.13 shows the spectral responsivity of the photodetectors as a function of the illumination wavelength and applied bias. It was observed that decreasing the wavelength below 400 nm sharply increased the responsivity that reached its peak value at about 370 nm. The responsivity increased by a factor of 7 (from 1.7 to 12.1 μA) by decreasing the wavelength from 390 to 370 nm. The sharp cut-off at wavelength of 370 nm is in good-agreement with the ZnO band gap of 3.37 eV (λ = 368 nm), confirming that these flame-made ZnO photodetectors are inherently visible-blind.

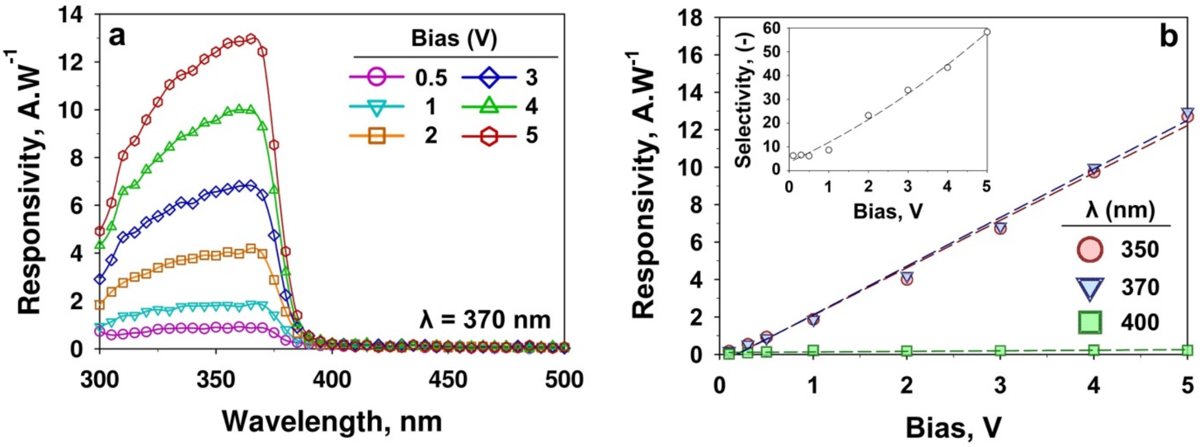

Figure 3.13. *(a) Responsivity of the ZnO ultra-porous photodetectors as a function of the light wavelength and applied bias. (b) Photodetector responsivity and (inset)* I_{370}/I_{400} *UV-visible selectivity as function of applied bias at a wavelength of 350, 370 nm and 400 nm light illumination.*

The photodetector responsivity was further investigated as a function of applied bias at different wavelengths in the UV-A and visible spectrum. A linear relationship (Figure 3.13b) was obtained with increasing bias from 0 to 5 V indicating no carrier mobility saturation or sweep effect up to the maximum applied bias. The ultraviolet selectivity, defined as a ratio of device response at a wavelength of 370 nm and 400 nm (Figure 3.13b, inset) reached 60 at a bias of 5 V. This is more than sufficient to enable very selective detection of low intensity of UV light without the need for high wavelength filters and further amplification.

Figure 3.14a shows the photoresponse of an ultra-porous ZnO nanoparticle film to the UV illumination with different light density at a wavelength of 370 nm. The photo-current increased linearly by a factor of 4.5 (from 260 µA to 1.2 mA) with increasing light intensity from 20 to 100 µW.cm^{-2} resulting in a maximal I_{photo}/I_{dark} ratio of 3.4×10^5. This shows that in these ultra-porous electro-depleted nanoparticle films, the charge carrier photo-generation efficiency is proportional to the applied photon flux. The photo- to dark-current ratio obtained here at 100 µW.cm^{-2} (3.4×10^5) is very high even in comparison to other highly performing photodetectors made of electron-depleted ZnO nanoparticles[2] that reached similar ratios (ca. 3×10^5) at higher light intensities (830 µW.cm^{-2}). Furthermore, to the best of our knowledge, achievement of milliampere photo-currents at low ultraviolet light intensity of 100 µWcm^2 while maintaining nanoampere dark-currents has not been previously reported (Table 5.1). This is a key improvement over state-of-the-art structures as it enables the direct integration of UV-photodetectors in CMOS-compatible micro-circuitry currently implemented in many wearable devices.

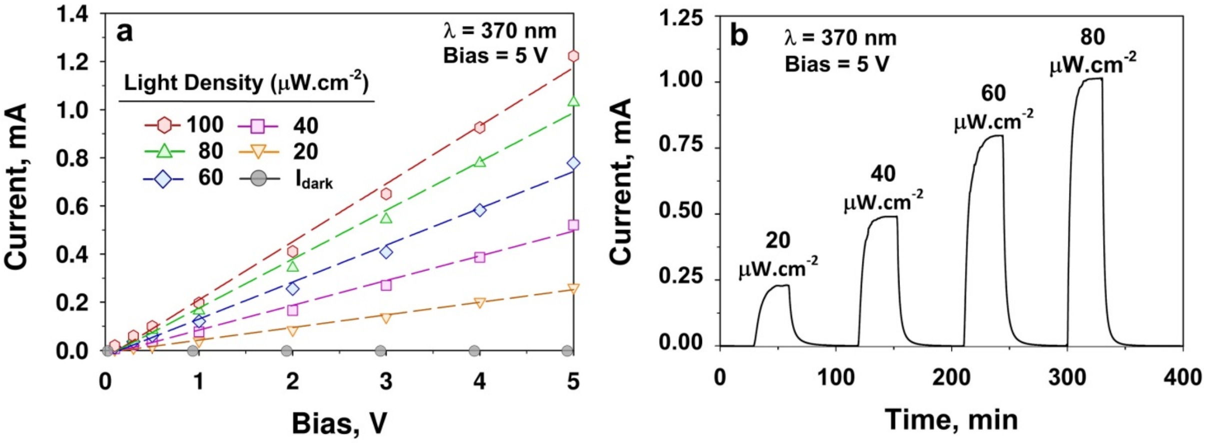

Figure 3.14. *(a) Photo-current as a function of applied bias and inset, light intensity demonstrating milliampere currents at low light intensities of 100 µW.cm^{-2}. (b) Time-dependent photodetector response to alternative exposure to increasing light intensity at a bias of 5 V and a wavelength of 370 nm.*

Figure 3.14b shows time-resolved photo-current measurements to alternating exposure to increasing UV light intensities (370 nm) and darkness. Regardless of the light intensities, the photo-current initially rapidly raised and thereafter gradually saturated under illumination, and then sharply dropped as the illumination was switched off. The initial response time of the ultra-porous ZnO films was less than 0.3 s in line with previous reports on electron-depleted ZnO nanoparticles[2]. Rise and decay times were computed from the time required for the current to increase to 90% of the steady-state photo-current value and to decrease again by 90%, respectively. The rise and decay times during the on/off cycles were 250 and 150 s, respectively, and thus in line with that expected for pure ZnO nanostructured photodetectors (Table 5.1). The relatively long times required to reach a steady-state photo- and dark-current are attributed to the chemi/physisorption and photo-desorption of oxygen molecules from the ZnO nanoparticle surface (Figure 3.8).[15,30] The rise and decay time could be further improved by replacing the ZnO nanoparticles with recently reported materials such as ZnS[4,31] that offer faster photo-current dynamics.

3.4 Conclusions

In conclusion, we have developed a novel structural design for CMOS-compatible visible-blind photodetectors featuring ultra-high milliampere photo-currents, very low dark currents, very low UV intensity detection limit and low operation voltages. This excellent performance was attributed to the high film porosity and electron-depleted composition of these nanoparticle networks. Decreasing the primary particle size below twice the ZnO Debye length and providing ultra-porous film morphology enhanced adsorption/desorption of oxygen molecules from the nanoparticle surface and facilitated the penetration of UV light into the lowest film layers resulting in an on/off switch behaviour to UV light exposure. Furthermore, we have demonstrated a flexible and low-cost platform technology for the rapid fabrication and integration of ultra-porous electron-depleted nanoparticle photodetectors in micro-machinable circuitry. This concept can be applied to other highly performing semiconductors such as wide bandgap SnO_2 for selective UV-B detection and fast-responding ZnS[4,31] for fibre optics.

Table 5.1. Figures of merit of state-of-the-art wide bandgap ZnO photodetectors.

Photodetector	**d_p**	**Bias**	**Dark-Current**	**Photo-current**	**I_{photo}/I_{dark} Ratio**	**Intensity**	**Rise Time**	**Decay Time**	**Ref.**
ZnO ultra-porous nanoparticle networks	20 nm	5 V	3.61 nA	1.2 mA	3.4×10^5	100 μW/cm^2	~250 s	~150 s	This Work
				512 μA	1.4×10^5	40 μW/cm^2			
				260 μA	7.2×10^4	20 μW/cm^2			
ZnO nanotetrapods network	--	2.4 V	--	~ 35 nA	4.5×10^3	≈20 mW.cm^{-2}	68 ms	32 ms	[1]
ZnO nanoneedles	50-200 nm	0.3 V	--	~ 250nA	312	≈15 mW.cm^{-2}	22 s	7-12 s	[1]
Colloidal ZnO nanoparticles	10 nm	5 V	7 pA	1.8 μA	≈2.6×10^5	830 μW/cm^2	--	--	[2]
ZnS/ZnO nanobelts	~ 100 nm	5 V	0.67 μA	4.64 μA	6.92	0.91 mW.cm^{-2}	0.3 s	1.7 s	[4]
ZnO-SnO_2	100-150 nm	10 V	1.7 pA	7.9 nA	4.6×10^3	0.45 mW.cm^{-2}	32.2 s	7.8 s	[5]
ZnO nanowire	30 nm	5 V	15 pA	270 pA	18	--	43.7 s	--	[9]
ZnO epitaxial films	--	3 V	--	--	1.56×10^3	300 W.cm^{-2}	--	--	[13]
ZnO quantum dot/graphene	5 nm	3 V	91.6 pA	0.83 μA	1.1×10^4	6 W.cm^{-2}	2 s	1 s	[14]
ZnO microtubes	~ 100 nm	5 V	1.5 μA	900 μA	600	21.7 mW.cm^{-2}	5.9 s	638 s	[15]
ZnS-coated ZnO arrays	100 nm	3 V	--	--	1.25	150 W.cm^{-2}	120 s	180 s	[30]
ZnO nanowire	60-70 nm	5 V	10 nA	100 μA	10^4	40 mW.cm^{-2}	--	--	[32]
ZnO nanorods	150-300 nm	5 V	--	13 μA	85	--	> 500 s	500 s	[33]
ZnO nanowire	150 nm	1 V	0.13 pA	--	1000	1.3 mW.cm^{-2}	40 s	300 s	[34]
ZnO nanowire array	40 nm	5 V	~ 71 μA	~ 100 μA	1.4	--	0.4 ms	--	[35]

3.5 References

1. Gedamu, D.; Paulowicz, I.; Kaps, S.; Lupan, O.; Wille, S.; Haidarschin, G.; Mishra, Y. K.; Adelung, R., Rapid Fabrication Technique for Interpenetrated ZnO Nanotetrapod Networks for Fast UV Sensors. *Adv. Mater.* **2014,** *26*, 1541-1550.

2. Jin, Y.; Wang, J.; Sun, B.; Blakesley, J. C.; Greenham, N. C., Solution-Processed Ultraviolet Photodetectors Based on Colloidal ZnO Nanoparticles. *Nano Lett.* **2008,** *8*, 1649-1653.

3. Sun, J.; Liu, F.-J.; Huang, H.-Q.; Zhao, J.-W.; Hu, Z.-F.; Zhang, X.-Q.; Wang, Y.-S., Fast response ultraviolet photoconductive detectors based on Ga-doped ZnO films grown by radio-frequency magnetron sputtering. *Appl. Surf. Sci.* **2010,** *257*, 921-924.

4. Hu, L.; Yan, J.; Liao, M.; Xiang, H.; Gong, X.; Zhang, L.; Fang, X., An Optimized Ultraviolet-A Light Photodetector with Wide-Range Photoresponse Based on ZnS/ZnO Biaxial Nanobelt. *Adv. Mater.* **2012,** *24*, 2305-2309.

5. Tian, W.; Zhai, T.; Zhang, C.; Li, S.-L.; Wang, X.; Liu, F.; Liu, D.; Cai, X.; Tsukagoshi, K.; Golberg, D.; Bando, Y., Low-Cost Fully Transparent Ultraviolet Photodetectors Based on Electrospun ZnO-SnO_2 Heterojunction Nanofibers. *Adv. Mater.* **2013,** *25*, 4625-4630.

6. Hongsith, N.; Wongrat, E.; Kerdcharoen, T.; Choopun, S., Sensor response formula for sensor based on ZnO nanostructures. *Sens. Actuators B Chem.* **2010,** *144*, 67-72.

7. Hatch, S. M.; Briscoe, J.; Dunn, S., A Self-Powered ZnO-Nanorod/CuSCN UV Photodetector Exhibiting Rapid Response. *Adv. Mater.* **2013,** *25*, 867-871.

8. Liu, R.; Jiang, D.; Duan, Q.; Sun, L.; Tian, C.; Liang, Q.; Gao, S.; Qin, J., Origin of the responsivity characteristics of Au/ZnO/MgZnO and Au/MgZnO/ZnO structured ultraviolet photodetectors. *Appl. Phys. Lett.* **2014,** *105*, 043505.

9. Ahn, S.-E.; Ji, H. J.; Kim, K.; Kim, G. T.; Bae, C. H.; Park, S. M.; Kim, Y.-K.; Ha, J. S., Origin of the slow photoresponse in an individual sol-gel synthesized ZnO nanowire. *Appl. Phys. Lett.* **2007,** *90*, 153106.

10. Mamat, M. H.; Khusaimi, Z.; Musa, M. Z.; Sahdan, M. Z.; Rusop, M., Novel synthesis of aligned Zinc oxide nanorods on a glass substrate by sonicated sol–gel immersion. *Mater. Lett.* **2010,** *64*, 1211-1214.

11. Liu, J.; Lu, R.; Xu, G.; Wu, J.; Thapa, P.; Moore, D., Development of a Seedless Floating Growth Process in Solution for Synthesis of Crystalline ZnO Micro/Nanowire Arrays on Graphene: Towards High-Performance Nanohybrid Ultraviolet Photodetectors. *Adv. Funct. Mater.* **2013,** *23*, 4941-4948.

12. Hernandez-Como, N.; Moreno, S.; Mejia, I.; Quevedo-Lopez, M. A., Low-temperature processed ZnO and CdS photodetectors deposited by pulsed laser deposition. *Semicond. Sci. Technol.* **2014,** *29*, 085008.

13. Ji, L.; Wu, C.; Lin, C.; Meen, T.; Lam, K.; Peng, S.; Young, S.; Liu, C., Characteristic Improvements of ZnO-Based Metal–Semiconductor–Metal Photodetector on Flexible Substrate with ZnO Cap Layer. *Jpn. J. Appl. Phys.* **2010,** *49*, 052201.

14. Ick Son, D.; Yeon Yang, H.; Whan Kim, T.; Il Park, W., Photoresponse mechanisms of ultraviolet photodetectors based on colloidal ZnO quantum dot-graphene nanocomposites. *Appl. Phys. Lett.* **2013,** *102*, 021105.

15. Cheng, J.; Zhang, Y.; Guo, R., ZnO microtube ultraviolet detectors. *J. Cryst. Growth* **2008,** *310*, 57-61.

16. Height, M. J.; Mädler, L.; Pratsinis, S. E.; Krumeich, F., Nanorods of ZnO Made by Flame Spray Pyrolysis. *Chem. Mater.* **2005,** *18*, 572-578.

17. Bo, R.; Nasiri, N.; Chen, H.; Caputo, D.; Fu, L.; Tricoli, A., Low-Voltage High-Performance UV Photodetectors: An Interplay between Grain Boundaries and Debye Length. *ACS Appl. Mater. Interfaces* **2017,** *9*, 2606-2615.

18. Elmøe, T. D.; Tricoli, A.; Grunwaldt, J.-D.; Pratsinis, S. E., Filtration of nanoparticles: Evolution of cake structure and pressure-drop. *J. Aerosol Sci.* **2009,** *40*, 965-981.

19. Tricoli, A.; Graf, M.; Mayer, F.; Kuühne, S.; Hierlemann, A.; Pratsinis, S. E., Micropatterning Layers by Flame Aerosol Deposition-Annealing. *Adv. Mater.* **2008,** *20*, 3005-3010.

20. Tian, W.; Zhang, C.; Zhai, T.; Li, S.-L.; Wang, X.; Liu, J.; Jie, X.; Liu, D.; Liao, M.; Koide, Y.; Golberg, D.; Bando, Y., Flexible Ultraviolet Photodetectors with Broad Photoresponse Based on Branched ZnS-ZnO Heterostructure Nanofilms. *Adv. Mater.* **2014,** *26*, 3088-3093.

21. Muthukumaran, S.; Gopalakrishnan, R., Structural, FTIR and Photoluminescence Studies of Cu Doped ZnO Nanopowders by Co-Precipitation Method. *Opt. Mater.* **2012,** *34*, 1946-1953.

22. Xiong, G.; Pal, U.; Serrano, J. G.; Ucer, K. B.; Williams, R. T., Photoluminesence and FTIR Study of ZnO Nanoparticles: The Impurity and Defect Perspective. *Phys. Stat. Sol. C* **2006,** *3*, 3577-3581.

23. Srikant, V.; Clarke, D. R., Optical absorption edge of ZnO thin films: The effect of substrate. *Journal of Applied Physics* **1997,** *81*, 6357-6364.

24. Tricoli, A.; Righettoni, M.; Teleki, A., Semiconductor Gas Sensors: Dry Synthesis and Application. *Angew. Chem. Int. Ed.* **2010,** *49*, 7632-7659.

25. Tricoli, A.; Elmøe, T. D., Flame spray pyrolysis synthesis and aerosol deposition of nanoparticle films. *AIChE J.* **2012,** *58*, 3578-3588.

26. Tricoli, A.; Graf, M.; Pratsinis, S. E., Optimal Doping for Enhanced SnO_2 Sensitivity and Thermal Stability. *Adv. Funct. Mater.* **2008,** *18*, 1969-1976.

27. Righettoni, M.; Tricoli, A.; Pratsinis, S. E., Thermally Stable, Silica-Doped ε-WO_3 for Sensing of Acetone in the Human Breath. *Chem. Mater.* **2010,** *22*, 3152-3157.

28. Ogawa, H.; Nishikawa, M.; Abe, A., Hall measurement studies and an electrical conduction model of tin oxide ultrafine particle films. *J. Appl. Phys.* **1982,** *53*, 4448-4455.

29. White, M. S.; Olson, D. C.; Shaheen, S. E.; Kopidakis, N.; Ginley, D. S., Inverted bulk-heterojunction organic photovoltaic device using a solution-derived ZnO underlayer. *Appl. Phys. Lett.* **2006,** *89*, 143517.

30. Lupan, O.; Chai, G.; Chow, L.; Emelchenko, G. A.; Heinrich, H.; Ursaki, V. V.; Gruzintsev, A. N.; Tiginyanu, I. M.; Redkin, A. N., Ultraviolet photoconductive sensor based on single ZnO nanowire. *Phys. Status Solidi A* **2010,** *207*, 1735-1740.

31. Bera, A.; Basak, D., Photoluminescence and photoconductivity of ZnS-coated ZnO nanowires. *ACS Appl. Mater. Interfaces* **2010,** *2*, 408-12.

32. Soci, C.; Zhang, A.; Xiang, B.; Dayeh, S. A.; Aplin, D. P. R.; Park, J.; Bao, X. Y.; Lo, Y. H.; Wang, D., ZnO Nanowire UV Photodetectors with High Internal Gain. *Nano Lett.* **2007,** *7*, 1003-1009.

33. Manekkathodi, A.; Lu, M.-Y.; Wang, C. W.; Chen, L.-J., Direct Growth of Aligned Zinc Oxide Nanorods on Paper Substrates for Low-Cost Flexible Electronics. *Adv. Mater.* **2010,** *22*, 4059-4063.

34. Liu, K.; Sakurai, M.; Liao, M.; Aono, M., Giant Improvement of the Performance of ZnO Nanowire Photodetectors by Au Nanoparticles. *J. Phys. Chem. C* **2010,** *114*, 19835-19839.

35. Hou, Y.; Mei, Z.; Du, X., Semiconductor ultraviolet photodetectors based on ZnO and $Mg_x Zn_{1-x} O$. *J. Phys. D: Appl. Phys.* **2014,** *47*, 283001.

Chapter Four

Structural Engineering of Nano-Grain Boundaries for Low-Voltage UV-Photodetectors with Gigantic Photo- to Dark-Current Ratios

Publication relevant to this chapter:

Noushin Nasiri, Renheng Bo, Hongjun Chen, Thomas P White, Lan Fu, Antonio Tricoli, "*Structural Engineering of Nano-Grain Boundaries for Low-Voltage UV-Photodetectors with Gigantic Photo-o Dark-Current Ratios*", **Advanced Optical Materials**, 4, 1787-1795, **2016**.

Abstract

Ultraporous networks of ZnO nanoparticles (UNN) have recently been proposed as a highly performing morphology for portable ultraviolet light photodetectors. Here, we show that structural engineering of the nanoparticle grain boundaries can drastically enhance the performance of UNN photodetectors leading to gigantic photo to dark current ratios with operation voltages below 1 V. Ultraporous nanoparticle layers were fabricated by scalable low-temperature deposition of flame-made ZnO aerosols resulting in highly transparent layers with more than 95% visible light transmittance and 80% UV-light absorption. Optimal thermally-induced necking of the ZnO nanoparticles increased the photo- to dark-current ratio, at a low light density of 86 μW.cm^{-2}, from 1.4×10^4 to 9.3×10^6, the highest so far reported. This is attributed to the optimal interplay of surface depletion and carrier conduction resulting in the formation of an open-neck grain boundary morphology. These findings provide a robust set of guiding principle for the design and fabrication of nanoparticle-based optoelectronic devices.

4.1 Introduction

Portable UV photodetectors have application in numerous optoelectronic devices and components such as piezoelectric transducers, space communications, flame and missile launch detectors, and chemical sensors.[1-4] Often, highly sensitive detectors with low UV-light detection limit and high signal-to-noise ratio are required. Most commercial devices are based on Si-based homojunctions and photomultipliers.[5-7] Notwithstanding their numerous advantages, Si-based UV photodetectors exhibits some intrinsic limitations, such as detection of visible and infrared light photons, photo-degradation under sustained UV illumination, and requirement for cooling.[8] Wide bandgap semiconductors such as GaN,[9-11] ZnO[12-13] and TiO_2[14-15] have been proposed as alternative visible-blind materials for high performance UV-photodetectors.

Recently, nanoscale engineering of ZnO-based devices, an n-type wide bandgap semiconductor, has led to significant performance enhancement and excellent photodetection properties.[16-17] The ZnO absorption edge (3.37 eV) is conveniently located at the end of the visible spectrum and its direct bandgap structure provides a sharp photo-response contrast between the visible and UV spectra.[12] Furthermore, ZnO is earth-abundant, and has high electron mobility[18-22] both of which are favourable for fabrication of low-cost portable photodetectors. Nanostructured ZnO-based photodetectors with enhanced UV photoresponse have been fabricated by electrospinning,[23] CVD[24] and spin coating.[17] Very recently, flame-made ultraporous networks of ZnO UNN have been reported[12] as a highly performing super-structural design for visible-blind UV-photodetectors. These UNN devices demonstrated high milliampere photocurrents to light densities of 100 $\mu W.cm^{-2}$, low nanoampere dark-currents and operation bias of few volts.[12]

Optimization of the nanoscale structure of these UNN has the potential to enhance their portability and performance while providing further insights on their photodetection mechanism. In addition to the material composition, the key structural properties impacting the performance of wide bandgap photodetectors are the film porosity,[12] particle morphology,[25] thickness[26] and grain necking.[27] A major design parameter that has been so far poorly addressed is the type of inter-particle grain boundaries. Notably, as demonstrated for semiconductor gas sensors,[28] the transduction of surface states-based chemo- and photo-electric response is significantly enhanced at the inter-grain boundary and its optimization can drastically improve device performance.[29]

Here, we demonstrate that by structural engineering of the grain boundaries of wide bandgap semiconductor nanoparticles, superior UV-photodetectors featuring ultra-low dark-currents, very low operation voltages and high photocurrents in response to low light densities can be fabricated. Transparent ultraporous nanoparticle networks with transmission of ca. 95% of visible light (500 nm) and absorption of ca. 80% of UV light (340 nm) are rapidly synthesized by deposition of flame-made ZnO aerosols. The photoelectrical response measurement reveals that thermally-induced necking of the grain boundaries is essential for efficient photodetection. An optimal grain-boundary morphology leads to picoamperes dark-currents and a strong photoresponse resulting in the highest photo- to dark-current ratio (9.3×10^6) so far reported at low light densities of 86 μW.cm^{-2}. These findings provide a robust set of guiding principles for the engineering of portable nanoparticle-based UV-photodetectors.

4.2 Experimental

4.2.1 Nanoparticles Deposition

A flame spray pyrolysis (FSP) system was used for the synthesis and direct deposition of ZnO nanoparticle aerosols onto the glass substrates featuring a set of interdigitated electrodes. The photodetector nanoparticles were prepared as follows: Zinc Naphthenate (10% Zn, Sigma Aldrich) was diluted in Xylene (Sigma Aldrich) with a total metal atom concentration of 0.3 mol.L^{-1} for Zn. The prepared solution was supplied at a rate of 5 mL.min^{-1} through a syringe pump, and dispersed into a fine spray with 7 L.min^{-1} oxygen at a constant pressure drop of 2 bars. The spray was ignited by supporting premixed methane/oxygen flames (CH_4 = 1.2 L.min^{-1}, O_2 = 2 L.min^{-1}). A water-cooled substrate holder placed at 20 cm height above the burner (HAB) was utilized to keep the substrate temperature below 150 °C. The photodetector substrates were made of glass with interdigitated platinum lines with 5µm width and spacing and a total electrode area of 7×5 mm (G-IDEAU5, DropSens, Oviedo, Spain). More details about the device design and geometry were reported in previous work.[12] All substrates were cleaned with multiple ethanol/drying cycles and pre-annealed (Brother High Temperature Furnace XD-1.2KN) at 300 °C for 12 h at ambient pressure prior photo-detecting tests before nanoparticles deposition.

4.2.2 Materials Characterization

The morphology and patterning characteristics of the deposited particles and films were investigated by a Hitachi H7100FA transmission electron microscope (TEM) at 100 kV and an analytical scanning electron microscopy (SEM), using Zeiss Ultraplus (FESEM) at 3 kV. The crystal phases, size (d_{XRD}) and surface compositions were characterized by X-Ray diffraction using Bruker system (XRD, D_2 Phaser, U.S.A) equipped with Cu Ka radiation of average wavelength 1.54059 Å. The surface compositions were analysed by Fourier transform infrared spectroscopy (FTIR-ATR, Bruker-Alpha, U.S.A). The ZnO specific surface area (SSA) was measured by N_2 adsorption/desorption at -196.15 ºC (Micromeritics, TriStar II, U.S.A), after degassing at 160 °C for 12 h. The prepared films were annealed in a furnace (Brother High Temperature Furnace XD-1.2KN) at different annealing temperature for 12 h at ambient pressure prior photo-detecting tests, to stabilize the nanoparticle size, avoid resistive-sintering during the photo-detection measurements and finding the optimal annealing temperature.

4.2.3 Photodetection Analysis

The specific detectivity, *D,* and external quantum efficiency, *EQE%*, of the photodetectors annealed at different temperature were calculated as follows:

$$D = \frac{R}{\left(2e \, . \frac{I_{dark}}{A}\right)^{1/2}} \tag{4.1}$$

$$EQE\% = \frac{R \times 1240}{\lambda(nm)} \times 100 \tag{4.2}$$

where *R* is the responsivity, *e* is the electron charge, I_{dark} is the device dark current and λ is the wavelength. The optical properties of the ultraporous ZnO films were measured with a Perkin-Elmer (Lambda 1050 UV/Vis/NIR) Spectrophotometer and a 150 mm integrating sphere. All optical measurements were carried out at room temperature. For I-V measurements, DC currents were measured using a Picoammeter / Voltage source (Model 6487, Keithley). The detection of UV light was performed using a Newport Xenon lamp source 66920.

4.3 Results and Discussion

4.3.1 Nanostructured Device Characterization

Figure 4.1a-c shows a schematic of the ultraporous nanoparticle networks obtained by thermophoretic-driven deposition of ZnO aerosols on photodetector substrates (Figure 4.1a). ZnO nanoparticle aerosols were generated by atomization and combustion of a zinc naphtenate solution. The Zn-atom precursor solution concentration was set to 0.3 mol.l^{-1} in order to control the ZnO nanoparticle size. More details about the fabrication method were reported in previous work.[12] In line with our recent report,[12] gas-phase deposition of flame-made ZnO nanoparticles results in the self-assembly of homogenous films of nanoparticles with ca. 98% porosity, high purity, visible light transparency and ca. 80% UV light absorption.

The ZnO UNN surface was homogenous over hundreds of micrometres and contains both meso- and macropores (Figure 4.2a,b). Cross-section SEM images of the nanostructured film shows (Figure 4.2a) a UNN film thickness of approximately ca. 8.5 μm and a typical fractal-like[30] composition (Figure 4.2b). The UNN growth rate was ca. 5 μm.min^{-1} and thus in good agreement with previous reports.[12,31] In this work, upon deposition, thermally-induced annealing of the nanoparticle grain boundaries was performed from 250 °C to 400 °C (Figure 4.1b). Characterization of the photodetector performance was pursued as a function of the illumination light intensities and annealing temperature, providing new insights of their photodetection mechanism and structural optimization (Figure 4.1c).

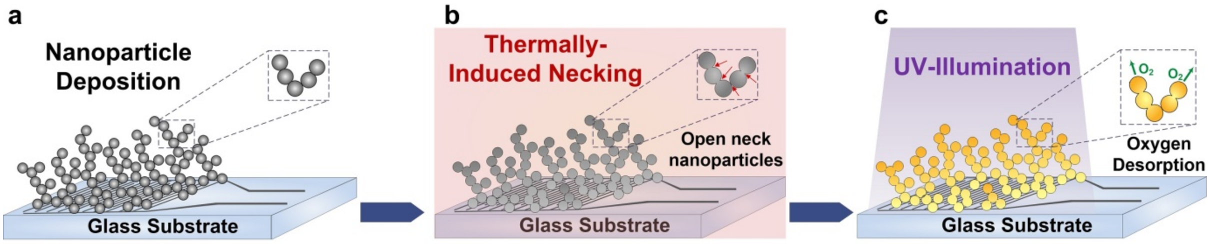

Figure 4.1. *Schematic of (a) ultraporous ZnO nanoparticle network (UNN) self-assembly on glass substrates with interdigitated Pt electrodes. (b) Grain boundary necking was induced by annealing from 250 °C to 400 °C (c) The UV photodetection performance was characterized for each samples under direct exposure.*

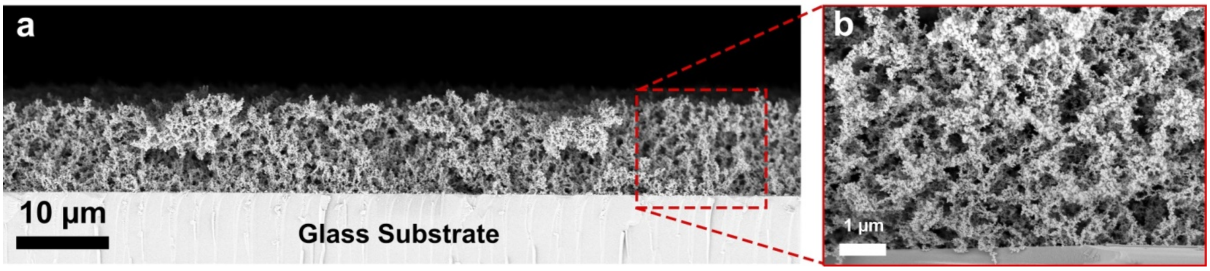

Figure 4.2. *SEM cross-section images of a UNN ZnO device reveals (a) a fractal-like ultraporous morphology with (b) micro-scale pore sizes.*

4.3.2 Optical Properties

Figure 4.3a shows the optical transmittance of the ZnO UNNs deposited on blank glass substrates as a function of their isothermal annealing temperature. The film average integral transmittance for both UV and visible light is computed by subtraction of the fraction lost through the glass substrates as follows:

$$T_{Film} = \frac{I_{Film\_Out}}{T_{Glass}} \times 100 \tag{4.3}$$

where T_{Film} is the film average transmittance, I_{Film_Out} is the transmittance through the glass and the film, and T_{Glass} is the glass transmittance.

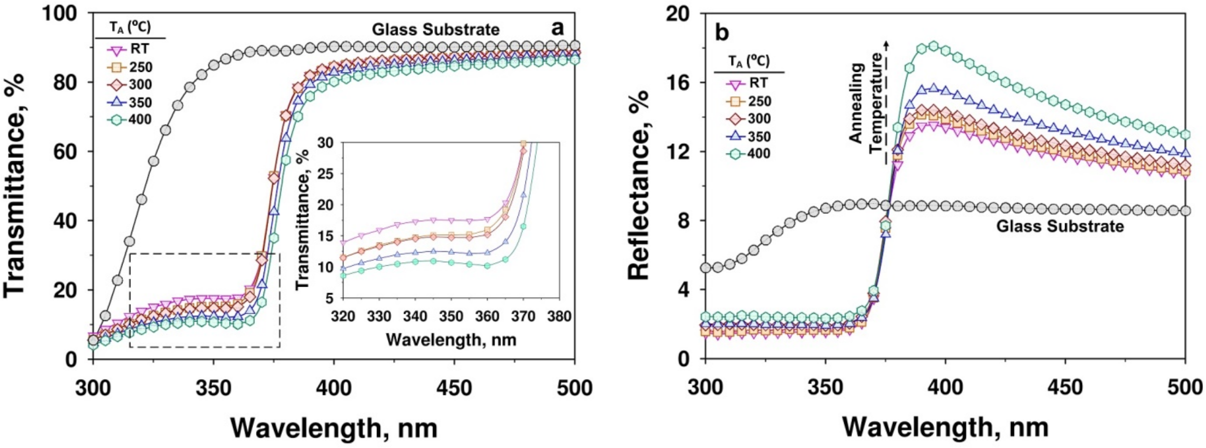

__Figure 4.3.__ Optical (a) transmittance and (b) reflectance spectra of the ultraporous ZnO nanoparticle networks deposited on blank glass substrates (grey circles) as a function of the annealing temperature from 250 °C to 400 °C.

An annealing time of 12 h was selected to achieve a thermodynamically-stable grain size. After subtraction of the optical loses through the glass at 500 nm (10%), the films average transmittance was > 95% for the sintering temperatures. In the UV, the films had a sharp absorption cut-off above 370 nm. This is conveniently close to the end of the visible spectrum (400 nm) and well within the UV-A range (400 - 320 nm).[12,32] Upon removing the fraction lost through the glass, the UV light transmittance through the film at a wavelength of 340 nm was computed to decrease from 22% of the as-prepared to 18% of the annealed samples at 250 °C. Further increasing the annealing temperature to 400 °C (Figure 4.3a, inset) decreased the UV light transmittance through the film to 14% (λ = 340 nm). This is likely due to the decrease of interstitial oxygen vacancies and a slight increase in surface roughness that may increase the optical density of these layers[33].

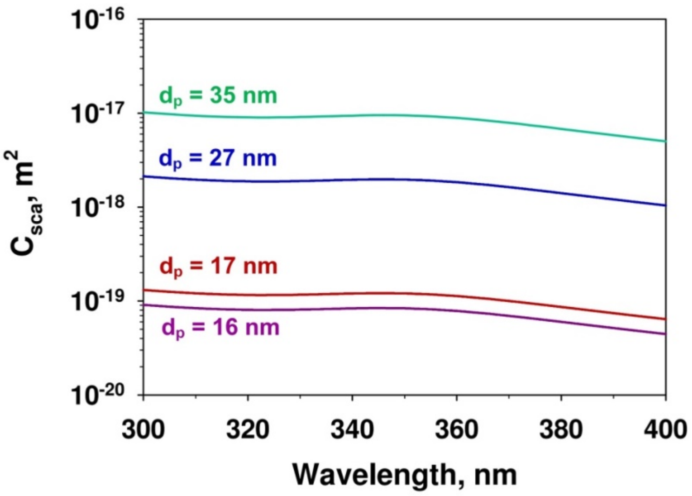

Figure 4.4. *The scattering cross-section of particles with diameter of 16 nm (RT and 250ºC), 17 nm (300ºC), 27 nm (350ºC) and 35 nm (400ºC) at different illumination wavelengths.*

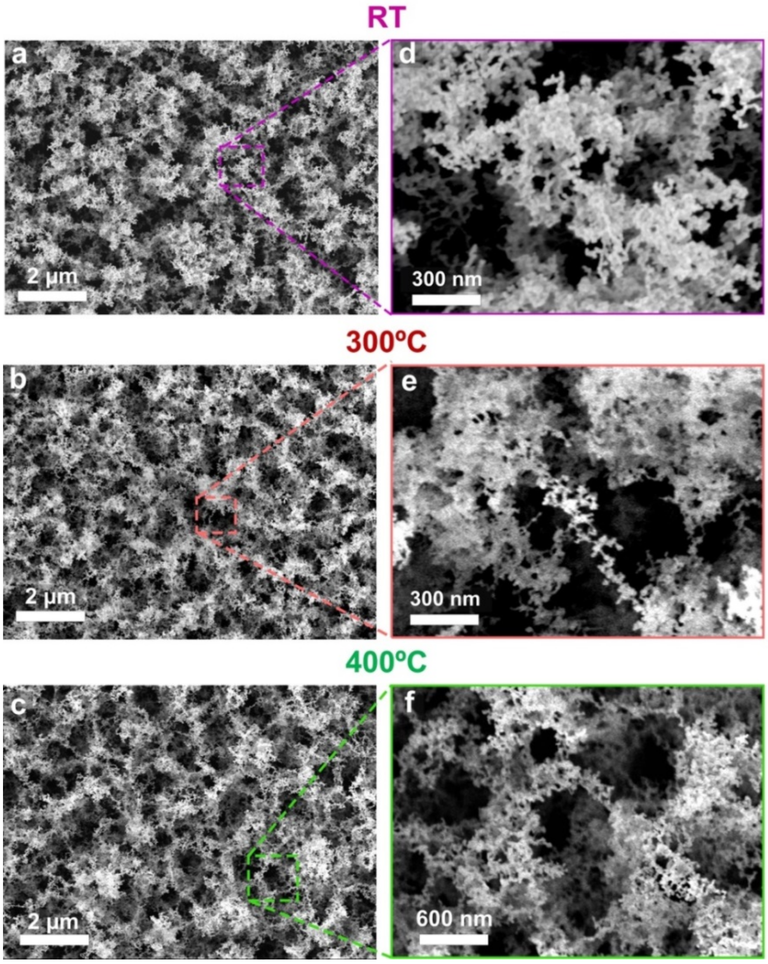

Figure 4.5. *SEM images of an exemplary film deposited of ZnO after 100 s deposition time on glass substrate at HAB of 20 cm (a,d) before and after annealing at (b,e) 300 °C and (c,f) 400 °C for 12 h. Higher magnification SEM of the UNN morphology reveals (e) some thin bridges of partially annealed ZnO nanoparticles and (f) large pores with diameter of several μm. Annealing preserve these ultraporous micro-scale morphology.*

The reflectance spectra of these ZnO ultraporous films before and after annealing are shown in Figure 4.3b. The reflectance of the UNN increased with annealing temperature from 13.4% at 400 nm of the as-prepared to 18% of the annealed ones at 400 °C. This is consistent with the expected particle growth during annealing and it is in line with previous reports.[34-35] The scattering cross-section calculations for ZnO spherical nanoparticles with different particle size of 16, 17, 27 and 35 nm are shown in Figure 4.4 in the Supporting Information. Notably, at this scale, a small increase in particle size results in a drastic increase in light scattering, as predicted by the Rayleigh-scattering regime.[36]

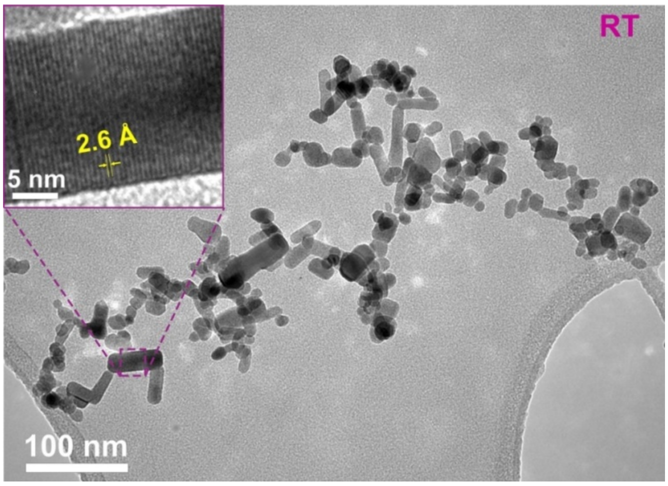

Figure 4.6. *(a) Representative transmission electron microscopy images of exemplary as-prepared ZnO nanoparticles deposited on glass substrates. (inset) The interplanar spacing of 2.6 Å corresponds well to the distance between two (002) planes of the hexagonal ZnO structure.*

Figure 4.5 shows the evolution of the ZnO UNN morphology as a function of the annealing temperature. The films are highly porous and consist of large aggregates of ZnO nanoparticles, forming a three-dimensional, ultraporous network in line with recent modelling of their self-assembling.[12] Their surface was characterized by a hierarchical nano-micro structure (Figure 4.2a,b) with thin bridges of ZnO particles enclosing large micro-pores. Usually, for low-temperature deposition as here (< 150 °C), the morphology of UNNs (Figure 4.5a,d) is mainly determined by the nanoparticle deposition dynamics[37] as the substrate temperature is too low to induce any significant annealing of the ZnO nanoparticles.[12,38]

Here, SEM analysis of the UNN surface morphology revealed that annealing up to 400 °C has no detectable impact on the microscale film morphology (Figure 4.5b-f). This is attributed to the limited sintering of the ZnO particles that at this moderate temperature does not result in micro-scale but only nano-scale restructuring.

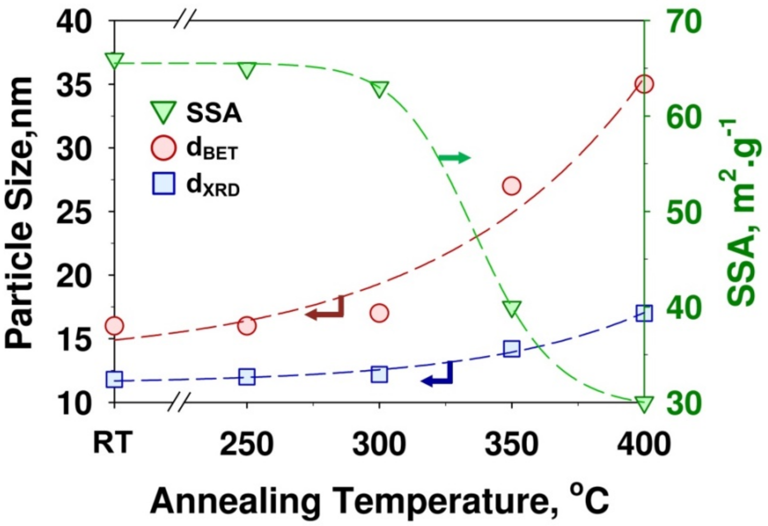

Figure 4.7. *Sauter diameter (d_{BET}), crystal size (d_{XRD}) and ZnO nanoparticles specific surface area (SSA) of the UNN as a function of the annealing temperature.*

Figure 4.6 shows a TEM image of ZnO nanoparticles collected from the photodetector substrates. Most of the as-deposited particles were spherical nanoparticle with average diameter (d_{TEM}) of ca. 16 nm. This is in line with their sauter diameter of 16 nm (d_{BET}), measured by nitrogen absorption (Figure 4.7, red circles). Most of the as-deposited particles (Figure 4.6, inset) have no sintering necks and are held together in the UNN by van der Waals forces. Some nanorod-like structures were also observed (Figure 4.6, inset) which form due to ZnO preferential growth along its (100) plane.[12,39] At higher magnifications, it is possible to identify clear lattice fringes with an interplanar spacing of ca. 2.6 A° (Figure 4.6, inset), which corresponds well to the distance between two (002) planes of the hexagonal wurtzite ZnO phase.[39]

Figure 4.8a-b show the XRD and FTIR spectra of the ZnO nanoparticles before and after annealing. All the XRD patterns corresponded to the wurtzite ZnO phase (JCPDS No. 36-1451)[12,23] with no secondary and amorphous components observed. Upon annealing up to 400 °C the crystal phase was preserved. However, the narrowing of the peaks width indicates a growing crystallite size from 11.6 nm of the as-deposited to 17 nm of the 400 °C annealed. Similarly, the sauter diameter of the ZnO nanoparticles increased from 16 to 35 nm.

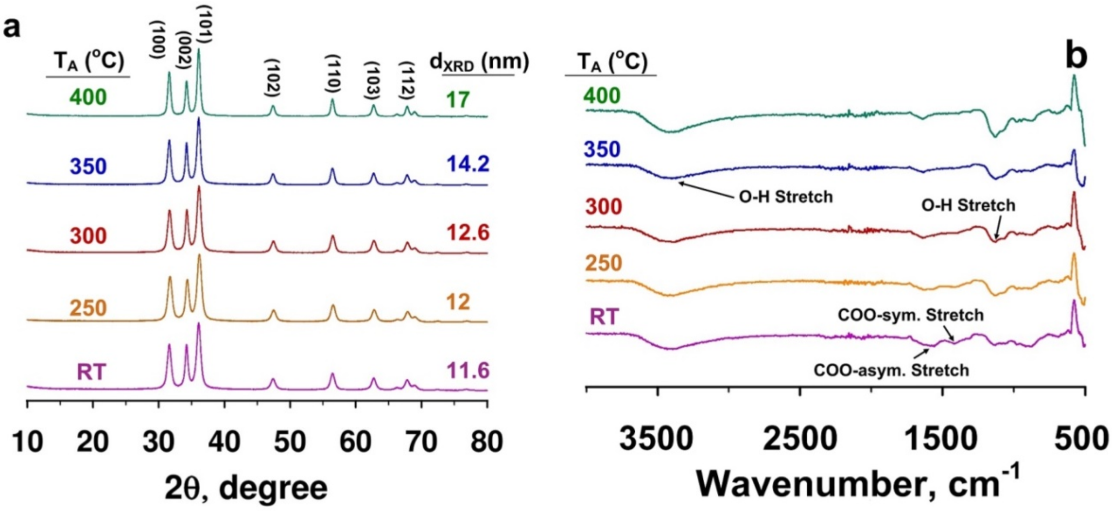

Figure 4.8. *(a) XRD patterns and (b) FTIR spectra of the UNN as a function of the annealing temperature.*

The impurity content of the flame-made ZnO nanoparticles and UNNs were investigated by FTIR (Figure 4.8b). The FTIR spectra of the as-prepared samples indicate the weak presence of adsorbed organics and moistures. In particular, the broad peaks at 3455 and 1146 cm^{-1} are assigned to the O-H stretching vibration of hydroxyl groups attributed to the adsorption of atmospheric moisture.[40] The two sharp peaks around 1600 and 1400 cm^{-1} are attributed to the asymmetrical and symmetrical stretching of zinc carboxylate, respectively, and may form due to adsorption of atmospheric CO_2.[41] Upon annealing, the UNNs maintained a similar FTIR spectra indicating that moisture and CO_2 are rapidly re-adsorbed on the ZnO nanoparticle surface.

4.3.3 Photodetection Properties

The spectral photo-detector responsivity of the UNN was investigated as a function of the annealing temperature in the UV and visible spectrum (Figure 4.9a). Figure 4.9b compares the device responsivity as a function of the annealing temperature from 250 to 400 °C at three different wavelengths, namely 350 nm (rectangles), 370 nm (circles) and 400 nm (triangles).

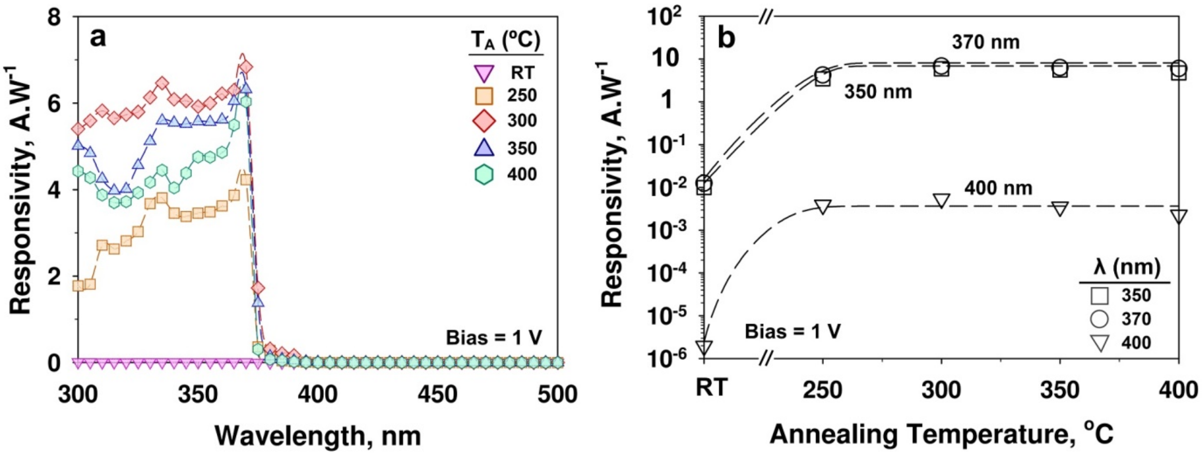

Figure 4.9. *(a) Spectral responsivity of the UNN photodetectors as a function of the annealing temperature and illumination wavelengths. (b) Device responsivity as a function of the annealing temperature at a wavelength of 350, 370 nm and 400 nm and applied bias of 1 V.*

All UNN photodetectors had negligible response to visible light down to a wavelength of 400 nm (Figure 4.9a,b). The visible-light responsivity for all annealed devices was in the order of 0.005 A.W^{-1} at 400 nm (Figure 4.9b). This shows that independently of the grain morphology all UNN are visible-blind. The responsivity increased drastically with the illumination wavelength decreasing from 400 to 370 nm (Figure 4.9a). The maximal responsivity peaked at ca. 7 A.W^{-1} for the 300 °C annealed UNN (Figure 4.9b) under a light illumination with wavelength of 370 nm, which matches well the bandgap of ZnO (3.37 eV).

Figure 4.10 shows the photoresponse of the ZnO UNN to 370 nm UV light with an intensity of 62 and 86 μW.cm^{-2}. The photo-current shows a stable response to repetitive on/off cycles with a rapid initial increase before slow saturation. Upon switching off the UV light, the photocurrent drops initially sharply, and thereafter more slowly while approaching the initial values. Rise and decay times were computed from the time taken for the current to increase from 10% to 90% of the peak value and vice versa, respectively.

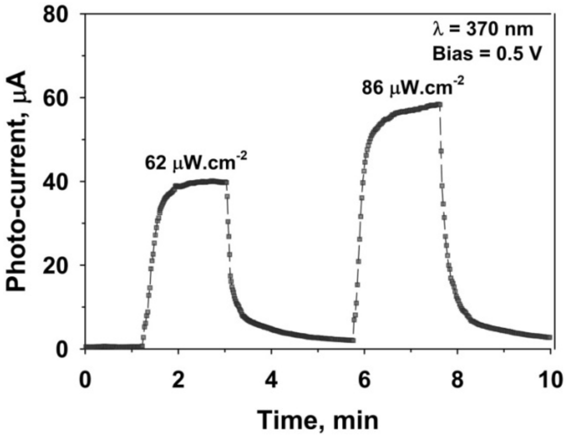

Figure 4.10. *Time-dependent photodetector response of the UNN annealed at 300 ˚C to alternative exposure of light with a light density of 62 and 86 μW.cm*$^{-2}$ *at a bias of 0.5 V and a wavelength of 370 nm.*

The rise and decay times of the detector annealed at 300 ºC are 145 s and 181 s, respectively, which are in line with that reported for pure ZnO nanostructured photodetectors.[12,42] These relatively long rise and decay times are attributed to the chemi/physisorption and photodesorption of oxygen molecules on ZnO nanoparticles surface.[12,42]

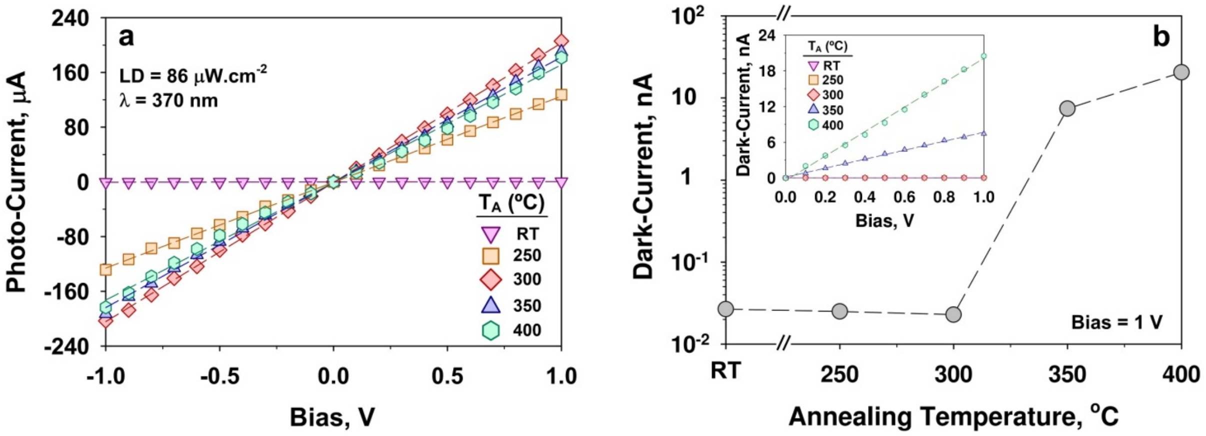

Figure 4.11. *(a) Photo- and (b) dark-current characteristics of the UNN devices as a function of the annealing temperature.*

Figure 4.11a-b show the *I-V* characteristics of the ZnO photodetectors as a function of the annealing temperature under different applied bias with (Figure 4.11a) and without (Figure 4.11b) UV illumination. The *I-V* response was linear and symmetrical (Figure 4.11a) indicating an Ohmic behaviour with sufficient availability of charge carriers to maintain high photocurrents (Figure 4.11a). All the samples exhibited ultra-low dark currents in the range of 22 pA up to 20 nA (Figure 4.11b). This is attributed to strong impact of surface states on the ZnO conductivity that results in electron-depleted grains, and the very high film porosity that reduces the number of neighbouring grains.[12] It was also found that removal of organic contaminants from the photodetector substrates by calcination at 300 °C before UNN deposition drastically decreases surface leakage and the dark currents that, here, are ca. 90 times smaller than that (2 nA)[12] was previously reported for similar ZnO UNNs.

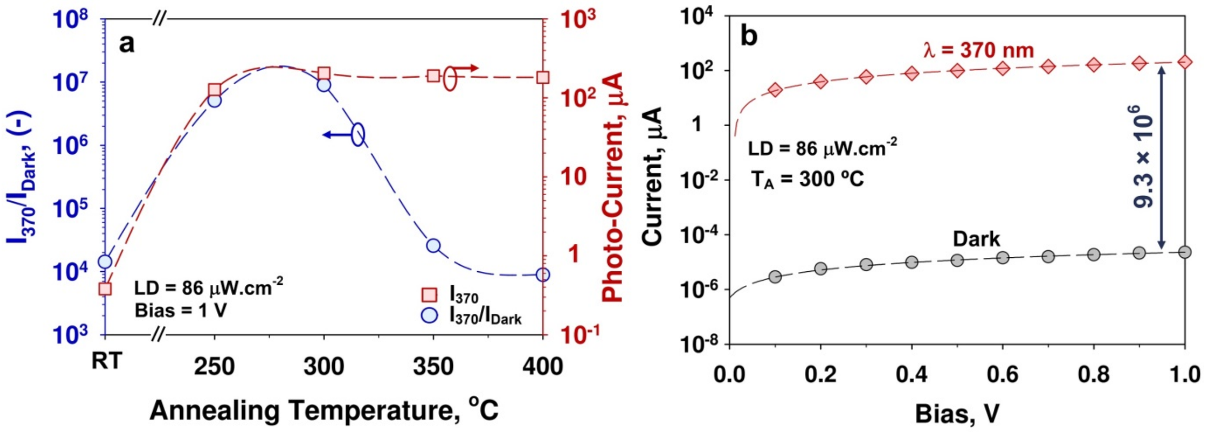

Figure 4.12. *(a) I_{photo}/I_{dark} ratio as a function of the annealing temperature and (b) dark- and photocurrent of the UNN annealed at the optimal temperature of 300 °C.*

Notably, the photocurrent (Figure 4.11a) increased drastically from 0.38 μA at 1 V of the as-prepared device to 128 μA of 250 °C annealed ones. The UNN annealed at 300 °C exhibited the highest photocurrent of 205 μA at 1 V. Annealing the UNN at higher temperatures, such as 350 °C and 400 °C decreased the photocurrent slightly to 190 and 182 μA, respectively. This is attributed to the increase of back scattering with increased particle size as discussed above (Figure 4.4). More important, the decrease in photoresponse was accompanied by a large increase in dark-current from 22 pA for device annealed at 300 °C to 7.5 and 20.5 nA for photodetectors annealed at 350 °C and 400 °C, respectively (Figure 4.11b). The highest photocurrent (205 μA) coupled with the lowest dark-current (22 pA) resulted in the highest performance of the device annealed at 300 °C (Figure 4.11c,d).

Figure 4.12a shows the I_{photo}/I_{dark} of ZnO photodetectors annealed as a function of the annealing temperature under illumination of 370 nm with intensity of 86 $\mu W.cm^{-2}$ at bias of 1 V. The I_{photo}/I_{dark} photoresponse increases from 1.4×10^4 of the as-deposited UNN to 9.3×10^6 of the ones, annealed at 300 °C (Figure 4.12b). However, further increasing the annealing temperature to 350 °C and 400 °C decreases the I_{photo}/I_{dark} to 2.6×10^4 and 0.9×10^4, respectively. In addition, a specific detectivity and an External quantum efficiency (EQE%) of ca. 10^{12} and 2.3×10^3, respectively, have been computed (Figure 4.13) for the UNN photodetector annealed at 300 °C. The detectivity decreased rapidly for sintering temperatures below 250 °C and above 300 °C.

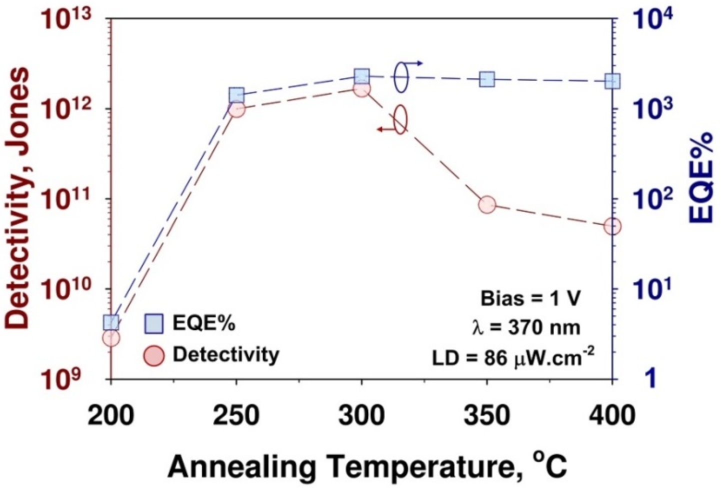

Figure 4.13. *The detectivity and EQE% of the devices after annealing at different temperature under the applied bias of 1 V and light density of 86 $\mu W.cm^{-2}$.*

4.3.4 Photodetection Mechanism

This optimal performance of the UNN annealed at 300 °C is attributed to the distinct contribution of light absorption, electron conduction and surface states in the resulting photocurrent and dark current, as discussed below. In fact, the initial rise in photocurrent is attributed to the formation of sintering neck between the ZnO nanoparticles (Figure 4.14) that results in better electron transport through the ultraporous nanoparticle networks. The drop in photocurrent for annealing temperature above 350 °C is attributed to smaller specific surface area (SSA) for particles annealed at higher temperature. In fact, the ZnO nanoparticles SSA decreased significantly from 63 to 30 $m^2.g^{-1}$ by increasing the annealing temperature from 300 °C to 400 °C. This is schematically shown in Figure 4.14 for the as-prepared (Figure 4.14a) and annealed (Figure 4.14b-c) UNNs. Annealing at 300 °C has almost negligible effect on the particle size (Figure 4.14b and Figure 4.7, red circles) and morphology (Figure 4.5d). In contrast, annealing at 400 °C increased their sauter diameter from 16 to 35 nm (Figure 4.14c and Figure 4.7, red circles), this indicates a significant amount of grain necking, which is further confirmed by the TEM analysis.

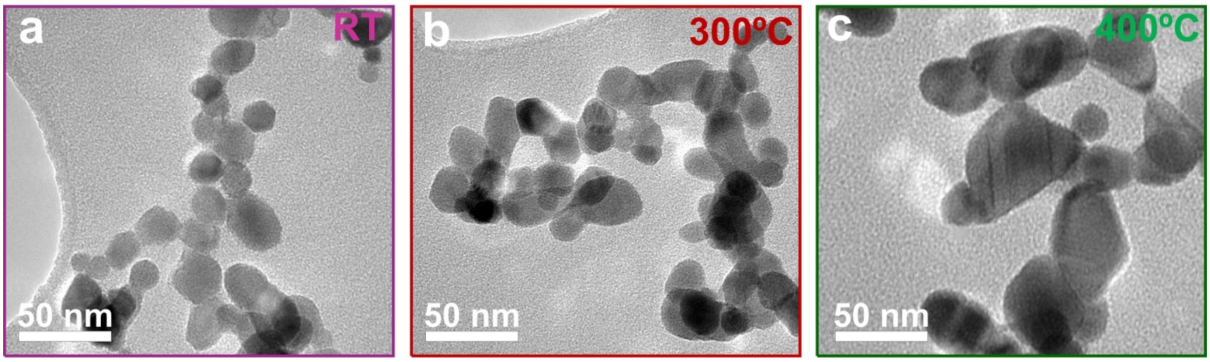

Figure 4.14. *TEM images of the ZnO nanoparticles collected from the UNN (a) before and after annealing at (b) 300 °C and (c) 400 °C.*

The photo-response and electron conduction mechanisms of the ZnO UNN are discussed as a function of the annealing temperature and resulting structural properties in Figure 4.15a-c. Zinc oxide is a n-type semiconductor with electrical conductivity dominated by electron transport. The latter is characterized by three main regimes, namely the inner grain, the grain surface and the inter-grain boundary. The inner grain is usually defined as the region of the particle where bulk electrical conductivity is reached and the effect of surface states is negligible. The surface region lays within the semiconductor Debye's length from the surface and is characterized by a strong band bending and electron depletion due to adsorption of atmospheric O_2 that trap electrons from the semiconductor conduction band.[28] For n-type materials this results in significantly lower electrical conductivity.

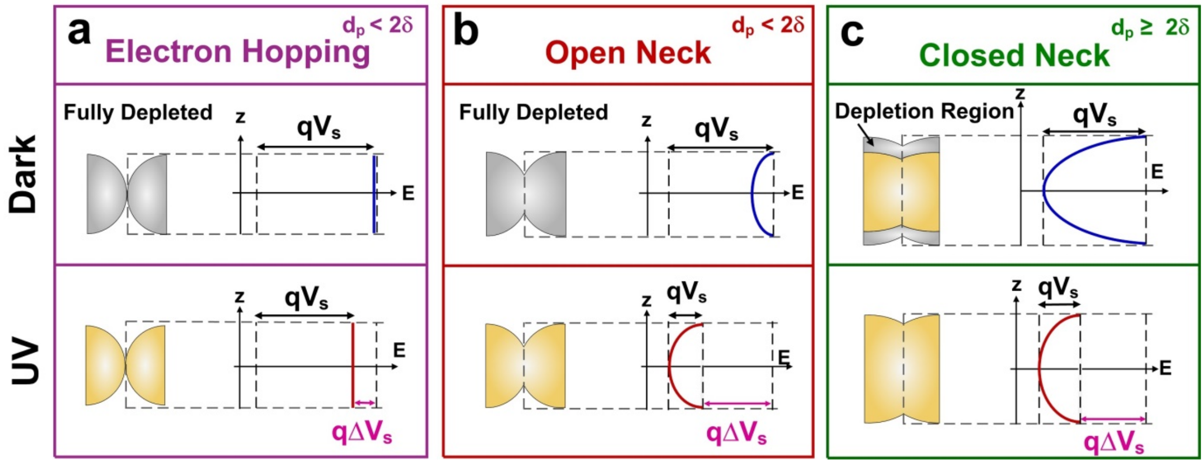

Figure 4.15. *Schematic representation of the ZnO nanoparticle photodetection and inter-grain conduction as a function of the grain boundary morphology for the devices (a) before and after annealing at (b) 300 °C and (c) 400 °C.*

The inter-grain boundaries are strongly affected by the type of annealing necks formed between the nanoparticles (Figure 4.15a-c). On one extreme, non-annealed particles that are held together by van der Waals forces experience very high electrical resistance as the charge carrier needs to be hopping between the grains (Figure 4.15a). Annealed particles are distinguished by their grain boundary morphology. Open necks are grain boundaries which are smaller than twice the Debye's length (2δ) and thus experience similar electrical conduction as the surface region. Closed necks are large, strongly annealed grain boundaries with size greater than twice the Debye's length and approaching bulk conductivity.

Here, the Debye length[28] was computed as follows [43]:

$$\delta = \sqrt{\frac{\varepsilon_s K_b T}{e^2 nc}} \tag{4.4}$$

where ε_s is the static dielectric constant ($13.5\times8.5\times10^{-12}$ F/m in ZnO), K_b is the Boltzmann's constant (1.38×10^{-23} J/K), T is an absolute temperature (K), e is the electrical charge of the carrier (1.6×10^{-19} C), and nc is the carrier concentration (ca. 5×10^{16} cm^{-3})[44]. At room temperature (T = 298 K) for ZnO, this results in a Debye length of ca. 19 nm. According to the TEM images (Figure 4.14a), the non-annealed particles are smaller than twice the Debye's length and fully depleted in dark condition (Figure 4.15a and Figure 4.11b) but due to the large number of inter-grain barriers caused by the lack of sintering necks, the device exhibits a high resistance and limited photocurrent rise under light illumination (Figure 4.15a and Figure 4.11a, purple triangles).

In contrast, annealing the UNN at 300 ^{o}C led to the formation of an open neck morphology between the ZnO nanoparticles (Figure 4.15b) and decreased the total film resistance resulting in the highest photocurrents rise (Figure 4.11a, red diamonds). Annealing the UNN at higher temperatures increased the particle size leading to a d_{BET} of 35 nm at 400 ^{o}C annealing temperature, which is very close to twice the Debye's length (2δ = 38 nm) of ZnO at room temperature. This results in a closed neck morphology (Figure 4.15c). In fact, the TEM analysis reveals that many particles have a diameter of significantly larger than 2δ (Figure 4.14c). As a consequence, these larger particles and inter-grain necks are only partially electron depleted[28] and exhibit a lower photo to dark current ratios under the same UV light illumination (Figure 4a, green hexagonal). In fact while their photocurrent is similar to the 300 ^{o}C UNN, their dark-current (20.5 nA) is 930 time higher (Figure 4.11b). Similar optimization mechanisms of the grain boundary morphology were found for SnO_2-based chemical sensors gas sensors[29] suggesting that enhancement of electro-transduction of chemical- and photo-induced variations in surface states may be optimally enhanced for a grain and neck size close to twice the Debye's length of the semiconductor.

4.4 Conclusions

In conclusion, we have investigated the effect of the grain boundary morphology on the photodetection mechanism of UNN-based UV-photodetectors. Although annealing, up to 400 ^{o}C, had no significant impact on the macro-scale morphology and optical properties, the inter-grain structure changed significantly resulting in different electron conduction mechanism. The optimized device featured ultra-low dark current of 22 pA and high photocurrent of 205 μA at a light intensity of 86 μW.cm^{-2} and bias of 1 V. The resulting I_{photo}/I_{dark} ratio (9.3×10^{6}) is the highest so far reported at this light intensity. This optimal performance was attributed to two main mechanisms, namely the inhibition of the photocurrent in the as-prepared samples due to electron hopping at the grain boundaries, and the increase of the dark-current in the strongly annealed samples due to their closed-neck grain morphology. In contrast, thermal-induced formation of an electron-depleted open-neck inter-grain morphology resulted in very low pA dark-currents and high photocurrents. These findings provide further insights on the photodetection mechanism of these wide bandgap semiconductors and a set of principles for the optimization of nanoparticle-based optoelectronic devices.

4.5 References

1. Hu, L.; Yan, J.; Liao, M.; Xiang, H.; Gong, X.; Zhang, L.; Fang, X., An Optimized Ultraviolet ‐ A Light Photodetector with Wide ‐ Range Photoresponse Based on ZnS/ZnO Biaxial Nanobelt. *Adv. Mater.* **2012,** *24*, 2305-2309.

2. Liu, X.; Gu, L.; Zhang, Q.; Wu, J.; Long, Y.; Fan, Z., All-printable band-edge modulated ZnO nanowire photodetectors with ultra-high detectivity. *Nature Commun.* **2014,** *5*, 4007.

3. Sun, F.; Shan, C.-X.; Wang, S.-P.; Li, B.-H.; Zhang, Z.-Z.; Yang, C.-L.; Shen, D.-Z., Ultraviolet photodetectors fabricated from ZnO p–i–n homojunction structures. *Mater. Chem. Phys.* **2011,** *129*, 27-29.

4. Yang, Q.; Guo, X.; Wang, W.; Zhang, Y.; Xu, S.; Lien, D. H.; Wang, Z. L., Enhancing Sensitivity of a Single ZnO Micro-/Nanowire Photodetector by Piezo-phototronic Effect. *ACS Nano* **2010,** *4*, 6285-6291.

5. Das, K.; Mukherjee, S.; Manna, S.; Ray, S. K.; Raychaudhuri, A. K., Single Si nanowire (diameter [less-than-or-equal] 100 nm) based polarization sensitive near-infrared photodetector with ultra-high responsivity. *Nanoscale* **2014,** *6*, 11232-11239.

6. Michel, J.; Liu, J.; Kimerling, L. C., High-performance Ge-on-Si photodetectors. *Nature Photon.* **2010,** *4*, 527-534.

7. Tsai, D.-S.; Lin, C.-A.; Lien, W.-C.; Chang, H.-C.; Wang, Y.-L.; He, J.-H., Ultra-High-Responsivity Broadband Detection of Si Metal–Semiconductor–Metal Schottky Photodetectors Improved by ZnO Nanorod Arrays. *ACS Nano* **2011,** *5*, 7748-7753.

8. Muñoz, E.; Monroy, E.; Pau, J. L.; Calle, F.; Omnès, F.; Gibart, P., III nitrides and UV detection. *J. Phys.: Condens. Matter* **2001,** *13*, 7115.

9. Li, D.; Sun, X.; Song, H.; Li, Z.; Chen, Y.; Miao, G.; Jiang, H., Influence of threading dislocations on GaN-based metal-semiconductor-metal ultraviolet photodetectors. *Appl. Phys. Lett.* **2011,** *98*, 011108.

10. Martens, M.; Schlegel, J.; Vogt, P.; Brunner, F.; Lossy, R.; Würfl, J.; Weyers, M.; Kneissl, M., High gain ultraviolet photodetectors based on AlGaN/GaN heterostructures for optical switching. *Appl. Phys. Lett.* **2011,** *98*, 211114.

11. Rigutti, L.; Tchernycheva, M.; De Luna Bugallo, A.; Jacopin, G.; Julien, F. H.; Zagonel, L. F.; March, K.; Stephan, O.; Kociak, M.; Songmuang, R., Ultraviolet Photodetector Based on GaN/AlN Quantum Disks in a Single Nanowire. *Nano Lett.* **2010,** *10*, 2939-2943.

12. Nasiri, N.; Bo, R.; Wang, F.; Fu, L.; Tricoli, A., Ultraporous Electron-Depleted ZnO Nanoparticle Networks for Highly Sensitive Portable Visible-Blind UV Photodetectors. *Adv. Mater.* **2015,** *27*, 4336-4343.

13. Soci, C.; Zhang, A.; Xiang, B.; Dayeh, S. A.; Aplin, D. P. R.; Park, J.; Bao, X. Y.; Lo, Y. H.; Wang, D., ZnO Nanowire UV Photodetectors with High Internal Gain. *Nano Lett.* **2007,** *7*, 1003-1009.

14. Liu, Z.; Li, F.; Li, S.; Hu, C.; Wang, W.; Wang, F.; Lin, F.; Wang, H., Fabrication of UV Photodetector on TiO_2/Diamond Film. *Sci. Rep.* **2015,** *5*, 14420.

15. Yanru, X.; Lin, W.; Qinghao, L.; Yanxue, C.; Shishen, Y.; Jun, J.; Guolei, L.; Liangmo, M., High-performance self-powered UV photodetectors based on TiO_2 nano-branched arrays. *Nanotechnology* **2014,** *25*, 075202.

16. Tricoli, A.; Graf, M.; Mayer, F.; Kuühne, S.; Hierlemann, A.; Pratsinis, S. E., Micropatterning Layers by Flame Aerosol Deposition-Annealing. *Adv. Mater.* **2008,** *20*, 3005-3010.

17. Jin, Y.; Wang, J.; Sun, B.; Blakesley, J. C.; Greenham, N. C., Solution-Processed Ultraviolet Photodetectors Based on Colloidal ZnO Nanoparticles. *Nano Lett.* **2008,** *8*, 1649-1653.

18. Hatch, S. M.; Briscoe, J.; Dunn, S., A Self-Powered ZnO-Nanorod/CuSCN UV Photodetector Exhibiting Rapid Response. *Adv. Mater.* **2013,** *25*, 867-871.

19. Manekkathodi, A.; Lu, M.-Y.; Wang, C. W.; Chen, L.-J., Direct Growth of Aligned Zinc Oxide Nanorods on Paper Substrates for Low-Cost Flexible Electronics. *Adv. Mater.* **2010,** *22*, 4059-4063.

20. Law, J. B. K.; Thong, J. T. L., Simple fabrication of a ZnO nanowire photodetector with a fast photoresponse time. *Appl. Phys. Lett.* **2006,** *88*, 133114.

21. Liu, K.; Sakurai, M.; Liao, M.; Aono, M., Giant Improvement of the Performance of ZnO Nanowire Photodetectors by Au Nanoparticles. *J. Phys. Chem. C* **2010,** *114*, 19835-19839.

22. Lupan, O.; Chai, G.; Chow, L.; Emelchenko, G. A.; Heinrich, H.; Ursaki, V. V.; Gruzintsev, A. N.; Tiginyanu, I. M.; Redkin, A. N., Ultraviolet photoconductive sensor based on single ZnO nanowire. *Phys. Status Solidi A* **2010,** *207*, 1735-1740.

23. Tian, W.; Zhai, T.; Zhang, C.; Li, S.-L.; Wang, X.; Liu, F.; Liu, D.; Cai, X.; Tsukagoshi, K.; Golberg, D.; Bando, Y., Low-Cost Fully Transparent Ultraviolet Photodetectors Based on Electrospun ZnO-SnO_2 Heterojunction Nanofibers. *Adv. Mater.* **2013,** *25*, 4625-4630.

24. Xu, L.; Li, X.; Zhan, Z.; Wang, L.; Feng, S.; Chai, X.; Lu, W.; Shen, J.; Weng, Z.; Sun, J., Catalyst-Free, Selective Growth of ZnO Nanowires on SiO_2 by Chemical Vapor Deposition for Transfer-Free Fabrication of UV Photodetectors. *ACS Appl. Mater. Interfaces* **2015,** *7*, 20264-20271.

25. Shewale, P. S.; Yu, Y. S., Structural, surface morphological and UV photodetection properties of pulsed laser deposited Mg-doped ZnO nanorods: Effect of growth time. *J. Alloys Compd.* **2016,** *654*, 79-86.

26. Tüzemen, E. Ş.; Eker, S.; Kavak, H.; Esen, R., Dependence of film thickness on the structural and optical properties of ZnO thin films. *Appl. Surf. Sci.* **2009,** *255*, 6195-6200.

27. McLaren, A.; Valdes-Solis, T.; Li, G.; Tsang, S. C., Shape and Size Effects of ZnO Nanocrystals on Photocatalytic Activity. *J. Amer. Chem. Soc.* **2009,** *131*, 12540-12541.

28. Tricoli, A.; Righettoni, M.; Teleki, A., Semiconductor Gas Sensors: Dry Synthesis and Application. *Angew. Chem. Int. Ed.* **2010,** *49*, 7632-7659.

29. Tricoli, A.; Graf, M.; Pratsinis, S. E., Optimal Doping for Enhanced SnO_2 Sensitivity and Thermal Stability. *Adv. Funct. Mater.* **2008,** *18*, 1969-1976.

30. Castillo, J. L.; Martin, S.; Rodriguez-Perez, D.; Perea, A.; Garcia-Ybarra, P. L., Morphology and Nanostructure of Granular Materials Built from Nanoparticles. *KONA Powder Part. J.* **2014,** *31*, 214-233.

31. Nasiri, N.; Ceramidas, A.; Mukherjee, S.; Panneerselvan, A.; Nisbet, D. R.; Tricoli, A., Ultra-Porous Nanoparticle Networks: A Biomimetic Coating Morphology for Enhanced Cellular Response and Infiltration. *Sci. Rep.* **2016,** *6*, 24305.

32. Tian, W.; Zhang, C.; Zhai, T.; Li, S.-L.; Wang, X.; Liu, J.; Jie, X.; Liu, D.; Liao, M.; Koide, Y.; Golberg, D.; Bando, Y., Flexible Ultraviolet Photodetectors with Broad Photoresponse Based on Branched ZnS-ZnO Heterostructure Nanofilms. *Adv. Mater.* **2014,** *26*, 3088-3093.

33. Gupta, V.; Mansingh, A., Influence of postdeposition annealing on the structural and optical properties of sputtered zinc oxide film. *J. Appl. Phys.* **1996,** *80*, 1063-1073.

34. Lee, P.; Saion, E.; Al-Hada, N.; Soltani, N., A Simple Up-Scalable Thermal Treatment Method for Synthesis of ZnO Nanoparticles. *Metals* **2015,** *5*, 2383.

35. Parra, M. R.; Haque, F. Z., Aqueous chemical route synthesis and the effect of calcination temperature on the structural and optical properties of ZnO nanoparticles. *J. Mater. Res. Technol.* **2014,** *3*, 363-369.

36. Bohren, C. F.; Huffman, D. R., In *Absorption and Scattering of Light by Small Particles*, Wiley-VCH Verlag GmbH: 2007; pp 130-157.

37. Nasiri, N.; Elmoe, T. D.; Liu, Y.; Qin, Q. H.; Tricoli, A., Self-assembly dynamics and accumulation mechanisms of ultra-fine nanoparticles. *Nanoscale* **2015,** *7*, 9859-9867.

38. Tricoli, A.; Elmøe, T. D., Flame spray pyrolysis synthesis and aerosol deposition of nanoparticle films. *AIChE J.* **2012,** *58*, 3578-3588.

39. Height, M. J.; Mädler, L.; Pratsinis, S. E.; Krumeich, F., Nanorods of ZnO Made by Flame Spray Pyrolysis. *Chem. Mater.* **2005,** *18*, 572-578.

40. Muthukumaran, S.; Gopalakrishnan, R., Structural, FTIR and Photoluminescence Studies of Cu Doped ZnO Nanopowders by Co-Precipitation Method. *Opt. Mater.* **2012,** *34*, 1946-1953.

41. Xiong, G.; Pal, U.; Serrano, J. G.; Ucer, K. B.; Williams, R. T., Photoluminesence and FTIR Study of ZnO Nanoparticles: The Impurity and Defect Perspective. *Phys. Stat. Sol. C* **2006,** *3*, 3577-3581.

42. Retamal, J. R. D.; Chen, C.-Y.; Lien, D.-H.; Huang, M. R. S.; Lin, C.-A.; Liu, C.-P.; He, J.-H., Concurrent Improvement in Photogain and Speed of a Metal Oxide Nanowire Photodetector through Enhancing Surface Band Bending via Incorporating a Nanoscale Heterojunction. *ACS Photonics* **2014,** *1*, 354-359.

43. Ogawa, H.; Nishikawa, M.; Abe, A., Hall measurement studies and an electrical conduction model of tin oxide ultrafine particle films. *J. Appl. Phys.* **1982,** *53*, 4448-4455.

44. White, M. S.; Olson, D. C.; Shaheen, S. E.; Kopidakis, N.; Ginley, D. S., Inverted bulk-heterojunction organic photovoltaic device using a solution-derived ZnO underlayer. *Appl. Phys. Lett.* **2006,** *89*, 143517.

Chapter Five

Tunable Band-Selective UV-Photodetectors by 3D Self-Assembly of Heterogeneous Nanoparticle Networks

Publication relevant to this chapter:

Noushin Nasiri, Renheng Bo, Tak Fu Hung, Vellaisamy A.L. Roy, Lan Fu, Antonio Tricoli, "*Tunable Band-Selective UV-Photodetectors by 3D Self-Assembly of Heterogeneous Nanoparticle Networks*", **Advanced Functional Materials**, 26, 7359-7366, **2016**.

Abstract

Accurate detection of ultraviolet radiation is critical to many technologies including wearable devices for skin cancer prevention, optical communication systems and missile launch detection. Here, we present a highly performing nanoscale architecture for band-selective UV-photodetectors that features unique tunability and miniaturization potential. The device layout relies on the 3D integration of ultraporous layers of tailored nanoparticles. By tailoring the transmittance window between the indirect band gap of TiO_2 nanoparticles and the sharp edge of the direct band gap of ZnO, we achieve a band-selective photoresponse with tunable bandwidth to less than 30 nm and photo- to dark-current ratios of several millions at a light intensity of 86 $\mu W.cm^{-2}$ and operation bias of 1 V. We showcase the potential of this integrated morphology by fabrication of the first inherent UVA photodetector with selectivity against the edge of the UVB and visible light of nearly 60 times. This tunable architecture and nanofabrication approach are compatible with state-of-the micromachining technologies, and provide a flexible solution for the engineering of wearable band-selective photodetectors.

5.1 Introduction

Ultraviolet radiation is the highest energy component of the solar spectrum reaching the earth's surface.[1] Nature relies on its unique attributes for numerous purposes. Band-selective absorption and reflection of UV-light is the invisible language of butterflies and enables the safe mating of numerous species.[2-3] In the skin, UV-light stimulates the synthesis of vitamin D, an essential compound for many metabolic processes.[4] UV radiation is also the most important environmental factor in the pathogenesis of skin cancer.[5] While UVC ($100 \leq \lambda < 280$ nm) radiation is blocked by the ozone layer,[6-7] UVA ($315 \leq \lambda < 400$ nm) and UVB ($280 \leq \lambda < 315$ nm) pass through and cause numerous diseases.[8] These include erythema,[9] DNA damage,[10] apoptotic cell death,[11] skin pigmentation[12] and skin cancer[13]. Studies over the past two decades[14-15] show that UVA damages skin cells called keratinocytes in the basal layer of the epidermis, where most skin cancers start.[16] UVB, the main cause of skin reddening and sunburn, tends to damage the skin's more superficial epidermal layers.[17] It also plays a contributory role in tanning, burning and photo-aging. Wearable devices for band-selective measurement of UVA and UVB have numerous applications including personal assessment of UV light exposure.[18-20]

Nanostructured wide bandgap semiconductors such as TiO_2[21] and ZnO[22-23] are inherently visible-blind and can detect very low intensity of ultraviolet light by variations in the concentration of their surface-states.[24-25] Jin et al.[24] reported a solution-processed UV photodetector based on colloidal ZnO nanoparticles with photo- to dark-current ratio of ca. 2.6×10^5 at 830 μW.cm^{-2} light density and applied bias of 5 V. Highly performing and scalable electrospun ZnO-SnO_2 nanofibers films[25] featured up to 4.6×10^3 I_{UV}/I_{dark} ratios under UV light intensities of 450 μW.cm^{-2}. Recently, ultraporous networks of electron-depleted ZnO nanoparticles,[23] made by aerosol self-assembly, have demonstrated excellent performance as photodetectors featuring milliampere high photocurrents, more than 10^5

photo- to dark-current ratios at 5 V bias and low light intensities of 86 μW.cm^{-2}. Furthermore, their aerosol-based synthesis approach is compatible with state-of-the-art CMOS-micromachining processes[26] enabling the parallel wafer-level fabrication of chip-size devices of few hundreds μm[2,27]. However, a key limitation of these wide band gap semiconductors is their broad photoresponse[23] that cannot distinguish between UVA and UVB radiation.

Fang et al.[28] have recently demonstrated the band-selective detection of visible light by tuning the bandgap of perovskite single-crystals. Ren et al.[29] reported the fabrication of band-selective infrared photodetectors based on $InAs_xP_{1-x}$ nanowires.[29] A key challenge of these approaches is the requirement of fine-tuning simultaneously multiple material properties, such as spectral absorbance, electron-hole recombination and carrier mobility.[29] For example, for $InAs_xP_{1-x}$ nanowires, the peak photocurrent decreased by an hundred fold from ca. 70 to 0.17 nA with increasing content from 0 to 0.7. An alternative approach, demonstrated for chemical sensors,[30] is the 3D integration of functional layers of semiconductor nanoparticles. In this type of devices, each material can be individually optimized for a specific function resulting in an outstanding device-level performance.

Here, we present a nanoscale architecture for band-selective UV photodetectors that features excellent tunability, light detection performance and miniaturization potential. The device layout relies on the 3D integration of ultraporous functional layers of ZnO, SiO_2 and TiO_2 nanoparticles. A band-selective photoresponse is obtained by exploiting the transmittance window between the indirect bandgap of TiO_2 and the sharp-edge of the direct bandgap of ZnO. The bandwidth of these integrated metal-oxide nanoparticle networks (IMONNs) can be easily tuned from 85 to less than 30 nm. Optimal devices can be efficiently operated below 1 V and achieve UVA- to dark-current ratio of several millions and selectivity of nearly 60 times over UVB and visible light irradiation. Higher applied voltages of up to 10 V[23-25] have been often utilized to obtain this high photo- to dark-current ratios.

This is a challenge for their integration in wearable devices, where reaching operation voltages of 10 V requires bulkier battery components. In addition to the rapid CMOS-compatible fabrication process, this flexible device architecture could be extended to the visible and infrared spectral regions by selection of the appropriate nanoparticle semiconductor layers.

5.2 Experimental Section

5.2.1 Nanoparticles Deposition

A flame spray pyrolysis system was used for the synthesis and direct deposition of ZnO, SiO_2 and TiO_2 nanoparticles films onto the glass substrates featuring a set of interdigitated electrodes. The photodetector nanoparticles were prepared as follows: Zinc Naphthenate (10% Zn, Sigma Aldrich), hexamethyldisiloxane (HMDSO, Sigma Aldrich, purity > 99%) and titanium (IV) isopropoxide (TTIP, Sigma Aldrich, purity > 97%) were diluted in Xylene (Sigma Aldrich) with a total metal atom concentration of 0.3, 0.05 and 0.5 $mol.l^{-1}$ for Zn, Si and Ti respectively. All the solutions were supplied at a rate of 5 $ml.min^{-1}$ through a syringe pump, and dispersed into a fine spray with 7 $L.min^{-1}$ oxygen at a constant pressure drop of 2 bars. The spray was ignited by supporting premixed methane/oxygen flames (CH_4 = 1.2 $L.min^{-1}$, O_2 = 2 $L.min^{-1}$). A water-cooled substrate holder placed at 20 cm height above the burner (HAB) was utilized to keep the substrate temperature below 150 °C. The photodetector substrates were made of glass with interdigitated platinum lines with 5µm width and spacing and a total electrode area of 7×5 mm (G-IDEAU5, DropSens, Oviedo, Spain). More details about the device design and geometry are reported in previous work.[23] All substrates were cleaned with multiple ethanol/drying cycles before nanoparticles deposition.

5.2.2 Materials Characterization

The morphology and patterning characteristics of the deposited particles and films were investigated by a Hitachi H7100FA transmission electron microscope (TEM) at 100 kV and an analytical scanning electron microscopy (SEM), using Zeiss Ultraplus (FESEM) at 3 kV. The crystal phases, size (d_{XRD}) and surface compositions were characterized by X-Ray diffraction using Bruker system (XRD, D_2 Phaser, U.S.A) equipped with Cu Ka radiation of average wavelength 1.54059 Å. The average primary particle diameter (d_{TEM}) was measured by TEM analysis at least 800 nanoparticles for each material and with the aid of an image processing software (ImageJ). This resulted in a visible primary particle diameter (d_{TEM}) of 18 ± 3 nm and 12 ± 2 nm for TiO_2 and ZnO, respectively. The substrates were kept in a furnace (Brother High Temperature Furnace XD-1.2KN) at 300 °C for 12 h, at ambient pressure prior photo-detecting tests, to decrease grain boundary barriers to electron conduction in the ZnO layer, increase the overall assembly stability and avoid resistive-sintering during the photo-detection measurements.

5.2.3 Photodetection Analysis

Absorbance spectra of the ultraporous and dense ZnO films deposited were measured with a Perkin-Elmer (Lambda 1050 UV/Vis/NIR) Spectrophotometer and a 150 mm integrating sphere. All optical measurements were carried out at room temperature. The film average integral transmittance is computed by subtraction of the fraction loss through the glass substrate. For *I-V* measurements, DC currents were measured using a Picoammeter / Voltage source (Model 6487, Keithley). The detection of UV light was performed using a Newport Xenon lamp source 66920 and the UV-Vis absorption spectra were recorded in the wavelength range 250-500 nm using Princeton Instrument Acton SP2500 (0.500m Imaging Triple Grating Monochromator/Spectrograph).

5.3 Results and Discussion

5.3.1 IMONN Device Characterization

Figure 5.1 shows a schematic description of the IMONN layout. The device consists of three vertically-stacked ultraporous metal-oxide nanoparticle networks. The bottom layer is a photoresistor composed of electron-depleted ZnO nanoparticles. This n-type semiconductor morphology, with a direct bandgap of ca. 3.37 eV, has recently demonstrated[23] excellent performance for broad-band detection (λ < 400 nm) of UV-light.

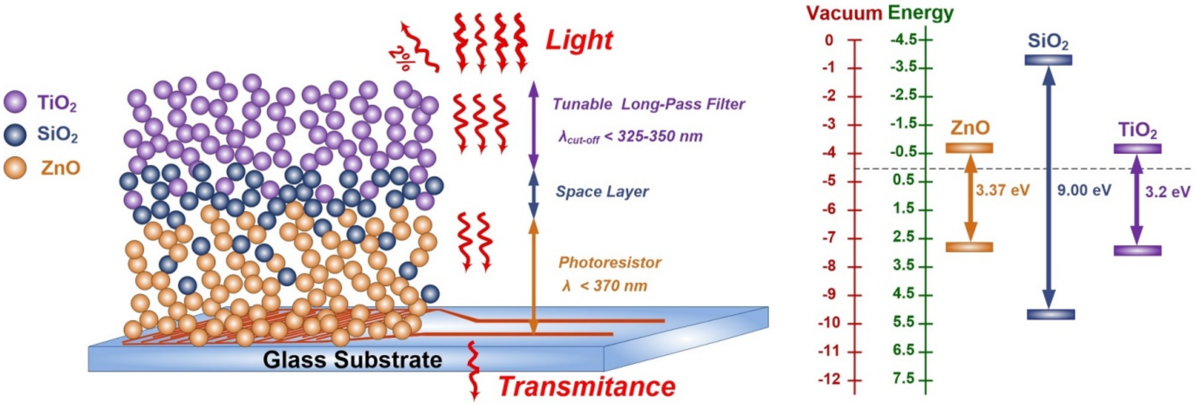

Figure 5.1. *Schematic and band diagram of a band-selective UV photodetector based on an integrated metal-oxide nanoparticle network (IMONN) architecture. This is comprised of a photoresistor ZnO bottom layer, a very thin amorphous* SiO_2 *space layer and an anatase* TiO_2 *long-pass filter top layer.*

The top layer acts as a tunable long-pass filter and is composed of an ultraporous network of anatase TiO_2 nanoparticles. The cut-off wavelength through this layer can be fine-tuned from 325 to ca. 400 nm by exploiting the wavelength-dependent absorbance of anatase TiO_2, an indirect band gap semiconductor. To electrically insulate the filter TiO_2 and photoresistor ZnO layer (Figure 5.1), a UV-transparent dielectric layer of SiO_2 nanoparticles is used as spacer. The theoretical upper and lower band-selective response of this TiO_2/SiO_2/ZnO IMONN layout correspond to the edge (λ_{upper} = 375 nm) of the ZnO bandgap and the cut-off wavelength of the anatase TiO_2 top layer (λ_{lower} = 325 - ca. 380 nm), respectively.

These devices were fabricated by sequential deposition of flame-made nanoparticle aerosols. The particle size of each metal-oxide layer was controlled by the metal-atom concentrations of the precursor solution set to 0.3, 0.05 and 0.5 mol.l^{-1} for the ZnO, SiO_2 and TiO_2 nanoparticles, respectively. Transmission electron microscopy (TEM) analysis of the ZnO and TiO_2 nanoparticles collected from the aerosols (Figure 5.2a-d) reveals a spherical shape and a visible primary particle diameter (d_{TEM}) of 18 ± 3 nm and 12 ± 2 nm, respectively. This is in good agreement with previous reports on the flame-made TiO_2[31-32] and ZnO[23]. The SiO_2 nanoparticles consisted of larger agglomerates with more strongly sintered primary particles. As the role of the SiO_2 is to act as a spacer between the ZnO and TiO_2 layers, and they do not play a role in the photo-generation of electron-holes, their larger size than the ZnO has no impact on the devices performance.

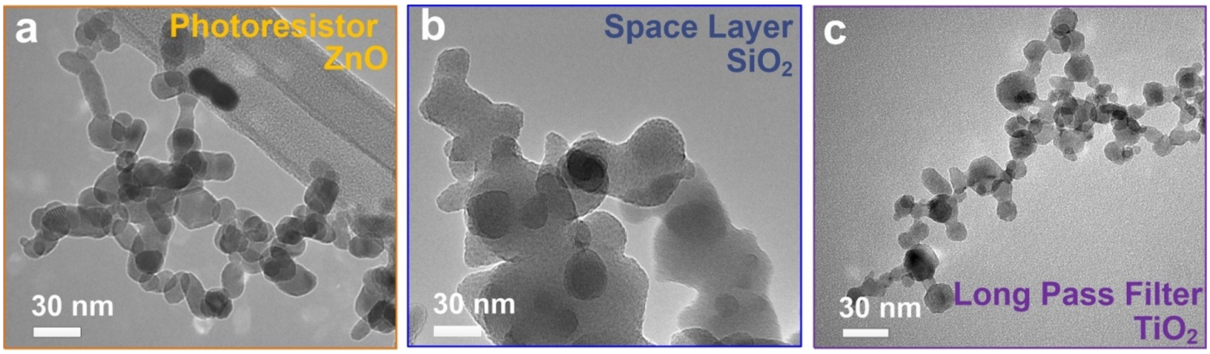

Figure 5.2. *TEM images of the constituents (a) ZnO, (b) SiO_2 and (c) TiO_2 nanoparticles.*

These nanoparticles were self-assembled on the photodetector substrate surface by sequential thermophoretic-driven aerosol deposition resulting in an ultraporous network of TiO_2, SiO_2 and ZnO nanoparticles. This approach has been recently modelled[33] and enables multi-layer morphologies with carefully controlled individual layer thickness and composition.[30] An aerosol deposition time of 100 s was chosen for ZnO in line with recent reports on high-performance broad-band UV photodetector[23]. A SiO_2 nanoparticle deposition time of 25 s was found to lead to excellent UV light transmittance and sufficient electrical insulation between the TiO_2 and ZnO layers. The impact of the TiO_2 layer thickness on the resulting optical properties and device performance was further investigated as a function of the TiO_2 film thickness from 1.6 to 6.6 μm.

Figure 5.3a shows SEM image of the top pure ZnO UNN. The surface morphology of an exemplary $TiO_2/SiO_2/ZnO$ IMONN consist of a ZnO, SiO_2 and TiO_2 layer with 9.5, 0.12 and 5.3 μm thickness is presented in Figure 5.3b.The morphology of the resulting layer is uniform and ultraporous with a hierarchical nano- and micro-scale pore size distribution. The film porosity of the $TiO_2/SiO_2/ZnO$ network, computed by gravimetric and cross-sectional SEM analysis, is ca. 98%. This is in good agreement with previous reports on single nanoparticle layers deposited by thermophoretic-driven aerosol self-assembly[26,34]. In fact, this integrated $TiO_2/SiO_2/ZnO$ morphology can hardly be distinguished from that of the bottom ZnO nanoparticle layer (Figure 5.3a,b).

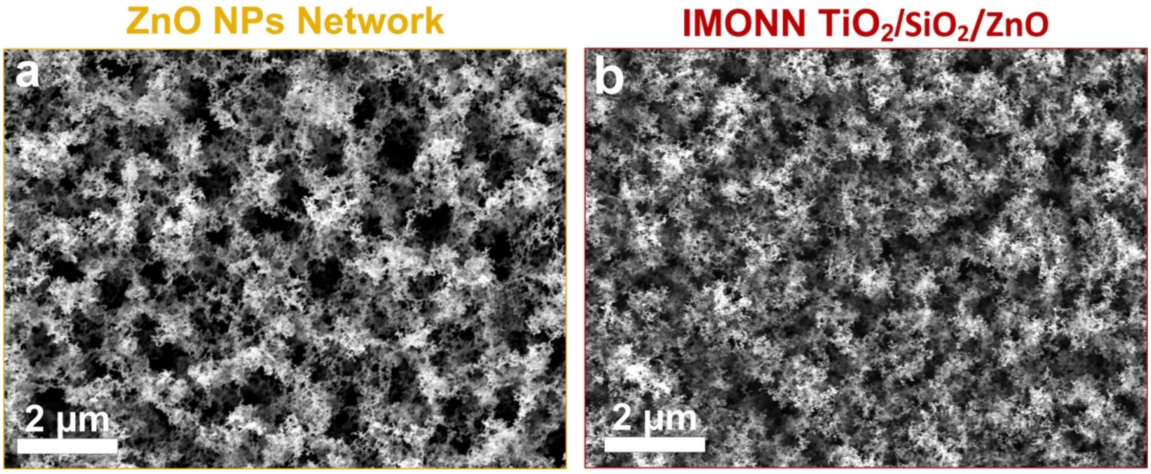

Figure 5.3. *Top-view SEM image of an exemplary (a) pure ZnO UNN and (b) $TiO_2/SiO_2/ZnO$ IMONN consist of a ZnO, SiO_2 and TiO_2 layer with 9.5, 0.12 and 5.3 μm thickness, respectively.*

The film morphology was not affected by the sequential deposition of the different aerosols and there were no variations in the morphology noticed (Figure 5.3a,b). Cross-sectional SEM analysis reveals that sequential aerosol deposition of the SiO_2 nanoparticles on the ZnO layer does not vary the average layer thickness (Figure 5.4). This is attributed to the high surface roughness of aerosol-deposited nanoparticle layers[33] and the very low SiO_2

precursor concentration (0.05 mol.l^{-1}) and aerosol deposition time (25 s) utilized here that results in the deposition of a very small SiO_2 nanoparticle volume[35]. In fact, the thickness of SiO_2 layer deposited for 25 s on a bare glass substrate was ca. 120 nm (Figure 5.5).

In contrast, aerosol deposition of TiO_2 nanoparticles for 75 s increased the SEM cross-sectional thickness from 9.5 μm of the ZnO bottom layer to ca. 16 μm (Figure 5.6a,b). This is in line with the significantly higher concentration (0.5 mol.l^{-1}) of the TiO_2 precursor[36]. The $TiO_2/SiO_2/ZnO$ network thickness increased linearly from 11 μm to 16 μm with increasing TiO_2 nanoparticle aerosol deposition time from 15 to 75 s indicating a constant TiO_2 layer growth rate of ca. 5 μm.min^{-1}.

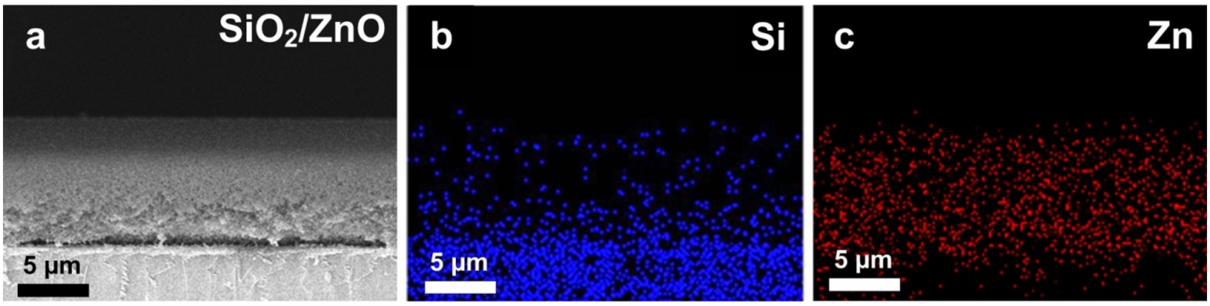

Figure 5.4. *(a) Cross-section SEM image of the SiO_2/ZnO structure and EDX qualitative elemental mapping along the cross-section revealing the location of the (b) Si and (c) Zn atoms.*

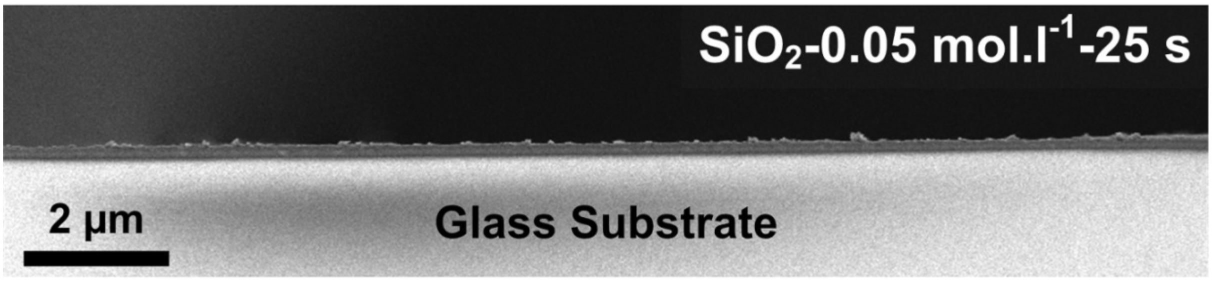

Figure 5.5. *Cross-section SEM image of a pure SiO_2 nanoparticle layer deposited on a glass substrate with an aerosol deposition time of 25 s.*

Figure 5.7a,b show the X-ray diffraction (XRD) and Fourier Transform Infrared Spectroscopy (FTIR) measurements of the $TiO_2/SiO_2/ZnO$ devices and that of the individual ZnO, SiO_2 and TiO_2 flame-made nanoparticles. The XRD spectra of ZnO and TiO_2 correspond to the hexagonal wurtzite (JCPDS No. 36-1451) and tetragonal anatase (JCPDS

No. 21-1272) phase, respectively. The resulting average ZnO and TiO_2 crystal sizes are 12.9±1 nm for both materials. Notably, the SiO_2 nanoparticles XRD spectrum was characteristic of an amorphous material with a broad hump at a 2θ of 22°. The XRD spectra of the $TiO_2/SiO_2/ZnO$ network (Figure 5.7a) matched well the combined XRD peaks of the individual ZnO and TiO_2 nanoparticles and the accentuated amorphous hump of the SiO_2. The average crystal sizes of the anatase and wurtzite phase in the $TiO_2/SiO_2/ZnO$ network are 15.8±1 nm and 15.3±1 nm, respectively, and thus close to that of the corresponding nanoparticle aerosols.

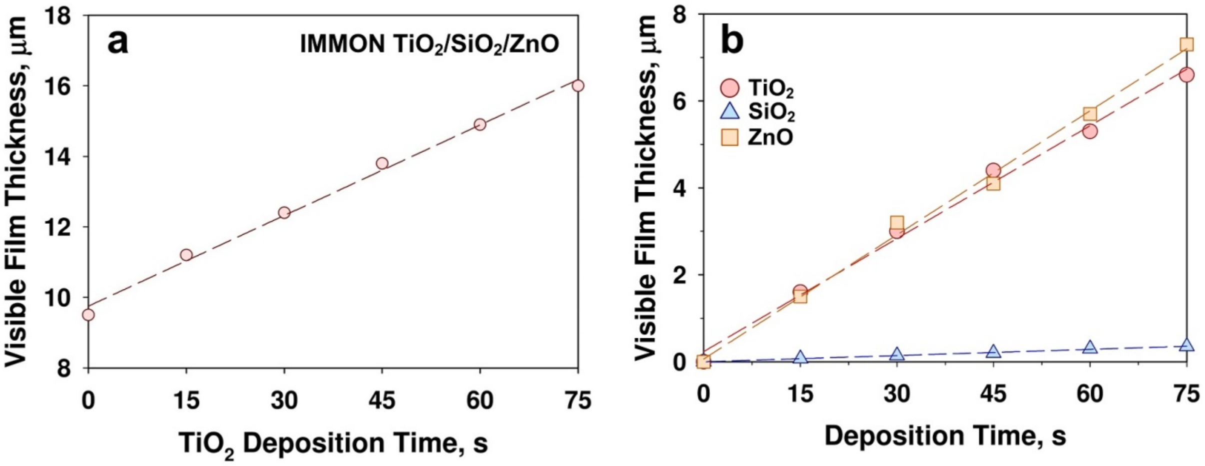

Figure 5.6. *Visible film thickness of (a) IMONN devices as a function of TiO_2 deposition time with a ZnO and SiO_2 deposition time of 100 and 25 s, respectively and of (b) the single layers as a function of aerosol deposition time.*

The composition of the $TiO_2/SiO_2/ZnO$ network was further assessed by FTIR analysis (Figure 5.7b). This confirmed the integration of these three nanoparticle aerosols in a single structure. For the ZnO nanoparticles, a strong absorption band was observed at 505 cm^{-1} which is usually associated with oxygen deficiency and/or oxygen vacancy (V_O) defect complex in ZnO[37]. The broad absorption band at 3438 cm^{-1} is assigned to the O-H stretching vibration of hydroxyl groups and attributed to adsorption of moisture.[38] The FTIR spectra of the SiO_2 nanoparticles was characterized by a strong broad IR band at 1089 cm^{-1} with a shoulder at 1200 cm^{-1} that are attributed to the transverse-optical and longitudinal-optical modes of the Si-O-Si asymmetric stretching vibrations.[39-40] The smaller band at 956 cm^{-1} is indicative of silanol groups[41] and Si-O$^-$ stretching vibrations[41]. The band at 800 cm^{-1} is attributed to the Si-O-Si symmetric stretching vibrations, whereas the band at 474 cm^{-1} is assigned to the O-Si-O bending vibrations.[42] In the $TiO_2/SiO_2/ZnO$ network, many of these bands overlap with the Ti-O modes and cannot be clearly assigned to the SiO_2. However, the Si-O-Si asymmetric stretching vibrations are detectable also on the $TiO_2/SiO_2/ZnO$ structure as a broad band from 1000 to 1250 cm^{-1}. In the TiO_2 spectra, the absorption bands at 672, 739 and 960 cm^{-1} are attributed to the Ti-O stretching modes.[43] The FTIR spectra of the $TiO_2/SiO_2/ZnO$ network (Figure 5.7b) matches the contributions of the individual nanoparticles further confirming the successful integration of these nanomaterials in a single ultraporous structure.

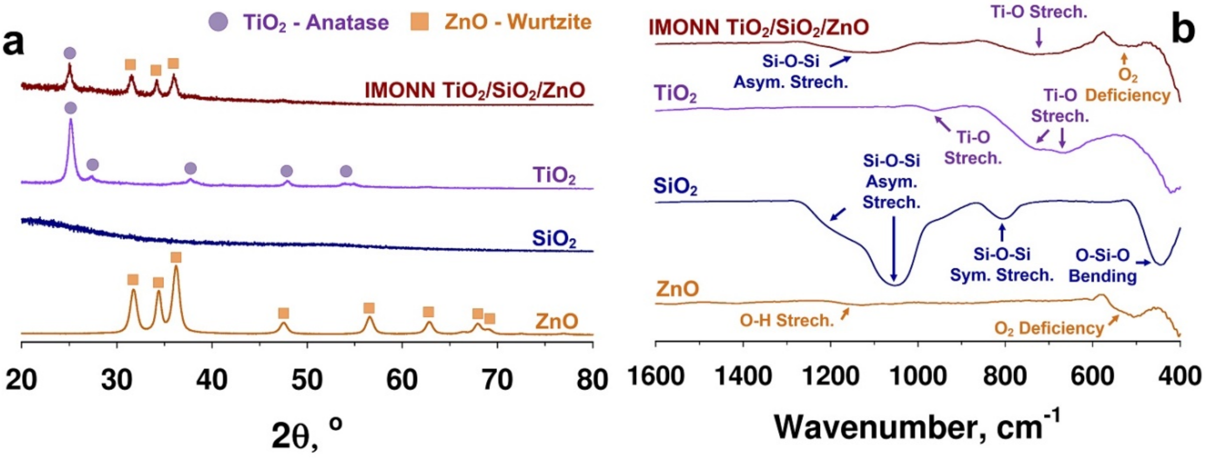

Figure 5.7. *(a) XRD and (c) FTIR spectra of the IMONN structure and of the individual ZnO, SiO_2 and TiO_2 nanoparticle constituents.*

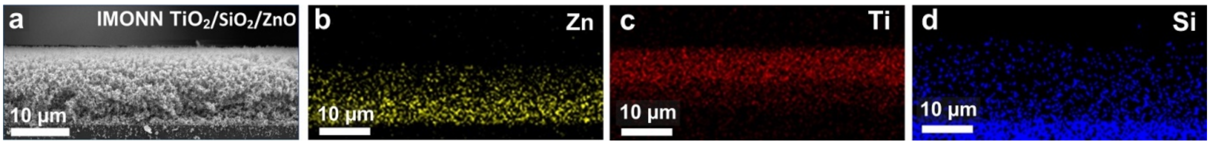

Figure 5.8. *(a) Cross-section SEM image of the IMONN structure reveals a uniform highly porous and crack-free morphology. EDX qualitative elemental mapping along the cross-section (d) of the IMONN reveals the location of the (e) Zn, (f) Ti and (g) Si atoms.*

The three-dimensional distribution of the ZnO, SiO_2 and TiO_2 nanoparticles in the network was investigated by cross-sectional SEM elemental mapping (Figure 5.8a-d). The vertical distribution of the Ti, Si and Zn atoms is in line with the sequence of aerosol deposition. The Zn is localized in the first 9.5 μm thickness (Figure 5.8b) while the Ti atoms (Figure 5.8c) are mostly relegated above 10 μm. In contrast, the Si atoms, strongly visible in the glass substrate, were randomly distributed within the ZnO layer (Figure 5.8d). This is in line with very rough top surface morphology[44] of these aerosol-deposited nanoparticle layers that can be easily penetrated and filled by deposition of a sequential nanoparticle aerosols. This cross-sectional composition is also in good agreement with the observed layer growth rates (Figure 5.6) and confirms the vertical stacking of the ZnO and TiO_2 nanoparticle layers.

5.3.2 Optical Properties

Figure 5.9 shows the optical transmittance spectra of single TiO_2 layers as a function of their film thickness (Figure 5.9a), and of a TiO_2/SiO_2/ZnO network upon sequential deposition of each nanoparticle aerosol (Figure 5.9b). All films were highly transparent to visible light. The optical transmittance spectra of the IMMON devices before and after subtraction of the fraction loss through the glass substrate and its optical image (inset) of the optical IMMON device with a 4.4 μm thick TiO_2 layer on glass substrates placed over a printed paper are presented in Figure 5.10. Notably, the film transmittance of TiO_2/SiO_2/ZnO structure with the thickest TiO_2 film of 6.6 μm is 91.6% at the wavelength of 500 nm. The single ZnO layer (Figure 5.9b) had a sharp drop in transmittance below 370 nm, in line with its direct bandgap of 3.37 eV[45]. This is quite close to the end of the visible spectrum (400 nm) and well within the UVA range (315-400 nm). This sharp absorption edge is not dependent from the thickness of the ZnO layer.[23] In stark contrast, the absorption edge and cut-off wavelength of the single TiO_2 layer was strongly dependent on its thickness. Notably, for the same thickness and a wavelength of 375 nm, the TiO_2 layer had significantly higher light transmittance than the ZnO layer (Figure 5.11a).

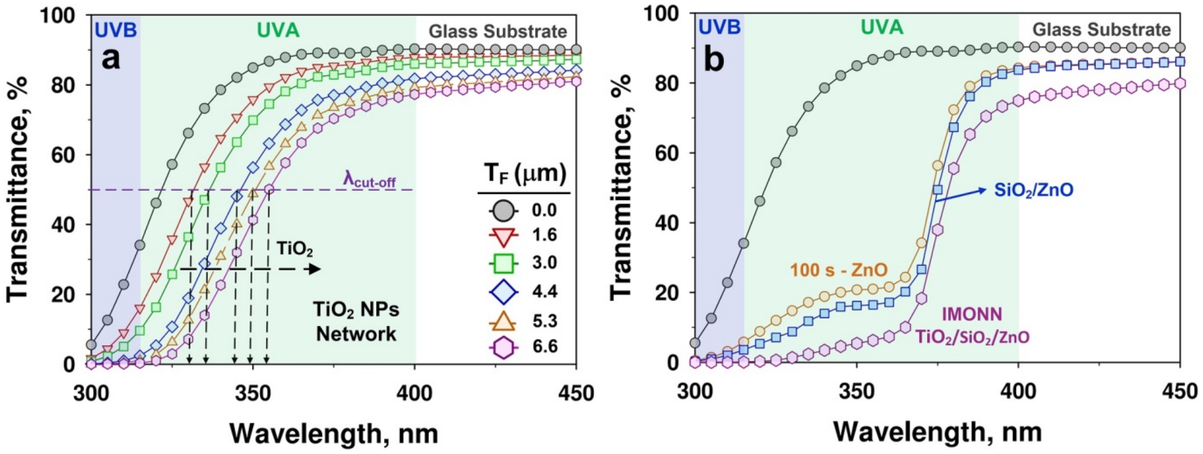

Figure 5.9. *Optical transmittance spectra of (a) a single ultraporous TiO_2 layers deposited on blank glass substrates (grey circles) with different film thickness. The arrow show the fine tuning of the cut-off wavelength by increasing the TiO_2 film thickness from 1.6 to 6.6 μm. (b) Comparison of the transmittance spectra of a pure ultraporous ZnO layer and of the IMONN structure upon each sequential step with a SiO_2 and TiO_2 film thickness of 0.12 and 6.6 μm, respectively.*

This is despite the anatase TiO_2 phase having a lower bandgap (3.2 eV) than the wurtzite ZnO phase (3.37 eV). The cut-off wavelength of the single TiO_2 nanoparticle layer increased from 325 to 350 nm (Figure 5.9a) with increasing TiO_2 layer thickness from ca. 1.6 μm to 6.6 μm. The blue-shift observed for the these ultraporous layers is attributed to the indirect band gap structure of anatase TiO_2[46-47]. This is in good agreement with previous studies[48] showing that the absorption edge of indirect bandgap semiconductors can be fine-tuned by adjusting the film porosity, and thus the effective refractive index and the film thickness. This is because the absorptivity of anatase TiO_2 increases with decreasing wavelength even for photons having energy above the TiO_2 bandgap and thus there is not a sharp transition. As a result, the effective transmittance is strongly dependent on the wavelength and film thickness.

In contrast, gross-tunning of the UV light absorption was achieved with the ZnO nanoparticle layer by changing its thicknesses. Hanini et al.[48] reported that annealing at 550

^{o}C for 20 min shifted the absorption edge of anatase TiO_2 from 3.42 to 3.04 eV and attributed it to an increase in film packing density and oxygen deficiency. Here, at the edge of the UVB spectrum (λ = 320 nm), the transmittance through the anatase TiO_2 layer decreased to less than 2% for a TiO_2 layer with 6.6 μm thickness, while 30% of UVA transmittance (λ = 340 nm) was preserved. As a result, these ultraporous TiO_2 layers can efficiently block UVB radiation while transmitting a significant fraction of UVA.

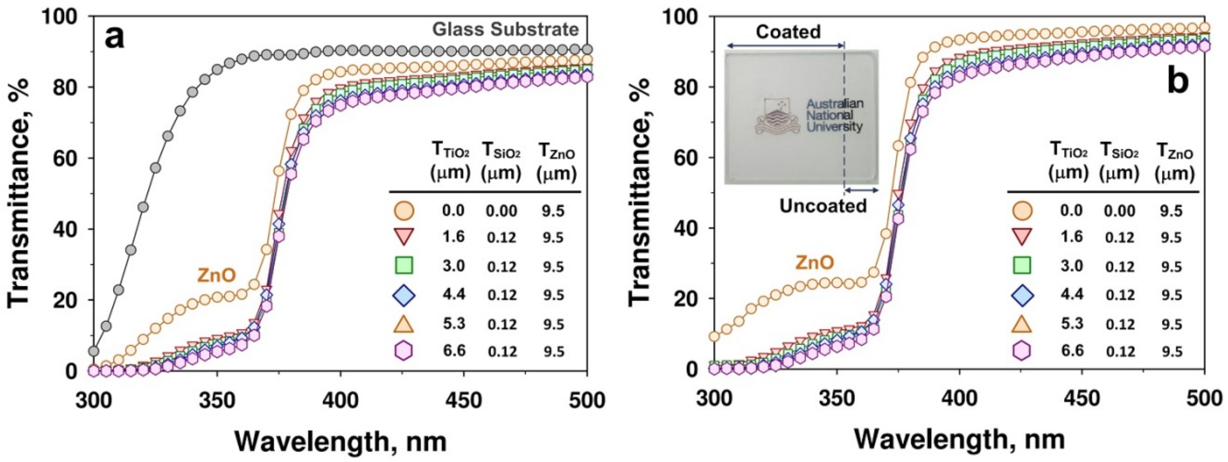

Figure 5.10. *Optical transmittance spectra of IMMON devices (a) before and (b) after subtraction of the fraction loss through the glass substrate and optical image (inset) of IMMON device with 4.4 mm thick* TiO_2 *layer (45 s) on a glass substrate placed over a printed paper.*

Figure 5.9b shows the evolution of the optical properties of the $TiO_2/SiO_2/ZnO$ network upon each aerosol deposition step. The spectrum of the ultraporous ZnO layer is in line with that recently reported[23] for single ZnO layer broad-band UV photodetectors. Upon deposition of the SiO_2 space layer, the spectrum of the resulting SiO_2/ZnO structure was undistinguishable from the ZnO. This is due to the high transparency of aerosol-deposited SiO_2 layer as previously discussed for their application as antifogging coatings[35]. In contrast, a TiO_2 film thickness of 1.6 μm drastically decreased the transmittance of UV light (Figure 5.11b). In the UVA (λ = 370 nm), the transmittance through the $TiO_2/SiO_2/ZnO$ network with a TiO_2 film thickness of 6.6 μm (Figure 5.9b) was ca. 20%, and decreased to only 0.1% in the UVB domain (λ = 310 nm). These results show that the optical properties of the

$TiO_2/SiO_2/ZnO$ network can be easily tuned by adjusting the thickness of the top TiO_2 layer. Most importantly, we demonstrate that, despite the closely located bandgap of ZnO (3.37 eV) and TiO_2 (3.2 eV), a tunable transmittance window (Figure 5.11b) can be engineered between the top TiO_2 filter and the bottom ZnO photoresistive layers.

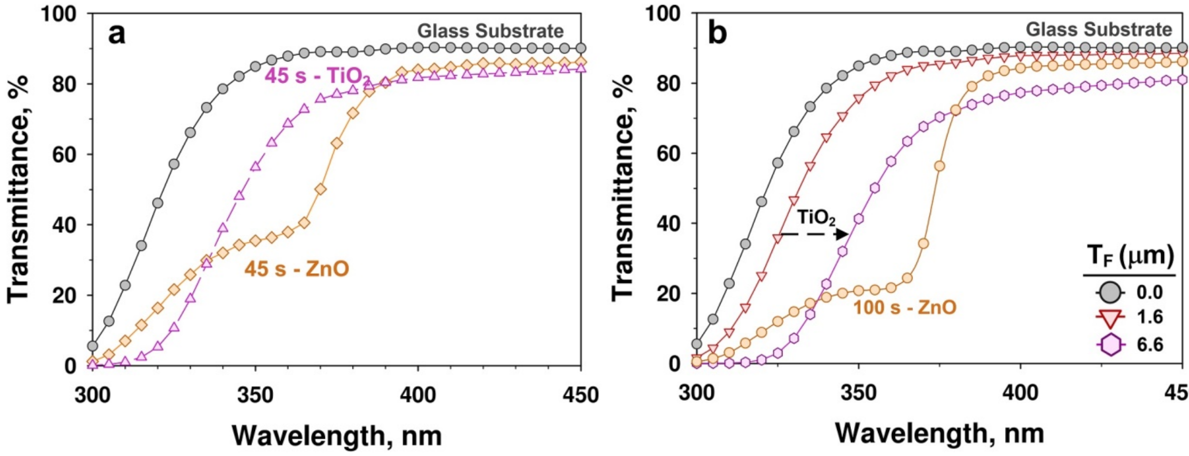

Figure 5.11. *Optical transmittance spectra of (a) ultraporous single ZnO and TiO_2 layers deposited on blank glass substrates (grey circles) after 45 s deposition time, and (b) ultraporous TiO_2 layers deposited on blank glass substrates (grey circles) as a function of the deposition time (15 and 75 s) and comparison with a ZnO film deposited with a deposition time of 100 s.*

5.3.3 Photodetection Properties

Figure 5.12a,b present the real and normalized photodetection performances of the $TiO_2/SiO_2/ZnO$ networks as a function of the TiO_2 layer thickness. Notably, deposition of a 1.6 μm thick layer of TiO_2 nanoparticles transformed the broad-band spectral response of the single ZnO layer (Figure 5.12b, circles) into a band-selective one (Figure 5.12b, down triangles). Increasing the TiO_2 film thickness from 1.6 to 6.6 μm narrowed the bandwidth of the spectral response while preserving the peak response at a wavelength of 370 nm. This spectral responsivity (Figure 5.12b) is ideally located in the UVA range. The bandwidth, defined as the full width at half maximum, of the photodetector response (Figure 5.13) decreased linearly from 85 nm of the pure ZnO layers to 29 nm of the $TiO_2/SiO_2/ZnO$ networks with 6.6 μm thick TiO_2 layer.

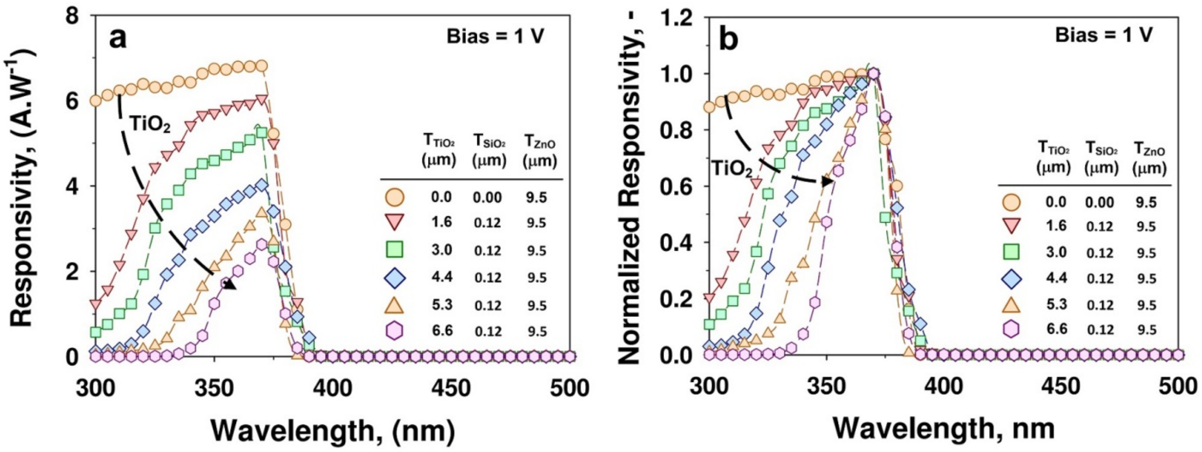

Figure 5.12. *(a) Real and (b) normalized responsivity spectra of the IMONN devices as a function of TiO_2 film thickness.*

Thicker TiO_2 layers are expected to lead to narrower bandwidth response with the lower limit being the amount of UV light reaching the bottom ZnO layer. As the $TiO_2/SiO_2/ZnO$ networks with a bandwidth of 29 nm have photo- to dark-current ratios in the order of millions, this architecture should easily reach bandwidth of a few nanometers. It is worth mentioning that in the absence of the SiO_2 layer (Figure 5.14), the TiO_2 layer contributes to the photo-response resulting in a broad-band detector. Notably, the photo-response of the TiO_2/ZnO was still lower than that of the pure ZnO below 350 nm.

However, it was significantly higher (e.g. 500% at 315 nm) than with the SiO_2 space layer. The drop in the photo-response of the TiO_2/ZnO layout is attributed to the lower conductivity of the TiO_2 layer than that of the pure ZnO. This results in lower photo-currents than for the single ZnO layer despite the photo-generation of electron/hole pairs in the TiO_2 layer. A major figure of merit of the $TiO_2/SiO_2/ZnO$ networks is that while the ultraporous TiO_2 layer efficiently blocks the UVB radiation reaching the underlying ZnO structure, it let a significant fraction of the UVA light through and did not affect the dark-current of the devices (ca. 18-22 pA).

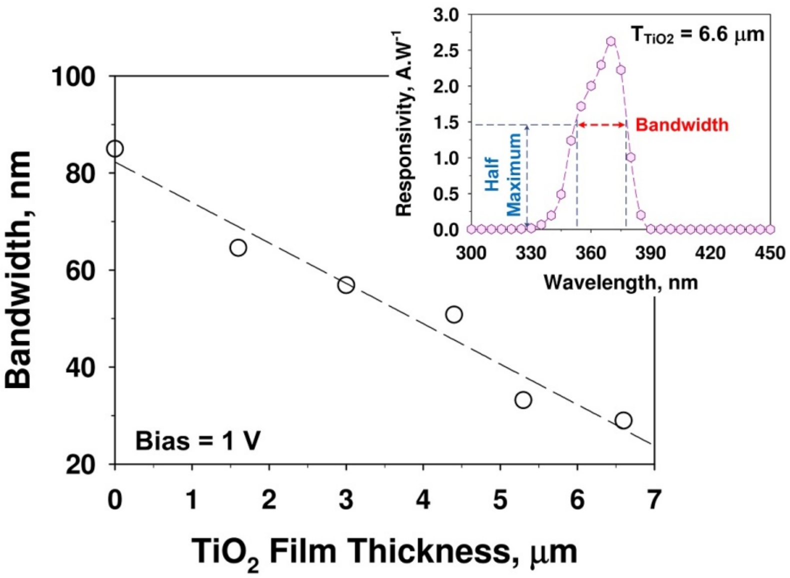

Figure 5.13. *Photoresponse bandwidth of the IMONN devices as a function of* TiO_2 *film thickness. (inset) Exemplary real responsivity spectra of a device with* TiO_2 *film thickness of 6.6* μ*m featuring a bandwidth of 29 nm.*

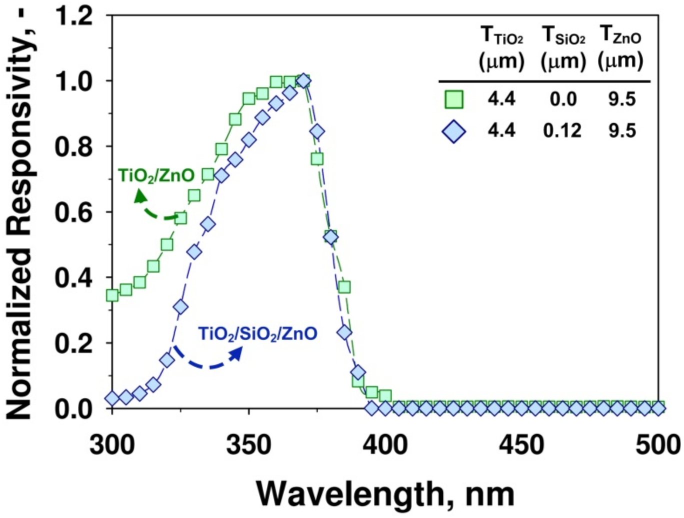

Figure 5.14. *Normalized responsivity spectra of a IMONN device with (squares) and without (diamonds) the* SiO_2 *space layer.*

For all devices, the *I-V* characteristics under dark and UV light (370 nm) reveal good ohmic contacts. Notably, the on/off photo- to dark-current ratios are in the order of several millions at a low light intensity of 86 μW.cm^{-2} and a bias of 1 V. This I_{UVA}/I_{dark} ratio (9.3×10^6) is ~ 465 times higher than the highest previously reported for similar light intensity and operation bias[23]. At a wavelength of 370 nm and a bias of 1V, the photocurrent decreased only from 205 μA to 79 μA with increasing TiO_2 film thickness from 1.6 to 6.6 μm (Figure 5.15). This corresponds to a relatively small change in photo- to dark-current ratio (Figure 5.16, circles) that, at a bias of 1 V and 40 μW.cm^{-2}, decreased linearly with increasing TiO_2 film thickness from 4.2×10^6 of the pure ZnO to 1.6×10^6 of the $TiO_2/SiO_2/ZnO$ networks with 6.6 μm thick TiO_2 layer. The latter photo- to dark-current ratio (1.6×10^6) is still ~180 times higher than the highest previously reported[23] (2×10^4) at the similar light intensity and bias. Notably, the UVA selectivity of these $TiO_2/SiO_2/ZnO$ networks against the edge (λ = 315 nm) of UVB (I_{UVA}/I_{UVB}) increased drastically from 0.82 to 58 with increasing TiO_2 film thickness from 1.6 to 6.6 μm (Figure 5.16), while the selectivity against the edge (λ = 400 nm) of the visible light spectrum (I_{UVA}/I_{vis}) decreased only from 92 to 59 (Figure 5.16, squares).

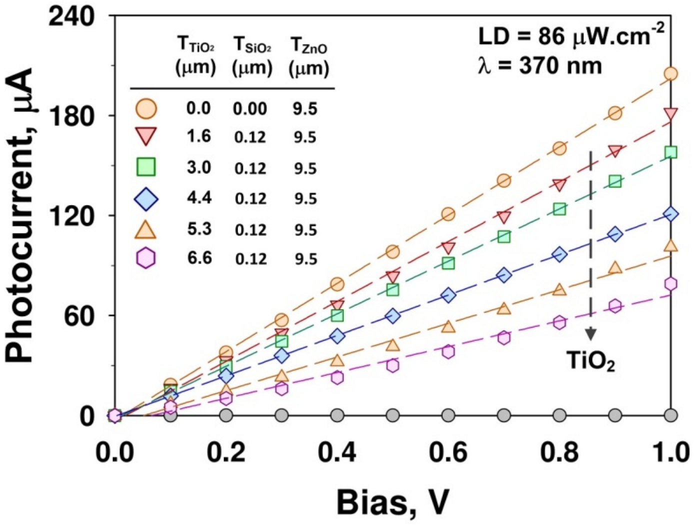

Figure 5.15. *I-V characteristics of the IMONN devices as a function of the TiO_2 film thickness at an illumination wavelength of 370 nm and light density (LD) of 86 μW.cm^{-2}.*

Figure 5.17 shows a comparison of the photodetector performance of a single ZnO layer (Figure 5.17a) and a $TiO_2/SiO_2/ZnO$ network with a 4.4 μm thick TiO_2 layer (Figure 5.17b). For both devices, the photocurrent increased linearly with increasing light density indicating no carrier mobility saturation and sweep-out effect up to the maximum light density investigated here. Notably, integration of an ultraporous TiO_2 layer with a thickness of ca. 4.4 μm increased the I_{UVA}/I_{UVB} selectivity by a factor of 20 (from ca. 0.82 to 16) while decreased the responsivity from 6.8 $A.W^{-1}$ of the single ZnO layer to 4.0 $A.W^{-1}$ of the $TiO_2/SiO_2/ZnO$ network. This resulted in an excellent performance with detection of low UVA light intensity of less than 10 $\mu W.cm^{-2}$ and a bandwidth of 51 nm.

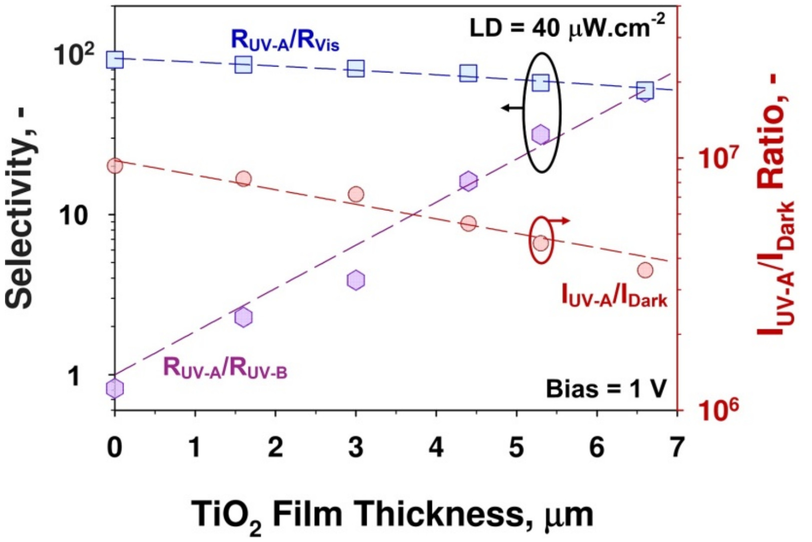

Figure 5.16. *Figure of merit of the IMMON devices as a function of the TiO_2 deposition time: photoresponse selectivity in terms of UVA to UVB (square) and visible light (hexagons) responsivity ratios and photo- to dark-current ratio (circles).*

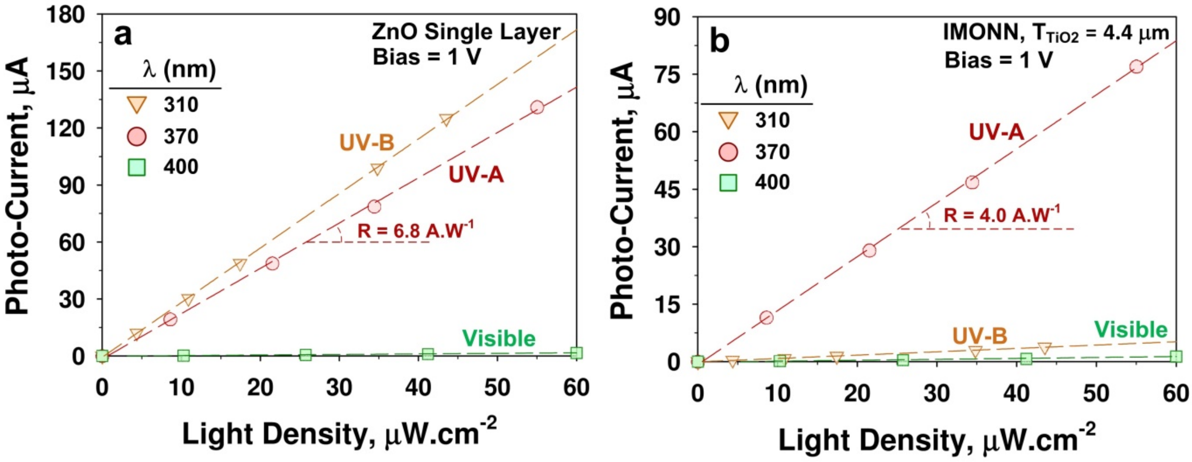

Figure 5.17. *Comparison of the photoresponse to the UVA, UVB and visible light of (a) a single layer ZnO and (b) an IMONN device 4.4 μm thick TiO_2 layer as a function of the light density. Notably, the IMONN shows excellent UVA selectivity while the single ZnO layer cannot distinguish between UVA and UVB.*

Current band-selective photodetector technologies are based on bulky assembly of Si-homojunctions and optical filters that have limited miniaturization potential and portability.[49-50] Amongst other, this design can enable the fabrication of portable dual UVA and UVB radiation monitors. While the UVA radiation can be directly obtained by a single or a series of band-selective $TiO_2/SiO_2/ZnO$ devices, the UVB component can be computed by measuring the whole UV spectrum with a broad-band ZnO devices and subtracting the UVA measured by a coupled IMONN device.

5.4. Conclusions

In conclusion, we have presented a novel solid-state architecture for high-performance tunable band-selective photodetectors. The device layout consists of an integrated ultraporous network of tailored nanoparticles with distinct functionalities, namely an electron-depleted photo-responsive nanoparticle layer, a dielectric spacer layer, and a tunable highly transparent filter layer. Notably, the spectral photo-response of the devices can be fine-tuned by the top filter layer. Rapid fabrication of band-selective UVA photodetectors with ultra-low dark currents of 22 pA, high photocurrents of 182 μA at low light intensities of 86 $\mu W.cm^{-2}$ and bias of 1V, were demonstrated. The bandwidth of these photodetectors was easily tuned from 85 to 29 nm. These band-selective devices featured the highest photo- to dark-current ratios so far reported at this light intensity with a I_{UVA}/I_{dark} of 8.2×10^6 for thinnest and 3.6×10^6 for the thickest TiO_2 layer, respectively. An outstanding UVA to UVB and to visible light selectivity in excess of 58 times was also achieved. This solid-state architecture can be implemented with other top - bottom layer compositions such as GaAs (1.4 eV) - Si (1.1 eV), and SnO_2 (3.7 eV) - ZnS (3.54 eV) enabling the fabrication of portable band-selective photodetectors for the UV, visible and infrared spectrums.

5.5. References

1. Kligman, L. H.; Akin, F. J.; Kligman, A. M., The Contributions of UVA and UVB to Connective Tissue Damage in Hairless Mice. *J. Investig. Dermatol.* **1985,** *84*, 272-276.

2. Sweeney, A.; Jiggins, C.; Johnsen, S., Insect Communication: Polarized Light as a Butterfly Mating Signal. *Nature* **2003,** *423*, 31-32.

3. Mäthger, L. M.; Shashar, N.; Hanlon, R. T., Do Cephalopods Communicate Using Polarized Light Reflections from Their Skin? *J. Exp. Biol.* **2009,** *212*, 2133-2140.

4. Liu, P. T.; Stenger, S.; Li, H.; Wenzel, L.; Tan, B. H.; Krutzik, S. R.; Ochoa, M. T.; Schauber, J.; Wu, K.; Meinken, C.; Kamen, D. L.; Wagner, M.; Bals, R.; Steinmeyer, A.; Zügel, U.; Gallo, R. L.; Eisenberg, D.; Hewison, M.; Hollis, B. W.; Adams, J. S.; Bloom, B. R.; Modlin, R. L., Toll-Like Receptor Triggering of a Vitamin D-Mediated Human Antimicrobial Response. *Science* **2006,** *311*, 1770-1773.

5. Smirnov, J. R. C.; Calvo, M. E.; Míguez, H., Selective UV Reflecting Mirrors Based on Nanoparticle Multilayers. *Adv. Funct. Mater.* **2013,** *23*, 2805-2811.

6. Taoye, W.; Tayirjan, T. I.; Jianfeng, C.; Sohrab, R., Transparent Nanostructured Coatings with UV-Shielding and Superhydrophobicity Properties. *Nanotechnology* **2011,** *22*, 265708.

7. Godar, D. E.; Lucas, A. D., Spectral Dependence of UV-Induced Immediate and Delayed Apoptosis: The Role of Membrane and DNA Damage. *Photochem. Photobiol.* **1995,** *62*, 108-113.

8. King, D. M.; Liang, X.; Carney, C. S.; Hakim, L. F.; Li, P.; Weimer, A. W., Atomic Layer Deposition of UV-Absorbing ZnO Films on SiO_2 and TiO_2 Nanoparticles Using a Fluidized Bed Reactor. *Adv. Funct. Mater.* **2008,** *18*, 607-615.

9. Parrish, J. A.; Jaenicke, K. F.; Anderson, R. R., Erythema and Melanogenesis Action Spectra of Normal Human Skin. *Photochem. Photobiol.* **1982,** *36*, 187-191.

10. Zhang, X.; Horibata, K.; Saijo, M.; Ishigami, C.; Ukai, A.; Kanno, S.; Tahara, H.; Neilan, E. G.; Honma, M.; Nohmi, T.; Yasui, A.; Tanaka, K., Mutations in UVSSA Cause UV-Sensitive Syndrome and Destabilize ERCC6 in Transcription-Coupled DNA Repair. *Nature Genet.* **2012,** *44*, 593-597.

11. Yoo, K.-C.; Yoon, C.-H.; Kwon, D.; Hyun, K.-H.; Woo, S. J.; Kim, R.-K.; Lim, E.-J.; Suh, Y.; Kim, M.-J.; Yoon, T. H.; Lee, S.-J., Titanium Dioxide Induces Apoptotic Cell Death through Reactive Oxygen Species-Mediated Fas Upregulation and Bax Activation. *Int. J. Nanomedicine* **2012,** *7*, 1203-1214.

12. Maddodi, N.; Jayanthy, A.; Setaluri, V., Shining Light on Skin Pigmentation: The Darker and the Brighter Side of Eeffects of UV Radiation†. *Photochem. Photobiol.* **2012,** *88*, 1075-1082.

13. Pfeifer, G. P.; Besaratinia, A., UV Wavelength-Dependent DNA Damage and Human Non-Melanoma and Melanoma Skin Cancer. *Photochem. Photobiol. Sci.* **2012,** *11*, 90-97.

14. Latonen, L.; Laiho, M., Cellular UV Damage Responses—Functions of Tumor Suppressor p53. *Biochim. Biophys. Acta* **2005,** *1755*, 71-89.

15. Mironava, T.; Hadjiargyrou, M.; Simon, M.; Rafailovich, M. H., The Effects of UV Emission from Compact Fluorescent Light Exposure on Human Dermal Fibroblasts and Keratinocytes In Vitro. *Photochem. Photobiol.* **2012,** *88*, 1497-1506.

16. Wu, S.; Han, J.; Vleugels, R. A.; Puett, R.; Laden, F.; Hunter, D. J.; Qureshi, A. A., Cumulative Ultraviolet Radiation Flux in Adulthood and Risk of Incident Skin Cancers in Women. *Br J. Cancer* **2014,** *110*, 1855-1861.

17. van der Veen, N.; de Bruijn, H. S.; Berg, R. J. W.; Star, W. M., Kinetics and Localisation of PpIX Fluorescence after Topical and Systemic ALA Application, Observed in Skin and Skin Tumours of UVB-Treated Mice. *Br. J. Cancer* **1996,** *73*, 925-930.

18. Sakurai, H.; Yasui, H.; Yamada, Y.; Nishimura, H.; Shigemoto, M., Detection of reactive oxygen species in the skin of live mice and rats exposed to UVA light: a research review on chemiluminescence and trials for UVA protection. *Photochem. Photobiol. Sci.* **2005,** *4*, 715-720.

19. Furusawa, Y.; Quintern, E. L.; Holtschmidt, H.; Koepke, P.; Saito, M., Determination of erythema-effective solar radiation in Japan and Germany with a spore monolayer film optimized for the detection of UVB and UVA – results of a field campaign. *Appl. Microbiol. Biotechnol.* **1998,** *50*, 597-603.

20. Monroy, E.; Omnès, F.; Calle, F., Wide-bandgap semiconductor ultraviolet photodetectors. *Semicond. Sci. Technol.* **2003,** *18*, R33.

21. Mubeen, S.; Hernandez-Sosa, G.; Moses, D.; Lee, J.; Moskovits, M., Plasmonic Photosensitization of a Wide Band Gap Semiconductor: Converting Plasmons to Charge Carriers. *Nano Lett.* **2011,** *11*, 5548-5552.

22. Tian, W.; Zhang, C.; Zhai, T.; Li, S.-L.; Wang, X.; Liu, J.; Jie, X.; Liu, D.; Liao, M.; Koide, Y.; Golberg, D.; Bando, Y., Flexible Ultraviolet Photodetectors with Broad Photoresponse Based on Branched ZnS-ZnO Heterostructure Nanofilms. *Adv. Mater.* **2014,** *26*, 3088-3093.

23. Nasiri, N.; Bo, R.; Wang, F.; Fu, L.; Tricoli, A., Ultraporous Electron-Depleted ZnO Nanoparticle Networks for Highly Sensitive Portable Visible-Blind UV Photodetectors. *Adv. Mater.* **2015,** *27*, 4336-4343.

24. Jin, Y.; Wang, J.; Sun, B.; Blakesley, J. C.; Greenham, N. C., Solution-Processed Ultraviolet Photodetectors Based on Colloidal ZnO Nanoparticles. *Nano Lett.* **2008,** *8*, 1649-1653.

25. Tian, W.; Zhai, T.; Zhang, C.; Li, S.-L.; Wang, X.; Liu, F.; Liu, D.; Cai, X.; Tsukagoshi, K.; Golberg, D.; Bando, Y., Low-Cost Fully Transparent Ultraviolet Photodetectors Based on Electrospun ZnO-SnO_2 Heterojunction Nanofibers. *Adv. Mater.* **2013,** *25*, 4625-4630.

26. Tricoli, A.; Graf, M.; Mayer, F.; Kuühne, S.; Hierlemann, A.; Pratsinis, S. E., Micropatterning Layers by Flame Aerosol Deposition-Annealing. *Adv. Mater.* **2008,** *20*, 3005-3010.

27. Kühne, S.; Graf, M.; Tricoli, A.; Mayer, F.; Pratsinis, S. E.; Hierlemann, A., Wafer-Level Flame-Spray-Pyrolysis Deposition of Gas-Sensitive Layers on Microsensors. *J. Micromech. Microeng.* **2008,** *18*, 035040.

28. Fang, Y.; Dong, Q.; Shao, Y.; Yuan, Y.; Huang, J., Highly Narrowband Perovskite Single-Crystal Photodetectors Enabled by Surface-Charge Recombination. *Nature Photon.* **2015,** *9*, 679-686.

29. Ren, P.; Hu, W.; Zhang, Q.; Zhu, X.; Zhuang, X.; Ma, L.; Fan, X.; Zhou, H.; Liao, L.; Duan, X.; Pan, A., Band-Selective Infrared Photodetectors with Complete-Composition-Range $InAs_xP_{1-x}$ Alloy Nanowires. *Adv. Mat.* **2014,** *26*, 7444-7449.

30. Tricoli, A.; Pratsinis, S. E., Dispersed Nanoelectrode Devices. *Nature Nanotechnol.* **2010,** *5*, 54-60.

31. Teoh, W. Y.; Mädler, L.; Beydoun, D.; Pratsinis, S. E.; Amal, R., Direct (one-step) Synthesis of TiO_2 and Pt/TiO_2 Nanoparticles for Photocatalytic Mineralisation of Sucrose. *Chem. Eng. Sci.* **2005,** *60*, 5852-5861.

32. Tricoli, A.; Wallerand, A. S.; Righettoni, M., Highly Porous TiO_2 Films for Dye Sensitized Solar Cells. *J. Mater. Chem.* **2012,** *22*, 14254.

33. Nasiri, N.; Elmoe, T. D.; Liu, Y.; Qin, Q. H.; Tricoli, A., Self-assembly dynamics and accumulation mechanisms of ultra-fine nanoparticles. *Nanoscale* **2015,** *7*, 9859-9867.

34. Nasiri, N.; Ceramidas, A.; Mukherjee, S.; Panneerselvan, A.; Nisbet, D. R.; Tricoli, A., Ultra-Porous Nanoparticle Networks: A Biomimetic Coating Morphology for Enhanced Cellular Response and Infiltration. *Sci. Rep.* **2016,** *6*, 24305.

35. Tricoli., A.; Righettoni., M.; Pratsinis., S. E., Anti-Fogging Nanofibrous SiO_2 and Nanostructured $SiO_2{-}TiO_2$ Films Made by Rapid Flame Deposition and in Situ Annealing. *Langmuir* **2009,** *25*, 12578-12584.

36. Ernst, F. O.; Tricoli, A.; Pratsinis, S. E.; Steinfeld, A., Co-Synthesis of H_2 and ZnO by in-Situ Zn Aerosol Formation and Hydrolysis. *AIChE J.* **2006,** *52*, 3297-3303.

37. Xiong, G.; Pal, U.; Serrano, J. G.; Ucer, K. B.; Williams, R. T., Photoluminesence and FTIR Study of ZnO Nanoparticles: The Impurity and Defect Perspective. *Phys. Stat. Sol. C* **2006,** *3*, 3577-3581.

38. Muthukumaran, S.; Gopalakrishnan, R., Structural, FTIR and Photoluminescence Studies of Cu Doped ZnO Nanopowders by Co-Precipitation Method. *Opt. Mater.* **2012,** *34*, 1946-1953.

39. Kalem, S.; Werner, P.; Ö, A.; Talalaev, V.; Nilsson, B.; Hagberg, M.; Frederiksen, H.; Södervall, U., Black Silicon with High Density and High Aspect Ratio Nanowhiskers. *Nanotechnology* **2011,** *22*, 235307.

40. Zhang, M.; Wu, Y.; Feng, X.; He, X.; Chen, L.; Zhang, Y., Fabrication of Mesoporous Silica-Coated CNTs and Application in Size-Selective Protein Separation. *J. Mater. Chem.* **2010,** *20*, 5835-5842.

41. Musi , S.; Filipovi -Vincekovi , N.; Sekovani , L., Precipitation of Amorphous SiO_2 Particles and Their Properties. *Braz. J. Chem. Eng.* **2011,** *28*, 89-94.

42. Mascagni, D. B. T.; Souza, M. E. P.; Freire, C. M. A.; Silva, S. L.; Rangel, R. C. C.; Cruz, N. C.; Rangel, E. C., Corrosion Resistance of 2024 Aluminum Alloy Coated with Plasma Deposited a-C:H:Si:O Films. *J. Mater. Res.* **2014,** *17*, 1449-1465.

43. Yunxia, J.; Guanghai, L.; Yong, Z.; Yunxia, Z.; Lide, Z., Photoluminescence of Anatase TiO_2 Thin Films Achieved by the Addition of $ZnFe_2O_4$. *J. Phys. Condens. Matter.* **2001,** *13*, L913.

44. Castillo, J. L.; Martin, S.; Rodriguez-Perez, D.; Perea, A.; Garcia-Ybarra, P. L., Morphology and Nanostructure of Granular Materials Built from Nanoparticles. *KONA Powder Part. J.* **2014,** *31*, 214-233.

45. Zhang, Y.; Wen, Y.-H.; Zheng, J.-C.; Zhu, Z.-Z., Direct to Indirect Band Gap Transition in Ultrathin ZnO Nanowires under Uniaxial Compression. *Appl. Phys. Lett.* **2009,** *94*, 113114.

46. Reyes-Coronado, D.; Rodríguez-Gattorno, G.; Espinosa-Pesqueira, M. E.; Cab, C.; Coss, R.; Oskam, G., Phase-Pure TiO_2 Nanoparticles: Anatase, Brookite and Rutile. *Nanotechnology* **2008,** *19*, 145605.

47. Yin, W.-J.; Chen, S.; Yang, J.-H.; Gong, X.-G.; Yan, Y.; Wei, S.-H., Effective band gap narrowing of anatase TiO_2 by strain along a soft crystal direction. *Appl. Phys. Lett.* **2010,** *96*, 221901.

48. Hanini, F.; Bouabellou, A.; Bouachiba, Y.; Kermiche, F.; Taabouche, A.; Hemissi, M.; Lakhdari, D., Structural, Optical and Electrical Properties of TiO_2 Thin Films Synthesized by Sol-Gel Technique. *IOSR J. Eng.* **2013,** *3*, 21-28.

49. Khadijeh, B.; Yuriy, V.; Andrei, S.; Mahdi, F.-B., Design, fabrication and characterization of an a-Si:H-based UV detector for sunburn applications. *Semicond. Sci. Technol.* **2006,** *21*, 1699.

50. Vigil, E.; Peter, L. M.; Forcade, F.; Jennings, J. R.; González, B.; Wang, H.; Curbelo, L.; Dunn, H., An ultraviolet selective photodetector based on a nanocrystalline TiO_2 photoelectrochemical cell. *Sens. Actuators A Phys.* **2011,** *171*, 87-92.

Chapter Six

Nanoarchitectonics of Three-Dimensional Heterojunctions for Fast-Responsive Visible-Blind UV Photodetectors

Publication relevant to this chapter:

Noushin Nasiri, Renheng Bo, Lan Fu, Antonio Tricoli, “*Three-dimensional nano-heterojunction networks: a highly performing structure for fast visible-blind UV photodetectors*”, **Nanoscale**, 9, 2059-2067, **2017**.

Abstract

Visible-blind ultraviolet photodetectors are a promising emerging technology for the development of a new class of optoelectronic devices with greatly reduced power consumption and size requirements. A standing challenge is to drastically improve the sluggish response time of these nanostructured devices. Here, we present a three-dimensional nanoscale heterojunction architecture for fast-responsive visible-blind UV photodetectors. The device layout consists of p-type NiO clusters densely packed on the surface of an ultraporous network of electron-depleted n-type ZnO nanoparticles. This 3D structure can detect very low UV light densities while operating with a near-zero power consumption of ca. 4×10^{-11} watts and a low bias of 0.2 mV. Most notably, heterojunction formation decreases the device rise and decay times by 26 and 20 times, respectively. These drastic enhancements in photoresponse dynamics are attributed to the stronger surface band bending and improved electron-hole separation of the nanoscale NiO/ZnO interface. These findings demonstrate a superior structural design and a simple, low-cost CMOS-compatible process for the engineering of high-performance wearable and integrated optoelectronic devices.

6.1 Introduction

Wide bandgap semiconductors, such as SiC, GaN, TiO_2 and ZnO have attracted considerable attention for their potential applications in nanoscale electronic and optoelectronic devices.[1-5] Among these materials, ZnO is a promising candidate for visible-blind UV photodetection due to its large and direct band gap (ca. 3.4 eV),[6-9] low-cost and ease of manufacturing. These excellent features enable efficient detection of UV light and a high selectivity against the visible spectrum (R_{UV}/R_{vis}).[6-7,10-12] An additional key requirement for many applications including biological and chemical analysis, missile detection, optical communication, and radiation monitoring are fast photoresponse dynamics.[7,13] Despite progress, the response dynamics of wide bandgap semiconductors such as ZnO is usually in the range of 30-200 s,[6-7,14-16] due to adsorption and desorption of O_2 trapping states.[17] To overcome this bottleneck, many studies have focused on the nanoarchitectonics of the ZnO morphology with efficient designs including nanowires,[18-19] nanorods,[1,20] nanodisks[21-22] and nanoparticles[6-7,23]. In particular, optimized Scotty contacts have led to faster photoresponse dynamics[1,24-25] but typically require high operation bias of up to 20 V to obtain sufficient responsivity.[26-27]

Several p-type semiconductors, such as GaN,[17,28] NiO,[29-30] Si[31-32] and Ge[33] have been explored as nanocomposite materials to enhance the response dynamics of n-type ZnO photodetectors. Among them, NiO, a p-type semiconductor with a room temperature bandgap of 3.6 eV, has attracted attention due to its transparency in the visible and UVA spectrum.[34-35] In addition, NiO presents a low lattice mismatch with ZnO (9%) and forms a type-II alignment with the ZnO n-type band structure.[36] Recently, Retamal et al.[15] coated the surface of ZnO nanowires with monocrystalline NiO nanoparticles increasing the photo- to dark-current ratios from ca. 16 of the pure ZnO nanowires to 3.7×10^4 of the NiO/ZnO at a bias of 10 V and light density of 314 μW.cm^{-2}. In addition, the decay time was decreased from 657 s of the pure ZnO to 133 s of the NiO-coated ZnO nanowires.[15] Despite these progresses, the photoresponse time of these visible-blind photodetectors is still too slow for many real-world uses.[15]

Here, we present a highly performing nanoscale architecture for the engineering of fast-responding wide bandgap UV photodetectors. Decoration of a 98% porous film of n-type ZnO nanoparticles with p-type NiO clusters resulted in a three-dimensional network of nanoscale heterojunctions (3DNH). The built-in electric fields between the nanoscale p- and n-type domains enable the rapid separation of the photogenerated electron-hole pairs decreasing the photo-current rise and decay times by 26- and 20 folds, respectively. This 3DNH design also features excellent responsivities of more than 12 $A.W^{-1}$, photo to dark ratios exceeding 10^7 and ultra-high directivities of up to 3×10^{12} Jones at a bias of 1 V and light density of 80 $\mu W.cm^{-2}$.

6.2 Experimental

6.2.1 Nanoparticles Deposition

A flame spray pyrolysis (FSP) system was used for the synthesis and direct deposition of ZnO nanoparticle aerosols onto the glass substrates fabricated with a set of interdigitated electrodes. The photodetector nanoparticles were prepared as follows: Zinc Naphthenate (10% Zn, Sigma Aldrich) was diluted in Xylene (Sigma Aldrich) with a total metal atom concentration of 0.3 $mol.L^{-1}$ for Zn. The prepared solution was supplied at a rate of 5 $mL.min^{-1}$ through a syringe pump, and dispersed into a fine spray with 7 $L.min^{-1}$ oxygen at a constant pressure drop of 2 bars. The spray was ignited by supporting premixed methane/oxygen flames (CH_4 = 1.2 $L.min^{-1}$, O_2 = 2 $L.min^{-1}$). A water-cooled substrate holder placed at 20 cm height above the burner (HAB) was utilized to keep the substrate temperature below 150 °C. The photodetector substrates were made of glass with interdigitated platinum lines with 5μm width and spacing and a total electrode area of 7×5 mm (G-IDEAU5, DropSens, Oviedo, Spain). More details about the device design and geometry were reported in previous work.[7] All substrates were cleaned with multiple ethanol/drying cycles and pre-annealed (Brother High Temperature Furnace XD-1.2KN) at 300 °C for 12 h, at ambient pressure prior photo-detecting tests before nanoparticles deposition.

6.2.2 Materials Characterization

The morphology and patterning characteristics of the deposited particles and films were investigated by a Hitachi H7100FA transmission electron microscope (TEM) at 100 kV and an analytical scanning electron microscopy (SEM), using Zeiss Ultraplus (FESEM) at 3 kV. Nickel oxide films were deposited by an AJA ATC 2400 magnetron sputtering system using a Ni target in an Ar/O_2 ambient (18/2 sccm). The chamber was evacuated to a base pressure of 9×10^{-7} Torr before deposition. Sputtering deposition was performed at a gas pressure of 4×10^{-3} Torr for 5, 25 and 40 seconds at room temperature with a power of 200 W. The prepared films were annealed in a furnace (Brother High Temperature Furnace XD-1.2KN) at 300 °C for 12 h, at ambient pressure prior photo-detecting tests, to stabilize the nanoparticle size and avoid resistive-sintering during the photo-detection measurements.

6.2.3 Photodetection Analysis

The optical properties of the ultraporous ZnO films were measured with a Perkin-Elmer (Lambda 1050 UV/Vis/NIR) Spectrophotometer and a 150 mm integrating sphere. All optical measurements were carried out at room temperature. For I-V measurements, DC currents were measured using a Picoammeter / Voltage source (Model 6487, Keithley), under the excitation of UV light from a Newport Xenon lamp source 66920.

6.3 Results and Discussion

6.3.1 Nanostructured Heterojunction Fabrication

Figure 6.1 shows a schematic of the 3DNH fabrication by rapid two-step gas-phase synthesis. First, a ZnO nanoparticle network is rapidly self-assembled on interdigitated electrodes by nanoparticle aerosol deposition (Figure 6.1a) as recently reported.[6-7,37]

This results in a very homogenous surface (Figure 6.2a) characterized by micro-sized pores between thin bridges of ultra-fine ZnO nanoparticles (Figure 6.2b). These nanoparticle networks have a film thickness of ca. 9 μm and an average porosity of 98%. Transmission electron microscopy (TEM) analysis of the ZnO particles collected from the substrates shows (Figure 6.2c) a spherical shape and a visible (d_{TEM}) average particle diameter of ca. 18 nm. Decoration of the ZnO surface with NiO clusters was achieved by magnetron sputtering using a Ni target in an Ar/O_2 ambient (18/2 sccm) at a flat-substrate deposition rate of 11 nm.min^{-1} (Figure 6.1b).

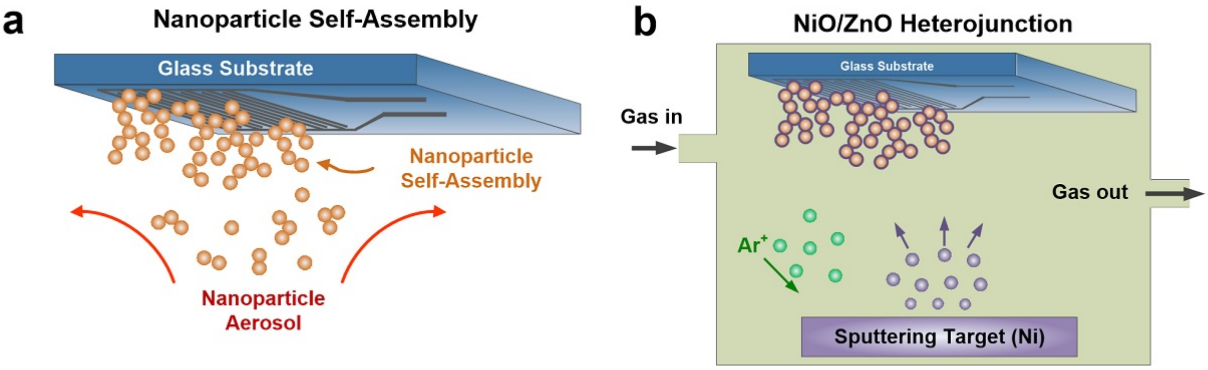

Figure 6.1. *(a) An ultraporous ZnO nanoparticle networks is self-assembled on glass substrate with interdigitated Pt electrodes by nanoparticle aerosol deposition. (b) Physical sputtering deposition of the NiO clusters on the ZnO nanoparticle networks.*

The resulting NiO/ZnO network is also uniform and ultraporous with no detectable changes in the micro-scale morphology (Figure 6.2d-e). However, TEM analysis (Figure 6.2f) revealed that upon sputtering, the ZnO nanoparticles are surrounded by a thin layer of nanoscale clusters 2 - 5 nm in diameter. In order to decrease the grain boundary barriers to electron conduction, these ultraporous NiO/ZnO networks were post-sintered at 300 ºC for 12 h with no assessable impact on the film morphology and crystallinity.[6-7]

Figure 6.3a shows the optical transmittance spectra of ZnO nanoparticles deposited on blank glass substrates as a function of NiO deposition time. Both the pure ZnO and the NiO/ZnO films were highly transparent to visible light with a relatively sharp cut-off below 370 nm. This is conveniently close to the end of the visible spectrum (400 nm) and well within the UV-A range (400 - 315 nm).

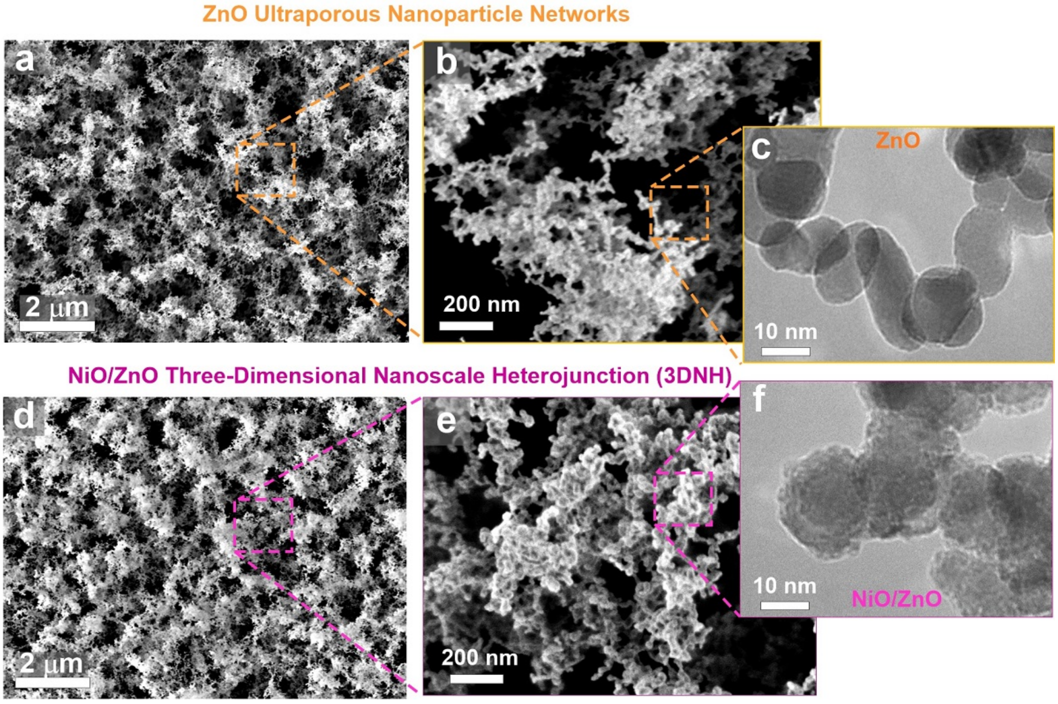

Figure 6.2. *(a,b) SEM images of an exemplary ZnO nanoparticle networks deposited for 100 s and composed of (c) ZnO nanoparticles with average particle diameter of 18 nm. (e) Physical sputtering deposition of the NiO clusters on the ZnO nanoparticle networks. (d,e) SEM images of the resulting NiO/ZnO morphology with 40 s NiO sputtering time. (f) TEM images of the NiO/ZnO grains removed from the films.*

6.3.2 Optical Properties

The optical transmittance spectra of the devices before and after subtraction of the fraction loss through the glass substrate are presented in Figure 6.3. The UV light transmittance, at a wavelength of 340 nm, (Figure 6.3) slightly decreased from 17% of the pure ZnO to 15% upon 40 s NiO sputtering time (equivalent to ca. 7.3 nm NiO bulk thickness). Similarly, the reflectance (Figure 6.4) of these ultraporous films at a wavelength of 400 nm increased from 14.3% of the pure ZnO to 16.6% upon 40 s NiO sputtering. This is attributed to grain growth, observed by TEM, upon NiO sputtering (Figure 6.2c,f), which is expected to increase light back-scattering[38].

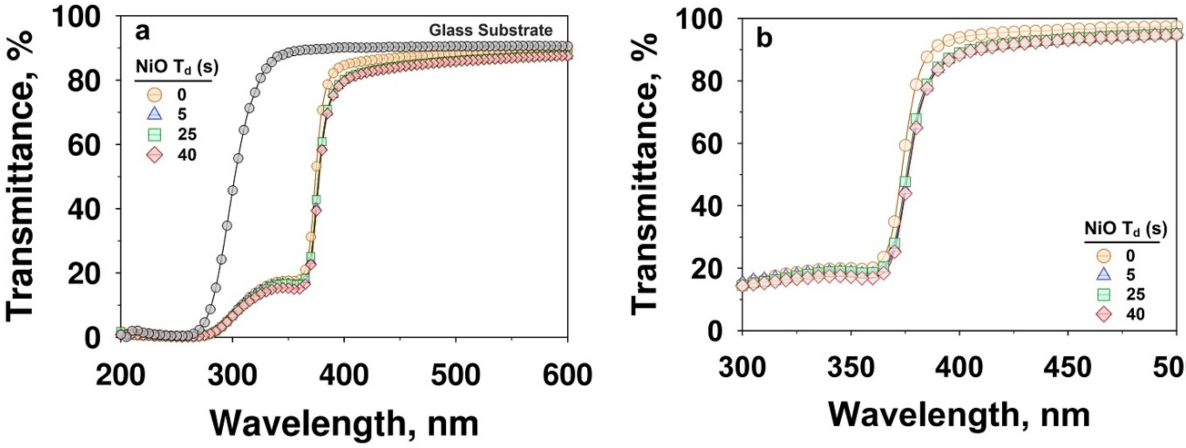

Figure 6.3. *Optical transmittance spectra of pure ZnO (orange circles) and NiO/ZnO networks deposited on blank glass substrates (grey circles) with different sputtering times of 5 s (blue triangles), 25 s (green rectangles) and 40 s (red diamonds) (a) before and (b) after subtraction of the fraction loss through the glass substrate.*

The three-dimensional distribution of the ZnO nanoparticles and NiO clusters in the ultraporous network was investigated by cross-sectional SEM elemental mapping (Figure 6.5a-d). Intensity line profiles extracted from the film cross-section show the normalized Zn, Ni and O element distributions (Figure 6.5e,f). It confirms that the self-assembled ZnO nanoparticle networks are porous enough for the Ni atoms to penetrate deep into the film and reach down to its bottom section. However, the Ni concentration is not uniform and it decreases approaching the substrate surface. The increase in oxygen atom signal toward the bottom of the film is attributed to the contribution from the glass substrate's oxygen atoms.

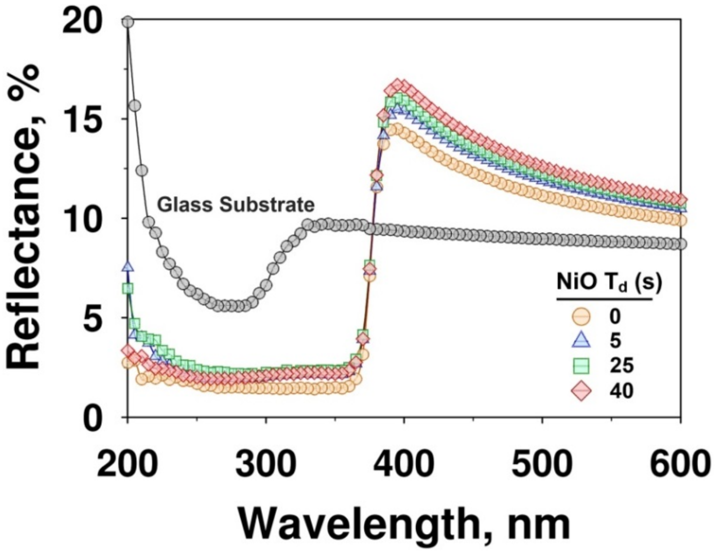

Figure 6.4. *Optical transmittance of the devices after subtraction of the fraction loss through the glass substrate.*

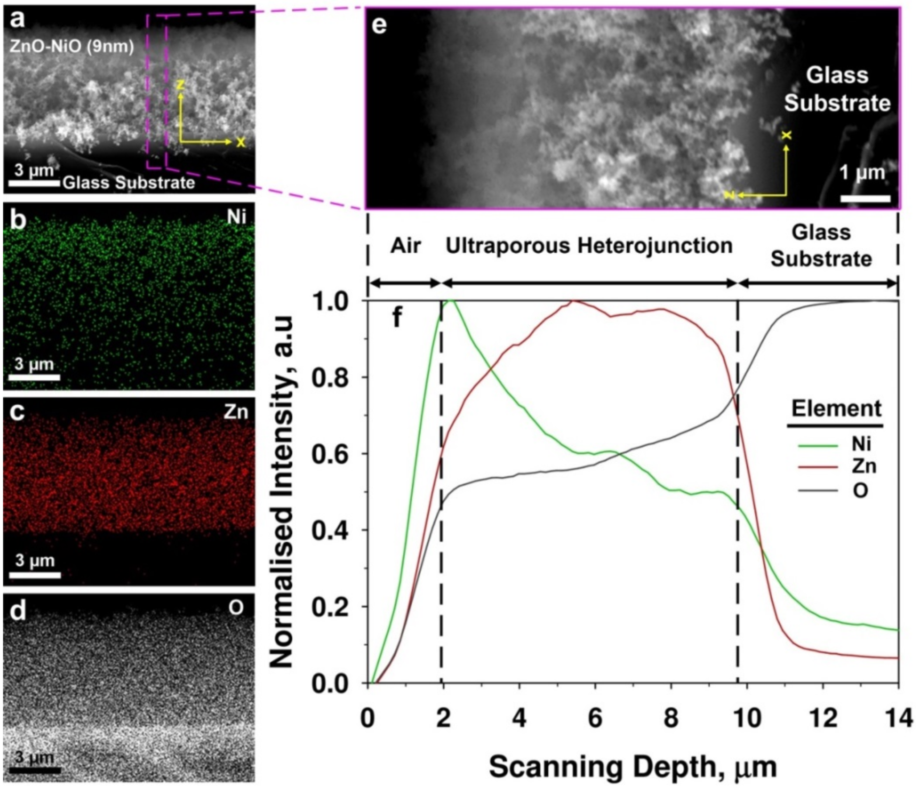

Figure 6.5. *(a) Cross-section SEM image of an exemplary NiO/ZnO networks with 40 s NiO sputtering time. EDX qualitative elemental mapping along the cross-section for (b) Ni, (c) Zn and (d) O atoms. (e) The film cross-section and (f) the extracted intensity line profiles showing the normalized Zn, Ni and O element distributions.*

6.3.3 Photodetection Properties

Figure 6.6 shows the spectral responsivity of the photodetectors as a function of the illumination wavelength for different NiO sputtering time at the applied bias of 1 V. All ultraporous photodetectors had negligible response to visible light down to a wavelength of 400 nm. By definition, responsivity is the ratio of photo-current obtained by a device per unit area to the incident light power at a given wavelength. The visible-light responsivity for all photodetector devices was very low in the order of 0.01 A.W^{-1} at 400 nm (Figure 6.6).

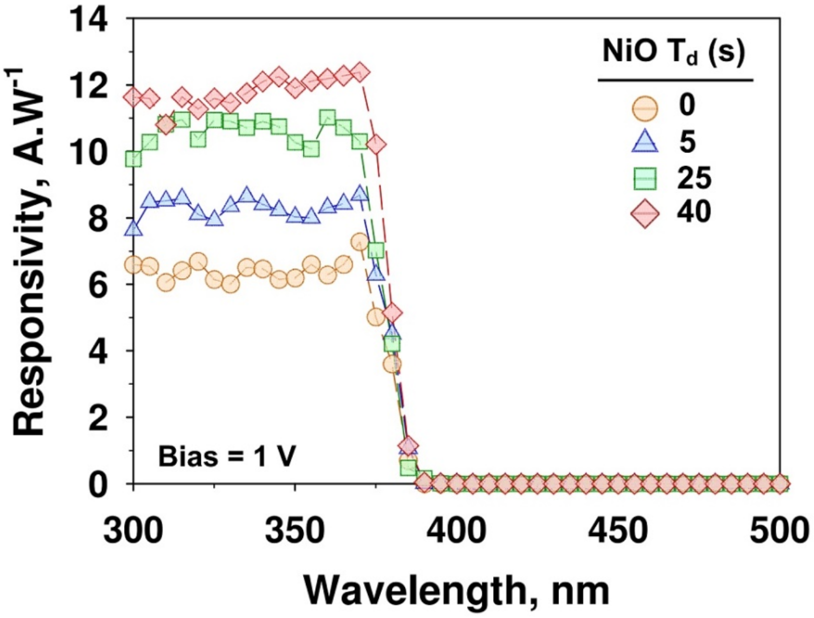

Figure 6.6. *Spectral responsivity of the pure ZnO and NiO/ZnO networks as a function of the NiO sputtering time, illumination wavelengths and applied bias.*

This corresponds to a photo-current of 360 nA. Notably, decreasing the wavelength below 400 nm, and thus entering the UV domain, sharply increased the responsivity of all devices, which reached their peak value at about 370 nm. The sharp cut-off at a wavelength of 370 nm is in good-agreement with the ZnO band gap of ca. 3.4 eV (λ = 370 nm) which is smaller than that of NiO (3.6 eV). This suggests that rise in photo-current is mostly due to photogeneration of electron-holes in the ZnO domain.[6-7] A maximal responsivity of ca. 13 A.W^{-1} was achieved with a 40 s NiO sputtering time (Figure 6.6). This responsivity (13 A.W^{-1}) is nearly twice as high as that of the pure ZnO devices (7.3 A.W^{-1}), and quite high with respect to that of other highly performing nanoparticle films (0.5 to 7 A.W^{-1})[6,13].

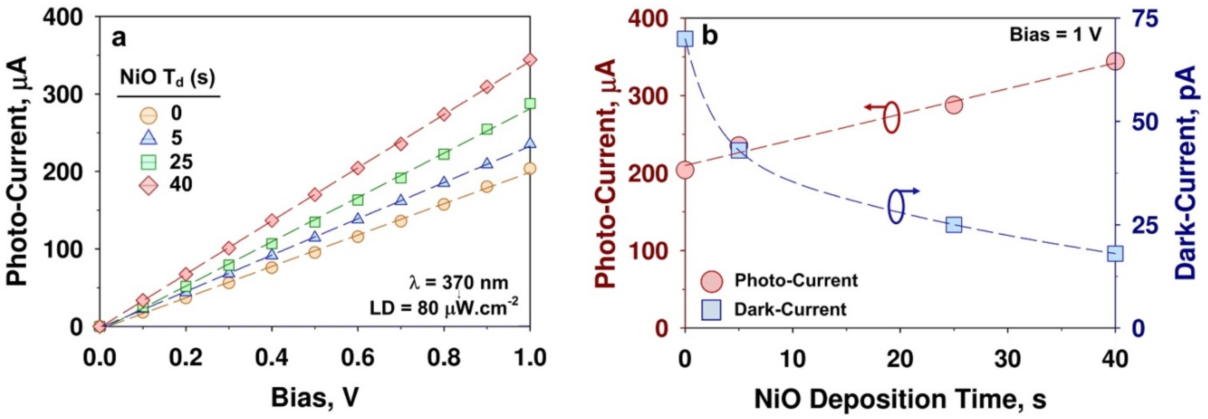

Figure 6.7. *(a) I-V characteristics of the pure ZnO and NiO/ZnO networks as a function of the NiO sputtering time, illumination wavelengths and applied bias. (c) Photo-currents at λ = 370 nm and dark-currents of the devices as a function of the NiO sputtering time.*

Figure 6.7a illustrates the *I-V* photoresponse of the pure ZnO and NiO/ZnO networks as a function of applied bias from 0 to 1 V at wavelength of 370 nm and a light density of 80 µW.cm^{-2}. For all samples, the *I-V* response was linear (Figure 6.7a) indicating an ohmic behaviour with sufficient availability of charge carriers. Notably, the photo-currents of the NiO/ZnO devices were significantly higher than those of the pure ZnO ones. Already after the shortest NiO sputtering time of 5 s, the photo-current increased slightly from 203 µA of the pure ZnO to 235 µA of the NiO/ZnO 3DNH. The devices with longest NiO sputtering time (40 s) exhibited the highest photo-currents of 345 µA (at 1 V), which is 70% higher than that of the pure ZnO (Figure 6.7a). Notably, in addition to increasing the photo-currents the NiO/ZnO 3DNH also decreased the dark-currents (Figure 6.7b).

In addition to the photodetectors responsivity, the specific detectivity (D) is a key figure-of-merit to describe the smallest detectable light density by a photodetector. This can be calculated accordingly to:

$$D = \frac{\sqrt{AB}}{NEP} \qquad (6.1)$$

where A is the effective area of the detector, B is bandwidth and NEP is the noise equivalent power. If the dark-current is the major contribution to the noise limiting the detectivity, this equation can be simplified to:[39]

$$D = \frac{R}{\left(2e \cdot \frac{I_{dark}}{A}\right)^{1/2}} \tag{6.2}$$

where R is the responsivity, e is the electron charge and I_{dark} is the device dark-current. Figure 6.8 shows the detectivity of the ZnO photodetectors before and after NiO sputtering and their corresponding responsivity at a bias of 1 V.

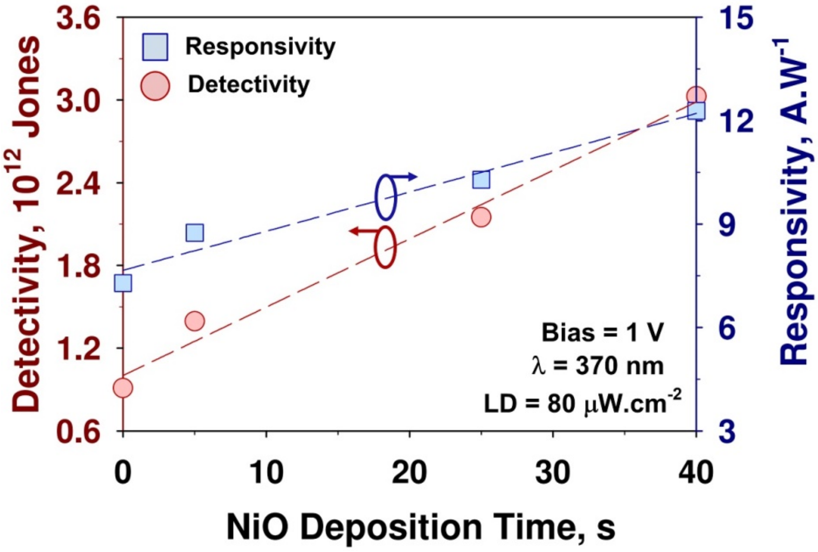

Figure 6.8. *The detectivity and responsivity of the fabricated devices as a function of the NiO sputtering time.*

The detectivity value increased from 0.9 $\times 10^{12}$ Jones of the pure ZnO to 1.4×10^{12} Jones of the NiO/ZnO 3DNH with 5 s NiO deposition time, and reached 3.0×10^{12} Jones with 40 s NiO deposition time (Figure 6.8). Notably, a detectivity as high as 3 trillion Jones obtained from this NiO/ZnO 3DNH architecture has not been reported for photodetectors made of one- and two-dimensional nanostructures, due to the challenge in achieving simultaneously high responsivity and low dark-currents.

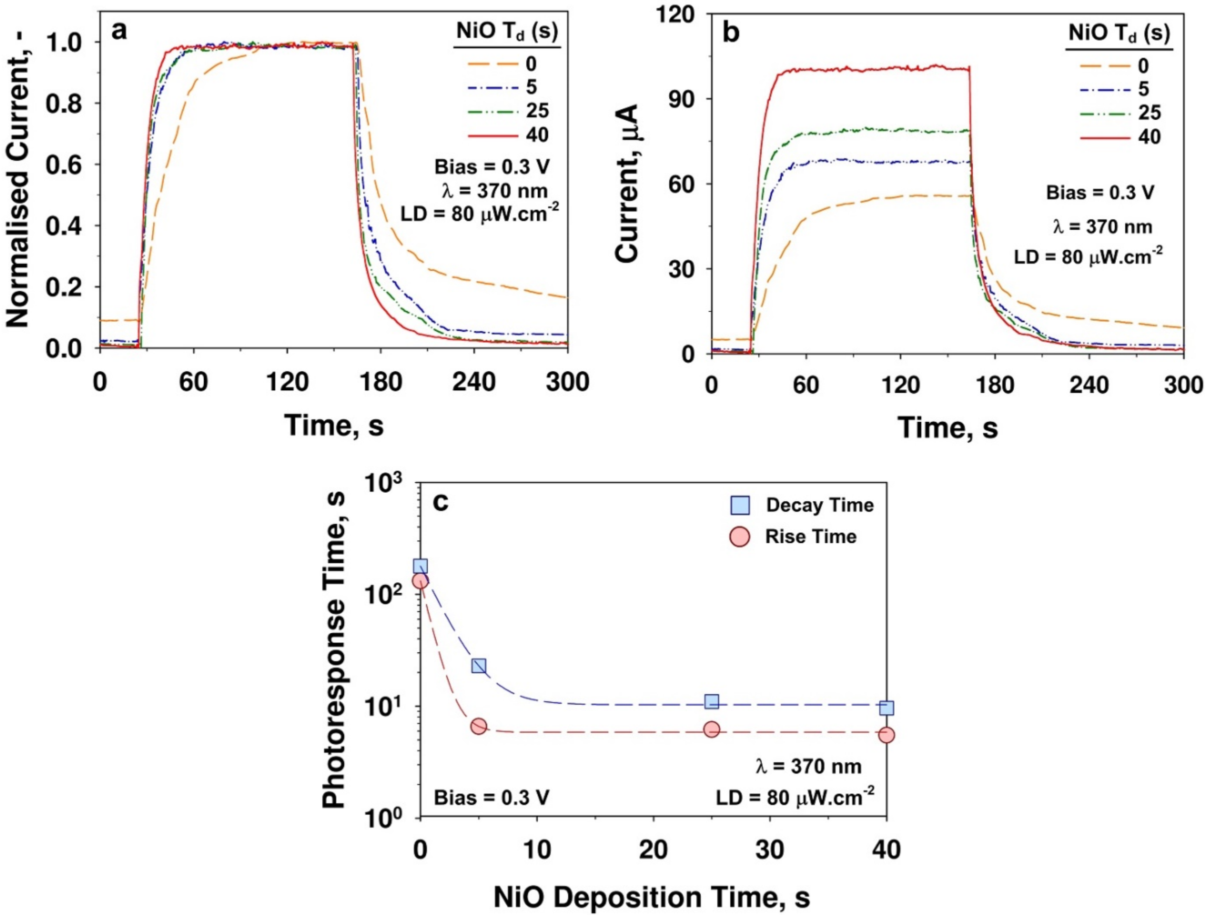

Figure 6.9. *(a) Normalised and (b) unnormalised photo-current dynamics and (c) rise (circles) and decay (square) times of the pure ZnO and NiO/ZnO networks as a function of the NiO sputtering time at a bias of 0.3 V, light density (LD) of 80 μW.cm^{-2} and illumination wavelength of 370 nm.*

Figure 6.9a shows the normalised time-resolved photo-response of the pure ZnO and NiO/ZnO networks to 370 nm UV light with a light density of 80 μW.cm^{-2}. The raw photo-currents are presented in Figure 6.9b. For all devices, the photo-current initially increased rapidly and thereafter gradually saturated under illumination, and then descended as the illumination was switched off. Rise and decay times were computed from the time required for the photo-current to increase to 90% of the steady-state value and to decrease again by 90%, respectively. The rise and decay times of the pure ZnO during the on/off cycles were 132 and 179 s, respectively (Figure 6.9c) which is in line with that reported[6-7,15] for pure ZnO nanostructured photodetectors. This relatively long time, required to reach the steady-states photo- and dark-currents, is attributed to the slow photo-desorption and chemi/physisorption of oxygen molecules on the ZnO nanoparticle surface.[6-7,15] Upon heterojunction formation, the photo-current rise and decay times decreased significantly (Figure 6.9c) reaching 5 and 9 s, respectively, with a NiO sputtering time of 40 s. This is attributed to the fast electron-hole separation in the nanoscale solid-state heterojunction, and partial passivation of the ZnO surface by NiO. The latter, replaces the slower O_2 adsorption/desorption processes resulting in 20-26 times faster response times.[40]

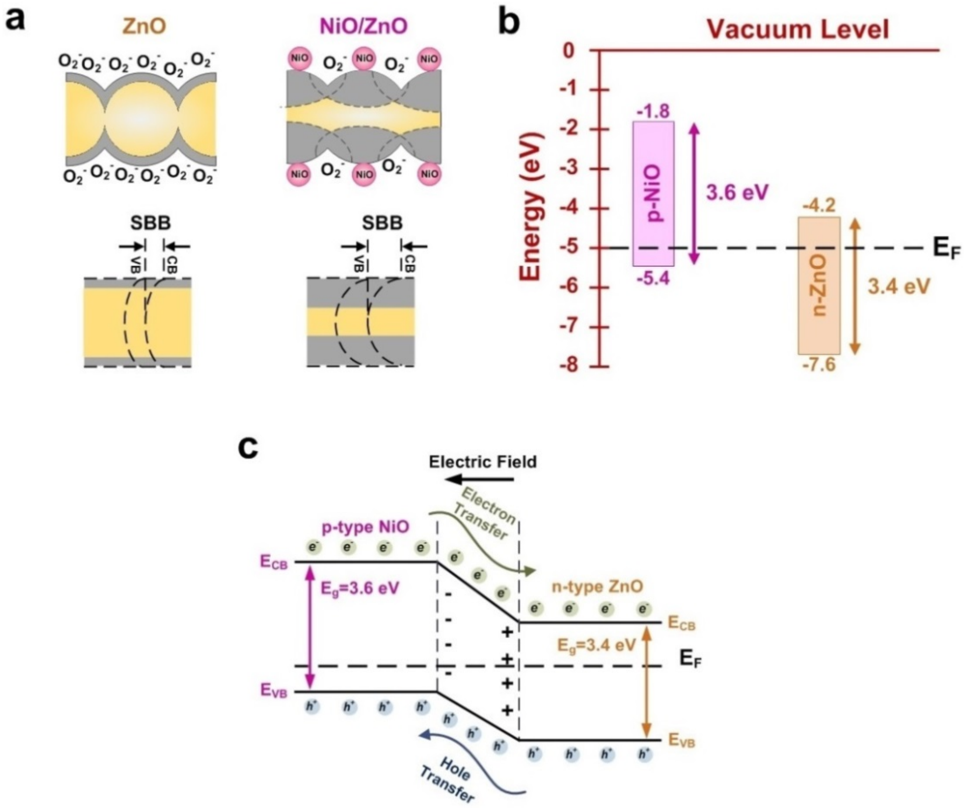

Figure 6.10. *(a) Schematic representation of the photodetection mechanism of the pure ZnO and NiO/ZnO networks with corresponding surface band bending (SBB). (b) Energy level diagrams of the p-type NiO and n-type ZnO domains with respect to the vacuum level. (c) Schematic of energy band structure and electron-hole pair separation in NiO/ZnO heterojunction with equilibrated Fermi level (E_F).*

6.3.4 Photodetection Mechanism

Figure 6.10a shows a schematic of the photo-detection mechanism of these NiO/ZnO networks vs. that of the pure ZnO ones. The lower dark-current and higher photo-current of NiO/ZnO devices are attributed to the formation of nanoscale open-circuit heterojunctions. In the dark, for the pure ZnO devices,[6-7,37] oxygen molecules adsorb on the nanoparticle surface and capture free electrons from the semiconductor conduction band (Figure 6.10a). This results in a low-conductivity depletion layer near the surface of the ZnO, which suppresses the dark-current of these ultraporous nanoparticle networks.[6-7,37] For the NiO/ZnO 3DNH devices, the Fermi energy equilibrates across the p-type and n-type domains resulting in a built-in electric field at the NiO/ZnO interface. This increases the electron-depletion of the ZnO surface resulting in a larger upward surface band bending (SBB) (Figure 6.10b,c)[41]and even lower dark-currents (Figure 6.7b) than the pure ZnO. As the fraction of the ZnO surface decorated with NiO increases with increasing NiO sputtering time, the dark-current of the NiO/ZnO devices is further decreased.

Under UV light illumination with photon energies exceeding the ZnO band gap, electron-hole pairs are generated.[6-7,13] For pure ZnO, the photogenerated holes migrate to the surface and discharge the adsorbed oxygen ions through surface electron-hole recombination. This reduces the depletion region and increases the free carrier concentration,[6] resulting in the observed photo-current rise. Once the UV illumination is terminated, the accumulated holes recombine with the unpaired electrons, while oxygen gradually reabsorbs on the ZnO surface resulting in a slow current decay.[6-7] For the NiO/ZnO networks, the photogenerated holes can rapidly migrate in the adjacent p-type domain,[15,41] leading to prolonged electron lifetime and thus increased photo-current. Once the UV illumination is terminated, the excited electron-holes can recombine at the NiO/ZnO interface resulting in a rapid decay of the photo-current as this solid-state process does not require re-adsorption of the O_2 molecules.

The faster solid-state photo-response dynamics, and higher photo-current (345 μA) and lower dark-currents (18 pA) of the NiO/ZnO networks resulted in significantly superior photodetector performance. Figure 6.11 shows the I_{UV}/I_{dark} ratio of ZnO photodetectors before and after NiO clusters deposition as a function of NiO deposition time under illumination of 370 nm with a light density of 80 $\mu W.cm^{-2}$ at a bias of 1 V. The I_{UV}/I_{dark} ratio increased from 2.9×10^6 of the pure ZnO to 5.5×10^6 of the NiO/ZnO 3DNH with 5 s NiO deposition time.

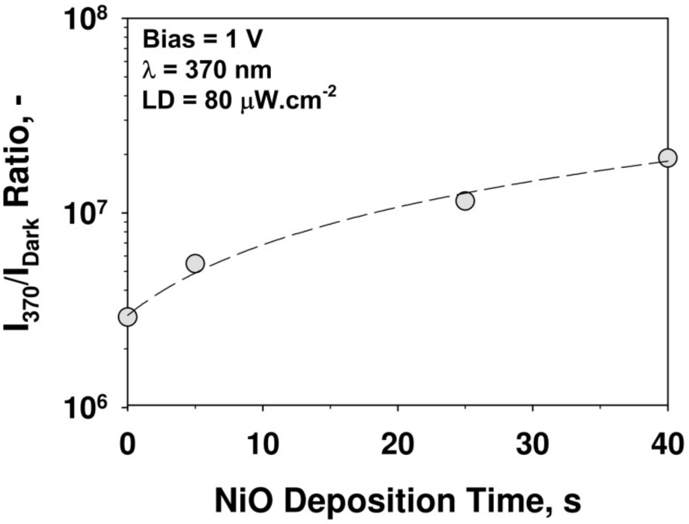

Figure 6.11. *I_{UV}/I_{dark} ratio of photodetector devices with different NiO deposition time at the wavelength of 370 nm and the applied bias of 1 V.*

Further increasing the NiO deposition time to 40 s increased the I_{UV}/I_{dark} to 1.9×10^7. This is ca. 6 times higher than that of the pure ZnO, and the highest ratio so far reported for UV photodetectors under similar illumination and applied bias.[7,11,37,42-43] This is attributed to the nanoscale size and 3D architecture of these carrier-depleted NiO/ZnO heterojunctions. While these NiO/ZnO networks absorb up to 80% of the incoming UV light (Figure 6.3), they are composed of individual nanoscale heterojunctions with a size of ca. 20 nm which is close to the Debye lengths of ZnO (19 nm)[6-7] and NiO (1-2 nm)[44]. This is different from previously reported NiO-coated nanowires,[15] where the electron-depletion layer is limited to a fraction (ca. 30%) of the ZnO nanowire radius (60 nm). As a result, the higher photo- to dark-current ratios obtained here (Figure 6.11) are attributed to the full depletion of the ZnO core and shorter hole migration lengths that results in significantly lower dark-currents and faster photo-response dynamics.

6.3.5 Low-Power Consumption Devices

In addition to fast response dynamics and high detectivity, low power-consumption is an important requirement for wearable devices. Here, the NiO/ZnO 3DNH with a sputtering time of 40 s NiO were operated down to a bias of less than 2 mV and were capable of detecting UV light densities below 80 μW.cm^{-2} with very large photo- to dark-current ratios. Figure 6.12a presents the *I-V* characteristics of the NiO/ZnO networks with 40 s NiO sputtering time, as a function of the applied bias from 0 to 2 mV in dark and under 370 nm UV light with a density of 80 μW.cm^{-2}. The *I-V* response was linear (Figure 6.12a) with a photo-current of 0.4 μA at a bias of only 0.2 mV. These relatively high photo-currents coupled with the very low dark-current of 1 pA resulted in a photo- to dark-current ratio of 4×10^{5} (Figure 6.12a), which is the highest ratio reported at this ultra-low voltage and low light density.[45-46]

The spectral responsivity of the NiO/ZnO 3DNH at the applied bias of 0.2 mV is illustrated in Figure 6.12b as a function of the illumination wavelength. It shows that this 3DNH architecture is able to detect low UV light density of 80 μW.cm^{-2} at a bias of 0.2 mV with a responsivity and detectivity of ca. 15 mA.W^{-1} and 1.14×10^{10} Jones, respectively. Recently, Shen et al.[47] fabricated a self-powered UV photodetector based on solution-processed p-NiO/n-ZnO nanorod array heterojunction featuring 0.23 s and 0.21 s rise and decay times, respectively. In another approach,[48] a self-powered ZnO/Spiro-MeOTAD heterojunction UV photodetector was demonstrated using spin coating and then, sputtering techniques resulting in shorter rise and decay times of 0.16 and 0.2 s, respectively at zero bias.

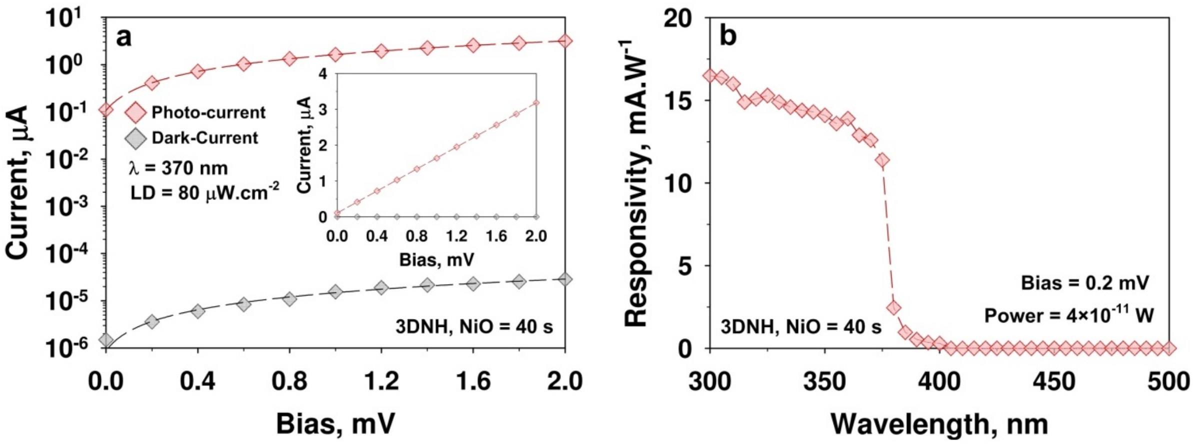

Figure 6.12. *(a) Logarithmic and linear (inset) I-V characteristics of the NiO/ZnO networks with 40 s NiO sputtering time with and without UV light at a bias from 0 to 2 mV. (b) Spectral responsivity of the NiO/ZnO networks with 40 s NiO sputtering time as a function of illumination wavelengths at a bias of 0.2 mV.*

However, these devices had low responsivities of 0.4 mA.W^{-2} and 0.22 mA.W^{-2}, respectively. [47,48] Notably, in addition to the excellent photodetector performance, this two-step fabrication approach is CMOS-compatible, low-cost and can be easily implemented on various substrates offering a powerful tool for the nanoarchitectonics of miniaturized optoelectronic devices.

6.4. Conclusions

In conclusion, we have presented a novel architecture for the engineering of visible-blind photodetectors featuring ultra-low external power consumption (4×10^{-11} watts), very high signal to noise ratios (> 10^5) and very low operation voltages (0.2 mV). The photoresponse dynamics of these 3D nanoscale heterojunctions is significantly faster (20-26 times) than that of equivalent photodetectors made of pure ZnO nanoparticle networks. This is attributed to the formation of open-circuit nanoscale heterojunctions at the NiO/ZnO interface and the very small migration length from the n-type to the p-type domains. This leads to a drastic decrease of the response and recovery times, from 132 and 179 s of the pure ZnO photodetectors to 5 and 9 s of these ultraporous NiO/ZnO networks. These findings demonstrate a superior architecture for the engineering of miniaturized wearable UV-photodetectors with largely suppressed dark-currents, fast photo-current dynamics and ultra-low power consumption.

6.5. References

1. Hatch, S. M.; Briscoe, J.; Dunn, S., A Self-Powered ZnO-Nanorod/CuSCN UV Photodetector Exhibiting Rapid Response. *Adv. Mater.* **2013,** *25*, 867-871.

2. Li, X.; Gao, C.; Duan, H.; Lu, B.; Wang, Y.; Chen, L.; Zhang, Z.; Pan, X.; Xie, E., High-Performance Photoelectrochemical-Type Self-Powered UV Photodetector Using Epitaxial TiO_2/SnO_2 Branched Heterojunction Nanostructure. *Small* **2013,** *9*, 2005-2011.

3. Wang, R. X.; Yang, L. C.; Zhang, Y. M.; Xu, S. J.; Fu, K.; Zhang, B. S.; Wang, J. F.; Xu, K.; Yang, H., The effect of Ga-doped nanocrystalline ZnO electrode on deep-ultraviolet enhanced GaN photodetector. *Appl. Phys. Lett.* **2013,** *102*, 212104.

4. Szyszka, A.; Lupina, L.; Lupina, G.; Schubert, M. A.; Zaumseil, P.; Haeberlen, M.; Storck, P.; Thapa, S. B.; Schroeder, T., Ultraviolet GaN photodetectors on Si via oxide buffer heterostructures with integrated short period oxide-based distributed Bragg reflectors and leakage suppressing metal-oxide-semiconductor contacts. *J. Appl. Phys.* **2014,** *116*, 083108.

5. Chong, H.; Yang, H.; Yang, W.; Zheng, J.; Shang, M.; Yang, Z.; Wei, G.; Gao, F., SiC Nanowire Film Photodetectors: A Promising Candidate Toward High Temperature Photodetectors. *J. Nanosci. Nanotechnol.* **2016,** *16*, 3796-3801.

6. Nasiri, N.; Bo, R.; Chen, H.; White, T. P.; Fu, L.; Tricoli, A., Structural Engineering of Nano-Grain Boundaries for Low-Voltage UV-Photodetectors with Gigantic Photo- to Dark-Current Ratios. *Adv. Opt. Mater.* **2016,** *4*, 1787-1795.

7. Nasiri, N.; Bo, R.; Wang, F.; Fu, L.; Tricoli, A., Ultraporous Electron-Depleted ZnO Nanoparticle Networks for Highly Sensitive Portable Visible-Blind UV Photodetectors. *Adv. Mater.* **2015,** *27*, 4336-4343.

8. Tricoli, A.; Nasiri, N.; Chen, H.; Wallerand, A. S.; Righettoni, M., Ultra-rapid synthesis of highly porous and robust hierarchical ZnO films for dye sensitized solar cells. *Sol. Energy* **2016,** *136*, 553-559.

9. Tian, W.; Zhang, C.; Zhai, T.; Li, S.-L.; Wang, X.; Liu, J.; Jie, X.; Liu, D.; Liao, M.; Koide, Y.; Golberg, D.; Bando, Y., Flexible Ultraviolet Photodetectors with Broad Photoresponse Based on Branched ZnS-ZnO Heterostructure Nanofilms. *Adv. Mater.* **2014,** *26*, 3088-3093.

10. Chen, M.; Hu, L.; Xu, J.; Liao, M.; Wu, L.; Fang, X., ZnO Hollow-Sphere Nanofilm-Based High-Performance and Low-Cost Photodetector. *Small* **2011,** *7*, 2449-2453.

11. Hu, L.; Yan, J.; Liao, M.; Xiang, H.; Gong, X.; Zhang, L.; Fang, X., An Optimized Ultraviolet-A Light Photodetector with Wide-Range Photoresponse Based on ZnS/ZnO Biaxial Nanobelt. *Adv. Mater.* **2012,** *24*, 2305-2309.

12. Zhu, H.; Shan, C. X.; Yao, B.; Li, B. H.; Zhang, J. Y.; Zhao, D. X.; Shen, D. Z.; Fan, X. W., High Spectrum Selectivity Ultraviolet Photodetector Fabricated from an n-ZnO/p-GaN Heterojunction. *J. Phys. Chem. C* **2008,** *112*, 20546-20548.

13. Jin, Y.; Wang, J.; Sun, B.; Blakesley, J. C.; Greenham, N. C., Solution-Processed Ultraviolet Photodetectors Based on Colloidal ZnO Nanoparticles. *Nano Lett.* **2008,** *8*, 1649-1653.

14. Lupan, O.; Chai, G.; Chow, L.; Emelchenko, G. A.; Heinrich, H.; Ursaki, V. V.; Gruzintsev, A. N.; Tiginyanu, I. M.; Redkin, A. N., Ultraviolet photoconductive sensor based on single ZnO nanowire. *Phys. Status Solidi A* **2010,** *207*, 1735-1740.

15. Retamal, J. R. D.; Chen, C.-Y.; Lien, D.-H.; Huang, M. R. S.; Lin, C.-A.; Liu, C.-P.; He, J.-H., Concurrent Improvement in Photogain and Speed of a Metal Oxide Nanowire Photodetector through Enhancing Surface Band Bending via Incorporating a Nanoscale Heterojunction. *ACS Photonics* **2014,** *1*, 354-359.

16. Ahn, S.-E.; Ji, H. J.; Kim, K.; Kim, G. T.; Bae, C. H.; Park, S. M.; Kim, Y.-K.; Ha, J. S., Origin of the slow photoresponse in an individual sol-gel synthesized ZnO nanowire. *Appl. Phys. Lett.* **2007,** *90*, 153106.

17. Bie, Y.-Q.; Liao, Z.-M.; Zhang, H.-Z.; Li, G.-R.; Ye, Y.; Zhou, Y.-B.; Xu, J.; Qin, Z.-X.; Dai, L.; Yu, D.-P., Self-Powered, Ultrafast, Visible-Blind UV Detection and Optical Logical Operation based on ZnO/GaN Nanoscale p-n Junctions. *Adv. Mater.* **2011,** *23*, 649-653.

18. Ren, L.; Tian, T.; Li, Y.; Huang, J.; Zhao, X., High-Performance UV Photodetection of Unique ZnO Nanowires from Zinc Carbonate Hydroxide Nanobelts. *ACS Appl. Mater. Interfaces* **2013,** *5*, 5861-5867.

19. Liu, X.; Gu, L.; Zhang, Q.; Wu, J.; Long, Y.; Fan, Z., All-printable band-edge modulated ZnO nanowire photodetectors with ultra-high detectivity. *Nature Commun.* **2014,** *5*, 4007.

20. Yao, I. C.; Tseng, T.-Y.; Lin, P., ZnO nanorods grown on polymer substrates as UV photodetectors. *Sens. Actuators A Phys.* **2012,** *178*, 26-31.

21. Alenezi, M. R.; Alshammari, A. S.; Alzanki, T. H.; Jarowski, P.; Henley, S. J.; Silva, S. R. P., ZnO Nanodisk Based UV Detectors with Printed Electrodes. *Langmuir* **2014,** *30*, 3913-3921.

22. Zhai, T.; Xie, S.; Zhao, Y.; Sun, X.; Lu, X.; Yu, M.; Xu, M.; Xiao, F.; Tong, Y., Controllable synthesis of hierarchical ZnO nanodisks for highly photocatalytic activity. *CrystEngComm* **2012,** *14*, 1850-1855.

23. Shao, D.; Yu, M.; Sun, H.; Hu, T.; lian, J.; Sawyer, S., High responsivity, fast ultraviolet photodetector fabricated from ZnO nanoparticle-graphene core-shell structures. *Nanoscale* **2013,** *5*, 3664-3667.

24. Nie, B.; Hu, J.-G.; Luo, L.-B.; Xie, C.; Zeng, L.-H.; Lv, P.; Li, F.-Z.; Jie, J.-S.; Feng, M.; Wu, C.-Y.; Yu, Y.-Q.; Yu, S.-H., Monolayer Graphene Film on ZnO Nanorod Array for High-Performance Schottky Junction Ultraviolet Photodetectors. *Small* **2013,** *9*, 2872-2879.

25. Park, C.; Lee, J.; So, H.-M.; Chang, W. S., An ultrafast response grating structural ZnO photodetector with back-to-back Schottky barriers produced by hydrothermal growth. *J. Mater. Chem. C* **2015,** *3*, 2737-2743.

26. Knigge, A.; Brendel, M.; Brunner, F.; Einfeldt, S.; Knauer, A.; Kueller, V.; Weyers, M., AlGaN photodetectors for the UV-C spectral region on planar and epitaxial laterally overgrown AlN/sapphire templates. *Phys. Status Solidi C* **2013,** *10*, 294-297.

27. Zhou, W.-j.; Jin, K.-j.; Guo, H.-z.; Ge, C.; He, M.; Lu, H.-b., Electrode effect on high-detectivity ultraviolet photodetectors based on perovskite oxides. *J. Appl. Phys.* **2013,** *114*, 224503.

28. Lupan, O.; Pauporté, T.; Viana, B., Low-Voltage UV-Electroluminescence from ZnO-Nanowire Array/p-GaN Light-Emitting Diodes. *Adv. Mater.* **2010,** *22*, 3298-3302.

29. Patel, M.; Kim, H.-S.; Park, H.-H.; Kim, J., Active Adoption of Void Formation in Metal-Oxide for All Transparent Super-Performing Photodetectors. *Sci. Rep.* **2016,** *6*, 25461.

30. Xi, Y. Y.; Hsu, Y. F.; Djurišić, A. B.; Ng, A. M. C.; Chan, W. K.; Tam, H. L.; Cheah, K. W., NiO/ZnO light emitting diodes by solution-based growth. *Appl. Phys. Lett.* **2008,** *92*, 113505.

31. Tsai, D.-S.; Lin, C.-A.; Lien, W.-C.; Chang, H.-C.; Wang, Y.-L.; He, J.-H., Ultra-High-Responsivity Broadband Detection of Si Metal–Semiconductor–Metal Schottky Photodetectors Improved by ZnO Nanorod Arrays. *ACS Nano* **2011,** *5*, 7748-7753.

32. Sun, K.; Jing, Y.; Park, N.; Li, C.; Bando, Y.; Wang, D., Solution Synthesis of Large-Scale, High-Sensitivity ZnO/Si Hierarchical Nanoheterostructure Photodetectors. *J. Am. Chem. Soc.* **2010,** *132*, 15465-15467.

33. Singh, S. D.; Ajimsha, R. S.; Sahu, V.; Kumar, R.; Misra, P.; Phase, D. M.; Oak, S. M.; Kukreja, L. M.; Ganguli, T.; Deb, S. K., Band alignment and interfacial structure of ZnO/Ge heterojunction investigated by photoelectron spectroscopy. *Appl. Phys. Lett.* **2012,** *101*, 212109.

34. Ohta, H.; Hirano, M.; Nakahara, K.; Maruta, H.; Tanabe, T.; Kamiya, M.; Kamiya, T.; Hosono, H., Fabrication and photoresponse of a pn-heterojunction diode composed of transparent oxide semiconductors, p-NiO and n-ZnO. *Appl. Phys. Lett.* **2003,** *83*, 1029-1031.

35. Wang, J.-Y.; Lee, C.-Y.; Chen, Y.-T.; Chen, C.-T.; Chen, Y.-L.; Lin, C.-F.; Chen, Y.-F., Double side electroluminescence from p-NiO/n-ZnO nanowire heterojunctions. *Appl. Phys. Lett.* **2009,** *95*, 131117.

36. Deng, R.; Yao, B.; Li, Y. F.; Zhao, Y. M.; Li, B. H.; Shan, C. X.; Zhang, Z. Z.; Zhao, D. X.; Zhang, J. Y.; Shen, D. Z.; Fan, X. W., X-ray photoelectron spectroscopy measurement of n-ZnO/p-NiO heterostructure valence-band offset. *Appl. Phys. Lett.* **2009,** *94*, 022108.

37. Nasiri, N.; Bo, R.; Hung, T. F.; Roy, V. A. L.; Fu, L.; Tricoli, A., Tunable Band-Selective UV-Photodetectors by 3D Self-Assembly of Heterogeneous Nanoparticle Networks. *Adv. Funct. Mater.* **2016,** *26*, 7359-7366.

38. Bohren, C. F.; Huffman, D. R., Absorption and Scattering by a Sphere. In *Absorption and Scattering of Light by Small Particles*, Wiley-VCH Verlag GmbH, Weinheim, Germany: 1998; pp 82-129.

39. Gong, X.; Tong, M.; Xia, Y.; Cai, W.; Moon, J. S.; Cao, Y.; Yu, G.; Shieh, C.-L.; Nilsson, B.; Heeger, A. J., High-Detectivity Polymer Photodetectors with Spectral Response from 300 nm to 1450 nm. *Science* **2009,** *325*, 1665-1667.

40. Lee, C.-H.; Lee, G.-H.; van der Zande, A. M.; Chen, W.; Li, Y.; Han, M.; Cui, X.; Arefe, G.; Nuckolls, C.; Heinz, T. F.; Guo, J.; Hone, J.; Kim, P., Atomically thin p–n junctions with van der Waals heterointerfaces. *Nature Nanotechnol.* **2014,** *9*, 676-681.

41. Abdul Rahman, I.; Ayob, M. T. M.; Radiman, S., Enhanced Photocatalytic Performance of NiO-Decorated ZnO Nanowhiskers for Methylene Blue Degradation. *J. Nanotechnol.* **2014,** *2014*, 8.

42. Liu, K.; Sakurai, M.; Aono, M., ZnO-based ultraviolet photodetectors. *Sensors* **2010,** *10*, 8604-8634.

43. Peng, L.; Hu, L.; Fang, X., Low-Dimensional Nanostructure Ultraviolet Photodetectors. *Adv. Mater.* **2013,** *25*, 5321-5328.

44. Seo, S.; Park, I. J.; Kim, M.; Lee, S.; Bae, C.; Jung, H. S.; Park, N.-G.; Kim, J. Y.; Shin, H., An ultra-thin, un-doped NiO hole transporting layer of highly efficient (16.4%) organic-inorganic hybrid perovskite solar cells. *Nanoscale* **2016,** *8*, 11403-11412.

45. Bai, Z.; Yan, X.; Chen, X.; Liu, H.; Shen, Y.; Zhang, Y., ZnO nanowire array ultraviolet photodetectors with self-powered properties. *Curr. Appl. Phys.* **2013,** *13*, 165-169.

46. Sarkar, S.; Basak, D., Self Powered Highly Enhanced Dual Wavelength ZnO@ CdS Core–Shell Nanorod Arrays Photodetector: An Intelligent Pair. *ACS Appl. Mater. Interfaces* **2015,** *7*, 16322-16329.

47. Shen, Y.; Yan, X.; Bai, Z.; Zheng, X.; Sun, Y.; Liu, Y.; Lin, P.; Chen, X.; Zhang, Y., A self-powered ultraviolet photodetector based on solution-processed p-NiO/n-ZnO nanorod array heterojunction. *RSC Adv.* **2015,** *5*, 5976-5981.

48. Shen, Y.; Yan, X.; Si, H.; Lin, P.; Liu, Y.; Sun, Y.; Zhang, Y., Improved Photoresponse Performance of Self-Powered ZnO/Spiro-MeOTAD Heterojunction Ultraviolet Photodetector by Piezo-Phototronic Effect. *ACS Appl. Mater. Interfaces* **2016,** *8*, 6137-6143.

Chapter Seven

Summary and Outlooks

In this thesis, the synthesis of ultraporous ZnO nanoparticle networks by flame spray pyrolysis (FSP) and their controlled direct deposition on electronic substrates for the fabrication of highly performing photodetectors were investigated. This is a significant improvement over established wide bandgap semiconductors that are produced by multi-step and wet-phase processes. In particular, novel flame-based methods used in this research for the synthesis of highly porous wide bandgap semiconductor (ZnO) films resulted in visible-blind UV photodetectors with significantly higher detecting performances compared to classical chemical and physical vapour deposition processes. The unique properties of these fully transparent ultraporous films are summarised in a new class of nanostructured photodetectors that combines several benefits of classical aerosol and wet-methods synthesis.

In this regard,[1] the self-assembly of nanomaterials into three-dimensional hierarchical structures was explored in second chapter by modelling and simulating the dynamic behaviours of ultra-fine nanoparticles from freely diffusing particles to ballistically depositing ones. In order to determine a comprehensive mechanistic description of the nanoparticles accumulation and their self-assembly behaviours, the dynamics of unbound nanoparticles was investigated over three orders of magnitude in scale. As a result, a novel deposition mechanism and regime, named Randomly Oriented Ballistic Regime, was proposed in which successfully capture the full spectrum of size-dependent self-assembly dynamics. This enables quantitative predictions of micro- to nano-particle interaction with their surroundings providing a unified model of their diverging self-assembly mechanisms.

In the third chapter,[2] a novel hierarchical morphology was presented for visible-blind UV photodetectors using ultraporous nanoparticle networks fabricated by flame spray pyrolysis synthesis and aerosol deposition of ZnO nanoparticle films. The fabricated device exhibited an extremely high photo- to dark-current ratio of 3.4×10^5 which was the highest ratio so far reported. This strong response is attributed to the unique morphology and composition of these films. In fact, the very high porosity of these nanoparticle networks facilitates the penetration of oxygen into the lowest nanoparticle layers and ensures the participation of the whole film in the photodetection mechanism. Decreasing the primary particle size below twice the ZnO Debye length and providing ultra-porous film morphology enhanced adsorption/desorption of oxygen molecules from the nanoparticle surface and facilitated the penetration of UV light into the lowest film layers resulting in an on/off switch behaviour to UV light exposure. These results show that electron-depleted particles are critical but not sufficient to obtain high photo- and low dark-currents at low UV light intensities.

In the fourth chapter,[3] optimal grain boundary morphologies for these wide bandgap semiconductor nanoparticles were explored by structural engineering of the grain boundaries of ZnO nanoparticles in ultraporous nanoparticle networks. The photoelectrical response measurement revealed that thermally-induced necking of the grain boundaries is essential for efficient photodetection. The annealing temperature of 300 °C was presented as the optimal annealing temperature for ultraporous networks made by ZnO nanoparticle resulting in optimal photodetection performance. This optimal performance was attributed to two main mechanisms, namely the inhibition of the photocurrent in the as-prepared samples due to electron hopping at the grain boundaries, and the increase of the dark-current in the strongly annealed samples due to their closed-neck grain morphology.

In the fifth chapter,[4] a nanoscale architecture was presented for band-selective UV photodetectors that featured excellent tunability, light detection performance and miniaturization potential. The device layout relies on the 3D integration of ultraporous functional layers of ZnO, SiO_2 and TiO_2 nanoparticles. A band-selective photoresponse was obtained by exploiting the transmittance dielectric window (SiO_2 layer) between the indirect bandgap of TiO_2 and the sharp-edge of the direct bandgap of ZnO. Under the UV illumination, the top layer acts as a tunable long-pass filter absorbing light photons with the wavelength below 325 nm while photons with longer wavelength can reach the bottom ZnO layer. However, to electrically insulate the filter TiO_2 and photoresistor ZnO layer, a UV-transparent dielectric layer of SiO_2 nanoparticles was used as spacer. In fact, although the top TiO_2 layer is absorbing short wavelength photons but as it is not electrically connected to the device, no significant absorption peak was detected for the wavelength below 325 nm. The bandwidth of these photodetectors was easily tuned from 85 to 29 nm by increasing the TiO_2 film thickness. This solid-state architecture can be implemented with other top - bottom layer compositions such as GaAs (1.4 eV) - Si (1.1 eV), and SnO_2 (3.7 eV) - ZnS (3.54 eV) enabling the fabrication of portable band-selective photodetectors for the UV, visible and infrared spectrums.

In the sixth chapter,[5] a highly performing nanoscale architecture was presented for the engineering of fast responding wide bandgap UV photodetectors. In order to improve the response speed of the device, a three-dimensional nanoscale heterojunction architecture was fabricated using p-type NiO clusters densely packed on the surface of an ultraporous network of electron-depleted n-type ZnO nanoparticles. The switching speed of the photocurrent dynamics was more than 20 times higher for three-dimensional network of nanoscale heterojunctions (3DNH) device (presented in chapter 6) compared to the other 3D structures (pure ZnO devices) presented in the thesis. This higher dynamic speed is attributed to the formation of nanoscale open-circuit heterojunctions. In fact, 3DNH structure caused fully depleted ZnO core and shorter hole migration lengths, that results in significantly lower dark-currents and faster photo-response dynamics compared to a pure ZnO device.

In summary, the findings of this thesis demonstrate a highly performing structure and a flexible and scalable platform technology for the rapid low-cost fabrication and integration of ultraviolet photodetectors in CMOS-compatible portable devices. This is a superior architecture for the engineering of miniaturized wearable UV photodetectors with largely suppressed dark-currents, fast photo-current dynamics and ultralow power consumption. This concept can be applied to other highly performing semiconductors such as wide bandgap for selective UV detection, fast photo-current dynamics and ultra-low power consumption devices.

7.1. References

1. Nasiri, N.; Elmoe, T. D.; Liu, Y.; Qin, Q. H.; Tricoli, A., Self-assembly dynamics and accumulation mechanisms of ultra-fine nanoparticles. *Nanoscale* **2015,** *7*, 9859-9867.

2. Nasiri, N.; Bo, R.; Wang, F.; Fu, L.; Tricoli, A., Ultraporous Electron-Depleted ZnO Nanoparticle Networks for Highly Sensitive Portable Visible-Blind UV Photodetectors. *Adv. Mater.* **2015,** *27*, 4336-4343.

3. Nasiri, N.; Bo, R.; Chen, H.; White, T. P.; Fu, L.; Tricoli, A., Structural Engineering of Nano-Grain Boundaries for Low-Voltage UV-Photodetectors with Gigantic Photo- to Dark-Current Ratios. *Adv. Opt. Mater.* **2016,** *4*, 1787-1795.

4. Nasiri, N.; Bo, R.; Hung, T. F.; Roy, V. A. L.; Fu, L.; Tricoli, A., Tunable Band-Selective UV-Photodetectors by 3D Self-Assembly of Heterogeneous Nanoparticle Networks. *Adv. Funct. Mater.* **2016,** *26*, 7359-7366.

5. Nasiri, N.; Bo, R.; Fu, L.; Tricoli, A., Three-dimensional nano-heterojunction networks: a highly performing structure for fast visible-blind UV photodetectors. *Nanoscale* **2017,** *9*, 2059-2067.

Chapter Eight

Future Work

This thesis has demonstrated superior structural design and a simple, low-cost CMOS-compatible process for the engineering of high-performance wearable devices using a rapid (≤ 100s) one-step synthesis and self-assembly of transparent ultra-porous films composed of electron-depleted crystalline ZnO nanoparticles. However, many opportunities for extending the scope of this thesis still remain. This section presents some of these directions.

8.1. Modelling

In the second chapter of this thesis, the dynamics of unbound nanoparticles is investigated over three orders of magnitude in scale aiming to determine a comprehensive mechanistic description of their accumulation and self-assembly behaviours. This enables quantitative predictions of micro- to nano-particle interaction with their surroundings providing a unified model of their diverging self-assembly mechanisms. However, modelling and simulation of light interaction with nanoparticles and its penetration through the film in both porous and dense structures would be significantly useful in terms of photodetection application.

8.2. Photoresponse Speed

Visible-blind ultraviolet photodetectors are an emerging technology for the development of wide bandgap optoelectronic devices with greatly reduced power consumption and size requirements. However, a standing challenge for many applications, including wearable monitors for skin cancer prevention, is to drastically improve the slow response time of these nanostructured devices. In this thesis, we demonstrate that nanoscale heterojunctions made of three-dimensionally co-located n- and p-type semiconductors enables more than 20 times faster photo-response dynamics while improving signal to noise ratio and detectivity. Despite this progress, the photoresponse speed of these visible-blind photodetectors is still too slow for many real-world uses.

8.3. Long Term Stability

The ultrahigh porosity of these ultraporous nanoparticle networks is beneficial to ensure penetration of oxygen and thus formation of electron-depleted ZnO particles in the whole film structure and in particular in the lowest layers adjacent to the electrodes. However, this high available surface area might have negative effect on the photodetector performance after storage in the air atmosphere for a long time. In fact, after a long time storage, a significant amount of water vapour might be absorbed on the surface and negatively impact the photodetection performance of the device. More investigation is required to find a way to passivate the surface of these ultraporous nanostructured devices to prevent reducing their performance with time passing.

8.4. Mechanical Stability

These ultra-porous nanoparticle coatings are usually characterized by a fragile structure that can be destroyed after a few cycle abrasion tests. This weak mechanical stability is attributed to ultrahigh porosity of these porous nanostructured devices. However, further studies are required to demonstrate a higher mechanical stability while preserving ultrahigh porosity of these nanostructures.

8.5. Flexibility

Development of flexible and stretchable sensing materials has recently shown the potential to offer additional opportunities to increase the selectivity of these nanostructured sensors. Here, in addition to the engineering of the ultraporous nanostructured devices, the realization of a flexible device can be very interesting and appealing. However, this requires further optimization and could be suited for a dedicated follow-up study. In that case, this research area can be greatly benefitting from the development of flexible and transferable electronics.

Appendix A

Ultra-Porous Nanoparticle Networks: A Biomimetic Coating Morphology for Enhanced Cellular Response and Infiltration

Publication relevant to this chapter:

Noushin Nasiri, Anthony Ceramidas, Shayanti Mukherjee, Anitha Panneerselvan, David R Nisbet, Antonio Tricoli, "*Ultra-Porous Nanoparticle Networks: A Biomimetic Coating Morphology for Enhanced Cellular Response and Infiltration*", **Scientific Reports**, 6, 24305, **2016**.

Abstract

Orthopedic treatments are amongst the most common cause of surgery and are responsible for a large share of global healthcare expenditures. Engineering materials that can hasten bone integration will improve the quality of life of millions of patients per year and reduce associated medical costs. Here, we present a novel hierarchical biomimetic coating that mimics the inorganic constituent of mammalian bones with the aim of improving osseointegration of metallic implants. We exploit the thermally-driven self-organization of metastable core-shell nanoparticles during their aerosol self-assembly to rapidly fabricate robust, ultra-porous nanoparticle networks (UNN) of crystalline hydroxyapatite (HAp). Comparative analysis of the response of osteoblast cells to the ultra-porous nanostructured HAp surfaces to that of spin coated HAp surfaces revealed superior osseointegrative properties of the UNN coatings with significant cell and filopodia infiltration. This flexible synthesis approach to engineering UNN HAp coatings on titanium provides a platform technology to study the bone-implant interface for improved osseointegration and osteoconduction.

A.1 Introduction

The rapid rise of nanofabrication technologies is enabling the engineering of hierarchical materials and surfaces that mimic the complex morphology and composition of biological tissue.[1-2] This is critical to bone tissue engineering where the interaction between the synthetic implant and bone is determined by the implant's surface properties. Bone injuries account for a large proportion of surgeries and healthcare expenditures.[2-3] These procedures often require the permanent implantation of synthetic structures such as prostheses and grafts in the bone. The success of these implants is determined by their osseointegration with the surrounding bone tissue. This long-term integration requires materials stability and careful engineering of biomimetic interfaces. This is challenging as mammalian bone is a composite material composed of hierarchically assembled mineralised collagen together with a small portion of non-collagenous protein and lipids. This assembly of mineralised collagen fibrils can lead to varied bone structure and morphologies depending on its location and function. The most biologically active section of mammalian bones, namely the trabecular region, features a honey-comb type spatial arrangement of mineralised collagen fibrils[4-5] with a porosity range of 30-95%[6-7].

Currently, much effort is focused on the nanofabrication of enhanced HAp coatings that may ultimately improve the integration of orthopaedic implants. Synthesis of nanostructured HAp coatings is currently pursued by numerous methods including plasma spraying,[8] sol-gel[9,10] and magnetron sputtering[11]. Plasma spraying is the gold standard for the commercial production of implant coatings. Notwithstanding its numerous merits, this approach results in dense films with limited chemical homogeneity and mechanical properties[12]. These two-dimensional plasma-sprayed interfaces do not adequately mimic the highly porous three-dimensional structure of bone tissue and may result in shorter in vivo residence times compared with a coating with superior biomimicry.[13] In other studies,[14,10] porous HAp coatings (15.5-75% porosity) were fabricated using micro-porous biphasic calcium phosphate (BCP) granules mixed with organic pore makers[14] and sol-gel[10]. The resulting calcium phosphate was amorphous and calcination at 600 °C[10] to 1050 °C[14] was required for crystallization.

Thermo-[15] and electrophoretically-driven[16] deposition of nanoparticle aerosols has been, recently, demonstrated as a flexible tool for the synthesis of three-dimensional morphologies[17] with excellent optoelectronic[18] and chemical properties[19]. This gas-phase approach shares some of the advantages of plasma-spraying such as scalability and high deposition rates while enabling fabrication of up to 98% porous morphologies[20] and more accurate control of the key structural features[21]. However, previous attempts to produce crystalline HAp aerosols by high-throughput spray flames have led to amorphous compounds.[22-24] Furthermore, these ultra-porous nanoparticle coatings are usually characterized by a fragile structure that is easily destroyed by capillary forces,[18] and are not suitable for biological applications. Enhancing their mechanical stability for operation in liquid environments has been only partially successful.[25]

Here, we demonstrate the synthesis of a three-dimensional nanocrystalline HAp morphology that mimics the high porosity and micro-nano structural hierarchy of the trabecular bone region. Ultra-porous nanoparticle networks of crystalline HAp are fabricated in one-step by rapid self-assembly of meta-stable core-shell nanoparticle aerosols and in-situ thermally-induced self-organization. This results in ultra-porous and micro-rough films composed of strongly sintered nanostructures that withstand capillary forces and handling. Up to five to ten times denser morphologies are obtained as a comparative structure by classical spin-coating of the same flame-made nanoparticles. The performance of this synthetic UNN morphology is assessed by primary osteoblast cultures revealing unique cellular response and infiltration. We believe that this rapid and scalable synthesis route offers a powerful platform for the large-scale and low-cost fabrication of ultraporous inorganic coatings with application extending from regenerative medicine to implantable devices.

A.2 Experimental

A.2.1 Precursor Preparation

Flame spray pyrolysis (FSP) was used for the synthesis and direct deposition of Hydroxyapatite (HAp) nanoparticles. Nanoparticles were prepared as follows: Calcium Naphthenate (Sigma Aldrich, $2(C_{11}H_7O_2)Ca$, ca. 35% in mineral spirits (4% Ca)) and Tributyl phosphate (Sigma Aldrich, $C_{12}H_{27}O_4P$) were mixed together at a Ca/P molar ratio of 1.667, matching the natural HAp composition. The solution was supplied at a rate of 5 mL min-1 through a needle and dispersed into a fine spray with an oxygen dispersion of 5 L min^{-1}. This spray was ignited by a supporting annular premixed methane/oxygen flame (CH_4 = 1.2 L min^{-1}, O_2 = 3.2 L min^{-1}).

A.2.2 HAp Coating Synthesis

Nanoparticles were deposited by orthogonal impingement of hot aerosol generated by FSP on the substrate placed at 6 cm height above the burner (HAB). The substrates were 1 mm thick Titanium alloy (Ti-6Al-4V, grade 5, Revolution Advanced Metals & Materials) disks with a diameter of 15 mm. Before nanoparticles deposition, the disk surface was cleaned in an ultrasonic bath with ethanol for 20 min. The aerosol temperature (T_F) on the exposed substrate surface was measured by digital thermometer (RS, model #206-3738). Dense morphologies were obtained by spin-coating of the same flame-made HAp nanoparticles collected on glass-fiber filters placed at 50 cm HAB. A quantity of 1 mL pure water and acetyl acetone with volume ratio of 10:1 was added to the 0.3 g of HAp particles with 2 droplets of Triton X-100 as a surfactant. A spin coater (VTC-100 Vacuum Spin Coater, MTI

Corporation) was used at a speed of 1000 rpm for 60 s to spin-coat the above solution on the Ti disk. These films were sintered at 850 ºC for 1 h to remove all impurities and achieve a 100% pure HAp. The morphology and patterning characteristics of the deposited particles and films were investigated by a Hitachi H7100FA transmission electron microscope (TEM) at 100kV and an analytical scanning electron microscopy (Zeiss Ultraplus FESEM) at 3kV. The crystal phases, size (d_{XRD}) and surface compositions were analyzed by X-ray diffraction with a D_2 Phaser (Bruker, U.S.A) and Fourier transform infrared spectroscopy (FTIR-ATR, Bruker-Alpha, U.S.A). The average crystal sizes of the HAp and calcium oxide phases were computed form the XRD peaks in the 2θ range of 30 - 35º and 35 - 40º, respectively. The HAp specific surface area (SSA) was measured by N_2 adsorption/desorption at -196.15 ºC (Micromeritics, TriStar II, U.S.A), after degassing at 300 °C for 4 h. The HAp/Ti alloy interface strength was investigated under the ASTM D4060-14 standard with a Taber abrasion (Dongguan Jianqiao Testing Equipment Co., LTD, Model JQ-802A). The test was performed under two-body (high-stress) condition using a pair of abrading wheels 52 mm in dimeter at 250 g load. The morphology of all coatings was investigated with a Zeiss Ultraplus FE-SEM at 3 kV and white light interferometer (WLI) (Veeco, Wyko NT9100, U.S.A). High temperature differential scanning calorimetry (DSC) analysis was conducted from 30 to 1000 °C at a 10 °C min^{-1} ramp under nitrogen atmosphere in a STA 8000 (Perkin Elmer, U.S.A).

A.2.3 Cell Culture

This procedure was approved by the Animal Research Ethics Committee of Australian National University (Reference Nr. A2013/41). Primary osteoblasts were isolated from femur bone of adult Swiss mice according to the ANU animal ethics guidelines. The femur was cleaned thoroughly, minced and digested using collagenase (Sigma Aldrich) at a concentration of 10 mg mL^{-1} at 37 ºC for 20 min. The digested mass was washed with phosphate buffered saline (PBS) and plated on tissue culture plates (TCP) and maintained with Dulbecco's Modified Eagle's medium (DMEM - HyClone) containing 10% foetal bovine serum (FBS, Gibco) and 1% penicillin streptomycin antibiotics (HyClone). Confluent cultures were mechanically detached using cell scrapers (HyClone) and seeded at a density of 10,000 cells per sample (HAp coating on Ti substrate) in 24 well plates.

A.2.4 Biological SEM sample preparation

Cell morphology was assessed after 14 days of culture. Culture medium was replaced with 3% glutaraldehyde and incubated for 2 h at room temperature for cell fixation. After fixation, the wells were washed with deionized water. The samples were then dehydrated in a series of graded ethanol solutions with final dehydration in 100% ethanol. The samples were then treated with hexamethyldisilazane (HMDS) and allowed to air dry.

A.2.5 Immunofluorescence analysis

Isolated primary murine bone cells cultures on the HAp coated samples were washed with PBS, and fixed with 4% paraformaldehyde (Sigma-Aldrich) for 10 min. Cells were permeabilized with 0.1% Triton X-100 (Sigma-Aldrich), blocked for non-specific staining using 3% bovine serum albumin (BSA, Sigma) and then immunostained with Phalloidin-TRITC (Millipore) and anti-osteocalcin antibody (R&D systems) for 1 h at room temperature. Thereafter, they were revealed with anti-species-specific Alexa fluor 488 (Life Technologies). The samples were mounted using anti-quenching mounting medium (Vectashiled, Vector laboratories) and observed under a fluorescence microscope for imaging (Olympus IX 71).

A.3 Results and Discussion

A.3.1 Flame Synthesis of Core-Shell Nanoparticle

Highly concentrated aerosols of hydroxyapatite (HAp) nanoparticles were produced by combustion of calcium naphthenate in tributyl phosphate solutions (Figure A.1). Previous attempts to produce crystalline hydroxyapatite nanoparticles by highly turbulent and scalable spray flames[26] have usually resulted in nearly completely amorphous Ca/P compounds[24]. To overcome this limitation, here, a custom-built atomizer design (Figure A.1) has been utilized that enables higher atomization pressure than previously investigated (≈ 1.5 bar)[24].

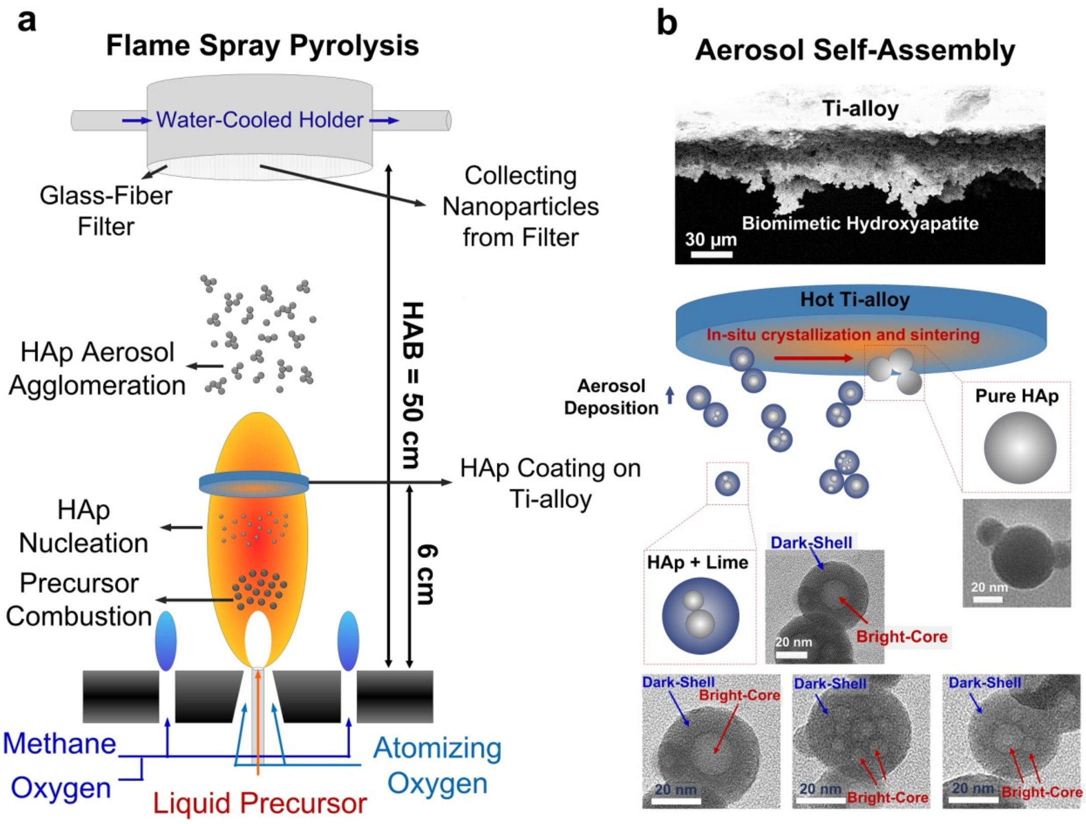

Figure A.1. *Schematics of (a) flame spray pyrolysis synthesis and (b) aerosol self-assembly of three dimensional ultra-porous films made of HAp nanoparticles at 6 cm height above the burner (HAB). The produced HAp nanoparticles have core-shell structure after nucleation while aerosol deposition on hot Ti-alloy leads to a pure HAp phase with no detectable trace of lime and other impurities.*

Figure A.2 shows the effect of the atomization pressure on the nanoparticle size and morphology. The atomization pressure was increased from 2 to 9 bar while maintaining a constant flow rate by radially decreasing the annular cross-section of the atomization gas (O_2) outlet. For all conditions, transmission electrons microscopy (TEM) analysis of the nanoparticle aerosols revealed a fraction of spherical core-shell nanoparticles (Figure A.2a-d, insets). These particles were characterized by bright cores and dark shells (Figure A.2a-d,

Figure A.1) indicating a phase segregation. X-ray diffraction (XRD) revealed a crystalline structural (Figure A.3a) composed of two phases matching the peaks of hydroxyapatite ($Ca_5(PO_4)_3OH$) and calcium oxide (CaO).

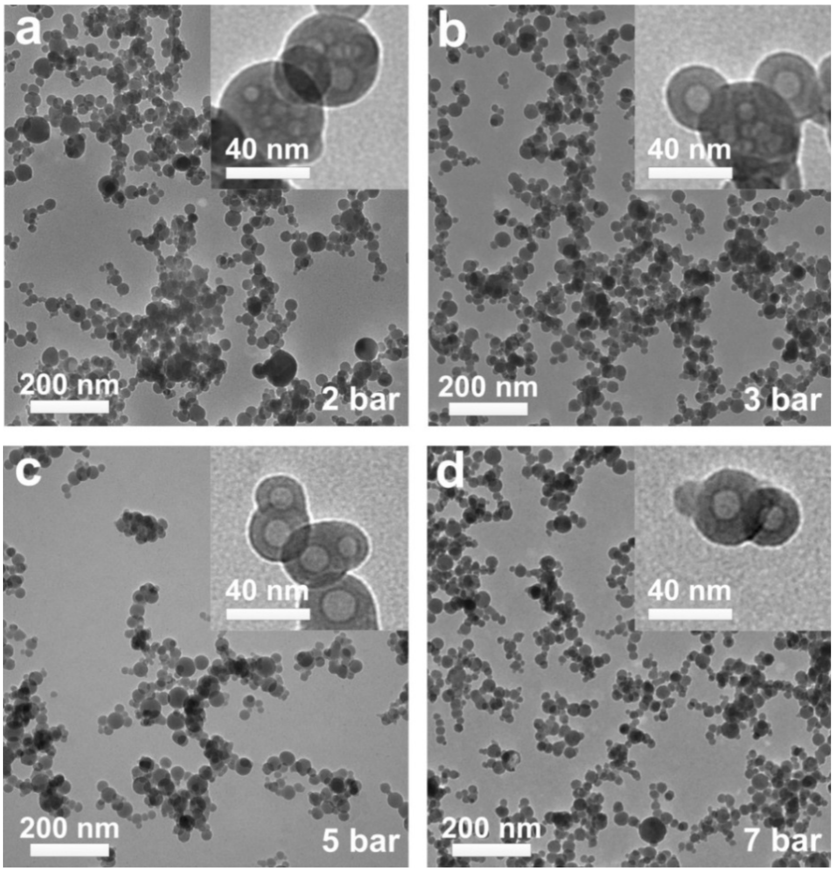

Figure A.2. *Representative transmission electron microscopy images of the flame-made HAp nanoparticle aerosols at an atomization pressure of (a) 2 bar, (b) 3 bar, (c) 5 bar and (d) 7 bar.*

At low atomization pressure (2 bar), some trace amounts of amorphous materials and/or very small crystals (< 3 nm) were indicated by an amorphous hump centered at a 2θ of 31° (Figure A.3a). The intensity of the latter decreased with increasing atomization pressure and above 5 bars highly crystalline powders were obtained. Similarly, the content of the calcium oxide impurities decreased significantly from 12% to 6% with increasing atomization pressure from 2 to 9 bar (Figure A.3a and Figure A.3b). These results were confirmed by FTIR analysis (Figure A.4). Bands commonly assigned to phosphates were observable in all samples at ~ 563, 604, 962, 1029 and 1087 cm^{-1}.[27]

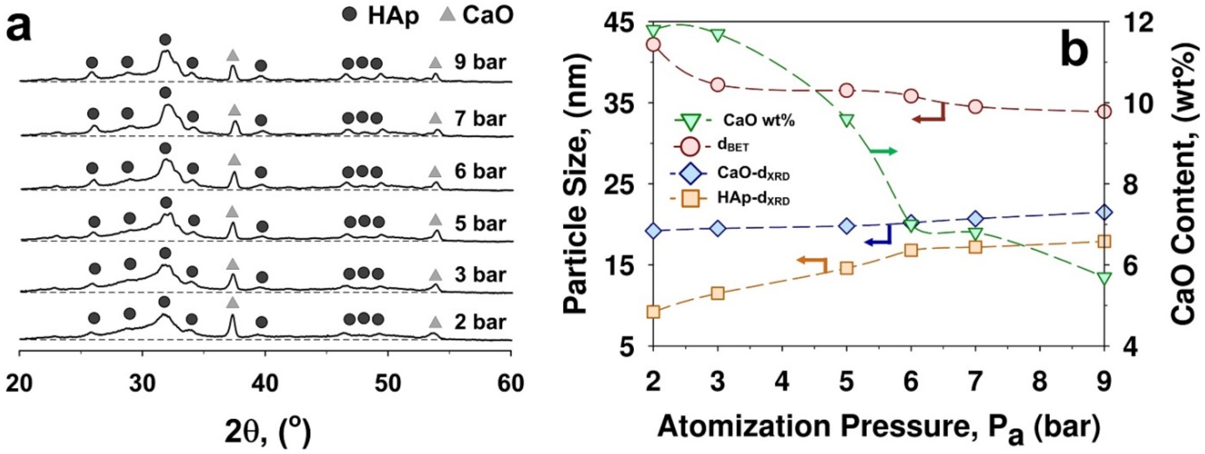

Figure A.3. *(a) Composition of the as-prepared HAp nanoparticles as a function of the atomization pressure by X-ray diffraction. (b) The particle size* (d_{BET})*, crystal size* (d_{XRD}) *and lime content of HAp nanoparticles collected from filter produced at atomization pressure from 2 up to 9 bar.*

The bands at 962, 1029 and 1087 cm^{-1} are attributed to the characteristic symmetric stretching of the phosphate (PO_4^{-3}) in HAp while those at 563 and 604 cm^{-1} are attributed to its bending mode.[28] A small hump centered around a wavenumber of ~875 cm^{-1} suggests partial replacement of PO_4^{-3} in HAp lattice by carbonate.[29] The incorporation of carbonate is common during the formation of biological apatite[30].

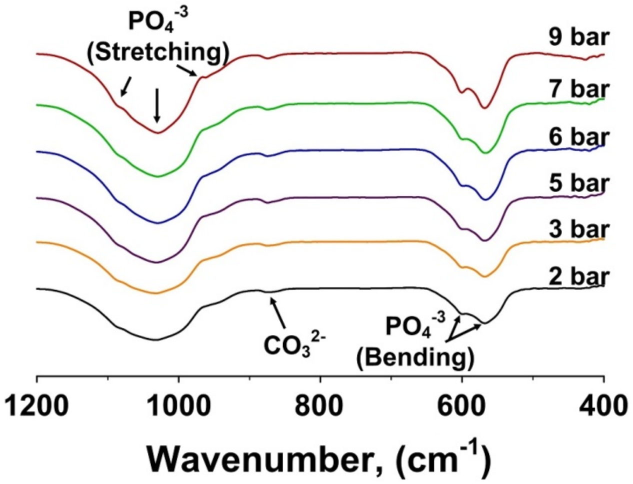

Figure A.4. *Composition of the as-prepared HAp nanoparticles as a function of the atomization pressure by Fourier transform infrared spectroscopy.*

Following the XRD phase composition, the nanoparticles' dark shells (Figure A.2a-d, Figure A.1) are attributed to the higher mass density of the CaO phase while the bright cores are associated with the hydroxyapatite phase in line with previous reports on segregated multi-components nanoparticles[31-32]. This is in good agreement with the high fraction of single-core structures observed at high atomization pressures and higher fraction of multi-core particles at low atomization pressures (Figure A.2a-d, insets).

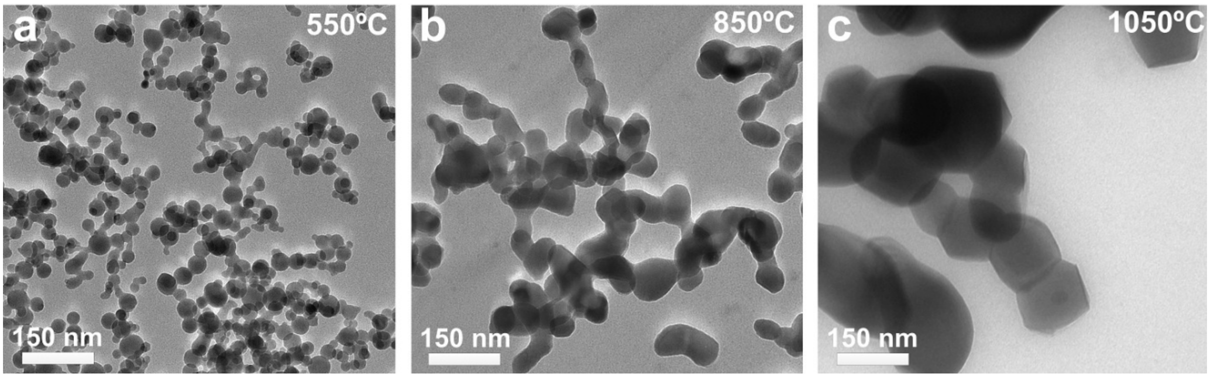

Figure A.5. *Representative TEM images of flame-made HAp nanoparticles upon sintering for 1 h at (a) 550 °C, (b) 850 °C and (c) 1050 °C.*

In fact, the HAp crystal size increased from 9 nm to 17.5 nm and the calcium oxide crystal size increased from 19 nm to 21.5 nm with increasing atomization pressure from 2 to 9 bar (Figure A.3b). The high amount of crystalline HAp, obtained here, is attributed to high partial water pressure[33] obtained by oxidation of the precursor solution. Its segregation in the particle core is tentatively attributed to the rapid heating and high temperatures experienced by the particles during their residence time in the flame that may lead to dehydroxylation of their surface. Higher atomization pressures are expected to result in smaller droplets and a shorter high temperature residence. This could decrease surface dehydroxylation and promote the formation of larger crystalline nanoparticle cores. Increasing the moderate temperature residence time (e.g. with an hot wall reactor) of the optimally synthesized core-shell nanoparticles at an atomization pressure of 7 bar is expected to eventually lead to fully crystalline single-phase HAp nanoparticles. This is in good agreement with the TEM analysis

(Figure A.2d, inset) showing an increase in HAp core with increasing atomization pressure from 2 to 7 bar. As a result, a pressure of 7 bar was chosen as the optimal atomization condition as it led to 94wt% of crystalline HAp phase and warranted stable spray flame conditions.

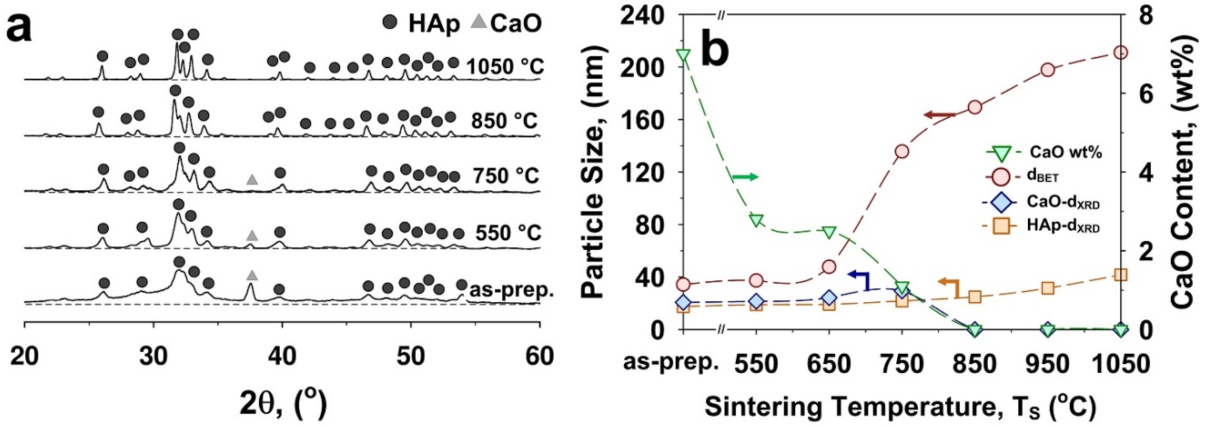

Figure A.6. *The (a) XRD patterns and b) particle size (d_{BET}), crystal size (d_{XRD}) and CaO content of HAp nanoparticles as a function of the sintering temperature.*

The synthesis mechanism of these core-shell nanoparticles is further analyzed below along their process parameters and thermodynamic stability. The sintering temperature had a significant impact on the particle morphology and composition (Figure A.5a-c**)**. Already at 550 ºC, formation of hard agglomerates was observed and the as-prepared core-shell morphology was replaced by a uniform composition (Figure A.5a-c). This is in contrast with the high thermal stability of crystalline HAp and suggests that the as-prepared nanoparticles are meta-stable nanocomposites captured due to the strong quenching in the flame reactors. In fact, the particle diameter (d_{BET}) increased from 35 to 210 nm with increasing sintering temperature from as-prepared to 1050 °C (Figure A.5c and Figure A.6b, red circles). Simultaneously, the HAp and calcium oxide crystal sizes increased from 17 and 20 nm to 22 and 30 nm, respectively, with increasing sintering temperature from as-prepared to 750 °C (Figure A.6b). This also led to a rapid drop in the CaO content from 7 wt% to less than 1 wt%

(Figure A.6b, green triangles). Sintering temperatures above 850 °C led to a pure HAp phase with no detectable trace of calcium oxide and other impurities (Figure A.6a).

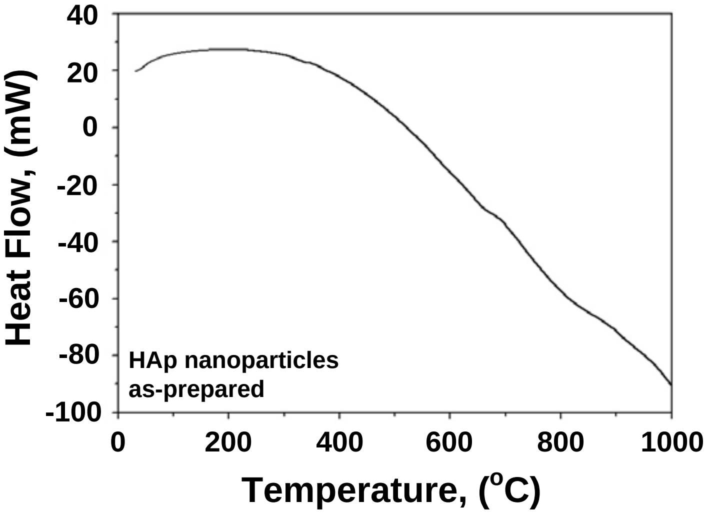

Figure A.7. *Differential scanning calorimetry (DSC) of the HAp nanoparticles collected from filter at an atomization pressure of 7 bar reveals no crystallization and decomposition up to 1000 ºC.*

These nanoparticle aerosols were further investigated by DSC and FTIR analysis. The former (Figure A.7) indicates that no amorphous to crystalline phase transformation and decomposition occurs up to 1000 ºC. This is in very good agreement with previous studies[23,34] and the very low content of calcium oxide impurities (≤ 6 wt%) of the as-prepared samples. The small nicks observed below 700 ºC and close to 900 ºC are within instrument accuracy. Figure A.8 shows the FTIR analysis of the HAp particles as a function of the sintering temperatures. Compared to the as-prepared particles (Figure A.4), the sintered ones showed characteristics of larger HAp crystals with well distinguishable FTIR peaks. A major difference notable in the sintered samples was the presence of OH band at 630 cm^{-1}. In contrast, the FTIR spectra of the (as-prepared) particles containing CaO did not have this OH band. This is commonly attributed to the stretching vibration mode of lattice OH.[27] Its post-sintering appearance is attributed to the transformation of the calcium oxide shell (CaO) into stoichiometric HAp ($Ca_5(PO_4)_3OH$) in good agreement with the XRD analysis (Figure A.6a).

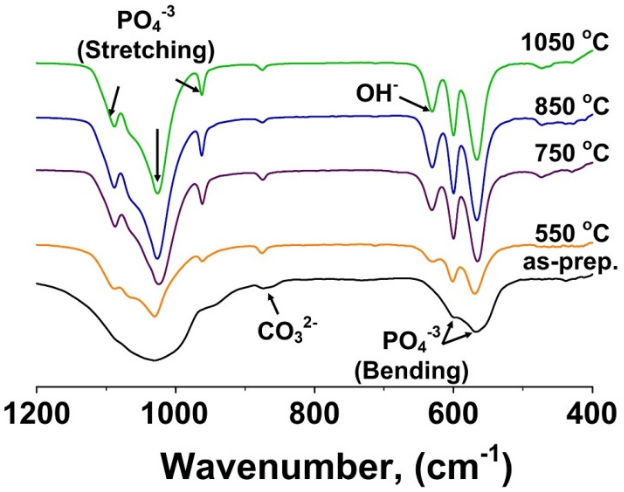

Figure A.8. *The FTIR spectra of HAp nanoparticles as a function of the sintering temperature.*

A.3.2 Rapid Nanofabrication of Biomimetic and Robust UNN

Ultra-porous nanoparticle networks were rapidly (< 30 s) fabricated by hierarchical self-assembly of these aerosols on Ti-alloys, commercially utilized for bone implants. The substrates were orthogonally aligned to the spray flame (Figure A.1) and at 6 cm height above the burner head resulting in a surface temperature of 1000 ± 10 ºC. This temperature is lower than that commonly utilized for commercial plasma spraying coating (> 1200 ºC)[35-36] and did not have any detectable effect on the substrate.

Figure A.9a shows a typical UNN film obtained by 10 s exposure of the substrate to the hot nanoparticle aerosols. The resulting film had a three-dimensional micro- and nano-scale surface roughness (Figure A.9a) characterized by large micro-scale pores surrounded by dense agglomerated regions. Analysis of the film cross-sections (Figure A.9b) revealed a homogeneous morphology over several hundred micrometres with a thickness of 19 μm and variations in the order of ± 2 μm. The substrate-film interface was continuous with no visible cracks and delamination suggesting a robust bond between the film and the Ti-alloy. An initial analysis of the bonding strength of the HAp/Ti interface was performed by 10 cycle abrasion tests with a Taber abrasion instrument (Dongguan Jianqiao Testing Equipment Co., LTD, Model JQ-802A) revealing a promising mechanical stability. In contrast to previous studies on UNN, the HAp films survived the capillary forces during immersion in simulated body fluid[18]. Further studies are required to provide a full characterization of the structural properties of these coatings.

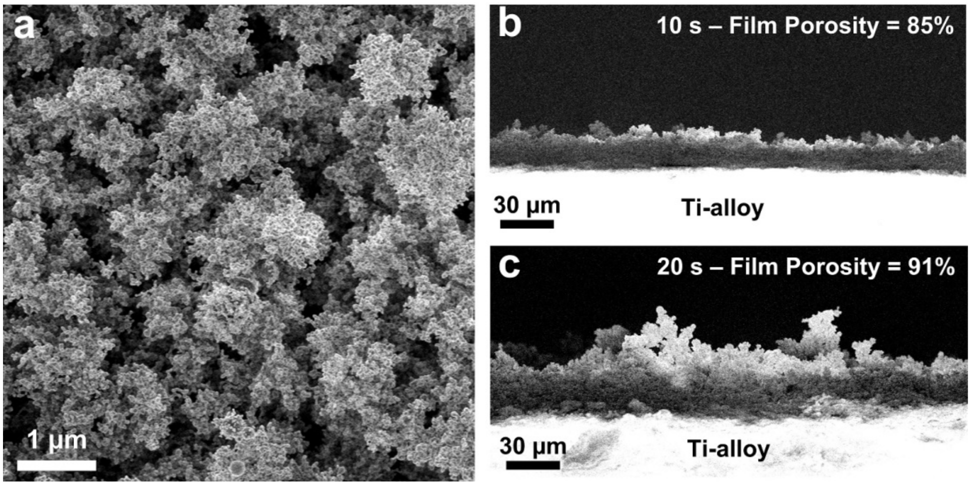

Figure A.9. *(a) Representative SEM images of an exemplary ultra-porous HAp nanoparticle network (UNN) self-assembled for 10 s on the surface of a Ti-alloy substrate. Cross-section SEM analyses of the (b,c) UNN coatings obtained at 10 and 20 s aerosol-deposition time. The cross-section SEM images in panel b and c are at the same scale.*

Furthermore, increasing the deposition time from 10 s to 20 s, increased the film thickness from 19 to 36 μm (Figure A.9b-c). This results in a very high film growth rate of 1.8 μm s^{-1}. Constant, but significantly lower film growth rates of 7 nm s^{-1} have been reported also for deposition of flame-made TiO_2[37] nanoparticles and are in line with that expected for thermophoretically-driven deposition[38]. The increase in surface roughness with increasing thickness is in good agreement with recent models of the self-assembly of nanoparticles from the gas phase onto solids[39]. The latter predicts that in the diffusion regime the density of first nanoparticle layers are up to 5 times higher than that obtained far from the surface where micro-scale branch-like agglomerated are formed.[39]

The film porosity was computed from the SEM cross-sectional thickness and deposited film mass density (Figure A.10). The latter increased from 0.54 to 0.99 mg cm^{-2} with increasing deposition time from 5 to 25 s. It is important to notice that during the first 10 s the surface of the substrate heats rapidly from room temperature to ca. 1000 ºC. This decreases the thermophoretically driven particle flux from 0.1077 mg cm^{-2} s^{-1} upon 5 s to 0.0083 mg cm^{-2} s^{-1} upon 15 s. The latter deposition rate remained constant with no variations up to the longest deposition time (25 s) investigated here. In contrast to previous studies,[18,25] the porosity increased from 81% to 93% with increasing deposition time from 5 to 25 s (Figure A.10). These porosities are significantly lower than that previously achieved by low (98%)[18,40] and moderate temperature (95%)[25] deposition of flame-made metal-oxide nanoparticles. This is attributed to the low thermodynamic stability of the core-shell nanoparticles undergoing in-situ sintering on the substrates during deposition from the gas-phase.

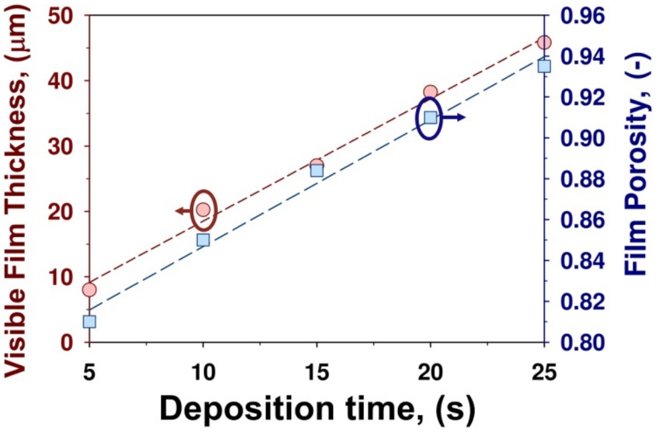

Figure A.10. *(a) Visible film thickness and porosity, (b) XRD patterns and (c) FTIR spectra of the HAp coatings as a function of the aerosol-deposition time.*

The UNN self-assembly dynamics was investigated as a function of the deposition time by TEM (Figure A.11), XRD (Figure A.12a) and FTIR analysis (Figure A.12b). All the as-prepared coatings had a pure HAp composition (Figure A.12) with no trace of CaO and/or other amorphous impurities. The relative intensity of the HAp peaks increased rapidly with increasing time in line with the rapid increase in film mass density. The HAp crystal size increased from 40 to 67 nm with increasing deposition time from 5 to 25 s. This is up to 4 times larger than the crystal size of the particles collected from the aerosols at the same atomization pressure (Figure A.3b). It confirms that significant densification of the coatings is due to in-situ sintering during deposition. The higher porosity of the thicker films is attributed to the self-assembly dynamics leading both to less particle neighbors and larger inter-branch pore as the film thickness increases[39].

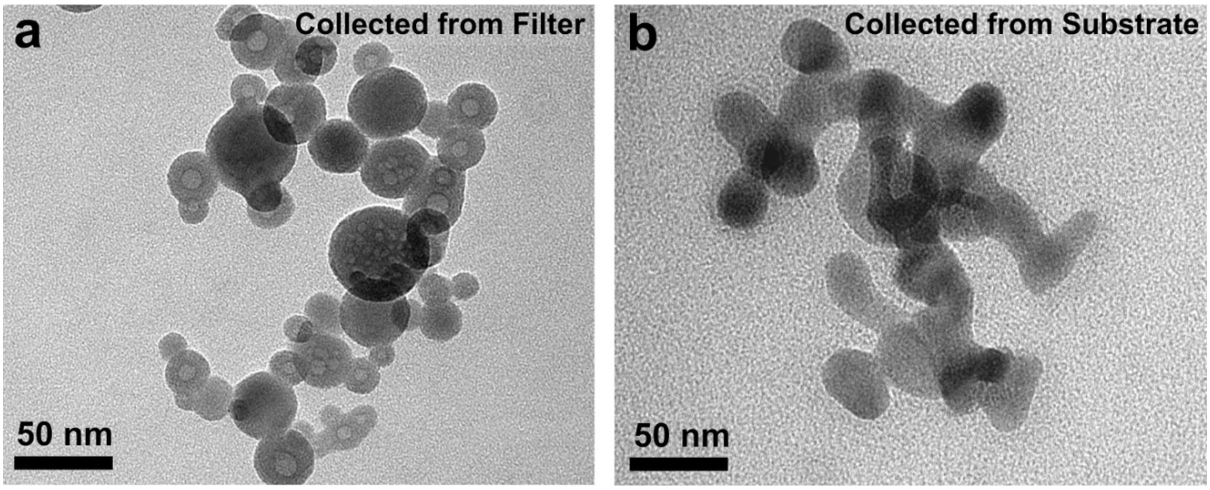

Figure A.11. *TEM images of the particles collected from (a) the filter and (b) removed from the substrates after 5 s aerosol-deposition.*

TEM analysis of the HAp particles collected from the substrates (Figure A.11b) revealed that all the core-shell structure had undergone a phase transformation resulting in a homogeneous HAp composition similar to that obtained upon sintering at 800 °C. The purity of the as-prepared coatings was assessed by FTIR analysis (Figure A.12b) revealing a pure inorganic composition. The FTIR main peaks at 550 - 606 cm^{-1} and 960 - 1080 cm^{-1} were attributed to the phosphate bonding and stretching, respectively. This is in line with previous studies and further confirms the achievement of a highly pure HAp phase. This is particularly important as the presence of CaO in HAp ceramics, designed for medical applications, is not desirable due to the conversion of CaO into $Ca(OH)_2$.[33] This results in gradual tension and formation of hairline cracks in the ceramic material[41] undermining its mechanical properties.

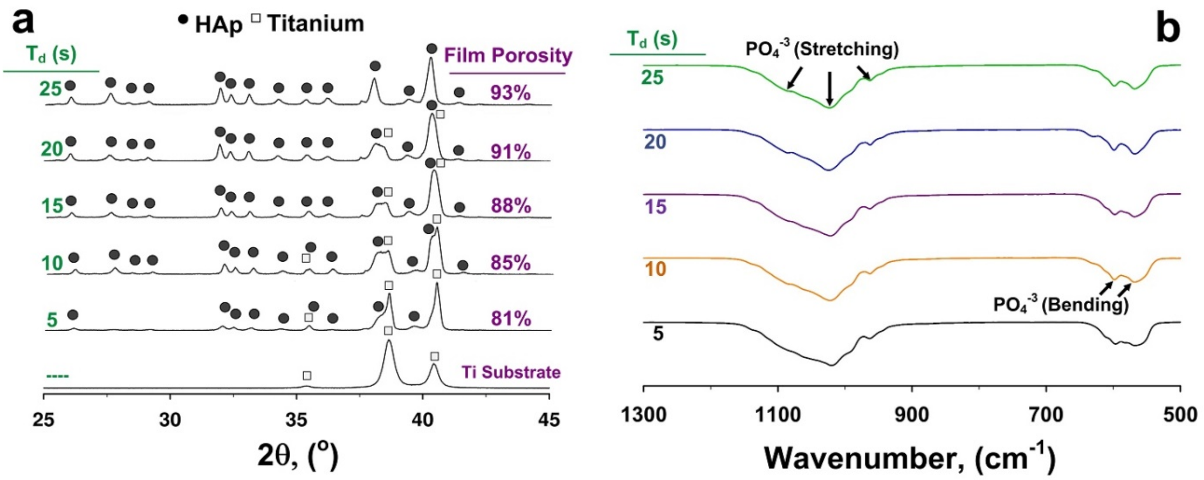

Figure A.12. *(a) XRD patterns and (b) FTIR spectra of the HAp coatings as a function of the aerosol-deposition time.*

A.3.3 Cellular adhesion and Infiltration

Promoting **c**ellular adhesion and infiltration into the ultra-porous HAp coatings are recognized as the first key steps for improving the osseointegration on metallic implants. Here, the biological performance of these three-dimensional UNN morphologies was explored using primary Swiss mice osteoblasts as a representative system for the interface of bone implants. To this aim, murine femur cells with osteocalcin producing osteoblasts were cultured in triplicate on HAp coated and spin coated Titanium alloys. Figure A.13 shows magnifications of SEM micrographs depicting cell-cell and cell-coating interactions after 14 days on a UNN and a spin-coated surface. The osteoblast were firmly attached to the ultra-porous coating (Figure A.13b) and responded to its morphology by formation of nano-scale filopodia of less than 100 nm in diameter (Figure A.13c-d). Filopodia are cytoskeletal projections of the cell membrane that probe the microenvironment and are known as a mode of recognition and interaction for the cells[42]. The latter infiltrated the coatings through its macro- and nano-pores. Here, a unique extensive penetration of nano-scale filopodia and cell infiltration into the inorganic coatings was observed. Previous studies[43-44] have reported that highly branched cellular morphologies on Ti implant surfaces resulted in higher mineralization with no significant differences in cell viability when compared with control substrate. Thus, this cellular response to our UNN indicates that our structures have higher osseointegration and in turn higher osteoconductivity than current plasma spraying technologies.

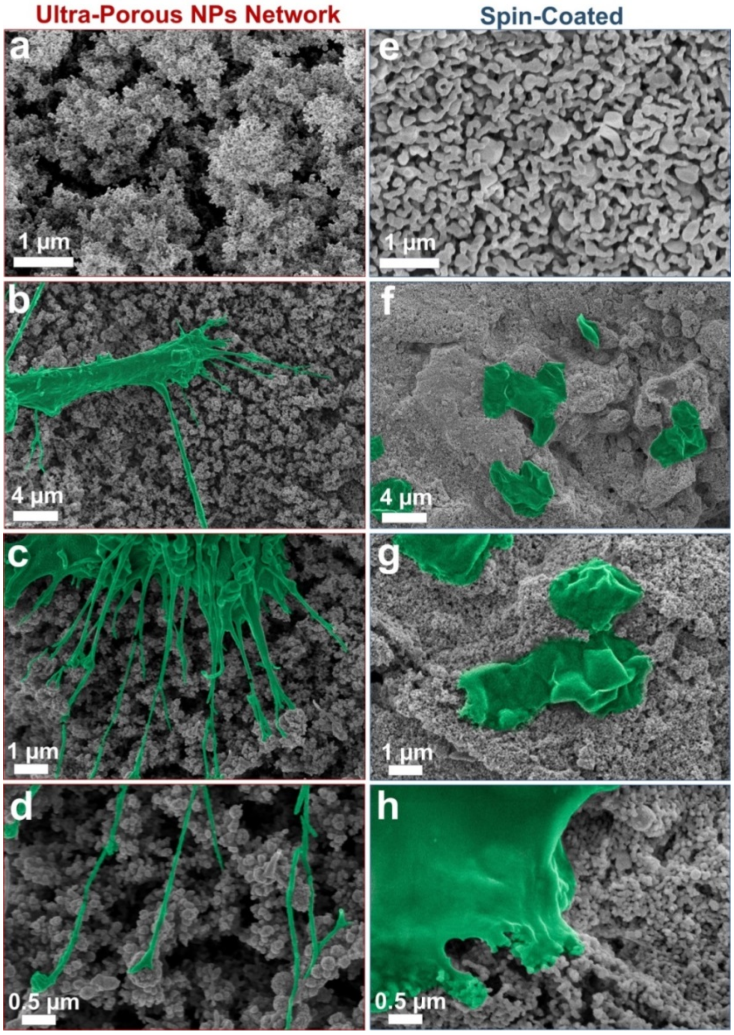

Figure A.13. *Representative SEM images of (a) the flame-made UNN and (b) dense spin-coated surface. False colored SEM micrographs of the osteoblast growth after 14 days on the surface of the (b-d) UNN and (f-h) dense spin-coated surfaces. On the ultra-porous nanoparticle network surface, the cell-cell and cell-materials interactions resulted in a visible attachment of osteoblasts to the coating surface (b-c). Magnifications show (d) the formation of nano-scale filopodia. In stark contrast, no cellular infiltration and filopodia formation was observed on the dense spin-coated surfaces (f-h).*

In stark contrast, the dense morphology obtained by spin-coating of the same flame-made nanoparticles resulted in poor cell adhesion and infiltration. These spin-coated surfaces were characterized by a smoother morphology having similar nano-scale texture (Figure A.13e) to the UNN coatings (Figure A.13a) but lacking the hierarchical micro-structure of the latter (Figure A.13a). SEM analysis of these spin-coated samples revealed that most of the cells failed to adhere to the nano-textured surface (Figure A.13f-h). Furthermore, no cellular infiltration and filopodia formation was observed. This cellular response is similar to that obtained with other approaches such as plasma spray,[45-46] sol-gel[47] and magnetron sputtering[45] that have been extensively used to fabricate nanostructured HAp surfaces[47]. These dense morphologies have not resulted in cellular infiltration inside the coating structure and only seldom in micro-scale filopodia formation. This is attributed to their micro-scale flat surface that do not may also result in poor cell adhesion.[48]

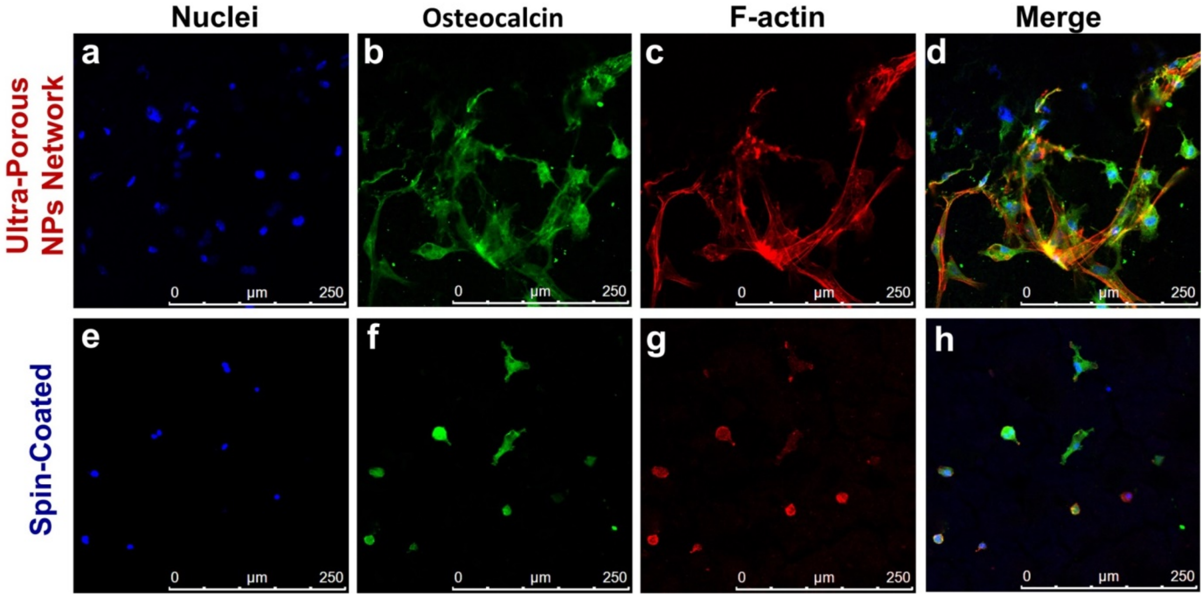

Figure A.14. *Immunostaining images of (a,e) Nuclei, (b.f) Osteocalcin and (c,g) F-Actin proteins on the surface of (a-d) the UNN self-assembled with an aerosol-deposition time of 20 s and (e-h) spin-coated sample. Topographical merge of the Nuclei, F-Actin and Osteocalcin distribution on (d) flame-made and (h) spin-coated samples.*

The very positive response of the osteoblasts to the UNN morphology was confirmed by immunostaining analysis of two key cytoskeletal markers, F-Actin (Figure A.14a) and Osteocalcin (Figure A.14b). Osteocalcin is a non-collagenous protein that is known to be secreted only by functional bone forming cells, osteoblasts.[49] F-Actin is a linear polymer microfilament that is essential for cellular functions such as mobility and contraction during division. The expression of cytoplasmic F-Actin and secreted osteocalcin (Figure A.14c) by bone cells on these ultra-porous and micro-rough morphologies suggest that its three-dimensional structure and composition positively influence the key cellular processes such as adhesion and protein expression. Both are required for osteoconduction and long-term osseointegration of bone implants.

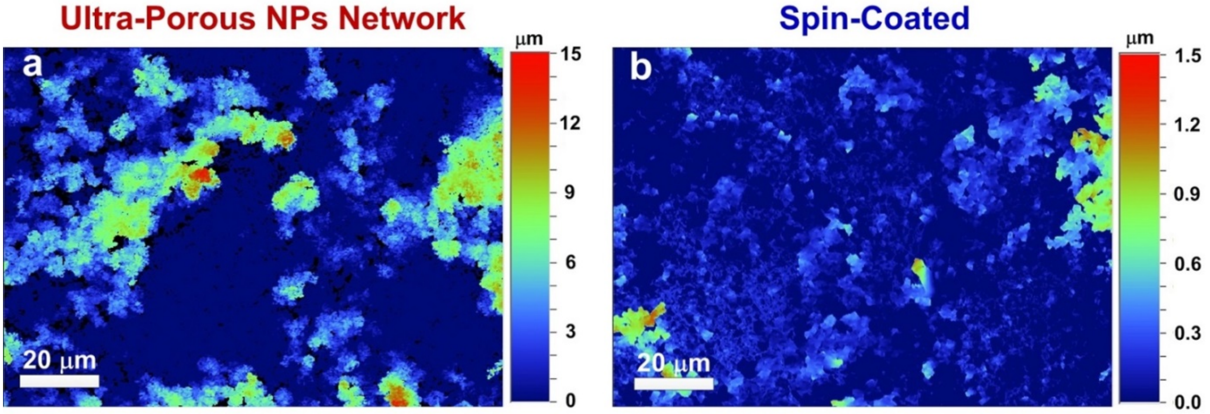

Figure A.15. *White Light Interferometry (WLI) micrographs of (a) ultra-porous HAp coating with 25 seconds deposition time compared to (b) spin-coated films.*

In natural bone, the structure of the extracellular matrix and function of cells are regulated by macro- and nano-scale cues provided by both the stroma and parenchyma. These include a pure composition, micro- and nano-scale pore sizes and, in the most active regions of the bone, up to 93% porosity that are all well matched by these flame-made structures. The pore size distribution of the flame-made coatings was investigated by white light interferometry (WLI) and shows that the pore size reaches up to hundreds of micrometer (Figure A.15a). Although this is still lower than that of cancellous bone, it is a significant improvement over plasma-sprayed coatings and spin-coating (Figure A.15b), where the coatings feature flat surfaces or sub-micrometer pore size distributions. These promising results substantiated by the excellent morphological response of the osteoblasts suggest that the UNN morphology is highly desirable for cellular growth.[50-51]

A.4. Conclusions

In summary, we have presented a biomimetic, fully inorganic material structure for tissue engineering that can be ultilized to study the early events of osseointegration and osteoconduction. Ultra-porous nanoparticle networks of nanocrystalline hydroxyapatite with up to 93% porosity were fabricated by a scalable and low-cost approach that enables the ultra-rapid coating of commercial grade implants. The response of bone cells to these morphologies was assessed by primary osteoblast cultures. It was found that the nano- and micro-scale hierarchical structures of the UNN surface demonstrated superior cell infiltration and nanoscale cell-cell and cell-biomaterial interaction that can result in enhanced osseointegration. These promising results demonstrate the potential of this scalable synthetic platform and structural design for the fabrication of biomaterials for bone tissue engineering with application extending from osseointegration of implantable devices to regenerative medicine.

A.5. References

1. Liu, K.; Yu, D.; Cho, Y.-Y.; Bode, A. M.; Ma, W.; Yao, K.; Li, S.; Li, J.; Bowden, G. T.; Dong, Z.; Dong, Z., Sunlight UV-Induced Skin Cancer Relies upon Activation of the p38α Signaling Pathway. *Cancer Res.* **2013,** *73*, 2181-2188.

2. Smirnov, J. R. C.; Calvo, M. E.; Míguez, H., Selective UV Reflecting Mirrors Based on Nanoparticle Multilayers. *Adv. Funct. Mater.* **2013,** *23*, 2805-2811.

3. King, D. M.; Liang, X.; Carney, C. S.; Hakim, L. F.; Li, P.; Weimer, A. W., Atomic Layer Deposition of UV-Absorbing ZnO Films on SiO_2 and TiO_2 Nanoparticles Using a Fluidized Bed Reactor. *Adv. Funct. Mater.* **2008,** *18*, 607-615.

4. Nakamura, S.; Takeda, H.; Yamashita, K., Proton transport polarization and depolarization of hydroxyapatite ceramics. *J. Appl. Phys.* **2001,** *89*, 5386-5392.

5. Clarke, B., Normal Bone Anatomy and Physiology. *Clin. J Am. Soc. Nephrol.* **2008,** *3*, S131-S139.

6. Gilbert, R. P.; Liu, Y.; Groby, J.-P.; Ogam, E.; Wirgin, A.; Xu, Y., Computing porosity of cancellous bone using ultrasonic waves, II: The muscle, cortical, cancellous bone system. *Math. Comput. Model.* **2009,** *50*, 421-429.

7. Renders, G. A. P.; Mulder, L.; Van Ruijven, L. J.; Van Eijden, T. M. G. J., Porosity of human mandibular condylar bone. *J. Anat.* **2007,** *210*, 239-248.

8. Yeung, W. K.; Reilly, G. C.; Matthews, A.; Yerokhin, A., In vitro biological response of plasma electrolytically oxidized and plasma-sprayed hydroxyapatite coatings on Ti–6Al–4V alloy. *J. Biomed. Mater. Res., Part B* **2013,** *101B*, 939-949.

9. Roest, R.; Latella, B. A.; Heness, G.; Ben-Nissan, B., Adhesion of sol–gel derived hydroxyapatite nanocoatings on anodised pure titanium and titanium (Ti6Al4V) alloy substrates. *Surf. Coat. Technol.* **2011,** *205*, 3520-3529.

10. Layrolle, P.; Ito, A.; Tateishi, T., Sol-Gel Synthesis of Amorphous Calcium Phosphate and Sintering into Microporous Hydroxyapatite Bioceramics. *J. Am. Ceram. Soc.* **1998,** *81*, 1421-1428.

11. López, E. O.; Mello, A.; Sendão, H.; Costa, L. T.; Rossi, A. L.; Ospina, R. O.; Borghi, F. F.; Silva Filho, J. G.; Rossi, A. M., Growth of Crystalline Hydroxyapatite Thin Films at Room Temperature by Tuning the Energy of the RF-Magnetron Sputtering Plasma. *ACS Appl. Mater. Interfaces* **2013,** *5*, 9435-9445.

12. Carradò, A., Nano-crystalline pulsed laser deposition hydroxyapatite thin films on Ti substrate for biomedical application. *J. Coating Tech. Res.* **2011,** *8*, 749-755.

13. Cheng, G. J.; Pirzada, D.; Cai, M.; Mohanty, P.; Bandyopadhyay, A., Bioceramic coating of hydroxyapatite on titanium substrate with Nd-YAG laser. *Mater. Sci. Eng. C* **2005,** *25*, 541-547.

14. Gamblin, A.-L.; Brennan, M. A.; Renaud, A.; Yagita, H.; Lézot, F.; Heymann, D.; Trichet, V.; Layrolle, P., Bone tissue formation with human mesenchymal stem cells and biphasic calcium phosphate ceramics: The local implication of osteoclasts and macrophages. *Biomaterials* **2014,** *35*, 9660-9667.

15. Agar, N. S.; Halliday, G. M.; Barnetson, R. S.; Ananthaswamy, H. N.; Wheeler, M.; Jones, A. M., The basal layer in human squamous tumors harbors more UVA than UVB fingerprint mutations: A role for UVA in human skin carcinogenesis. *Proc. Natl. Acad. Sci. U S A* **2004,** *101*, 4954-4959.

16. Taoye, W.; Tayirjan, T. I.; Jianfeng, C.; Sohrab, R., Transparent Nanostructured Coatings with UV-Shielding and Superhydrophobicity Properties. *Nanotechnology* **2011,** *22*, 265708.

17. Tricoli, A.; Pratsinis, S. E., Dispersed Nanoelectrode Devices. *Nature Nanotechnol.* **2010,** *5*, 54-60.

18. Tricoli, A.; Graf, M.; Mayer, F.; Kuühne, S.; Hierlemann, A.; Pratsinis, S. E., Micropatterning Layers by Flame Aerosol Deposition-Annealing. *Adv. Mater.* **2008,** *20*, 3005-3010.

19. Godar, D. E.; Lucas, A. D., Spectral Dependence of UV-Induced Immediate and Delayed Apoptosis: The Role of Membrane and DNA Damage. *Photochem. Photobiol.* **1995,** *62*, 108-113.

20. Nasiri, N.; Bo, R.; Wang, F.; Fu, L.; Tricoli, A., Ultraporous Electron-Depleted ZnO Nanoparticle Networks for Highly Sensitive Portable Visible-Blind UV Photodetectors. *Adv. Mater.* **2015,** *27*, 4336-4343.

21. Tricoli, A.; Righettoni, M.; Teleki, A., Semiconductor Gas Sensors: Dry Synthesis and Application. *Angew. Chem. Int. Ed.* **2010,** *49*, 7632-7659.

22. Ataol, S.; Tezcaner, A.; Duygulu, O.; Keskin, D.; Machin, N., Synthesis and characterization of nanosized calcium phosphates by flame spray pyrolysis, and their effect on osteogenic differentiation of stem cells. *J. Nanopart. Res.* **2015,** *17*, 1-14.

23. Cho, J. S.; Kang, Y. C., Nano-sized hydroxyapatite powders prepared by flame spray pyrolysis. *J. Alloys Compd.* **2008,** *464*, 282-287.

24. Loher, S.; Stark, W. J.; Maciejewski, M.; Baiker, A.; Pratsinis, S. E.; Reichardt, D.; Maspero, F.; Krumeich, F.; Günther, D., Fluoro-apatite and Calcium Phosphate Nanoparticles by Flame Synthesis. *Chem. Mater.* **2005,** *17*, 36-42.

25. Tricoli, A.; Wallerand, A. S.; Righettoni, M., Highly Porous TiO_2 Films for Dye Sensitized Solar Cells. *J. Mater. Chem.* **2012,** *22*, 14254.

26. Mueller, R.; Mädler, L.; Pratsinis, S. E., Nanoparticle synthesis at high production rates by flame spray pyrolysis. *Chem. Eng. Sci.* **2003,** *58*, 1969-1976.

27. Qi, C.; Zhu, Y.-J.; Lu, B.-Q.; Zhao, X.-Y.; Zhao, J.; Chen, F.; Wu, J., Hydroxyapatite Hierarchically Nanostructured Porous Hollow Microspheres: Rapid, Sustainable Microwave-Hydrothermal Synthesis by Using Creatine Phosphate as an Organic Phosphorus Source and Application in Drug Delivery and Protein Adsorption. *Chem. Eur. J.* **2013,** *19*, 5332-5341.

28. Amer, W.; Abdelouahdi, K.; Ramananarivo, H. R.; Zahouily, M.; Fihri, A.; Djessas, K.; Zahouily, K.; Varma, R. S.; Solhy, A., Microwave-assisted synthesis of mesoporous nano-hydroxyapatite using surfactant templates. *CrystEngComm* **2014,** *16*, 543-549.

29. Yamaguchi, I.; Tokuchi, K.; Fukuzaki, H.; Koyama, Y.; Takakuda, K.; Monma, H.; Tanaka, J., Preparation and microstructure analysis of chitosan/hydroxyapatite nanocomposites. *J. Biomed. Mater. Res.* **2001,** *55*, 20-27.

30. Chickerur, N. S.; Tung, M. S.; Brown, W. E., A mechanism for incorporation of carbonate into apatite. *Calcif Tissue Int* **1980,** *32*, 55-62.

31. Wilson, D. A.; Nolte, R. J. M.; van Hest, J. C. M., Autonomous movement of platinum-loaded stomatocytes. *Nature Chem.* **2012,** *4*, 268-274.

32. van Rhee, P. G.; Rikken, R. S. M.; Abdelmohsen, L. K. E. A.; Maan, J. C.; Nolte, R. J. M.; van Hest, J. C. M.; Christianen, P. C. M.; Wilson, D. A., Polymersome magneto-valves for reversible capture and release of nanoparticles. *Nature Commun.* **2014,** *5*, 5010.

33. Gross, K.; Berndt, C., Thermal processing of hydroxyapatite for coating production. *J. Biomed. Mater. Res.* **1998,** *39*, 580-587.

34. Cho, J. S.; Jung, D. S.; Han, J. M.; Kang, Y. C. In *Spherical shape hydroxyapatite powders prepared by flame spray pyrolysis*, J. Ceram. Proc. Res, 2008; pp 348-352.

35. Grinys, T.; Tamulevicius, S.; Zadvydas, M., Control of the substrate temperature during plasma spray deposition. *Mater. Sci.* **2004,** *10*, 221-224.

36. Berndt, C. C.; Hasddad, G. N.; Farmer, A. J. D.; Gross, K. A., Thermal spraying for bioceramic applications. *Mater. Forum* **1990,** *14*, 161-173.

37. Tricoli., A.; Righettoni., M.; Pratsinis., S. E., Anti-Fogging Nanofibrous SiO_2 and Nanostructured SiO_2-TiO_2 Films Made by Rapid Flame Deposition and in Situ Annealing. *Langmuir* **2009,** *25*, 12578-12584.

38. Tricoli, A.; Elmøe, T. D., Flame spray pyrolysis synthesis and aerosol deposition of nanoparticle films. *AIChE J.* **2012,** *58*, 3578-3588.

39. Nasiri, N.; Elmoe, T. D.; Liu, Y.; Qin, Q. H.; Tricoli, A., Self-assembly dynamics and accumulation mechanisms of ultra-fine nanoparticles. *Nanoscale* **2015,** *7*, 9859-9867.

40. Mädler, L.; Roessler, A.; Pratsinis, S. E.; Sahm, T.; Gurlo, A.; Barsan, N.; Weimar, U., Direct formation of highly porous gas-sensing films by in situ thermophoretic deposition of flame-made Pt/SnO_2 nanoparticles. *Sens. Actuators B Chem.* **2006,** *114*, 283-295.

41. Sobczak-Kupiec, A.; Wzorek, Z., The influence of calcination parameters on free calcium oxide content in natural hydroxyapatite. *Ceram. Int.* **2012,** *38*, 641-647.

42. Hotulainen, P.; Lappalainen, P., Stress fibers are generated by two distinct actin assembly mechanisms in motile cells. *J. Cell Biol.* **2006,** *173*, 383-394.

43. Engel, E.; Del Valle, S.; Aparicio, C.; Altankov, G.; Asin, L.; Planell, J. A.; Ginebra, M.-P., Discerning the Role of Topography and Ion Exchange in Cell Response of Bioactive Tissue Engineering Scaffolds. *Tissue. Eng. Part A* **2008,** *14*, 1341-1351.

44. Ellingsen, J. E., Surface configurations of dental implants. *Periodontol. 2000* **1998,** *17*, 36-46.

45. Philipp, M.; Aleksandrova, R.; Muller, U.; Ostermeyer, M.; Sanctuary, R.; Muller-Buschbaum, P.; Kruger, J. K., Molecular versus macroscopic perspective on the demixing transition of aqueous PNIPAM solutions by studying the dual character of the refractive index. *Soft Matter* **2014,** *10*, 7297-7305.

46. Reyes-Coronado, D.; Rodríguez-Gattorno, G.; Espinosa-Pesqueira, M. E.; Cab, C.; Coss, R.; Oskam, G., Phase-Pure TiO_2 Nanoparticles: Anatase, Brookite and Rutile. *Nanotechnology* **2008,** *19*, 145605.

47. Hanini, F.; Bouabellou, A.; Bouachiba, Y.; Kermiche, F.; Taabouche, A.; Hemissi, M.; Lakhdari, D., Structural, Optical and Electrical Properties of TiO_2 Thin Films Synthesized by Sol-Gel Technique. *IOSR J. Eng.* **2013,** *3*, 21-28.

48. Bloebaum, R. D.; Dupont, J. A., Osteolysis from a press-fit hydroxyapatite-coated implant: A case study. *J. Arthroplasty* **1993,** *8*, 195-202.

49. Ripamonti, U.; Roden, L. C.; Renton, L. F., Osteoinductive hydroxyapatite-coated titanium implants. *Biomaterials* **2012,** *33*, 3813-3823.

50. Dalby, M. J.; McCloy, D.; Robertson, M.; Agheli, H.; Sutherland, D.; Affrossman, S.; Oreffo, R. O. C., Osteoprogenitor response to semi-ordered and random nanotopographies. *Biomaterials* **2006,** *27*, 2980-2987.

51. Dalby, M. J.; Gadegaard, N.; Herzyk, P.; Agheli, H.; Sutherland, D. S.; Wilkinson, C. D., Group analysis of regulation of fibroblast genome on low-adhesion nanostructures. *Biomaterials* **2007,** *28*, 1761-9.

Appendix B

Hierarchically-Driven Cell-Cell Communication and Coating In-Growth

Manuscript under preparation:

Noushin Nasiri, Shayanti Mukherjee, David R. Nisbet, Antonio Tricoli, “*Hierarchically-Driven Cell-Cell Communication and Coating In-Growth*”.

Abstract

Understanding the mechanisms underlying the cellular response to a micro-environment is critical to the design of programmable biomaterials for tissue engineering and regenerative medicine. State-of-the-art nano-material synthesis and self-assembly processes can produce complex structures that mimic surface properties, composition and partially the morphology of biological systems. However, determining key structural properties that control cell attachment and proliferation has been challenging, and contradictory results are currently reported for similarly nano-structured materials. Here, we investigate osteogenesis, the process of laying down new bone material by osteoblast cells, on bio-inert substrates as an exemplary implantable organic-inorganic interface with the second highest frequency of surgical applications. We identify critical multi-scale features that drastically enhance the cellular response to the same nano-texture. It is observed that ultra-porous hierarchical morphologies promote early-stage osteo-induction as indicated by extensive coating in-growth and nano-filopodia formation. We propose that cellular integration is mediated by two-way recognition of specific nano- and micro-topographical cues between the host tissue and micro-environment providing a set of determinant features for engineering of enhanced third-generation biomaterials.

B.1 Introduction

Nano-texturing has been successfully applied to numerous biological interfaces demonstrating the potential to significantly improve the interaction of bio-inert materials with a surrounding cellular matrix.[1] Amongst surgically implantable structures, the surface of bone implants has been extensively investigated due to its vast social and economic impact potential.[2] Clinical trials have recently revealed that the most frequent cause for implant failure is insufficient early-stage bone formation at the biomaterial-tissue interface after implantation.[3-4] This is driving multi-disciplinary research efforts to elucidate the response of bone cells to biocompatible surfaces and accelerate early-stage bone healing.[2]

In an attempt to improve osteo-integration, hydroxyapatite (HAp), the main inorganic component of mammalian bones, is routinely applied as thin nanocrystalline coating on implantable bio-inert supports such as a titanium-based alloys.[5] Plasma spraying has emerged as the gold standard for commercial HAp coatings due to its scalability and reliability. However, the integration of plasma-sprayed implants into the bone parenchyma is insufficient for long-term use.[6] This is mainly attributed to their dense morphology that is impenetrable to osteoblasts resulting in insufficient adhesion.[7] Although it is broadly recognized that the coating's morphology has significant impact on the cellular response,[8-9] key structural parameters to promote the sought early-stage osteo-induction and long-term bonding strength have not yet been determined.

Several processes such as plasma spraying,[10-11] sol-gel[12-13] and electron beam sputtering[14] have been successfully applied to the nano-fabrication of synthetic HAp and other biocompatible calcium phosphate-based films. Sol-gel impregnation, for example, results in mesoporous films that may enable coating in-growth, and thus provide better long-term mechanical stability. However, mesoporous films have not demonstrated significant improvements over plasma spraying.[15] A promising alternative morphology is offered by the self-assembly of nanoparticle aerosols into ultra-porous, hierarchical micro-nano structures.[16-17] This is a flexible one-step process that can be easily scaled-up utilizing state-of-the-art flame synthesis reactors[18] as low-cost and continuous nanoparticle aerosol sources.

Aerosol self-assembled coatings are characterized by up to 98% porous morphologies composed of mesoporous nanoparticle agglomerates separated by micro-sized pores.[19] Furthermore, nanoparticle aerosol self-assembly allows nano-scale control over the key structural properties such as thickness, porosity[17] and composition.[20] This enables a systematic investigation and optimization of the coating properties. A major challenge to the application of aerosol self-assembly to bone tissue regeneration is the poor adhesion and cohesion of the resulting nanoparticle network. In fact, the fragile nanoparticle ultra-porous structures obtained by aerosol deposition results in weak van der Waals adhesion and rapidly disintegrates even upon immersion in liquid solutions.[19] However, partial sintering of the depositing nanoparticles during coating self-assembly has shown to significantly increase the resulting mechanical stability at the cost of a small porosity reduction.[17]

Here, we demonstrate the feasibility of controlling the response of cells to a surface by presenting a hierarchical nano-textured micro-environment. We synthesize robust, ultra-porous, nano-crystalline HAp coatings by high temperature aerosol self-assembly. Up to five times denser coatings are obtained as a comparative morphology by spin-coating of the same flame-made nanoparticles. The impact of the coating’s key structural properties is systematically investigated by topographical mapping of the chemical and mechanical responses of osteoblast cells to gradually more hierarchical micro-environments. These findings provide new key insights and a flexible synthesis platform for the design and fabrication of enhanced biomaterials for regenerative medicine, implantable electronics and biological interfaces.

B.2 Experimental

B.2.1 Nanoparticle Aerosol Generation

Flame spray pyrolysis was used for the synthesis and direct deposition of Hydroxyapatite (HAp) nanoparticles. Nanoparticles were prepared as follows: Calcium Naphthenate (Sigma Aldrich, approx. 35% in mineral spirits (4% Ca)) and Tributyl phosphate (Sigma Aldrich, $C_{12}H_{27}O_4P$) were mixed together at a Ca/P molar ratio of 1.677, similar to bone composition. The mixture was stirred robustly for 30 min. The solution was supplied at a rate of 5 $mL.min^{-1}$ through a custom-built atomizer and dispersed into a fine spray with 5 $L.min^{-1}$ oxygen at a pressure drop of 5 bar. The spray was ignited by a supporting ring-shaped premixed methane/oxygen flame (CH_4=1.2 $L.min^{-1}$, O_2=2 $L.min^{-1}$).

B.2.2 HAp Coating Synthesis

Nanoparticles were deposited by orthogonal impingement of hot aerosol generated by FSP on the substrate placed at 6 cm height above the burner (HAB). The substrates were 1 mm thick Titanium alloy (Ti-6Al-4V, grade 5, Revolution Advanced Metals & Materials) disks with a diameter of 15 mm. Before nanoparticles deposition, the disk surface was cleaned in an ultrasonic bath with ethanol for 20 min. The aerosol temperature (T_F) on the exposed substrate surface was measured by digital thermometer (RS, model #206-3738). Dense morphologies were obtained by spin-coating of the same flame-made HAp nanoparticles collected on glass-fiber filters placed at 50 cm HAB. A quantity of 1 mL pure water and acetyl acetone with volume ratio of 10:1 was added to the 0.3 g of HAp particles with 2 droplets of Triton X-100 as a surfactant. A spin coater (VTC-100 Vacuum Spin Coater, MTI Corporation) was used at a speed of 1000 rpm for 60 s to spin-coat the above solution on the Ti disk. These films were sintered at 850 ºC for 1 h to remove all impurities and achieve a 100% pure HAp. The morphology and patterning characteristics of the deposited particles and films were investigated by a Hitachi H7100FA transmission electron microscope (TEM) at 100kV and an analytical scanning electron microscopy (Zeiss Ultraplus FESEM) at 3kV. The crystal phases, size (d_{XRD}) and surface compositions were analyzed by X-ray diffraction with a D_2 Phaser (Bruker, U.S.A) and Fourier transform infrared spectroscopy (FTIR-ATR, Bruker-Alpha, U.S.A). The average crystal sizes of the HAp and calcium oxide phases were computed form the XRD peaks in the 2θ range of 30 - 35º and 35 - 40º, respectively. The HAp specific surface area (SSA) was measured by N_2 adsorption/desorption at -196.15 ºC (Micromeritics, TriStar II, U.S.A), after degassing at 300 °C for 4 h. The HAp/Ti alloy interface strength was investigated under the ASTM D4060-14 standard with a Taber abrasion (Dongguan Jianqiao Testing Equipment Co., LTD, Model JQ-802A). The test was performed under two-body (high-stress) condition using a pair of abrading wheels 52 mm in dimeter at 250 g load. The morphology of all coatings was investigated with a Zeiss Ultraplus FE-SEM at 3 kV and white light interferometer (WLI) (Veeco, Wyko NT9100, U.S.A). High temperature differential scanning calorimetry (DSC) analysis was conducted from 30 to 1000 °C at a 10 °C min^{-1} ramp under nitrogen atmosphere in a STA 8000 (Perkin Elmer, U.S.A).

B.2.3 Cell Analysis

This study was approved by the Animal Research Ethics Committee of Australian National University (Reference Nr. A2013/41). Primary osteoblasts were isolated from femur bone of adult Swiss mice according to the ANU animal ethics guidelines. The femur was cleaned thoroughly, minced and digested using collagenase (Sigma Aldrich) at a concentration of 10 $mg.mL^{-1}$ at 37 ºC for 20 min. The digested mass was washed with 1x

Phosphate Buffered Saline (PBS) and plated on tissue culture plate (TCP) and maintained with Dulbecco's Modified Eagle's medium (DMEM - HyClone) containing 10% Foetal Bovine Serum (FBS, Gibco) and 1% Penicillin Streptomycin antibiotics (HyClone). Confluent cultures were mechanically detached using cell scrapers (HyClone) and seeded at a density of 10,000 cells per sample in 24 well plates.

B.2.4 Proliferation studies

Cell adhesion and proliferation on the scaffolds were determined using the colorimetric Vybrant MTT Proliferation assay kit as per manufacturer’s protocols (Life Technologies). For the assay, samples were rinsed with PBS to remove unattached cells and incubated with 10% MTT reagent in a serum free medium for a period of 3 h at 37 °C. Absorbance of the obtained dye was measured at 490 nm using a spectrophotometric plate reader (TECAN Infinite® 200 PRO series).

B.2.5 Immunofluorescence analysis

Isolated primary murine bone cells grown on samples were washed with PBS, and fixed with 4% paraformaldehyde (Sigma) for 10 min. Cells were permeabilized with 0.1% Triton X-100 (Sigma), blocked for non-specific staining using 3% bovine serum albumin (BSA, Sigma) and then immunostained with Phalloidin-TRITC (Millipore) and anti-osteocalcin antibody (R&D systems) for 1 h at room temperature and then, revealed with anti-species-specific Alexa fluor 488 (Life Technologies). The samples were mounted using anti-quenching mounting medium (Vectashiled, Vector laboratories) and observed under a fluorescence microscope for imaging (Olympus IX 71).

B.3 Results and Discussion

B.3.1 Aerosol Self-Assembly of Ultra-Porous Hierarchical Coatings

Aerosols of nanoparticles were synthesized by atomization, combustion and in-flame nucleation of liquid precursor solutions as recently described for other oxides[17]. Hierarchical ultra-porous coatings were obtained in one-step by deposition of these hot nanoparticle aerosols having an initial average primary particle diameter of 34 nm. To achieve sufficient coating mechanical stability, here, the deposition distance from the burner was further decreased from 10 cm of previous studies[17] to 6 cm. This resulted in in-situ sintering of the depositing nanoparticle flux and covalent bonding of the self-assembled network. Figure B.1 shows exemplary morphologies obtained by short time (≤ 25 s) orthogonal impingement of these hot nanoparticle aerosols on implantable titanium alloy substrates. For all deposition times (Table B.1), a hierarchical coating morphology was observed. This was characterized by relatively dense mesoporous agglomerates separated by large micro-sized pores (Figure B.1a,b). Cross-sectional analysis revealed uniform coating of the underlying substrate and a very rough surface structure (Figure B.1d,e). Most importantly, although the flame temperature at the deposition height was ca. 1200 °C, the coatings preserved a nano-scale texture (Figure B.1b, inset) and were constituted by only partially sintered particles of a few tens of nanometers in diameter. These results are in line with the uniform collapse and multi-center re-agglomeration of low temperature (< 150 °C) aerosol-deposited ultra-porous (ca. 98%) nanoparticle networks upon in-situ flame annealing.[19]

Here, these partially sintered coatings had significantly improved mechanical properties and were able to withstand multiple wetting-drying cycles and handling. A more compact, also mechanical stable, morphology was obtained by spin-coating and post-sintering of the same flame-made nanoparticles collected on water-cooled glass fiber filters. These coatings were visibly more dense and characterized by a smoother surface (Figure B.1f) sporadically interrupted by some cracks extending throughout their cross-section (Figure B.1c). Cracks are commonly observed in wet-deposition of thick nanoparticle layers, and are usually attributed to solvent evaporation. Higher magnification images of the crack-free regions revealed a similar nano-scale texture (Figure B.1c, inset) to the aerosol-deposited coatings with the main difference being the lack of a hierarchical multi-scale micro-structure.

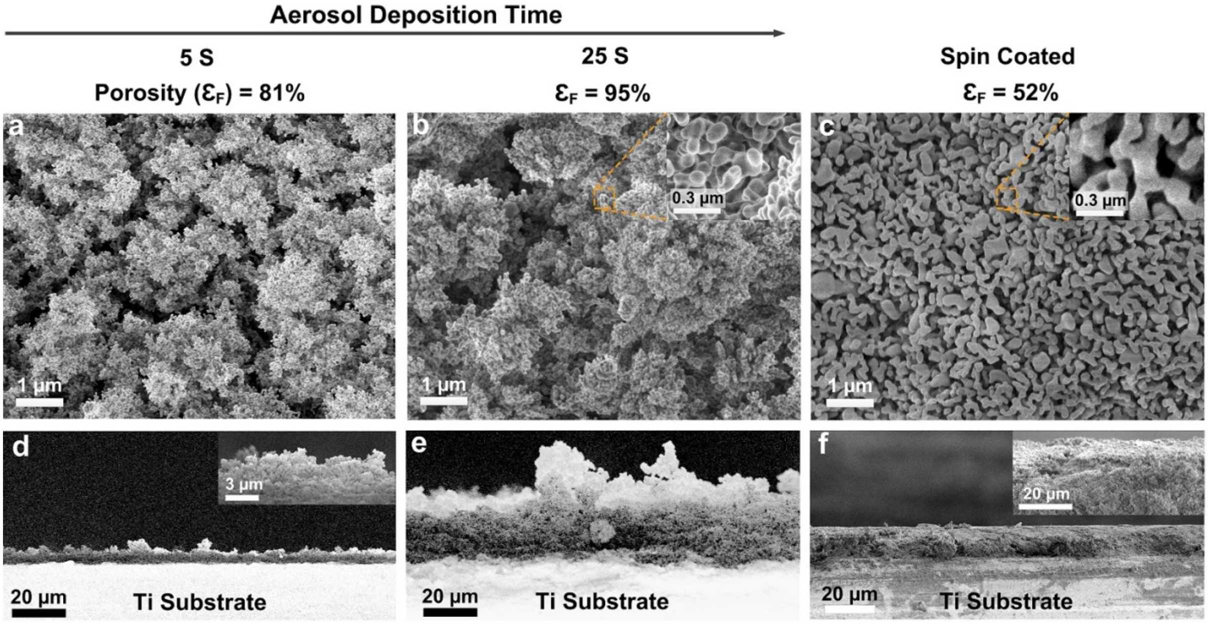

Figure B.1. *Surface morphology (a-c) and cross-section SEM images of HAp coatings on Ti substrates made by (a,d) 5 s and (b,e) 25 s aerosol-deposition and by (c,f) spin coating of the same flame-made particles.*

The surface morphology of all coatings was further investigated by white light interferometry (Figure B.2). It was found that increasing the aerosol deposition time from 5 to 25 s increased the root mean square (rms) surface roughness from 1.73 to 3.82 μm and the average coating porosity from 81% to 95%. In contrast, spin-coating led to a much less rough surface with a rms of 0.91 μm and an average porosity of 52%. These robust and well-reproducible coating morphologies enabled us to investigate the cellular response to similarly nano-textured crystalline HAp environments presenting, however, a systematically increased level of micro-structural hierarchy from 0.91 to 3.82 μm.

Table B.1. Summary of the coating key structural properties and cellular response.

T_d (s)	ε_F (%)	Ra (μm)	Optical Density		Filopodia Formation
			After Day 7	After Day 14	
Spin-Coated	52	0.92	0.11	0.15	none
5	81	1.73	0.1	0.4	none
10	85	2.43	0.12	0.42	none
15	89	2.96	0.14	0.46	some
20	92	3.34	0.14	0.48	some
25	95	3.82	0.15	0.51	extensive

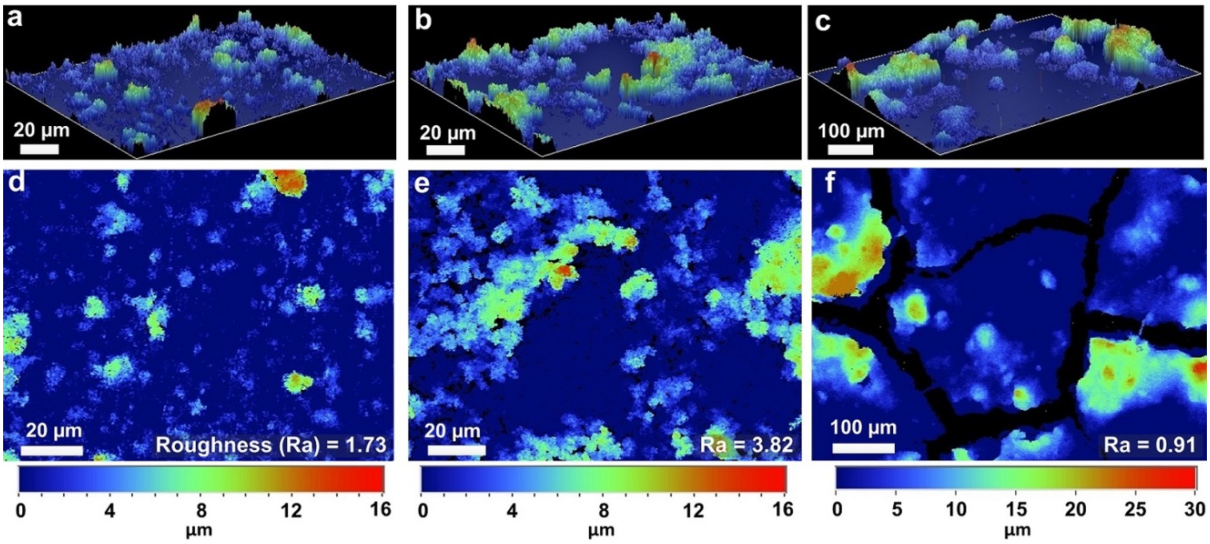

Figure 2. *WLI micrographs of aerosol-deposited coatings with (a,d) 5 s and (b,e) 25 s deposition time and comparison with the (c,f) spin-coated samples.*

B.3.2 Hierarchically-Driven Cell Response

The initial phases of cell communication with a surface are adhesion, spreading and proliferation. These cellular processes subsequently affect differentiation, mineralization and bio-integration.[21] Here, we have investigated the early-stage response of primary osteoblasts to six, well-defined, nano-textured micro-environments. From the cell's micro-scale perspective, the spin-coated surfaces are a quasi-two-dimensional topography (rms < 1 μm) while the aerosol-deposited coatings are micro-rough, three-dimensional environments. Murine femur cells with osteocalcin producing osteoblasts (Figure B.3a,b) were cultured in triplicate on each of the six HAp micro-environments and tissue culture plate, utilized as control.

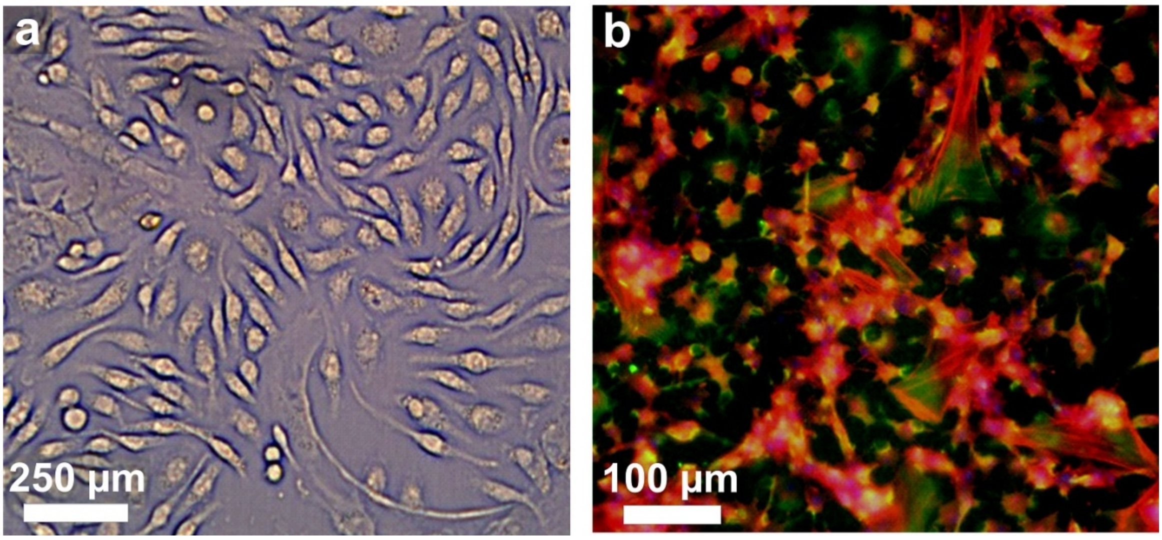

Figure B.3. *a) Isolated cells from mice femur, b) Osteocalcin producing osteoblasts.*

The response of murine osteoblast cells to these structurally different surfaces was initially assessed by proliferation assays and immunostaining. After 7 days of incubation, all micro-environments resulted in similar osteoblast proliferation (Figure B.4, blue bars). This reveals that the flame-made HAp nanoparticles are biocompatible and enable cell growth without additional surface functionalization. Most importantly, after 14 days, the proliferation dynamics on the different coating diverged and appeared to be promoted by the hierarchical structure. Between day 7 and 14, all the hierarchical coatings showed a statistically significant ($p \leq 0.05$), greater than 3-fold, increase in osteoblast proliferation (Figure B.4, pink bars). Increasing the average coating porosity from 81% to 95% increased the optical density from 0.41 to 0.52. Furthermore, while, in the tissue culture plates, cell numbers had roughly doubled after 14 days, the ultra-porous (95%) aerosol-deposited coatings resulted in a 3.5 fold increase in cell number indicating that very high porosity can promote cell proliferation. In stark contrast, on the spin-coated films very little proliferation was observed with the optical density increasing only from 0.15 to 0.11 (ca. 26%) during the same incubation period. This further substantiates that comparable composition and nano-texturing can result in drastically different cellular responses if presented in a different micro-structural context. As further discussed below, this is attributed to the promotion of early-stage surface adhesion that enables focal point signaling and re-mineralization.

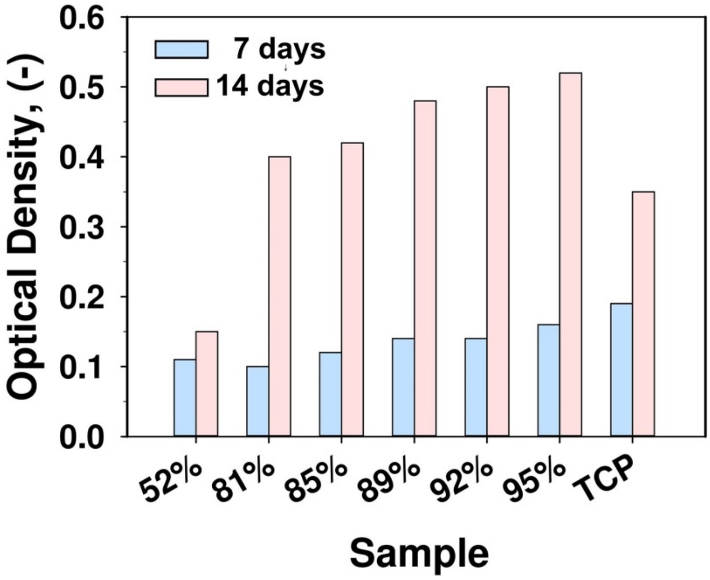

Figure B.4. *Optical density of samples with different film porosity (52 to 98%) and on the tissue culture plate (TCP) after 7 and 14 days incubation.*

Topographical analysis of cell spreading and protein expression revealed an increased cell-cell and cell-coating interaction with higher porosity. Figure B.5a-f show the co-expression of F-Actin and osteocalcin, a marker protein secreted only by osteoblast cells, on the surface of the 85% and 95% porous coatings. While the 85% porous coatings led to isolated high concentration of F-actin, the ultra-porous ones (95%) led to fibre interconnection across distant colonies, suggesting a higher level of cell-cell interaction. This significantly stronger and wide-spread F-actin expression suggests that the cells are responding to the micro- and nano-scale surface features of the ultra-porous coatings by early-stage adhesion and enhanced proliferation.

Mapping of osteocalcin expression confirmed that increasing structural hierarchy and porosity promote cell re-organization and biochemical activity. Osteocalcin is produced in the cytoplasm of osteoblasts and under optimal environmental conditions, is continuously secreted into the surrounding matrix. The 85% porous coatings were characterized by small osteocalcin domains co-localized with the F-actin expression, suggesting osteocalcin confinement to the cell cytoplasm. In contrast, in the 95% porous coatings, it was not possible to observe specific osteocalcin domains, suggesting its early-stage secretion from the cell into the HAp micro-environments. Osteocalcin secretion results in bone formation by promoting proliferation and stimulating expression of genes for collagen, osteonectin, osteopontin, and alkaline phosphatase production. This indicates that the ultra-porous coatings have reached an advanced stage of cellular re-organization that precedes osteon and bone formation.

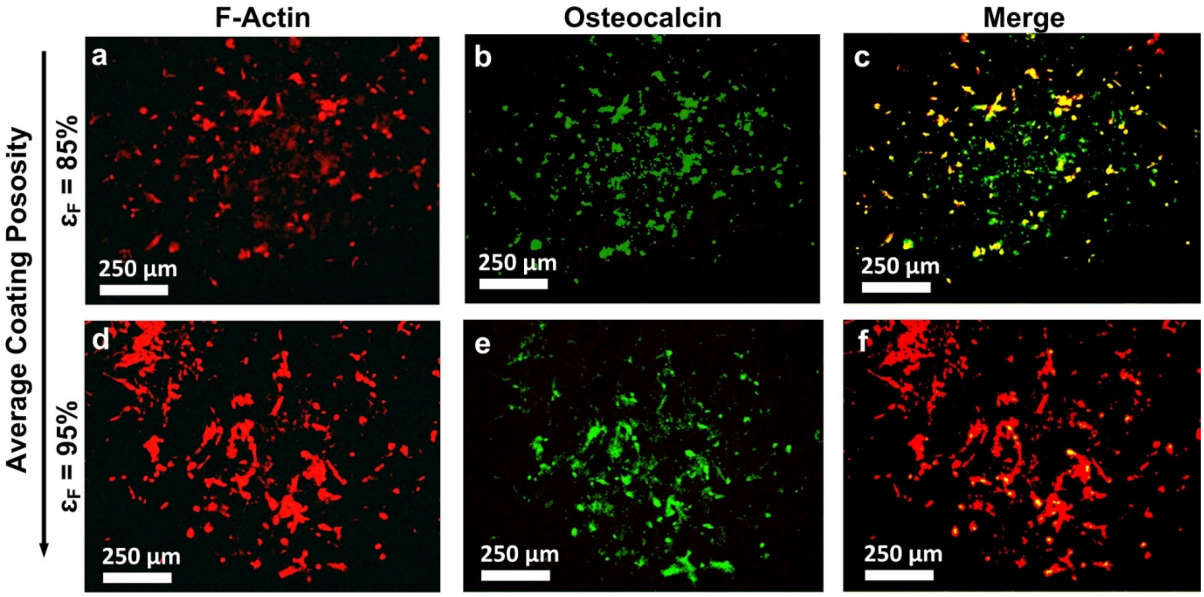

Figure B.5. *Cell spreading and the protein co-expression of F-Actin and Osteocalcin on the surface of HAp films with 85% (a-c) and 95% (d-f) porosities.*

The merged topographical mapping of F-actin and osteocalcin co-expression reinforces these observations demonstrating that the ultra-porous (95%) coatings induce osteocalcin expression between F-actin sites. As osteocalcin is a chemo-attractant,[22] the interaction between distantly located cells in these coatings is attributed to its secretion and collection along the surface micro-pores, resulting in a pathway for cell-cell recognition and communication. Our results suggest that, if accompanied by a nano-scale texturing, high micro-structural hierarchy (> 1 μm) is an osteo-inductive topographical feature. In fact, cellular adhesion is mediated by a series of adhesion proteins and specific integrin receptors at the cell membrane. In the first phase of attachment, the substratum gap between the cell and biomaterial is reduced from 50 nm to less than 15 nm resulting in the formation of F-actin rich focal adhesion points.[23] As a result of the observed protein co-expression, the hierarchical micro-roughness of the 95% porous coatings appear to reduce the migration time required by the cells to find a satisfactory location. This is expected to promote early-stage adhesion followed by signals that localize protein kinases and regulate the survival, growth, morphological deformation, migration, and differentiation of cells.[23]

B.3.3 Coating In-Growth and Cell-Cell Communication

The cell response was further investigated by scanning electron microscope (SEM) analysis of cell cultures after an incubation period of 14 days (Figure B.6). In line with the topographical mapping of the F-actin and osteocalcin co-expression, the cellular morphology was observed to respond to the coating porosity and structural hierarchy. The spin-coated samples were almost cell-free with a few surviving osteoblasts found mainly in the proximity of cracks (Figure B.6a). Surface examination revealed that most of the cells failed to adhere to the nano-textured surface. In contrast, the 81% porous coatings harboured a dense and homogenously distributed cell population (Figure B.6b). However, at this relatively low porosity, the cell morphology was predominantly circular with a diameter of a few micrometres and no visible cell-cell interaction. In these samples, only a few elongated cells were observed extending along the surface micro-pores. For both circular and elongated cells, the cell membrane showed minor deformations (Figure B.6f,j) in agreement with the observed F-actin and osteocalcin topography (Figure B.5a,b). This indicates an active and dense cell population but an early-stage of re-organization. Here, it is proposed that at 81%

porosity, the micro-sized pores (Table B.1) of the hierarchical coatings enable robust cell anchoring, but spatially-limit further growth resulting in mostly isolated semi-circular cells.

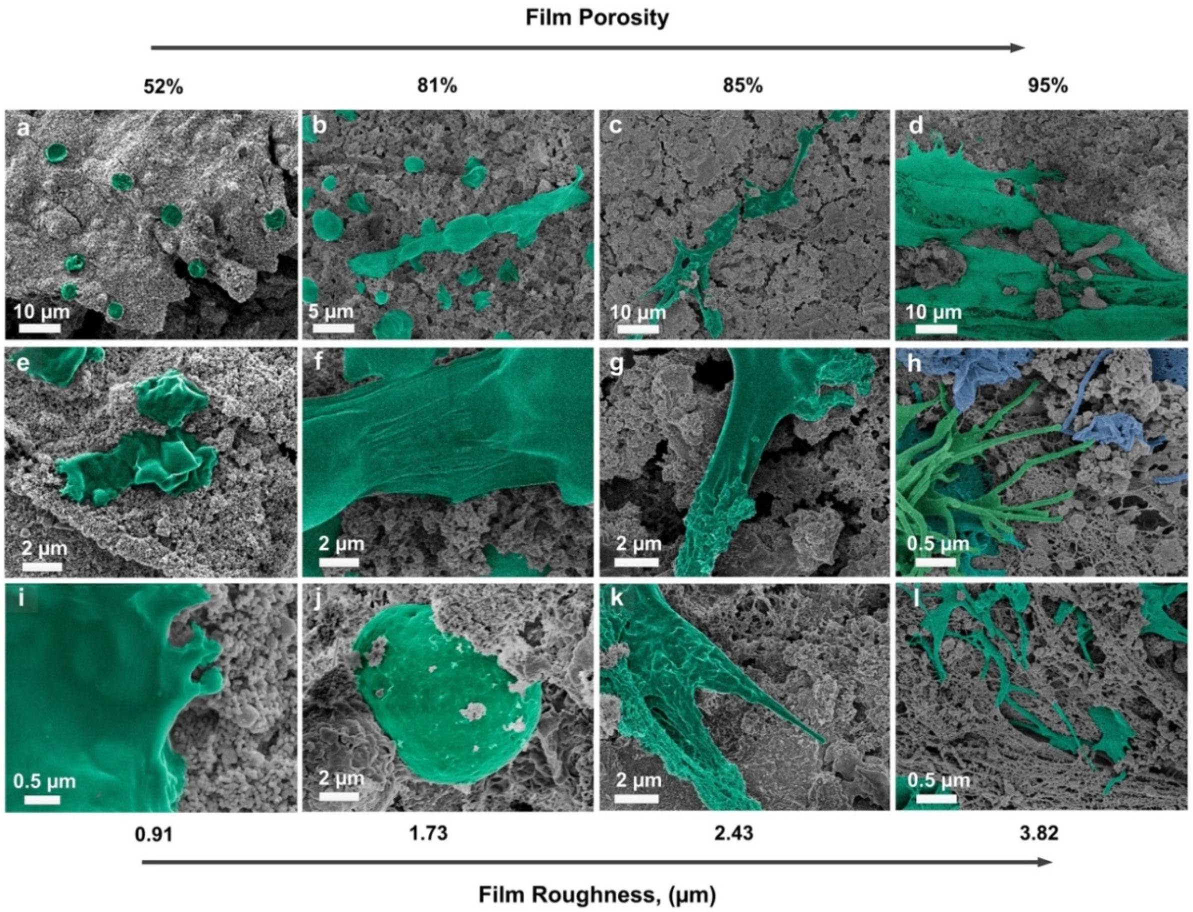

Figure B.6. *False colored SEM micrographs of cell attachment and growth on HAp coating prepared by (a,e,i) spin-coating and aerosol-deposition (b-l) with different porosity and micro-structural hierarchy.*

However, we found that increasing the structural hierarchy and porosity above 81% had a major impact on the resulting cell morphology and growth with cells becoming significantly bigger and exhibiting strong deformations of their membranes On the 95% porous coatings, we observed the formation of numerous nano-sized filopodia and tight junctions (Figure B.6.d,h,i). We also detected extensive penetration of these filopodia and cell infiltration into the inorganic coatings. Filopodia are F-actin rich cytoplasmic projections that cells use to probe their micro-environment. They are an important feature of cells during migration and wound healing. They serve as a first point of recognition and protrusion prior to signal transduction for cellular activity. Filopodia are known to play pivotal roles in cellular processes such as adhesion to the extracellular matrix, cellular migration and guidance towards organ development in embryogenesis. Here, filopodia formation and penetration into the underlying inorganic micro-environment is attributed to the multi-scale porosity of the ultra-porous coatings that enables early-stage cell adhesion and in-growth during gradual coating re-mineralization.[24]

B.3.4 Colonization Mechanisms of the Ultra-Porous Hierarchical Coatings

Hydroxyapatite micro-environments have been widely utilized for their promotion of cellular adhesion, differentiation[25] and osteogenesis[26]. However, here, we have observed for the first time that specific multi-scale nano- and micro-features can promote cell-cell communication and in-growth into an inorganic coating. This suggests that the contradictory results reported for similarly nano-textured HAp coatings may arise from different micro-scale features. These findings led us to propose a model (Figure B.7) of the key structural cues and surface colonization dynamics observed in the ultra-porous hierarchical coatings. We subdivide the cell's response in three main phases. In the first phase, the cells start the adhesion process by rapidly localizing stable adhesion/anchoring sites in the surface micro-pores. For the hierarchical coatings, this results in uniform colonization of the hierarchical surface, whereas on the quasi-two-dimensional surfaces, the cells seem to preferentially adhere to the proximity of cracks formed during the solvent evaporation process (Figure B.6a).

During the second phase, the adhered cells start to respond to the surrounding hierarchical environment. All the HAp coatings exhibit similar properties due to the equivalent nano-scale features and composition that results in comparable Ca^{2+} and PO_3^{-4} ion release rates. It is during this phase, where the combined micro- and nano-scale porosity plays a key role.

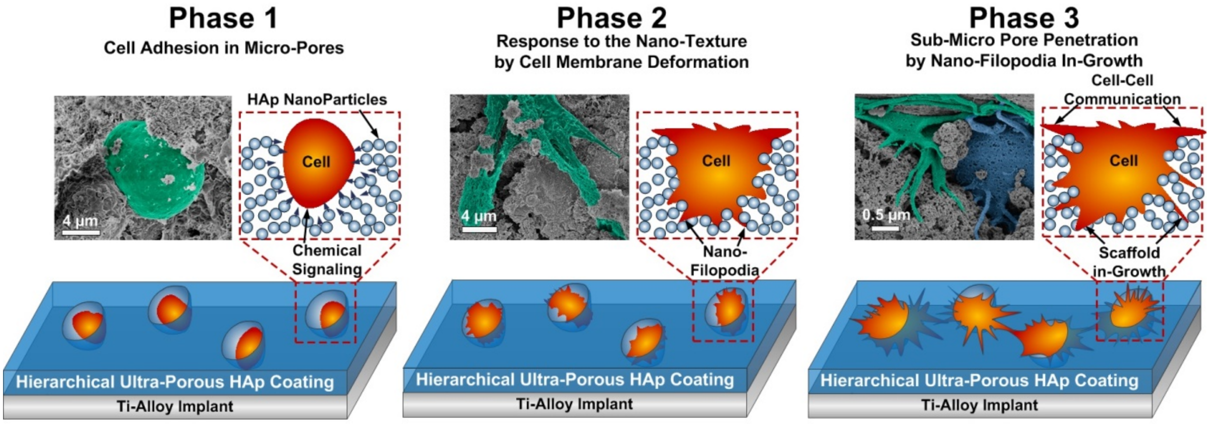

Figure B.7. *Schematic of the three main phases of micro-environment colonization proposed for the hierarchical ultra-porous (95%) nano-textured HAp coatings*

First, the large micro-size pores enable unconstrained cell growth and enhanced adhesion as observed by the extensive F-actin expression (Figure B.5d). Thereafter, the ultra-high porosity of these coatings signals to the cells low local-density, and thus space for growth promoting deformation of the cell membrane. In contrast, the cells perceive the small mesopore of the spin-coated films as a dense, impenetrable surface inhibiting cell growth and activity (Figure B.6a,e,i). The coating porosity required to induce widespread membrane deformation was found to be above 90%. This is similar to the density of the most active human trabecular bone regions.

In the third phase, the optimally adhered cells that are surrounded by sufficiently porous and chemically favorable micro-environments start to release osteocalcin. Its infiltration into the porous coating structure guides the growth of filopodia that respond to the mesopore texture by producing nano-scale elongated morphologies. This ultimately results in cellular in-growth into the coating improving bio-integration and long-term mechanical stability. In parallel to this vertical migration, the horizontal spreading of osteocalcin through the surface micro-pores enables cell-cell communication and recognition. This ultimately results in their inter-connection and very early-stage osteon formation. This last phase was observed only in the ultra-porous (95%) hierarchical coatings revealing that a set of specific multi-scale morphological features is required to advance from an osteo-conductive, second generation, biomaterial to an osteo-inductive third generation micro-environment able to communicate programmable cues for the adhesion, growth, proliferation and differentiation of cells.

B.4. Conclusions

In summary, natural cellular growth is characterized by active communication between neighbouring cells and surrounding extracellular matrix. Recent advances in biomaterial research have repeatedly proven the importance of nano-structures for successful tissue engineering. However, contrasting results have been reported for similar composition and nano-scale features. Here, we show that an extracellular nano- and micro-structural hierarchy can provide input to growing cellular tissue to promote proliferation, adhesion and scaffold in-growth. We demonstrate the one-step ultra-fast (≈ 25 s) synthesis of hierarchical coatings that significantly enhance bio-integration. This is driven by a synergistic chemical and morphological response of cells to more than 90% porous, micro-rough, nano-textured surfaces that results in early-stage cell adhesion, membrane deformation and nano-filopodia formation. These findings provide a well-defined set of structural parameters and a flexible ultra-fast coating technology to control the early-stage response of bone cells with potential application extending from bone grafting to implantable devices such as micro-chips for drug release, neural and cardiac function monitoring.

B.5. References

1. George, P. M.; Lyckman, A. W.; LaVan, D. A.; Hegde, A.; Leung, Y.; Avasare, R.; Testa, C.; Alexander, P. M.; Langer, R.; Sur, M., Fabrication and biocompatibility of polypyrrole implants suitable for neural prosthetics. *Biomaterials* **2005,** *26*, 3511-3519.

2. Junker, R.; Dimakis, A.; Thoneick, M.; Jansen, J. A., Effects of implant surface coatings and composition on bone integration: a systematic review. *Clin. Oral Implants Res.* **2009,** *20*, 185-206.

3. Goodman, S. B.; Yao, Z.; Keeney, M.; Yang, F., The future of biologic coatings for orthopaedic implants. *Biomaterials* **2013,** *34*, 3174-3183.

4. Ripamonti, U.; Roden, L. C.; Renton, L. F., Osteoinductive hydroxyapatite-coated titanium implants. *Biomaterials* **2012,** *33*, 3813-3823.

5. Roy, M.; Bandyopadhyay, A.; Bose, S., Induction plasma sprayed nano hydroxyapatite coatings on titanium for orthopaedic and dental implants. *Surf. Coat. Technol.* **2011,** *205*, 2785-2792.

6. Carradò, A., Nano-crystalline pulsed laser deposition hydroxyapatite thin films on Ti substrate for biomedical application. *J. Coating Tech. Res.* **2011,** *8*, 749-755.

7. Bloebaum, R. D.; Dupont, J. A., Osteolysis from a press-fit hydroxyapatite-coated implant: A case study. *J. Arthroplasty* **1993,** *8*, 195-202.

8. Alves, N. M.; Pashkuleva, I.; Reis, R. L.; Mano, J. F., Controlling Cell Behavior Through the Design of Polymer Surfaces. *Small* **2010,** *6*, 2208-2220.

9. Martínez, E.; Engel, E.; Planell, J. A.; Samitier, J., Effects of artificial micro- and nano-structured surfaces on cell behaviour. *Ann. Anat.* **2009,** *191*, 126-135.

10. Fielding, G. A.; Roy, M.; Bandyopadhyay, A.; Bose, S., Antibacterial and biological characteristics of silver containing and strontium doped plasma sprayed hydroxyapatite coatings. *Acta Biomater.* **2012,** *8*, 3144-3152.

11. Yeung, W. K.; Reilly, G. C.; Matthews, A.; Yerokhin, A., In vitro biological response of plasma electrolytically oxidized and plasma-sprayed hydroxyapatite coatings on Ti–6Al–4V alloy. *J. Biomed. Mater. Res., Part B* **2013,** *101B*, 939-949.

12. Roest, R.; Latella, B. A.; Heness, G.; Ben-Nissan, B., Adhesion of sol–gel derived hydroxyapatite nanocoatings on anodised pure titanium and titanium (Ti6Al4V) alloy substrates. *Surf. Coat. Technol.* **2011,** *205*, 3520-3529.

13. Tredwin, C. J.; Young, A. M.; Georgiou, G.; Shin, S.-H.; Kim, H.-W.; Knowles, J. C., Hydroxyapatite, fluor-hydroxyapatite and fluorapatite produced via the sol–gel method. Optimisation, characterisation and rheology. *Dent. Mater.* **2013,** *29*, 166-173.

14. Surmeneva, M. A.; Kovtun, A.; Peetsch, A.; Goroja, S. N.; Sharonova, A. A.; Pichugin, V. F.; Grubova, I. Y.; Ivanova, A. A.; Teresov, A. D.; Koval, N. N.; Buck, V.; Wittmar, A.; Ulbricht, M.; Prymak, O.; Epple, M.; Surmenev, R. A., Preparation of a silicate-containing hydroxyapatite-based coating by magnetron sputtering: structure and osteoblast-like MG63 cells in vitro study. *R. Soc. Chem. Adv.* **2013,** *3*, 11240-11246.

15. Sato, M.; Slamovich, E. B.; Webster, T. J., Enhanced osteoblast adhesion on hydrothermally treated hydroxyapatite/titania/poly (lactide-co-glycolide) sol–gel titanium coatings. *Biomaterials* **2005,** *26*, 1349-1357.

16. Ko, S. H.; Lee, D.; Kang, H. W.; Nam, K. H.; Yeo, J. Y.; Hong, S. J.; Grigoropoulos, C. P.; Sung, H. J., Nanoforest of Hydrothermally Grown Hierarchical ZnO Nanowires for a High Efficiency Dye-Sensitized Solar Cell. *Nano Lett.* **2011,** *11*, 666-671.

17. Tricoli, A.; Wallerand, A. S.; Righettoni, M., Highly Porous TiO_2 Films for Dye Sensitized Solar Cells. *J. Mater. Chem.* **2012,** *22*, 14254.

18. Tricoli, A.; Elmøe, T. D., Flame spray pyrolysis synthesis and aerosol deposition of nanoparticle films. *AlChE J.* **2012,** *58*, 3578-3588.

19. Tricoli, A.; Graf, M.; Mayer, F.; Kuühne, S.; Hierlemann, A.; Pratsinis, S. E., Micropatterning Layers by Flame Aerosol Deposition-Annealing. *Adv. Mater.* **2008,** *20*, 3005-3010.

20. Liu, Y.; Zha, S.; Liu, M., Novel Nanostructured Electrodes for Solid Oxide Fuel Cells Fabricated by Combustion Chemical Vapor Deposition (CVD). *Adv. Mater.* **2004,** *16*, 256-260.

21. Zaborowska, M.; Bodin, A.; Bäckdahl, H.; Popp, J.; Goldstein, A.; Gatenholm, P., Microporous bacterial cellulose as a potential scaffold for bone regeneration. *Acta Biomater.* **2010,** *6*, 2540-2547.

22. Wei, J.; Karsenty, G., An overview of the metabolic functions of osteocalcin. *Reviews in endocrine & metabolic disorders* **2015,** *16*, 93-98.

23. Sheets, K.; Wunsch, S.; Ng, C.; Nain, A. S., Shape-dependent cell migration and focal adhesion organization on suspended and aligned nanofiber scaffolds. *Acta Biomater.* **2013,** *9*, 7169-7177.

24. Hotulainen, P.; Lappalainen, P., Stress fibers are generated by two distinct actin assembly mechanisms in motile cells. *J. Cell Biol.* **2006,** *173*, 383-394.

25. Shih, Y.-R. V.; Hwang, Y.; Phadke, A.; Kang, H.; Hwang, N. S.; Caro, E. J.; Nguyen, S.; Siu, M.; Theodorakis, E. A.; Gianneschi, N. C.; Vecchio, K. S.; Chien, S.; Lee, O. K.; Varghese, S., Calcium phosphate-bearing matrices induce osteogenic differentiation of stem cells through adenosine signaling. *Proc. Natl. Acad. Sci. USA* **2014,** *111*, 990-995.

26. Venugopal, J.; Prabhakaran, M. P.; Zhang, Y.; Low, S.; Choon, A. T.; Ramakrishna, S., Biomimetic hydroxyapatite-containing composite nanofibrous substrates for bone tissue engineering. *Philos. Trans. A Math. Phys. Eng. Sci.* **2010,** *368*, 2065-81.